University of Kentucky
UKnowledge

University of Kentucky Doctoral Dissertations | Graduate School

2009

UTILIZING MIXED SURFACTANTS FOR SIMULTANEOUS PORE TEMPLATING AND ACTIVE SITE FORMATION IN METAL OXIDES

Mohammed Shahidur Rahman
University of Kentucky, msrahman@uky.edu

Right click to open a feedback form in a new tab to let us know how this document benefits you.

Recommended Citation

Rahman, Mohammed Shahidur, "UTILIZING MIXED SURFACTANTS FOR SIMULTANEOUS PORE TEMPLATING AND ACTIVE SITE FORMATION IN METAL OXIDES" (2009). *University of Kentucky Doctoral Dissertations*. 693.
https://uknowledge.uky.edu/gradschool_diss/693

This Dissertation is brought to you for free and open access by the Graduate School at UKnowledge. It has been accepted for inclusion in University of Kentucky Doctoral Dissertations by an authorized administrator of UKnowledge. For more information, please contact UKnowledge@lsv.uky.edu.

ABSTRACT OF DISSERTATION

Mohammed Shahidur Rahman

The Graduate School

University of Kentucky

2009

UTILIZING MIXED SURFACTANTS FOR SIMULTANEOUS PORE TEMPLATING AND ACTIVE SITE FORMATION IN METAL OXIDES

ABSTRACT OF DISSERTATION

A dissertation submitted in partial fulfillment of the
requirements for the degree of Doctor of Philosophy in the
College of Engineering
at the University of Kentucky

By

Mohammed Shahidur Rahman

Lexington, KY

Director: Dr. Stephen E. Rankin, Professor of Chemical Engineering

Lexington, Kentucky

2009

Copyright © Mohammed Shahidur Rahman 2009

ABSTRACT OF DISSERTATION

UTILIZING MIXED SURFACTANTS FOR SIMULTANEOUS PORE TEMPLATING AND ACTIVE SITE FORMATION IN METAL OXIDES

Self-assembled nonionic alkyl glycoside surfactants are of interest for creating functional adsorption and catalytic sites at the surface of mesoporous metal oxides, but they typically impart poor long-range order when used as pore templates. Improved order and control over the functional site density may be achieved by mixing them with a cationic surfactant. To confirm this hypothesis, we investigate the lyotropic liquid crystalline (LLC) phase behavior of aqueous solutions of the functional nonionic surfactant n-dodecyl β-D-maltoside ($C_{12}G_2$) and cationic cetyltrimethylammonium bromide (C_{16}TAB). A ternary phase diagram of the C_{16}TAB-$C_{12}G_2$-water system is developed at 50 °C. By replacing the volume of water in the phase diagram with an equivalent volume of silica, ordered mesoporous materials are prepared by nanocasting with variable $C_{12}G_2$/C_{16}TAB ratios. Metal oxide mesophases can almost always be predicted from the ternary phase diagram, except that silica prepared with high $C_{12}G_2$/C_{16}TAB ratios are very weakly ordered, perhaps due to differences in hydrogen bonding or rate of assembly.

Based on the ternary phase diagram of the system, a systematic approach is taken to the incorporation of titania sites via complexation to the maltoside headgroup of $C_{12}G_2$. Complexation to a saccharide is expected not only to guide titanium to the pore surface, but also to prevent uncontrolled hydrolysis and condensation of the (usually quite reactive) titanium precursor. Tetrahedrally coordinated titanium atoms incorporated into a silica network are believed to be the active oxidation sites required for heterogeneous silica-supported titania oxidation catalysts. To promote well-ordered materials and to allow control over titania site density, the mixed $C_{12}G_2$ / C_{16}TAB system is used for pore templating. Series of Si-Ti mixed oxide thin films and bulk materials are synthesized with different amounts of titanium loading by utilizing pre-complexation between $C_{12}G_2$ and titanium isopropoxide. The degrees of homogeneity (indicated by tetracoordinated Ti) in these films are superior to those of films synthesized with the same loading of titanium but without $C_{12}G_2$ or without pre-complexation. Transition metal-carbohydrate complexation provides highly dispersed, tetrahedrally coordinated titanium atoms rather than the octahedral sites found without saccharide complexation.

KEYWORDS: Mesoporous, mixed surfactant templating, mixed metal oxides, nano-casting, evaporation induced self-assembly

Mohammed Shahidur Rahman

02/03/2009

UTILIZING MIXED SURFACTANTS FOR SIMULTANEOUS PORE TEMPLATING AND ACTIVE SITE FORMATION IN METAL OXIDES

By

Mohammed Shahidur Rahman

Dr. Stephen E. Rankin
Director of Dissertation

Dr. Barbara L. Knutson
Director of Graduate Studies

Date: 02/03/2009

RULES FOR THE USE OF DISSERTATIONS

Unpublished dissertations submitted for the Doctor's degree and deposited in the University of Kentucky Library are as a rule open for inspection, but are to be used only with due regard to the rights of the authors. Bibliographical references may be noted, but quotations or summaries of parts may be published only with the permission of the author, and with the usual scholarly acknowledgments.

Extensive copying or publication of the dissertation in whole or in part also requires the consent of the Dean of the Graduate School of the University of Kentucky.

A library that borrows this dissertation for use by its patrons is expected to secure the signature of each user.

Name Date

_____

_____

_____

_____

_____

_____

_____

_____

_____

_____

DISSERTATION

Mohammed Shahidur Rahman

The Graduate School

University of Kentucky

2009

UTILIZING MIXED SURFACTANTS FOR SIMULTANEOUS PORE TEMPLATING AND ACTIVE SITE FORMATION IN METAL OXIDES

DISSERTATION

A dissertation submitted in partial fulfillment of the
requirements for the degree of Doctor of Philosophy in the
College of Engineering
at the University of Kentucky

By

Mohammed Shahidur Rahman
Lexington, KY

Director: Dr. Stephen E. Rankin, Professor of Chemical Engineering
Lexington, Kentucky

2009

Copyright © Mohammed Shahidur Rahman 2009

This Dissertation is Dedicated to My Father,

Md. Wahidur Rahman:

Who inspired me the most throughout my life.

ACKNOWLEDGEMENTS

The work documented in this dissertation was benefited from the tremendous inspiration, insight, assistance, and guidance of several people throughout the entire work. First and foremost, I would like to express my deepest gratitude to my advisor, Dr. Stephen E. Rankin, for giving me the opportunity to be a part of his research group at the University of Kentucky. Without his consistent scholarly guidance and support throughout this work, this research work and this dissertation would have never existed. He definitely helped me to develop and polish my independent thinking and problem solving approaches, essential components to conduct challenging research work.

I would like to give special thank to Dr. Alan Dozier of the Electron Microscopy Facility for his valuable time in helping me to perform some electron microscopic studies of my samples. I would also like to thank Dr. Barbara Knutson, Dr. Kimberly Anderson and Dr. Dibakar Bhattacharyya for allowing me to use their optical microscopy facilities. My special thanks go to my some lab mates, especially Rong Xing and Venkat Koganti who helped me initially to start my research and made my research work enjoyable.

In addition I am extremely grateful for the support and encouragement from my parents, my wonderful wife, and from the rest of my family. For all your encouragement and continuous support throughout my graduate school, I thank you all. Especially I would like to thank my wife, Mehnaz Sultana, for her day-to-day support, encouragement, and persistent patience. None of this would have been possible without the constant encouragement from my father, who passed away on May 14, 2008. Every single of his advice has motivated me to be a better person. There are no words to adequately express my appreciation and gratitude to him.

TABLE OF CONTENTS

Acknowledgements iii

List of Tables vii

List of Figures viii

Chapter 1. Introduction 1
1.1 Research Hypotheses and Objectives 3
1.2 Dissertation Outline 4

Chapter 2. Literature Review 6
2.1 Surfactant Templated Mesoporous Materials 6
2.2 Titanium-Containing Silica Mesoporous 8
2.3 Surfactant Templates in Nanoporous Silica Synthesis 10
2.4 Liquid Crystal Phases and Their Identifications 13
2.5 Surfactant-Templated Mesostructured Silica Formation Routes 14
2.5.1 Cooperative Self-Assembly 15
2.5.2 True Liquid Crystal Templating (LCT) 17
2.5.3 Evaporation Induced Self-Assembly (EISA) 17
2.6 Sol-Gel Processing 20
2.6.1 Silica Polymerization 20
2.6.2 Gelation and Aging 24
2.6.3 Drying 25
2.7 Predictive Synthesis of Mesostructured Materials 26
2.8 Mixed Surfactant Templating 27
2.9 Materials Characterization Techniques 29
2.9.1 Nitrogen Sorption Analysis 29
2.9.2 Fourier Transform Infrared (FTIR) Spectroscopy 33
2.9.3 Powder X-ray Diffraction (PXRD) 34
2.9.4 Transmission Electron Microscopy (TEM) 35
2.9.5 Ultraviolet-Visible (UV-vis) Spectroscopy 36

Chapter 3. Ternary Lyotropic Liquid Crystalline Phase Diagram of Aqueous Mixtures of Maltoside and Cationic Surfactants and Its Use for Predictive Synthesis of Ordered Mesoporous Silica 40
3.1 Summary 40
3.2 Introduction 41
3.3 Experimental 44
3.3.1 Materials 44
3.3.2 Phase characterization 44
3.3.3 Predictive Synthesis of Mesoporous silica 45
3.3.4 Characterization 46

3.4 Results and Discussion 47
3.4.1 Phase Behavior of the Ternary C16TAB-DM-Water System 47
3.4.2 Predictive Synthesis of Mesoporous Silica 50
3.5 Conclusions 56

Chapter 4. Incorporation of Isolated Ti Sites into Silica Thin Films with 3-D Accessible Pores by Surfactant Complexation 67
4.1 Summary 67
4.2 Introduction 68
4.3 Experimental 72
4.3.1 Materials 72
4.3.2 Film Synthesis 72
4.3.3 Characterization 74
4.4 Results and Discussion 75
4.4.1 Pore Structure Characterization by XRD and TEM 77
4.4.2 N_2 Sorption Characterization 81
4.5 Quantitative Comparison between the Liquid Crystalline Phase and the Observed Mesostructure 81
4.6 Conclusions 83

Chapter 5. Synthesis of Si-Ti Mixed Oxide Mesoporous Powders by Sugar Surfactant Complexation 89
5.1 Summary 89
5.2 Introduction 89
5.3 Experimental 93
5.2.1 Materials 93
5.2.2 Synthesis 93
5.2.3 Characterization 95
5.4 Results and Discussion 95
5.5 Conclusions 98

Chapter 6. Glucose Molecular Imprinting of Silica 105
6.1 Summary 105
6.2 Introduction 106
6.2.1 Non-covalent Imprinting in Silica 109
6.2.2 Imprinting Process 111
6.3 Experimental 116
6.3.1 Chemicals 116
6.3.2 Synthesis methods 116
6.3.3 Glucose Adsorption Experiments 120
6.3.4 Methods 121
6.4 Results and Discussion 123
6.4.1 Materials Characterization 123
6.4.2 Glucose Adsorption 127
6.5 Conclusions 130

Chapter 7. Conclusions and Future Work.....148
7.1 Conclusions.....148
7.2 Future Work.....153

References.....156

Vita.....175

LIST OF TABLES

TABLE PAGE

3.1 Structural Properties of Series-1 Materials (Samples 1 to 6).....58

5.1 Structural Properties of the calcined materials 99

6.1 Examples of successful non-covalent molecular imprinting of silica 132

6.2 Structural properties of some non-imprinted silicas. 132

LIST OF FIGURES

FIGURE PAGE

2.1 Schematic representation of an ideal sequence of the formation of surfactant micelles structures along with their relationship with packing parameters and shapes of surfactant in micelles on increasing surfactant volume fraction in water (solvent). Also the expected typical lyotropic liquid crystalline phases for such aggregates are shown. 38

2.2 IUPAC classification of gas adsorption isotherms. 39

3.1 Low angle powder XRD patterns of the representative LLC phases observed with the $C_{16}TAB$-$C_{12}G_2$-water system investigated at 50 °C. (a) H_I phase ($C_{16}TAB$ = 35 wt%, $C_{12}G_2$ = 35 wt%, H_2O = 30 wt%); (b) Q_I phase ($C_{16}TAB$ = 35 wt%, $C_{12}G_2$ = 40 wt%, H_2O = 25 wt%); (c) L_α phase ($C_{16}TAB$ = 30 wt%, $C_{12}G_2$ = 65 wt%, H_2O = 5 wt%), (d) R phase ($C_{16}TAB$ = 75wt%, $C_{12}G_2$ = 5wt%, H_2O = 20 wt%). 59

3.2 Ternary phase diagram of $C_{16}TAB$-$C_{12}G_2$-water system at 50 °C. The accuracy of all phase boundaries except the ones plotted with dashed lines should be within ±1 wt%. The accuracy of dashed phase boundaries could be > ±1 wt%. Black stars represent a set of synthesized mesoporous silica materials consistent with the phase diagram. ○: Series-1 materials (Samples 1-6); ■: Series-2 materials (Samples 7-9); ◊: Series-3 materials (Samples 10-16). 60

3.3 Representative powder XRD patterns of the as-synthesized silica with (a) 2D-hexagonal phase with p6mm space group ($C_{16}TAB$ = 20 wt%, $C_{12}G_2$ = 50 wt%, H_2O = 30 wt%) and (b) cubic phase with Ia3d space group ($C_{16}TAB$ = 40 wt%, $C_{12}G_2$ = 50 wt%, H_2O = 10 wt%). 61

3.4 Powder X-ray diffraction patterns of the as-synthesized (left column) and calcined (right column) mesoporous silica materials of Series-1, Sample-1 to -6, prepared from mixed micelles of $C_{16}TAB$ and $C_{12}G_2$ with various ratios (wt%) of $C_{12}G_2$/$C_{16}TAB$. The ratios are (a) 0/60, (b) 20/40, (c) 30/30, (d) 40/20, (e) 50/10, and (f) 60/0. 62

3.5 Representative TEM images of as-synthesized silica with (a) well-ordered 2D-hexagonal structure ($C_{16}TAB$ = 20 wt%, $C_{12}G_2$ = 40 wt%, H_2O = 40 wt%) and (b) disordered hexagonal or wormhole-like structure $C_{16}TAB$ = 10 wt%, $C_{12}G_2$ = 50 wt%, H_2O = 40 wt%). 63

3.6 (a) Nitrogen adsorption-desorption isotherms of the calcined Samples -1 to -6. (b) KJS (modified BJH) pore size distributions for Samples -1 to -6, derived from their corresponding adsorption isotherm branches. 64

3.7 (a) Powder XRD patterns of the as-synthesized Series-2 (Sample-7 to -9) materials prepared with pure $C_{12}G_2$ surfactant; (b) representative low angle powder XRD patterns of the H_I (60 wt% $C_{12}G_2$ in water) and Q_I (76.5 wt% $C_{12}G_2$ in water) LLC phases observed with pure $C_{12}G_2$ surfactant. 65

3.8 Comparison of powder XRD patterns of the as-synthesized Series-3 materials synthesized along the phase boundary separating H_I from Q_I phase: (a) Sample-10 (C_{16}TAB = 65 wt%, $C_{12}G_2$ = 12.5 wt%); (b) Sample-11 (C_{16}TAB = 52.5 wt%, $C_{12}G_2$ = 22.5 wt%); (c) Sample-12 (C_{16}TAB = 40 wt%, $C_{12}G_2$ = 30 wt%); (d) Sample-13 (C_{16}TAB = 35 wt%, $C_{12}G_2$ = 40 wt%); (e) Sample-14 (C_{16}TAB = 60 wt%, $C_{12}G_2$ = 20 wt%); (f) Sample-15 (C_{16}TAB = 50 wt%, $C_{12}G_2$ = 30 wt%); (g) Sample-16 (C_{16}TAB = 35 wt%, $C_{12}G_2$ = 45 wt%). The peaks represented by star are from the C_{16}TAB crystalline salt. 66

4.1 UV-visible transmission spectra of calcined Si-Ti mixed oxide thin films coated on quartz glass substrate. (a) Spectra of Type-1 films at different Ti loadings and (b) Type-2 films at different Ti loadings and Type-3 film with a Ti loading of Si/Ti= 42. 84

4.2 XRD patterns of as-synthesized and calcined Si-Ti mixed oxide thin films at various Ti loadings coated on Si wafer substrate. (a) As-synthesized Type-1 films. Inset: variation of FWHM width of (100) reflection with Ti loading; (b) calcined Type-1 films; (c) as-synthesized Type-2 films. Inset: FWHM width of (100) reflection as a function of Ti loading, and (d) calcined Type-2 films. 85

4.3 Low-angle X-ray diffraction patterns obtained from the corresponding powder samples of Si-Ti mixed oxides thin films prepared with Si/Ti = 86. (a) Type-1 films: I- as-synthesized and II- calcined. (b) Type-2 films: I- as-synthesized and II- calcined. Both confirm the formation of Pm3n cubic phases. In both figures (a) and (b), inset shows the relationship between $1/d_{hkl}$ and $(h^2 + k^2 + l^2)^{1/2}$. 86

4.4 STEM images for the Pm3n cubic mesostructured Si-Ti mixed oxides thin films prepared with Si/Ti = 86. Images a – c of the calcined Type-1 film are recorded along the [100], [110], and [210] directions, respectively. Images e and f of the calcined Type-2 film are recoded along the [110] and [111] directions, respectively. 87

4.5 N_2 adsorption-desorption isotherms obtained from the calcined power sample of Type-1 films (Si/Ti = 86). (•): adsorption and (o): desorption. Inset: The corresponding KJS pore size distribution curve obtained from the adsorption branch.....88

5.1 Ternary phase diagram of the β-$C_{12}G_2$-C_{16}TAB-water system at 50 ˚C, used to guide the synthesis of Si-Ti mixed oxides materials. Selected surfactants compositions for predictive synthesis are shown on the arrow, indicating a constant surfactant content line equivalent of 54 wt% of water. 100

5.2 Low angle powder XRD patterns recorded on both the as-synthesized and calcined Si-Ti mixed oxides materials with variable Ti loadings: (a) Si/Ti = 86, (b) Si/Ti = 28, and (c) Si/Ti = 16. Solid lines represent as-synthesized samples and dotted lines are for the calcined samples.....101

5.3 Nitrogen sorption isotherms of the calcined samples at 77 K. (a) Nitrogen adsorption-desorption isotherms obtained from the different Si-Ti mixed oxides materials with variable compositions of Si/Ti, (b) adsorption-desorption isotherms shown in logarithmic scale.....102

5.4 Representative standard high-resolution αs-plot for the sample prepared with Si/Ti = 86.. 103

5.5 KJS pore-size distributions of the samples with variable Si/Ti ratios, obtained from their corresponding adsorption branches. 104

6.1 Schematic representation of the formation of recognition cavity into the silica matrix by non-covalent molecular imprinting. A and B could be different organic functional groups with silanes, such as -$CH_2CH_2CH_2NH_2$ or $CH_2CH_2CH_2NHCONH_2$. 133

6.2 FTIR-ATR Calibration curve of aqueous glucose solution 134

6.3 FTIR-ATR absorption spectra of aqueous glucose solutions used to construct calibration curve. (a) Spectra of nine different aqueous glucose samples ranging from 0.025M to 0.35M with water spectrum, and (b) difference spectra of the same samples when spectrum of water subtracted from that of different glucose solutions. 135

6.4 Results of the colorimetric glucose assay. (a) Characteristic absorption curves of D-glucose, and (b) calibration curve for D-glucose.....136

6.5 The relation between the gelation time in the base-step and the amount of 0.1N NaOH added as a base catalyst. Molar ratio of TEOS: water (acidic fraction): ethanol is 1.0:4.0:2.5 with [HCl]= 0.01 M.....137

6.6 (a) Nitrogen adsorption-desorption isotherms of the non-imprinted silica prepared with different amount of 0.1 N NaOH base catalyst and (b) their corresponding BJH pore size distribution derived from adsorption branches.....138

6.7 FT-IR absorption spectra of glucose imprinted non-functionalized silica. (a) as-synthesized; (b) after 2nd step of water extraction; (c) after 4th step of water extraction.....139

6.8 (a) Nitrogen adsorption-desorption isotherms for the imprinted silica upon removal the template glucose and the non-imprinted sample, and (b) the corresponding BJH pore size distributions derived from their adsorption branches.. 140

6.9 FTIR spectra of (a) amine-functionalized as-synthesized non-imprinted silica, and (b) non-functionalized non-imprinted silica. 141

6.10 Nitrogen adsorption-desorption isotherms of the glucose imprinted amine functionalized silica upon removal of templates. Insert: Corresponding BJH pore size distribution derived from the adsorption branch. 142

6.11 Nitrogen adsorption-desorption isotherms of the non-imprinted amine functionalized silica. Insert: Corresponding BJH pore size distribution derived from the adsorption branch. 143

6.12 D-glucose adsorption isotherms developed from the glucose imprinted and the non-imprinted silicas. (a) In the dilute concentration range, and (b) in the higher concentration range. 144

6.13 D-Glucose adsorption isotherms estimated in the lower glucose concentration range. (a) The amine-functionalized non-imprinted silica, and (b) the amine-functionalized D-glucose imprinted silica. 145

6.14 D-glucose adsorption isotherms for the amine-functionalized silica estimated in the higher concentration range: (a) non-imprinted, and (b) imprinted silica. 146

6.15 Glucose adsorption isotherms derived from the glucose imprinted and non-imprinted silica thin films. 147

CHAPTER 1
INTRODUCTION

Porous materials are of scientific and technological interests because of their applications in a variety of fields including catalysis, separations, adsorbents, sensors, drug delivery, optics, electronics, etc.[1-4] According to the International Union of Pure and Applied Chemistry (IUPAC) definition of pore size, porous materials are categorized into three classes: microporous materials with pore sizes smaller than 2 nm, mesoporous materials with pore sizes 2 to 50 nm and macroporous materials with pore sizes larger than 50 nm.[5] Among the different classes of porous materials, zeolites, pillared layered solids, ordered mesoporous silicas, porous gels, and porous glasses are widely studied because of their applications as versatile catalysts, supports for catalysts, adsorbents, and size-selective separation media. Crystalline microporous zeolites are hydrated aluminosilicates with cage-like frameworks consisting of three-dimensional arrays of tetrahedral units of SiO_4 and $A1O_4$ connected via the oxygen atoms at the corner points of the tetrahedra.[6] Zeolites constitute one of the most important classes of microporous materials. They possess desirable catalytic properties such as (a) high surface area, (b) narrow pore size distribution, (c) active acidic sites with tailorable densities, strengths, distributors, and stabilities, (d) tunable molecule-scale pores that make them true shape-selective molecular sieves, and (e) high thermal and chemical stability.[2] All these properties have led to extremely successful applications of zeolites as catalysts for modern petroleum and chemical industries. However, their applications are limited to relatively small molecules because of their small cavities and channels. Therefore a rational synthesis approach has been taken to make porous materials with larger pores. Larger pores are present in porous glasses and gels, but their pores are disordered and their pore size distributions are very broad. In the search for materials with narrowly distributed meso- and macro- pores, researchers have synthesized pillared layered solids from layered oxide materials by supporting amorphous oxide layer with inorganic pillars in the interlamellar region.[7] Unfortunately, these types of materials also have failed to

exhibit narrow mesopore size distributions, and it is difficult to avoid the presence of additional micropores.

In 1992, scientists at Mobil Research and Development Corporation reported the breakthrough synthesis of regularly ordered mesoporous aluminosilicate / silicate molecular sieves with very narrow pore size distributions by extending the concept of zeolite templating with quarternary ammonium salts to surfactant arrays.[8, 9] These materials are designated as members of the M41S family and are characterized by highly organized pores with a constant pore dimension in the range from 1.5 to over 10.0 nm and high specific surface areas up to 1500 m^2/g.

Mesoporous silica molecular sieves containing isolated transition metals have drawn a great deal of attention in the past decade as an important class of heterogeneous supported catalysts. Silica by itself is not catalytically active, but the synthesis of surfactant templated mesoporous materials has opened a new door to doping mesoporous silica materials with a variety of metals for the development of catalytically active materials.[4, 10-14] Catalytic activity arises from the variable oxidation states of transition metals, a property not possessed by silica. Also because of their electronic structure, this class of materials is not only useful in catalysis, but also in electronic, magnetic and optical applications.

The silica surface can also be functionalized and imprinted to make imprinted silica gels and thin films with high selectivity and specificity for molecular recognition in solution. Generation of specific binding sites at the silica surface has been proposed to be possible via the polymerization of silica monomers around an imprint / template molecule. The recognition property of the imprinted cavity is hypothesized to be mainly due the well-defined shape of the imprinted sites and the predetermined orientation of the functional groups on the silica surface.[15] Sometimes the molecular selectivity of the imprinted material can be improved through the incorporation of organic moieties into the silica network.[16] Silica gels and thin films with highly specific recognition sites have great potential for applications in separations, catalysis, chemical sensing, and enzyme mimicry.[15, 17-19]

1.1 Research Hypotheses and Objectives

Self-assembled nonionic alkyl glycoside surfactants are of interest for creating functional adsorption and catalytic sites at the surface of mesoporous sol-gel-derived materials. These types of carbohydrate based surfactants can serve as "green" alternatives to traditional surfactants as they are biodegradable and are synthesized from naturally occurring renewable resources. They also possess multiple closely-spaced hydroxyl groups through which they can bind to metal oxide precursors and surfaces. However, it is sometimes very difficult to assemble nonionic surfactants into liquid crystals and template materials with a high degree of long-range order, as they typically participate in relatively weak hydrogen bonding (rather than electrostatic) interactions with water, silicates and other inorganic oxides present during material synthesis. Sugar-based surfactants can also show strong headgroup packing effects that impair their ability to assembly into lyotropic phases. Thus they impart poor long-range order when they are used as pore templates. Our hypothesis is that improved mesostructural ordering and control over the functional site density can be achieved by mixing the alkyl polyglycoside surfactant n-dodecyl β-D-maltoside ($C_{12}G_2$) with a cationic surfactant, such as the frequently used cetyltrimethylammonium bromide (C_{16}TAB). One of our objectives here is to accomplish this without trial-and-error experimentation by developing a lyotropic liquid crystalline phase diagram of this mixed surfactants system in water that provides a fundamental basis for the selection of compositions for the predictive synthesis of rationally designed nanoporous materials.

The use of a sugar-based surfactant is hypothesized to be particularly beneficial for catalyst preparation by the sol-gel method. Sol-gel chemistry provides an opportunity to produce well mixed metal oxides materials using mixtures of purified metal alkoxide precursors, but the high reactivity of titanium precursors compared to analogous silicon precursors impedes the molecular-level incorporation of Ti(IV) into a silica matrix by Si-O-Ti bridges. Tetrahedrally coordinated Ti(IV) ions within a silica matrix are believed to be the active sites for heterogeneous oxidation catalysis in titanosilicates such as the zeolite TS-1. Modification of transition metal alkoxides by bidentate chelating agents has been shown to be a viable approach for stabilizing transition metal alkoxides for subsequent hydrolysis and condensation. Saccharides and their derivatives are well

known as potential ligands for transition metals in inorganic chemistry and biology. The hypothesis underlying the use of sugar-based surfactants for catalyst preparation is that preferential interactions or possible complexation between the titanium atoms of a Ti precursor and the maltoside headgroup of the sugar-based surfactant should not only position Ti selectively at the micelle / silica interface, but also inhibit fast hydrolysis and condensation of the titanium alkoxide, thus promoting homogeneous incorporation of titania at the pore surface. In this dissertation, we utilize the possibility of chelation between titanium and the headgroup saccharides of n-dodecyl β-D-maltoside ($C_{12}G_2$) to stabilize a titanium alkoxide and to develop a novel methodology for the synthesis of silica-supported titanium catalytic sites. To promote well-ordered materials and to allow control over titanium site density, the mixed surfactant system of $C_{12}G_2$ and C_{16}TAB will be used for pore templating. This part of the dissertation work involves spectroscopic investigations to confirm that complex formation between maltoside and titanium alkoxide leads to the incorporation of Ti(IV) ions selectively into a silica network.

Low temperature sol-gel processing of silica offers another advantage – the possibility of creating recognition sites on the silica surface through molecular imprinting. This concept is explored in this dissertation by the synthesis of non-covalent molecularly imprinted bulk sol-gel materials with the goal of determining whether they can adsorb the imprint molecule from an aqueous solution at a higher level compare to their non-imprinted counterparts. Another objective of this part of the dissertation is to demonstrate the degree to which affinity and recognition for the imprint molecule can be improved by incorporating organic function groups at the binding sites through one-pot co-condensation of silica precursors with organically modified silanes.

1.2 Dissertation Outline

This chapter presented only a very brief introduction to different types of porous materials and some unique advantages of surfactant templated mesoporous materials over other microporous and mesoporous materials. This will be expanded in Chapter 2 with a brief review of pertinent literature on synthesis and applications of mesoporous silica and titanosilicate materials, thermodynamics of formation of surfactant liquid crystalline

phases and their application in the synthesis of nanoporous materials, sol-gel chemistry of silica to yield different mesostructures and morphologies, advantages of mixed surfactant templating, and finally different characterization techniques used in this dissertation. Development of the lyotropic liquid crystalline phase diagram of aqueous surfactant mixtures of cetyltrimethylammonium bromide (C_{16}TAB) and n-dodecyl β-D-maltoside ($C_{12}G_2$/DM) and predictive synthesis of ordered mesoporous silica materials are described in Chapter 3. Preferential interactions or possible complexation between the nonionic maltoside surfactant and titanium precursor are utilized to incorporate isolated titanium ions in mesoporous silica films and this is described in Chapter 4. This is followed by the synthesis of Si-Ti mixed oxide mesoporous powders by sugar-based surfactant complexation for potential applications in heterogeneous catalysis in Chapter 5. Utilization of the non-covalent molecular imprinting approach to synthesize D-(+)-glucose imprinted functionalized and non-functionalized silica materials is discussed in Chapter 6. The last chapter gives a summary of the dissertation and some suggestions for future work.

CHAPTER 2
LITERATURE REVIEW

This chapter is primarily intended to provide an overview of surfactant templated silica mesoporous materials, with particular emphasis on titanium incorporation. A concise introduction to the synthesis and applications of titanium-containing silica mesoporous materials is given first. This chapter also summarizes some important aspects related to the formation of different lyotropic liquid crystalline phases from self-assembled surfactants and their direct applications as templates in the synthesis of nanoporous inorganic oxide materials. The chapter continues with a brief description of different synthesis routes that have yielded silica with different morphologies, along with the mechanisms of their formation. The transformations expected during various sol-gel processing steps are discussed, along with the advantages of using mixed surfactant templates. Finally, brief descriptions of the main methods used for characterization of nanoporous materials in this dissertation are presented.

2.1 Surfactant Templated Mesoporous Materials

Scientists at Mobil Research and Development Corporation first reported the synthesix of surfactant templated ordered mesoporous (alumino)silicate molecular sieves with narrow pore size distributions.[8, 9] This breakthrough synthesis of a new family of porous materials was achieved by using self-assembled surfactants as structure directing agents to generate solid materials analogous to lyotropic liquid crystals. This family of materials is designated as the M41S family and is characterized by highly organized pores with a constant pore dimension in the range from ~2 to over 10.0 nm and high specific surface areas of up to 1500 m^2/g. The M41S family consists of well-ordered 2D-hexagonal columnar (MCM-41, p6mm symmetry), bicontinuous cubic (MCM-48, Ia3d symmetry group), and stable lamellar (MCM-50) molecular sieves. Different synthesis conditions lead to the formation of these different mesostructured materials. The original synthesis of M41S materials was developed by analogy to zeolite synthesis and is based

on precipitation of silicate and aluminum species with a cationic alkyltrimethylammonium surfactant under hydrothermal conditions at high pH. The approach was subsequently generalized and extended to acidic[20-22] and neutral reaction conditions and shown to occur with different types of templating agents such as cationic,[9] anionic,[23] and nonionic surfactants,[20, 24, 25] and various combinations of these surfactant types,[26-29] gemini[30] and bolaform surfactants,[31, 32] and a variety of amphiphilic polymers.[33, 34] An attractive feature of these surfactant templated mesoporous silicates is that their pore sizes and shapes can be tailored by adjusting the templating agents, reaction conditions (such as pH, temperature, surfactant / precursor ratio, presence of swelling agent, type of alcohol used, etc.) and post-synthesis treatment methods.[4, 35-37]

Besides the M41S family of materials, a variety of nanostructured materials with different mesophases have been prepared by the sol-gel method including three-dimensional hexagonal ($P6_3/mmc$),[38] cubic mesophases with different symmetry groups (such as Pm3n,[39] Pm3m,[33] bicontinuous Ia3d,[40] bicontinuous Pn3m,[41] etc.), SBA materials[33, 39] (prepared by nonionic surfactant templating), wormhole-like structures,[42] etc. Due to their well-defined pore structures, these materials have potential applications in separations, catalysis, chemical and biological sensing, microelectronics materials, optics, drug-delivery, etc.[2, 6, 24, 39, 43] Recent research in the area of mesoporous silica materials has not primarily been focused on synthesis of mesoporous silicate materials with a wide variety of mesophases, but on design and tailoring the characteristics of the particles including particle size, pore shape and size, specific surface area, thermal and mechanical stability, and control of surface chemistry and reactivity through introduction of organic functional groups (hybrid silica-organic materials) and transition metals. Sol-gel synthesis of mesoporous metal oxide materials provides an extremely high level of flexibility and control over the surface and pore-structural properties of the materials.[14, 44, 45] During the sol-gel process, alkoxysilane precursors are hydrolyzed and undergo polycondensation to generate a metal oxide network near ambient conditions in a liquid phase. Because of the mild conditions of this approach, organic surfactant molecules can be added to co-assemble with hydrolyzed precursors and form a liquid crystal-like phase that gradually condenses to give a mesoscopically ordered composite material. Cooperative structure directing interactions among surfactants and inorganic species

bring inorganic species to the micelle interface and the ongoing polycondensation reactions of metal oxide oligomers contribute to the formation of thin metal oxide walls. The size and ordering of the final porous structured materials, which under appropriate conditions can be retained upon removal of the organic surfactants by calcination or solvent extraction, mimics the size and ordering of micelles in lyotropic liquid crystals.

2.2 Titanium-Containing Mesoporous Silica

Because of their high specific surface area and uniform pore size in the 15 Å to 300 Å range, one can easily imagine using surfactant-templated mesoporous silica materials as supports to disperse catalytically active transition metals such as Ti, V and Cr. Mesoporous silica molecular sieves containing isolated transition metals have drawn particular attention in the past decade because it is hypothesized that they contain well-defined sites useful for heterogeneous catalysts. Catalytic activity arises from variable oxidation states of transition metals and acidity generated by metals of differing electronegativity on the catalyst surface, properties not possessed by pure silica. This class of materials not only useful in catalysis, but tuning their electronic properties can make them promising candidate materials in electronic, magnetic and optical applications.[46, 47]

Of all silica-supported transition metals, titanium-containing silicas are the best studied because of their versatile applications as active and selective oxidation catalysts. Titanium-containing zeolites, such as MFI and MEL based titanosilicates TS-1[48] and TS-2,[49] respectively, drew initial interest as mixed metal oxide catalysts for selective oxidation of small alkenes using the inexpensive and environmentally friendly oxidizing agent aqueous hydrogen peroxide.[50, 51] Moreover, these mixed oxide materials allow redox reactions to be conducted at mild operating conditions with dilute peroxide where water is a major by product. However, because of the size of the zeolite pores, their applications are limited to organic molecules with kinetic diameters less than 5.5 Å. To extend the advantages of peroxide oxidation chemistry to larger molecules, Ti has been incorporated successfully into β zeolites, but still the pore size limits the applicability to molecules smaller than 7 Å. To catalyze selective oxidation of bulkier molecules, it

would be necessary to have silica supports with pore sizes in the mesopore range (2-50 nm), pore sizes not available in truly crystalline zeolite-like materials. However, shortly after the breakthrough synthesis of the M41S family of materials by Mobil scientists, Corma et al.[13] and Tanev et al.[14] almost simultaneously reported the synthesis of Ti-containing MCM-41 using ionic surfactants and neutral primary amine surfactants, respectively. Recent results indicated that the catalytic activities of Ti-containing mesoporous silica materials are strongly affected by the presence of water in the reaction system, because of a large amount of hydrophilic silanol groups at the amorphous silica surface compared to that in zeolites. Catalytic activities for selective epoxidation of small hydrocarbons with aqueous hydrogen peroxide have been found to be much lower in mesoporous titanosilicates than in Ti-containing zeolites, such as TS-1.[52, 53] However, higher activities relative to TS-1 have been obtained upon changing the oxidant from H_2O_2 to tert-butyl hydroperoxide (TBHP). Ti-containing mesoporous materials also showed higher selectivities and activities for oxidation of large organic molecules compare to TS-1, even with H_2O_2, presumably due to easy access of catalytic active sites.[53] Consistent with an accessibility effect, the difference in the catalytic activity between mesoporous and microporous titanosilicates increases as the size of the substrate molecule increases.[52, 54] These initial results not only show the promise of titanium-containing silica mesoporous materials for oxidization of bulky organic molecules for fine chemical production, but also show that the catalytic sites can be improved to be more similar to those found in titanosilicate zeolites.

In Ti-containing zeolites, titanium can be found in two different positions – either within the zeolite framework or in extraframework sites. The framework sites are thought to form by direct substitution of Si(IV) with Ti(IV) in the zeolite framework to create tetracoordinated sites. Titanium atoms in extraframework positions are not constrained in terms of oxidation state, and can be found in a mixture of coordination environments including penta- and hexa-coordinated states. They can be either isolated or partly polymerized. TiO_x species, with coordination number higher than four, and are connected to the silica host via one or two Ti-O-Si bonds. Aggregration of titania sites into clusters can lead to extraframeowork titanium-rich domain. These extraframework atoms are problematic because the unique catalytic properties of Si-Ti mixed oxides materials have

been proposed to come from tetracoordinated framework atoms connected to the silicate matrix by Si-O-Ti bridges. In zeolites, these tetrahedrally coordinated, isolated titanium ions formed by isomorphic substitution of Si(IV) by Ti(IV), are believed to be the active oxidation sites for heterogeneous Si-Ti catalysts.[55-57] Framework Ti(IV) ions are homogeneously distributed throughout the silica network and isolated by the long O-Si-O-Si-O structural fragments in all directions.

The sol-gel synthesis process provides an opportunity to produce well dispersed framework titanium sites, but the high reactivity of titanium alkoxides in comparison with analogous silicon precursors impedes the molecular level incorporation of Ti(IV) in a silica matrix. The stabilization of titanium alkoxides can help to generate catalytically active sites in Si-Ti mixed oxides materials by allowing the precursors to react together at comparable rates. Stabilized Ti alkoxides should exhibit reduced rates of hydrolysis and condensation, thus promoting isomorphic substitution of Si(IV) by Ti(IV). Several methods of stabilizing transition metal alkoxides have been proposed, such as prehydrolysis of Si precursors with a sub-stoichiometric amount of water before adding the transition metal precursor;[58, 59] ligand assisted methods where bidentate molecules are used to modify transition metal precursors chemically to reduce their reactivity;[60-62] and the non-hydrolytic sol-gel method which avoids the difference in hydrolysis reactivity entirely.[63, 64] Here we use the ligand-assisted method to synthesize mesoporous Si-Ti mixed oxide materials, as described in Chapter 4 and 5, but a novel feature of the work described here is that the ligand used to control reactivity also serves as a surfactant and as a pore template, a role which will be discussed in more detail in the next section.

2.3 Surfactant Templates in Nanoporous Silica Synthesis

Surfactants (a contracted expression meaning surface active agents) segregate to the interfaces between polar and apolar phases at low concentrations and lower the interfacial energies between the phases.[65] This surface active property of surfactants is due to the fact that molecules are amphiphilic in nature, meaning that their molecular structures contain both lyophilic and lyophobic parts. When a surfactant is in an aqueous solution, the lyophilic and lyopobic parts are referred to as hydrophilic and hydrophobic,

respectively. Usually the hydrophilic and hydrophobic parts of a surfactant are called the "headgroup" and the "tail" (usually a long-chain hydrocarbon residue). Most surfactants are sparingly soluble in water. Above a certain concentration called the critical micelle concentration (CMC), surfactants self-assemble into aggregates called micelles by minimizing the unfavorable interactions of hydrophobic tails with water, and thereby minimizing the total free energy of the system. The hydrophobic part of a surfactant is directed toward the interior core of a micelle while the hydrophilic part is in direct contact with the solvent. The balance between the strength of the repulsive forces acting between headgroups and the strength of the driving force for separation of the tails out of the continuous aqueous phase is one of the most important factors determining the size and shape of micelles a surfactant forms. Additional important internal and external factors that influence the size and shape of micelles include the molecular structure of the surfactant, the temperature, pH, surfactant concentration, pressure, and the presence of any counterions (for ionic surfactants).

Surfactants are classified into four different classes based on the nature of their polar headgroups - anionic (negatively charged), cationic (positively charged), nonionic (no charge on the headgroup), and zwitterionic (both positively and negatively charged). When the concentration of surfactant is just above the CMC, surfactants tend to aggregate into micelles of a preferred shape. In the case of dilute solutions, when each micelles can be considered isolated, Israelachvili[66] proposed a method of predicting the preferred shape of micelles at equilibrium by correlating them with the value of a dimensionless micellar packing parameter (g), which is defined as $g = V/a_o l_c$. In this expression, V is the effective molar volume of the hydrophobic surfactant tail, l_c is the effective length of the hydrocarbon tail, and a_o is the mean aggregate surface area per hydrophilic headgroup. a_o is actually a thermodynamic quantity and can approximately be defined as, $a_o = (\alpha/\sigma)^{1/2}$, where α is the headgroup repulsion parameter, and σ is the interfacial free energy.[67] l_c is typically defined as: $l_c \leq 1.5 + 1.265n$ (Å), where n is the number of carbon atoms in the tail chain, or one less.[68] The exact value of l_c depends on the extension of the tail within a micellar aggregate, and is expected to decrease at high temperature (where all-trans hydrocarbon configurations are less likely) or when the headgroups repel each other strongly.

The relationship between the packing parameter and the preferred micelle shape is presented in Figure 2.1. For a packing parameter of $0 \leq g \leq 1/3$, spherical micelles (surfactants packed into conical shapes) are formed; for $1/3 \leq g \leq 1/2$, cylindrical micelles (surfactants packed into truncated conical shapes) are formed; for $1/2 \leq g \leq 1$, planar bilayers (surfactants packed into cylinders) are formed, and inverse structures (surfactants packed into reverse (truncated) conical shapes) are obtained for $g > 1$. The equilibrium headgroup area per molecule (a_o) is a thermodynamic quantity rather than a simple geometric factor and it controls the equilibrium micelle structure.[67] Therefore the equilibrium thermodynamic parameter a_o needs to be derived by the minimizing the total Gibbs free energy of the system that includes many complex physico-chemical factors such as conformational effects associated with tail packing in the micellar core, hydrophobic interactions between the tail and residual water, curvature-dependent interfacial effects at the micelle interface, and the steric and electrostatic interactions between headgroups.[69, 70] Strengths and combinations of these interactions explicitly and the elongation of tail explicitly or implicitly determine the value of a_o and hence the preferred micelles size and shape.[67]

When the surfactant concentration is increased further beyond the CMC, the interactions between individual micelles become important and they can aggregate together into a number to defined geometric arrangements, known as liquid crystals, depending upon the shape of the component micelles. The resulting lyotropic liquid crystal phase structures are functions of the packing parameter and surfactant concentration (as implied by the term lyotropic). Other solution conditions such as long range (ionic / dipolar) interactions, ionic strength, pH, concentration of any co-surfactant, and temperature can influence the values of V, l_c and a_o implicitly. Thus surfactant packing parameter in combination with its concentration in solution determines the liquid crystal phase type or the micelle interfacial curvature, as depicted in Figure 2.1. Larger values of packing parameter (g) are correlated with smaller values of interfacial curvature. Compact spherical micelles form cubic liquid crystal phase, cylindrical micelles form (2D columnar) hexagonal liquid crystals, and bilayer micelles have tendency to form lamellar or bicontinuous structures. Hexagonal phase has high interfacial curvature, whereas lamellar phase has zero curvature. Intermediate phases

such as bicontinuous cubic and rectangular (space group cmm) have intermediate level of curvature. For instance, the gyroid bicontinuous cubic phase (space group Ia3d) corresponds to a complex mathematic surface made up of locally saddle-like domains with zero mean curvature.

Packing parameter values can be employed in designing mesoporous materials with a desire mesostructure. For example, surfactants with larger headgroups tend to form spherical micelles, and surfactants with smaller headgroups have a preference to form cylindrical micelles. In predicting the structure of the liquid crystals formed from a mixture of surfactants, the following packing parameter has been proposed:[71]

$$g_{mix} = \sum x_i V_i (a_o \times l_i) \qquad (2.1)$$

where x_i is the mole fraction of surfactant i, V_i and l_i are the volume and critical length of tail of the surfactant i, respectively and a_o is the average packing area between headgroups at equilibrium (which as noted above may depend on the local solvation and ionic environment near the headgroup in a micelle).

2.4 Liquid Crystal Phases and Their Identification

With an increase of surfactant concentration, an isotropic micellar phase (I) typically undergoes a transition to an anisotropic hexagonal phase (H) and then to a lamellar phase (L_α). This is because the solvent is compatible with the headgroups of the micelle and thus tends to expand the polar part of the mesophase. As the solvent is removed, the average area per headgroup decreases, which increases *g* and leads to the typical sequence of mesophases. In addition to hexagonal and lamellar phases, a number of intermediate bicontinuous cubic phases have also been reported between these simple liquid crystalline phases, as shown in Figure 2.1. These are thought to form by branching and interconnection of cylindrical micelles to form a bicontinous cubic phases. Phases found on the water (or polar solvent) rich side of the lamellar phase (zero curvature) are considered to be “normal” or Type-I phases, and liquid crystalline phases observed on water-poor side of lamellar phase on the surfactant phase diagram are known as “inverted” or Type- II phases.

Development of lyotropic liquid crystal phase diagrams are accomplished under isothermal conditions with a combination of polarized optical microscopy (POM) and x-ray diffraction (XRD). Cubic phases are optically isotropic and they appear dark under POM. Hexagonal and lamellar phases are optically anisotropic and hence birefringent under POM. A hexagonal phase is identified based on a fan-like POM texture and a lamellar phase is identified by its marble-like or streaky multicolored POM texture. XRD and sometimes neutron diffraction are used to identify lyotropic phases and unit cell dimensions based on indexing reflections to specific patterns. A hexagonal phase is characterized by Bragg reflections with reciprocal d-spacing ratios of 1: √3: 2, etc. at low angles, corresponding to allowed reflections from a 2D p6mm space group. A lamellar liquid crystal is identified from reflections with reciprocal d-spacing values in the ratio of 1: 2: 3, etc. Accurate identification of a bicontinuous cubic liquid crystal phases requires good quality diffraction data with at least four Bragg reflections. The most commonly observed space group of bicontinuous cubic phases in surfactant-water phase diagrams is Ia3d. This "gyroid" phase gives Bragg reflections with reciprocal d-spacing ratios of √6: √8: √14: √16: √20: √22, etc. that can be indexed to the (210), (220), (321), (400), (420), (332), etc. reflections, respectively.[72] Detailed identifications of bicontinuous cubic phases with other space groups such as Pm3n, Im3m, Fd3m, etc. are available in the literature.[73-76]

2.5 Surfactant-Templated Mesostructured Silica Formation Routes

Surfactant-templated silica materials with periodic mesostructures can be prepared by three different synthesis routes using either dilute surfactant solutions[8, 9] or within concentrated surfactant solutions that are in or near a liquid crystalline state.[77] Depending on the synthesis route, the final forms of surfactant-inorganic composites vary from precipitated powders, cast thick films / monoliths, or thin film coatings on solid or porous substrates. The most commonly used silica source in the sol-gel synthetic route is either a molecular precursor such as a silicon alkoxide or an alkaline solution of dissolved silicate oligomers such as sodium silicate. Here we discuss three different surfactant-

templated synthesis routes to mesoporous silica materials along with their formation mechanisms.

2.5.1 Cooperative Self-Assembly

The first route of synthesizing surfactant-templated mesostructured silica is that used to prepare the M41S family and related materials.[9] This route is now known as cooperative self-assembly in recognition that it is driven by co-assembly of hydrolyzed precursors and surfactants driven by charge density matching or hydrogen bonding at the surfactant / inorganic interface. In this route, the final forms of the materials are powders as they precipitate from a very dilute surfactant solution (sometimes at or below the critical micelle concentration). Two different mechanisms have been proposed for this synthetic route. The first is called the liquid crystal templating mechanism (LCT), and presumes that preformed surfactant liquid crystalline mesophase clusters that mimics the final mesostructure of the material exist and that added silicon precursors condense and deposit around the micelle structures.[8, 9] By now it is clear that this is not the correct formation pathway of this synthetic route, because Chen et al.[78] have confirmed that no such liquid crystalline phases exist in such dilute surfactant solution media without added inorganic precursors. While this hypothesis was eventually abandoned for the M41S family,[79] this mechanism inspired researchers to create surfactant-templated materials using a concentrated lyotropic liquid crystal phase as the structure directing agent (as discussed below).

The second mechanism that has been proposed for the precipation of ordered surfactant-metal oxide composite particles has been widely accepted in the material science community and is known as cooperative self-assembly.[40, 80] In this mechanism, the surfactant and inorganic precursor combine into a new precipitated phase and cooperative interfacial interactions between the surfactant and silicate oligomers generated during the course of the reactions are considered an important driving force for forming silicate-surfactant supramolecular aggregates. This does not preclude the possibility that micelles might exist prior to formation of the new surfactant / inorganic composite phase, but it acknowledges the importance of the inorganic/organic microphase interface and the evolving structure of the inorganic species in determining

the final structure of the material. In this mechanism, no preformed liquid crystal phase is necessary, but because of partitioning between the bulk dilute phase and the precipitated aggregates, the structure of the product is difficult to predict.

During the process of cooperative self-assembly, charge density matching between the inorganic polymer and the organic surfactant at the interface can lead to the formation of an interface with desired curvature and hence the desired mesophase. The original self-assembly mechanism during the synthesis of MCM-type mesoporous materials occurred with negatively charged silicates dissolved in an alkaline aqueous solution and cationic quaternary ammonium surfactants. At the high pH used to form these materials (pH = 9-14), silicates are anionic. This templating pathway is the best described in general terms as S^+I^-, where S is the surfactant, the superscript "+" indicates that it is cationic, and I^- is an anionic inorganic phase. Later this cooperative self assembly mechanism was extended to five other different pathways leading to the formation of mesostructured materials.[39, 42, 81] They are S^-I^+, $S^+X^-I^+$, $S^-X^+I^-$, S^oI^o, and S−I mechanisms, where X is a mediating ion. All of these new synthetic pathways have opened doors to synthesizing new mesoporous materials with desired functionalities for desired applications. In acidic media (well below of silica isoelectric point, pH ~ 2), silica is thought to be positively charged and thus cooperative interaction can be achieved between the cationic inorganic phase (I^+) and a negatively charged surfactant (S^-). This pathway is labeled as S^-I^+.[82] However it is also possible to make ordered porous materials by using positively charged surfactant (S^+) in acidic medium (I^+) and negatively charged surfactant (S^-) in basic medium (I^-) with the help of a oppositely charged mediating ion, X^- and X^+, respectively. These pathways are known as $S^+X^-I^+$ and $S^-X^+I^-$, respectively.[39] Beside ionic surfactants, neutral (N^o) or nonionic (S^o) surfactants have been employed to synthesized ordered mesoporous materials through cooperative self-assembly processes. Nonionic surfactants such as those with a polyethylene oxide headgroup under neutral condition form meostructures by a S^o/N^oI^o pathway, where hydrogen bonding between the inorganic species and surfactant headgroups is the driving force.[24, 42] However, this mechanism is more correctly depicted as the $(S^oH^+)(X^-I^+)$ pathway because the acid counterion (X^-) plays an important role in structure formation.[33] The pathway is termed as S−I when the organic template is covalently linked to inorganic material precursors.[30]

2.5.2 True Liquid Crystal Templating (LCT)

The second synthesis route, originally demonstrated by Attard et al.,[77] is known as liquid crystal templating (LCT) method. This is also known as the nano-casting method. Here a relatively concentrated surfactant solution (≥30 wt%) is used in which a preformed liquid crystalline phase acts as the structure directing agent and template for the final mesostructure. The final morphological form of the material synthesized via this route is either a monolith or a thick film. Casting of a mesophase silica-surfactant thick film is achieved by simply dropping the sol solution into a Petri dish or a substrate and heating to solidify the hydrolyzed metal oxide precursors. Attard et al. used a concentrated solution of a nonionic surfactant (a ~50 wt% aqueous solution of octaethylene glycol dodecyl ether ($HO\text{-}(EO)_8\text{-}C_{12}H_{25}$) to make highly ordered mesoporous silica materials, where hydrogen bonding and hydrophilic/hydrophobic interactions are mainly responsible for bringing silicates to the micelles interface. To be more precise, the silica precursors and surfactants in the concentrated solution form a homogeneous liquid crystal upon evaporation of the alcohol produced during hydrolysis and of excess water that may be needed to drive hydrolysis to completion. Here the formation of mesostructure was initially thought to be dictated by the preformed LC phase, but it is more likely that the final composition after curing of the silica can be made to imitate lyotropic phase diagram of the surfactant. This route offers the advantage of being able to predict the final mesostrusture of the surfactant-silicate complex. Because surfactants can form different types of liquid crystal phases in water, this method makes it possible to design porous materials with desired pore organization by replicating a desired liquid crystalline phase. In this dissertation, we will use this synthesis route to prepare mixed (cationic and nonionic) surfactant-templated silica and silica-titania mixed oxides materials with predictable mesostructures, as described in Chapters 3 and 5, respectively.

2.5.3 Evaporation Induced Self-Assembly (EISA)

In this synthesis route, mesostructural ordering of the inorganic-organic composite occurs through a solvent evaporation induced self-assembly (EISA) process. In the initial solution, the concentration of surfactant is far below its critical micelle

concentration (C_o << CMC) and the precursor is prehydrolyzed but dilute which prevents uncontrolled precipitation. After forming this sol into an aerosol droplet, line of "ink", or a thin film, rapid solvent evaporation brings the surfactant concentration above the liquid crystal CMC value and thus acts as the driving force for the organization of dispersed surfactants into structured aggregates. This rapid solvent evaporation induces both long-range self-assembly of surfactants and condensation of the inorganic network at the interface. Thick and thin films, deposited on substrates, can be synthesized by this method by using either spin- or dip-coating techniques. The first successful attempt at making surfactant templated mesoporous silica thin films (film thickness ~1 μm) was reported by Ogawa,[83] using a spin-coating technique. Layered silicate-surfactant nanocomposites oriented parallel to the substrate have been found in the films.[84, 85] The mesophase is thought to be assembled here via an anion-mediated $S^+X^-I^+$ pathway promoted by the rapid solvent evaporation. Almost at the same time, Lu et al.[86] reported the use of an EISA approach to synthesizing mesostructured thin films by dip coating. Thin films with different mesostructural ordering were synthesized by employing an acidic dilute alcoholic solution of cationic cetyltrimethylammonium bromide (C_{16}TAB) and tetraethyl orthosilicate (TEOS). Thin films with various types of mesostructural ordering such as 3D interconnected hexagonal ($p6_3/mmc$), bicontinuous cubic (pm3n, Ia3d, Im3m, etc.), 2D- hexagonal (P6mm), and lamellar have been synthesized using the EISA method.[86-89]

In the EISA method, the first important step is preparing a well-defined, reactive sol. The initial solution usually contains prehydrolyzed ceramic precursor(s), templating agent(s), catalyst (usually acidic), water, and solvent (usually an alcohol). Cagnol et al.[90] and Crepaldi et al.[88] have studied the in-situ formation of thin films and they proposed a pathway that involves several complex dynamic steps. These are: (I) the fast evaporation of the solvent (alcohol) rich vapor, which only last for about ~20-30 seconds, (II) slower evaporation of water and acid catalyst from the mixture, (III) the equilibration of water rich film with the coating environment, where micelles are disoriented, and (IV) the departure of the remaining water and acid catalyst that allows further condensation of the ceramic network and final periodic organization of micelles. The third step, also known as a modulable steady state (MSS), was identified as an important step.[90] Even though the

initial disordered mesostructure is formed by that time, the structure is still flexible enough to be modified by the coating environment including variables such as relative humidity, alcohol vapor pressure, and temperature.

Similar to the liquid crystal templating method mentioned above, it is possible to synthesize mesoporous thin films with a desired mesostructure and thickness for different potential applications by varying coating parameters including surfactant / inorganic precursor ratio, extent of inorganic precursor condensation prior to coating, deposition rate, relative humidity and temperature. Among these parameters, surfactant / precursor ratio and the extent of ceramic precursor condensation are the critical parameters that dictate the final mesostructure. As in lyotropic liquid crystals, the surfactant / precursor ratio (surfactant concentration in the final film) is the main critical coating parameter controlling the final mesostructure of the thin films.[87, 91] For instance, with C_{16}TAB surfactant-templated silica mesoporous thin films, Besson et al.[92] observed a sequence of mesophases from 3D-hexagonal ($P6_3/mmc$) to cubic (Pm3n) to 2D-hexagonal (p6mm) by increasing the C_{16}TAB/Si ratio for a constant aging of the initial sol. Several other researchers also observed that the volume fraction of the surfactant in the films controls the final mesophase.[88, 91] An optimal degree of inorganic network condensation prior to coating is another important factor to obtain well-ordered mesophases. Too little curing or too much can lead to a different phase than expected or a disordered material because micelle assembly is interrupted. Mild acidic sol conditions are desirable for silica to minimize the rate of condensation after deposition, and thus give the film time to assemble into a well-ordered composite.[87] Film deposition rate does not affect the type of mesostructure but it can affect the degree of ordering and film thickness.[87] Relative humidity of the coating environment is an important parameter as it controls the rate of exchange of water between the coating and its environment. Keeping all other coating parameter same but by changing relative humidity and alcohol vapor pressure, researches have synthesized thin films with different mesostructures.[88, 90] We have to keep in mind that relative humidity can change the volume fraction of the polar species in the film and which in turn changes the volume fraction of the surfactant phase (and possibly the type of mesophase). Temperature influences the solvent evaporation rate and the condensation rate and thus the organization of micelles into films. Considering the influence of all

these coating parameters on the final mesophase of nanostructured thin films obtained via the EISA method is essential for rational design and reproduction of thin films for the applications in microelectronics, catalysis, sensing, separation, optics, etc. In this dissertation, surfactant-templated silica-titania mixed oxides thin films are synthesized by the EISA method using dip-coating, as discussed in Chapter 4.

2.6 Sol-Gel Processing

As noted above, the low temperature used for sol-gel processing enables the incorporation of organic surfactant or imprint molecules into the silica network. The sol-gel process is a convenient route to pure, homogeneous silica materials and the structural properties of the fabricated materials, such as mean pore size, pore size distribution, and pore interconnectivity, can be tuned using the process parameters described below. Because of its influence on the structure of silica gels, the mechanism of the sol-gel silica formation process is discussed here, as well as the effects of process parameters on the properties of the final material.

2.6.1 Silica Polymerization

The alkoxide method[93] and the colloidal method[94, 95] are the two main sol-gel silica gel preparation routes. As the name implies, the latter involves controlled aggregation of pre-existing colloidal particles, and is not ideal for the formation of materials with well-defined features at the molecular scale. Therefore in this study, the alkoxide sol-gel method is used to make SiO_2. In principle, the first step in this method is the generation of silicic acid ($Si(OH)_4$) via the hydrolysis reactions of silicon alkoxides. Various tetraalkoxysilanes can be used to make silica, and tetraethyl orthosilicate (TEOS) is the most commonly used one. Sol-gel reactions are usually carried out in a batch reactor in the presence of water, which acts both as a reactant and (in some cases) as either a solvent or an anti-solvent. Hydrolysis (Equation 2.2) is initially facilitated in the presence of alcohol that acts as a mutual solvent for water, precursor and siloxane oligomers. The alcohol usually matches the alkoxide ligands to avoid ligand exchange, e.g. TEOS is usually solubilized with ethanol.

$$\equiv Si - OR + H_2O \underset{esterification}{\overset{hydrolysis}{\rightleftharpoons}} \equiv Si - OH + ROH \quad (2.2)$$

where R is an alkyl group. Hydrolysis reactions occur by the nucleophilic attack of the oxygen in a water molecule on the silicon atom in the precursor molecule.[96] In reality, full hydrolysis to silicic acid is difficult to achieve, and partially hydrolyzed monomers are formed of molecular formula $Si(OH)_x(OR)_{4-x}$. Depending on the nature of the by-product formed during the condensation reactions, they are classified as either alcohol-forming condensation (Equation 2.3) or water-forming condensation (Equation 2.4). The main purpose of the condensation reaction is to produce siloxane bonds ($\equiv Si - O - Si \equiv$) from silanol groups.

$$\equiv Si - OR + HO - Si \equiv \underset{siloxane\,alcoholysis}{\overset{alcohol\,condensation}{\rightleftharpoons}} \equiv Si - O - Si \equiv + R - OH \quad (2.3)$$

$$\equiv Si - OH + HO - Si \equiv \underset{siloxane\,hydrolysis}{\overset{water\,condensation}{\rightleftharpoons}} \equiv Si - O - Si \equiv + H_2O \quad (2.4)$$

Condensation reactions initially produce dimers (Equation 2.3 – 2.4 with all remaining ligands being either alkoxides or hydroxides) and because each silane has four hydrolysable alkoxides initially, polycondensation continues to build larger and larger siloxane-containing polymers or particles. The resulting particles or oligomers link together to form chains which crosslink with each other to form a network in the liquid medium, and eventually the solution thickens into a gel.[96] The structural properties of the porous silica materials depend on the relative rates of hydrolysis and condensation reactions and precipitation of siloxane oligomers, which are influenced by the catalyst employed in sol-gel reactions.[97]

In the imprinting work discussed in chapter 6, a two-step (acid-base) sol-gel process is used to prepare silica or organo-functionalized silica. In the latter case, extra restrictions are imposed because it is sometimes necessary to avoid rapid precipitation with organofunctional silanes. However, in both cases the polymerization mechanism is similar. In the two-step method, the sol-gel process is divided into an acidic step and a basic step. A two-step process is often selected to eliminate the possibility of phase separation and precipitation (common in base-catalyzed reaction) and to decrease the gelation time significantly relative to an acid-catalyzed reaction.[98] Slow gelation is advantageous when forming coating sols or for liquid crystal templating, so the discussion of the first (acidic) step will be relevant to Chapters 3-5. In this work HCl is

used as a catalyst in the acidic-step and NaOH in the base catalyzed step. Acid catalyzes the hydrolysis much faster than condensation. Hydrolysis of multifunctional silanes, such as TEOS, under acidic condition is usually fast enough to reach to a pseudoequilibrium condition with an equilibrium coefficient of about 15-20.[99] It has been found that the extent of hydrolysis established in the acidic step strongly influences the gelation time in the basic step of a two-step process.[97] The gelation time, which is defined as the time interval between the addition of base to the acidic mixture and the time when the sample loses its fluidity completely, is inversely proportional to the HCl concentration.[100] An increase in hydrolysis rate constant has been found with the extent of hydrolysis of a monomer,[101, 102] which in turn has a linear relationship with the concentration of H^+ in acidic mixtures of TEOS, ethanol and water.[103] A longer acid-catalyzed step compare to that used in prior studies was selected here to allow not only the hydrolysis of TEOS to reach pseduoeqilibrium, but also the partial condensation of monomers to form small siloxane oligomers. With a short acid-step, mainly hydrolyzed monomers are present at the start of the base-step. These monomers rapidly precipitate after base addition to form large particles, which may produce meso- / macro- porous rather than micro- / meso-porous silica. For the acid step an HCl concentration of 0.01M, which corresponds to a pH value of 2.0, was used because gelation has been found to be extremely slow at this concentration.[104] When the pH value is close to the point-of-zero-charge (PZC) of silica, condensation is the rate limiting step. At moderate pH (~3.5-8) condensation is fast relative to hydrolysis and also at very high HCl concentration (pH<1), it has been found that sols gel quite rapidly due to increased condensation rates, but that they also tend to be cloudy and heterogeneous due to precipitation.[104] The two-step procedure seeks to avoid this possibility by controlling the relative reaction rates of hydrolysis and condensation in each step.

In the second step, which is base-catalyzed, the condensation reaction is expected to be faster than in the acid catalyzed step because it has been found that bases catalyze condensation preferentially over hydrolysis above the isoelectric point of silica (pH ~ 2).[96] In the acid step under mild acidic condition, hydrolysis steps are fast but because they are at equilibrium, they have little influence on the development of the silica network.[105] In contrast during the base step, polymerization of both isolated and partially

condensed molecules into macromolecules determines the nature and properties of the pores created in the final material.[105] At an intermediate pH value (~ 3.5-8), condensation is fast relative to hydrolysis.[96] Therefore, gelation occurs rapidly in this pH range and gives rise to a mesoporous or micro- /meso- porous silica gels. Gels prepared at pH less then 3.5 are typically microporous.[96] As the pH increases, silica precipitates with increasing particle size, and the gel time decreases. Thus the microstructure of the dried silica gels can be controlled by adjusting the pH during the second, base-catalyzed step of the two-step acid/base sol-gel process.

When amine-functional organosilane is added to the sol to modify the nature of the imprinted site, as discussed in Chapter 6, a one step acidic sol-gel process instead of a two-step process will be used. Amine groups are basic in character and any increase in pH value beyond the point-of-zero-charge of silica (pH~ 2.0) in the presence of amine functional groups may lead to rapid condensation and precipitation. Even when the pH is adjusted, the amine-containing systems still gel reasonably quickly, so a two-step procedure is not required. Also, some silica gels have been prepared by a one-step acidic process when the goal is to prepare microporous material with a pore size closely matching the size and shape of the imprint molecule.

Water to TEOS Molar Ratio: The water to tetraethyoxysilane (TEOS) molar ratio is a very important factor that significantly affects the structural properties of the final sol-gel product. The overall sol-gel reaction to produce anhydrous silica can be written as:

$$Si(OR)_4 + 2H_2O \rightarrow SiO_2 + 4ROH \qquad (2.5)$$

Since water is a by product of the water producing condensation reaction, Equation (2.5) indicates that a mole ratio of 2 is sufficient for complete hydrolysis and condensation.[97] However, because the hydrolysis equilibrium coefficient is only moderately large, an insufficient initial amount of water in the system may lead to incomplete hydrolysis (especially in the presence of added ethanol).[106] Therefore in all experiments described in this dissertation, the water to TEOS molar ratio exceeds 2. In the acid catalyzed system, the hydrolysis reaction has been found to be first order with respect to both TEOS and water concentrations.[107] Therefore an additional advantage to conducting the hydrolysis reaction with a superstoichiometric water: TEOS molar ratio is that the gelation time should decrease the in the base-step (due to faster, more complete hydrolysis). Note

however that there is a limit to how much water is desirable. As the water: TEOS ratio is increased while maintaining a constant solvent: TEOS ratio, the TEOS is diluted, which reduces the rates of hydrolysis and condensation, leading to an increase in the gel time. Thus, there is an optimal amount of water for each concentration of TEOS to get a minimum gel time. Also for imprinting (Chapter 6), it is desirable to avoid excess water, to minimize competitive hydrogen bonding with the silica network.

***Ethanol to TEOS Molar Ratio*:** The effect of the initial alcohol to TEOS molar on gelation kinetics is important. Ethanol acts as a mutual solvent to allow a mixture of water, TEOS and polymerization products to form a homogeneous mixture. However, dilution of TEOS with excessive ethanol increases the gel time by decreasing the rate of both hydrolysis and condensation. A second and important effect of excessive alcohol is that it promotes the alcoholysis of siloxane bonds and silanols. Also because alcohols are protic solvents with labile protons, they can influence the extent of the reverse reaction such as siloxane bond alcoholysis and hydrolysis.[96] Therefore, a balance in the alcohol-water-TEOS needs to be found to homogenize the solution and promote forward sol-gel reactions without promoting reverse reactions.

2.6.2 Gelation and Aging

In sol-gel processing, a gel will form from the sol after hydrolysis and condensation proceed for a certain period of time. Gelation happens as clusters of condensed silica species or colloidal particles grow through condensation into a network. Eventually a cluster of particles links together into a sample-spanning three-dimensional network, called the gel. At the gelation point, the viscosity of the sol increases sharply and the gel (a liquid-filled porous solid object) takes the shape of the vessel. The network formed has a large enough elastic modulus that it can support a small stress, for example by tilting the vessel, without flowing. The sudden increase in viscosity with a loss of fluidity indicates the gel point, so the gelation time can be approximated (at least as a lower estimate) as the time at which the fluid loses its fluidity. While the gel point signals a dramatic change in connectivity of the network in the sample, hydrolysis and condensation are not complete, and they continue after the gelation point so that during aging, short chain polymers adhere to the gel.[96] This strengthens the gel, but also can

create internal stress which causes a gel to shrink and react through a process called syneresis. In this way, the properties of the gel continue to evolve for a significant time after gelation.

As noted above, the synthesis pH plays an important role on the pore structure and the morphology of the gels by controlling the relative rate of hydrolysis, condensation and their reverse reactions, and this continues to be true after gelation. Gels prepared under mild acidic condition (pH<3.5) are microporous, whereas gels prepared at higher pH (~3.5-8) are mesoporous.[108] Silica has a greater dissolution rate in basic solutions due to deprotonation of silanols.[96] Depolymerization of siloxane bonds by alcoholysis (reverse of alcohol-producing condensation) and hydrolysis (reverse of water-producing condensation) occur in basic conditions, which facilitates the continual restructuring of the growing polymers to cause the formation of highly condensed colloidal particles. This leads to the redistribution of silica from low-molecular-weight polymers to high-molecular-weight polymers and particles. Therefore, gels formed at high pH tend not only to form as heterogeneous colloidal aggregates, but also to have walls that thicken during aging. The resulting materials are fairly stable towards drying and tend to produce mesoporous xerogels. At low pH, the rate of siloxane bond breaking is low, and the kinetics of condensation can be modeled as irreversible. Homogeneous gels form by slow condensation of small silicates and bond breakage and restructuring do not occur rapidly, which results in weakly branched gels.[104] Shrinkage during the drying of these weak gels usually gives microporous xerogels.

2.6.3 Drying

During the drying process, solvent and the reaction byproducts (water and alcohol) evaporate from the pores of the gel. Initially the volume shrinkage of the gel is equal to the volume of liquid evaporated and at this point an air-liquid interface exists at the exterior surface of the gel body.[96] Loss of liquid from the interior of the gel creates tensile stress in the liquid and compressive stress on solid.[109] At this stage the bulk modulus of the gel determines the extent of its shrinkage.[110] As drying proceeds, the solid network becomes increasingly stiff because of ongoing localized condensation.[96] When the body becomes too stiff to shrink, the network stops shrinking and further capillary

evaporation causes liquid menisci to recede into the pores. Once the pores are empty, the compressive stress on the gel is released. However, if condensation reactions occurred while the gel was compressed, tensile stress develops.[111] Because gels are more resistant to compressive stress than tensile stress, the dried gel may crack unless they are dried very slowly or under conditions that reduce surface tension (such as supercritical drying). Most gels prepared under acidic conditions break apart during drying, while gels prepared under basic conditions may retain their integrity because of both greater network strength and less shrinkage during drying. Breakage of gels is not problematic in the current case because when samples are prepared to be used as adsorbents and catalysts, they are usually ground to a uniform powder prior to the actual application.

2.7 Predictive Synthesis of Mesostructured Materials

Alberius et al.[91] outlined a general method for predictive synthesis of surfactant templated mesostructured materials with mesophases similar to the liquid crystalline phases found in the binary surfactant-water phase diagram, by using the sol-gel process to generate a metal oxide to replace water in the phase diagram. Originally this method has been proposed for thin film synthesis, but it can be extended to liquid crystal templating (LCT) method. From the mechanism of thin film synthesis (as discussed in Section 2.5.3), we have seen that the final mesostructures do not form until the evaporation of all the alcohol, HCl, and excess water. Based on this, Alberius et al. assumed that the volume of hydrophilic inorganic species (V_{inorg}) in the surfactant-inorganic composites should be equal to the volume of fully hydrolyzed and uncondensed metal oxides, $M(OH)_4$ (M could be Si and/or Ti). Then in turn this inorganic volume (V_{inorg}) is assumed to equal the sum of the volume of the equivalent amount of fully condensed metal oxides (SiO_2 and/or TiO_2) plus the amount of water released during the condensation of the fully hydrolyzed precursor. For a given number of moles of metal (M = Si and/or Ti) in the initial coating solution (N_M), V_{inorg} can be calculated from the following relationship-

$$V_{inorg} = V_{M(OH)_4} = V_{MO_2} + V_{H_2O}$$
$$= \frac{m_{MO_2}}{\rho_{MO_2}} + \frac{m_{H_2O}}{\rho_{H_2O}} \qquad (2.6)$$
$$= \frac{N_M M_{MO_2}}{\rho_{MO_2}} + 2\frac{N_M M_{H_2O}}{\rho_{H_2O}}$$

Here V, m, M, and ρ represent the volume, mass, molecular weight, and density, respectively. Assuming that the walls are fully condensed and amorphous, the densities of silica (SiO_2) and titania (TiO_2) are taken as 2.2 g/cm^3 and 3.0 g/cm^3, respectively. The number of moles of water released during complete cross-linking of each mole of $M(OH)_4$ to MO_2, which is two, is assumed to be the relevant quantity here. This method is also based on a hypothesis that the volume of inorganic species (V_{inorg}) can replace the water in a LLC phase to generate a material with the same mesophase. Then by equating this inorganic volume to the volume of water corresponding to the desire phase structure in the surfactant phase diagram, the amount of metal precursor(s) to be added in the initial solution is calculated.

2.8 Mixed Surfactant Templating

In most practical applications, surfactants are used in formulations containing mixture of two different surfactants, rather than one surfactant. In most cases, surfactant mixtures improve the properties of final product. Synergistic behavior from mixture of surfactants is usually seen, meaning that the properties of surfactant mixtures are better than that attainable by the individual surfactants themselves. Improvement of several interfacial phenomena can be achieved, for example reduction of surface or interfacial tension and formation of micelles at a lower solution phase total surfactant concentration than that required of either surfactant by itself. The synergistic behavior of surfactant mixtures is due to the favorable forces acting between the surfactants.[65, 112] Forces are favorable when the attraction force acting between two different surfactants is stronger than that between two individual surfactants with themselves and the repulsive force acting between two different surfactants is weaker than that between two individual surfactants with themselves.

Surfactant mixtures are also advantageous when used as templates to make porous materials. The synergistic behavior of surfactant mixture was exploited by Chen et al.,[27] when synthesizing MCM-48 (Ia3d symmetry group) silica materials using mixtures of cationic and anionic surfactants at relatively low concentrations. Attractive forces between these surfactants facilitate mixed micelle formation where the headgroup area is smaller than that of the pure surfactants (and this, in turn, favors a bicontinuous intermediate phase). Nonionic surfactants in mixtures of nonionic and ionic surfactants can also lower the total electrostatic repulsive forces acting between the charged headgroups of ionic surfactants, and thus facilitates the formation of mixed micelles. Recently, surfactant mixtures have been employed by several researchers to synthesize a variety of mesostructures. At high pH, sugar-based nonionic maltoside ($C_{12}G_2$) surfactant becomes deprotonated (negatively charged) and thus interacts strongly with a cationic surfactant.[113] Peng et al.[114] showed the basic medium synthesis of MCM-48 type silica material with good thermal stability by utilizing this favorable interaction between C_{16}TAB and sugar surfactant n-dodecyl-β-D-maltoside ($C_{12}G_2$) as co-surfactant. Cubic mesoporous silica molecular sieve MCM-48 has been synthesized using surfactant mixtures of cationic-nonionic,[28] anionic-nonionic,[115, 116] and cationic-anionic surfactant mixtures.[27] Mesoporous silica molecular sieve MCM-41 has been synthesized using cationic-cationic,[117] cationic–nonionic,[29] and nonionic-nonionic[118] surfactant mixtures. Lind and coworkers synthesized vesicle-like mesoscopically ordered silica mesoporous materials using a mixture of cationic and anionic surfactants.[119]

The capacity to make porous materials with controllable pore sizes is of paramount importance for their industrial catalytic applications. Although the pore structure of composite materials can be controlled by using different surfactants, sometimes it is difficult to obtain materials with desire pore sizes and shapes because of geometric limitations in how certain types of surfactants will pack. In general, the packing parameter of a hydrocarbon surfactant mixture with favorable interactions can be considered as a simple average of packing parameters of individual surfactants, which provides an effective and simple way of controlling pore sizes and shape. Fine tuning of pore sizes can be achieved by varying the relative composition of surfactant in a mixture of surfactants with different tail lengths or polar headgroups.[120] The pore diameter

increases with an increase in the amount of a surfactant with a longer tail length mixed in micelles with a surfactant with a shorter tail.[120] Dia et al.[121] showed that pore sizes of materials can be controlled either by changing the ratio of nonionic to cationic surfactant or by increasing the non-polar chain length of the nonionic surfactant. Song et al.[29] achieved control of pore dimension by changing the ratio of nonionic to cationic surfactants in mixed micellar aggregates. In addition to pore sizes, the shape of aggregates can be controlled with mixed surfactant templates by adjusting the interfacial curvature of aggregates to produce specific and novel ordered porous materials.[115, 122] For example by adjusting the ratio of anionic sodium dioctyl sulfosuccinate (AOT) to the nonionic triblock copolymer surfactant F127, Chen et al.[115] showed that the mesophase changes from cubic Fm3m to Im3m and then to 2D-hexagonal p6mm symmetry. In Chapters 3, 4, and 5, we investigate the application of combinations of the cationic surfactant C_{16}TAB with the sugar-based nonionic surfactant n-dodecyl-β-D-maltoside ($C_{12}G_2$) as mixed templates in the preparation of ordered mesoporous silica and silica-titania mixed oxide materials.

2.9 Materials Characterization Techniques

2.9.1 Nitrogen Sorption Analysis

One of the characteristic properties of a sol-gel material is its pore structure. Nitrogen adsorption-desorption isotherms data were used in the experiments conducted as part of this dissertation to obtain information about specific surface area and pore structure parameters of the synthesized materials. Isotherms were measured at 77K with a Micromeritics Tristar 3000 automated nitrogen adsorption instrument using the static volumetric determination technique. Before measurement, all samples were degassed by heating at elevated temperature under flowing nitrogen. As shown in Figure 2.2, gas adsorption isotherms have been classified by IUPAC into six different types. Type I is a characteristic adsorption isotherm from microporous solids. Types II, III, and VI are obtained due to adsorption in non-porous or macroporous materials, and Types IV and V arise from adsorption in mesoporous materials. Hysteresis loops appear in Type-IV and V isotherms due to the irreversible nature of capillary condensation / evaporation, but these

types of isotherms can be reversible too (indicated by adsorption and desorption branches that lie on top of each other).

(a) Specific Surface Area: Specific surface areas of the finely divided porous materials were evaluated using the standard Brunauer-Emmett-Teller (BET) multilayer adsorption model.[123] The BET method is based on the determination of the monolayer capacity, which is defined as the quantity of adsorbed molecules in a single filled molecular layer on the surface of a material. BET monolayer capacity was calculated by fitting the experimental adsorption data to the linearized form of the BET equation (Equation 2.7) in the range of relative pressures from 0.05 to 0.2:[124]

$$\frac{x}{v(1-x)} = \frac{1}{v_m c} + \left(\frac{c-1}{v_m c}\right)x \qquad (2.7)$$

where v is the amount of nitrogen adsorbed at any relative pressure $x(\equiv p/p_o)$, v_m is the monolayer capacity, and c is a constant related to the heat of adsorption in the first layer. It has been found that the shape of the isotherms in the BET range depends on the numerical value of c, becoming sharper as the heat of adsorption in the first layer increases. To be consistent while comparing the specific surface areas of different samples, the same relative pressure range was used for all surface area calculations. Monolayer capacity is obtained from the values of slope $\left(\equiv \frac{c-1}{v_m c}\right)$ and intercept $(\equiv 1/v_m c)$ of the linear BET plot. The monolayer capacity thus obtained was multiplied by the cross-sectional area of the adsorbed N_2 (assumed to be 0.162 nm^2 based on hexagonal close packing of nitrogen) to estimate the specific surface area of the material.[5]

(b) Pore Size Distribution: Pore size distributions (PSD) were estimated from the adsorption branch of the isotherms using the Barrett-Joyner-Halenda (BJH) method[125] with the corrected form of the Kelvin equation and the Harkins-Jura statistical film thickness equation as described by Kruk, Jaroniec and Sayarai (the KJS method).[126] It has been suggested by Kruk and Jaroniec[127] that adsorption rather than desorption data should be used to calculate the PSD of ordered porous materials. This is because network imperfections can delay capillary evaporation, while capillary instability can lead to premature evaporation from small pores in materials with hysteresis loops.[128]

Historically, the Kelvin equation has been used to obtain the curvature radius of the meniscus formed at the interface between adsorbate and adsorbent at a given relative pressure. This curvature radius is known as the core radius which is confined by the adsorbed film on the pore walls. The BJH method using the Kelvin equation gives an accurate distribution of the pore sizes in the limit of large pores but severely underestimate the pore sizes when applied to narrow pores in materials that interact strongly with nitrogen (including silica).[129, 130] Therefore in order to improve the reliability of the BJH method used in this study a correction for the statistical film thickness on pore walls was incorporated with the Kelvin equation to evaluate the PSD in the pore size range of 0.5-300 nm.[131] The Kelvin model assumes cylindrical meniscus shape during capillary condensation along the adsorption branch and a hemispherical meniscus shape during capillary evaporation along the desorption branch. Accordingly, the following two forms of Kelvin equation were obtained for the adsorption and desorption branches respectively:[128]

$$r_k = -\frac{\gamma V_L}{RT \ln\left(p / p_O\right)} \tag{2.8}$$

$$r_k = -\frac{2\gamma V_L}{RT \ln\left(p / p_O\right)} \tag{2.9}$$

where γ is the surface tension at the liquid/vapor interface, V_L is the molar volume of the liquid adsorbate, θ is the contact angle between the adsorbate and adsorbent, R is the universal gas constant, and T is the liquid nitrogen temperature. The contact angle for nitrogen at 77K can be taken as zero. The other parameters used here were obtained from Nano et al.[132] From Equation (2.8) and (2.9), it can be easily seen that for a given pore radius capillary evaporation occurs at a relatively lower pressure that that for the capillary condensation. The actual pore radius instead of the core radius was used to calculate the PSD by means of the modified BJH method. In order to get the actual pore radius, the core radius calculated from Kelvin equation was corrected for the statistical film thickness on the pore walls. It has been found that the Kelvin equation for the hemispherical meniscus is in good agreement with experimental data for adsorption in MCM-41 type materials.[131] Finally the following modified form of the Kelvin equation

was proposed to calculate PSDs by means of BJH method without underestimating pore sizes:[131]

$$r_k = -\frac{2\gamma V_L}{RT\ln\left(p/p_O\right)} + t(p/p_o) + 0.3\,nm \tag{2.10}$$

The film thickness was calculated for a particular relative pressure from the Harkins-Jura thickness Equation (2.11) of the following form:[131]

$$t = 0.1\left[\frac{60.65}{0.03071 - \ln(p/p_O)}\right]^{0.3968}. \tag{2.11}$$

(c) High Resolution α_s-Method: Recently, increasing numbers of researchers have started employing comparative plots of adsorption data to characterize the structural properties of porous adsorbents. Structural properties such as micropore and mesopore volumes, external surface area of mesopores, and total surface area can be determined by this method. The main idea behind the comparative methods is to compare the adsorption isotherm of the porous material under study with that of a reference macroporous material of the same surface properties with respect to the adsorbate used.[127] Among all the available comparative plot methods, such as the t-plot, α_s-plot, and θ-plot, the high resolution α_s-plot has been specifically applied to mesoporous silica materials. In the α_s-method, the amount adsorbed on the porous material under study is plotted against the reduced standard adsorption α_s. The standard reduced adsorption α_s is defined as $\alpha_s = V_{ref}(p/p_O)/V_{ref}(0.4)$, where $V_{ref}(p/p_O)$ is the amount adsorbed on the reference material as a function of the relative pressure p/p_O, and $V_{ref}(0.4)$ is the amount adsorbed at the relative pressure of 0.4. In this study, Li-Chrospher Si-1000 (EM Separations, Gibbstown, NJ) silica gel with BET surface area of 25 m^2/g was used as a reference material, according to the adsorption data published in the literature for this material.[133]

Three different linear segments are typically observed in the α_s-plots of mesoporous metal oxides corresponding to multilayer adsorption on the pore wall, capillary condensation, and adsorption on the external surface.[134] The procedure used in this study for determining the total surface area and pore volumes was adapted from Sayari et al.[124] The lower limit of the lower linear segment should be higher than the $\alpha_{s,mi}$ value, which corresponds to the nitrogen condensation in micropores, and the upper

limit should be lower than $\alpha_{s,pm1}$ value, which corresponds to the capillary condensation in primary mesopores. The slope of the lower linear segment was used to evaluate the total surface area of the material and the intercept with the vertical axis (α_s=0) was used to calculate the micropore volume. When this initial linear segment passes through the origin, it indicates the absence of micropores. Similarly, the lower limit of the upper linear segment should be greater than $\alpha_{s,pm2}$ value, which corresponds to the upper limit of condensation in the primary mesopores and the upper limit should be lower than $\alpha_{s,sm}$ value, which corresponds to capillary condensation in the secondary mesopores or textural pores between particles. The slope of the upper linear segment was used to calculate the external surface area and the intercept value was used to calculate the primary mesopore volume. Then, the primary mesopore surface area was simply calculated from the difference between the total surface area and the external surface area.

2.9.2 Fourier Transform Infrared (FTIR) Spectroscopy

Molecules that make up a material are excited to a higher vibrational energy state when they absorb infrared radiation (IR). The atoms in a molecule are always vibrating; the vibrational motions exhibited by molecules are characteristic of their atomic makeup and bonding structure.[135] An infrared spectrum represents a fingerprint of a material, with several absorption peaks corresponding to the frequencies of vibrations of different bonds. Two different modes of vibrational motion are infrared active. They are stretching (symmetric and asymmetric) and bending (scissoring, rocking, wagging and twisting).[136] Fourier transform infrared spectroscopy (FTIR) is preferred over the older scanning infrared technology because it allows rapid scanning and averaging of multiple scans for improved signal-to-noise ratios. FTIR produces a pattern called an "interferogram", a wave-like pattern containing all the infrared frequencies generated from the source.[136] In FTIR, the interferogram is converted into a plot of intensity versus frequency via a Fourier transform (FT). The change in intensity at each frequency relative to the background is due solely to absorptions of infrared radiation by the sample exposed to the modulated IR beam. The resulting spectrum is then analyzed by comparing with known

signatures of identified molecules in the FTIR library or those of specific reference compounds.

Fourier transform infrared (FT-IR) spectroscopy in the mid-infrared (MIR) region coupled with an attenuated total reflectance (ATR) accessory was used in this dissertation research to quantify glucose in aqueous solutions. Glucose concentration in highly absorbing liquids, such as aqueous solutions, can be measured accurately by ATR because the IR beam penetrates the sample only a short distance (1-50 μm), which means the effective path length is short. The path length of transmission IR is usually too long for this application, and strong water absorption bands would obscure the characteristic peaks from glucose. The infrared spectra were collected with a ThermoNicolet Nexus 470 FT-IR spectrometer equipped with a deuterated triglycine sulphate (DTGS) detector (spectral range 4000-650 cm^{-1}) and potassium bromide (KBr) beam-splitter. In order to get a satisfactory signal-to-noise ratio, 128 interferogram scans at 4 cm^{-1} resolution were used. The instrument was purged with nitrogen gas to suppress the specrtral contribution from atmospheric carbon dioxide and water vapor. The IR beam from the spectrometer was directed onto the horizontally aligned zinc selenide (ZnSe) crystal at a 45° angle of incidence. At this experimental condition, the sample on the crystal is exposed to 12 reflections with a penetration depth of 2.0μm. A background spectrum was collected first of the ZnSe crystal in contact with air. Then MIR absorption spectra of aqueous glucose solutions were collected after pouring sample onto the crystal. For solid samples, on the other hand transmission spectra could be obtained. Before analyzing solid samples by transmission FTIR, samples were finely ground and diluted to 1 wt% with KBr powder before being pressed into translucent pellet.

2.9.3 Powder X-ray Diffraction (PXRD)

X-ray diffraction (XRD) experiments are commonly used to determine the spatial arrangements of atoms in periodic materials. In a diffraction experiment, an incident x-ray beam is directed into the sample and a detector is typically moved about to capture the diffracted x-rays to obtain crystallographic information.[137] Here we used x-ray diffraction to identify mesostructural ordering of the materials. Since the pore spacings of typical mesoporous materials are on the order of a few nanometers, the diffracted peaks

appear at low angles. The widths of the peaks in the XRD patterns can be used to determine the degree of crystallinity of the porous material. Diffraction patterns from ordered nanoporous materials look like diffraction pattern from imperfect crystals, where crystals with defects are less precisely periodic and give rise to relatively broad peaks. Peaks are detected as a function of angle between the incident and the diffracted seam, which is defined as 2θ. The geometry used to obtain 1-D PXRD patterns is known as the Bragg – Brentano geometry, where the incident beam is fixed and the detector moves to angle 2θ to maintain the correct θ-2θ geometry. According to Bragg's law, constructive wave interference and hence the appearance of diffraction peaks occurs when the difference in path length between photons reflected from neighboring planes of atoms or pores (2dsinθ) is equal to an integer multiple of the wavelength of the x-rays:

$$2d\sin\theta = n\lambda \qquad (2.12)$$

where n is an integer. The diffraction pattern from a material contains several reflected peaks, each corresponding to a different interplanar d-spacing corresponding to a different crystallographic plane. Based on the relationship between the reciprocal d-spacings (1/d) of these peaks, the pore geometry and symmetry group can be determined. The 2D-hexagonal phase (p6mm symmetry group) of nanoporous material is identified by well resolved Bragg reflections with reciprocal d-spacing ratios of 1: √3: √4: √7: √9, etc. that can be indexed to the (100), (110), (200), (210), (300), etc. reflections. A three-dimensional cubic phase with Pm3n symmetry group (same space group as SBA-1 material) is identified by Bragg reflections with reciprocal d-spacing ratio of √2: √3: √4: √5: √6: √8: √9: √10: √11: √12 etc. that can be indexed to the (110), (111), (200), (210), (211), (220), (300), (310), (311), etc. A bicontinuous cubic phase with Ia3d symmetry group is identified by Bragg reflections with reciprocal d-spacing ratios of √6: √8: √10: √14: √16: √18: √20 etc. that can be indexed to the (211), (220), (321), (400), (420), (332), (422), etc. Lamellar phase allows the Bragg reflections of (100), (200), (300), etc. which give reflections with reciprocal d-spacing ratios of 1: 2: 3, etc.

2.9.4 Transmission Electron Microscopy (TEM)

Transmission Electron Microscopy (TEM) is a powerful tool that provides the opportunity to analyze the microstructure, composition, and crystal structure of materials.

In TEM a parallel (coherent) stationary beam of electrons is used to illuminate an area of sample and a portion of beam passing through the specimen is used in image formation.[138] The spatial resolution of a light microscope using green light in the middle of the visible spectrum (wavelength λ = 550 nm) is about 300 nm, whereas a TEM operating at 100 kV can achieve resolution on the order of an atomic size (~ 0.3 nm). This is because the spatial resolving power of microscope is directly proportional to the wavelength of illumination.[139] The visible spectrum possess wavelength in the range of 400 – 800 nm, whereas the high-energy electron possess a wavelength much smaller than interatomic dimensions, λ = 4 pm.[139, 140] However, a tradeoff for electron microscopy is that the sample to be analyzed must be thin enough that the high energy electrons corresponding to 100 kV or higher can pass through to give magnified image of the sample or an electron diffraction pattern.[138] For sample preparation, very finely divided particles from power samples or thin films (after scraping off from the substrate) are dispersed onto grid for TEM analysis. As the beam of electrons pass through the specimen, some primary beam electron will be elastically scattered and some electrons transmit through as unscattered. The unscattered electrons leaving the specimen are combined together to form bright-field (BF) image and some of the elastically scattered electrons are combined to form dark-field (DF) image. In scanning transmission electron microscopy (STEM), a sharp narrow (~2 - 20Å) focused electron beam is focused at the specimen and scanned to obtain the image. The STEM mode of operation is useful to obtain chemical mapping of the samples with the utilization of an energy dispersive x-ray spectroscopy (EDX or EDS) detector.[137]

2.9.5 Ultraviolet-Visible (UV-vis) Spectroscopy

Some useful information about the identity of many organic molecules and inorganic complexes can be derived from ultraviolet–visible (UV-vis) spectroscopy, which utilizes the electro-magnetic spectrum in the ultraviolet (UV) and visible (vis) regions (wavelength range from 190 nm to 800 nm).[135] When continuous radiation with wavelengths in this range passes through a transparent sample, a portion of the radiation may be absorbed. Analysis of the absorbed radiation as a function of wavelength with a detector yields an absorption spectrum. The energy absorbed represents that of transitions

between electronic ground states and excited states, and is quantized. Ultraviolet transmission radiation was used to identify the coordination environment of titanium in Si-Ti mixed oxides thin films (discussed in Chapter 4) and the visible radiation range (λ = 400 – 750) was used to quantify glucose in aqueous solutions using the phenol – sulfuric acid assay method (discussed in Chapter 6). Specific sampling and wavelength characteristics of those materials will be discussed in those chapters.

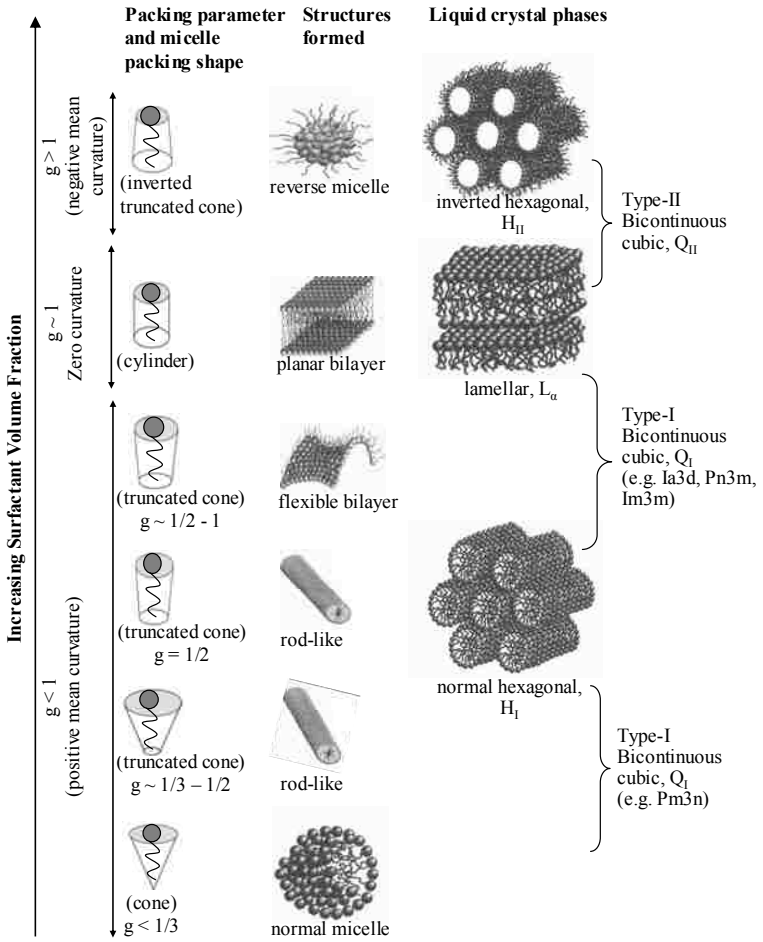

Figure 2.1. Schematic representation of an ideal sequence of the formation of surfactant micelles structures along with their relationship with packing parameters and shapes of surfactant in micelles on increasing surfactant volume fraction in water (solvent). Also the expected typical lyotropic liquid crystalline phases for such aggregates are shown. (An adaptation derived from figures used with permission from Hamely, I. W., *Introduction to Soft Matter*, John Wiley & Sons (2000)[141] and Holmberg, K; Jönsson, B; Kronberg, B. and Lindman, B., *Surfactants and Polymers in Aqueous Solution*, 2nd Edition, John Wiley & Sons (2003)[142])

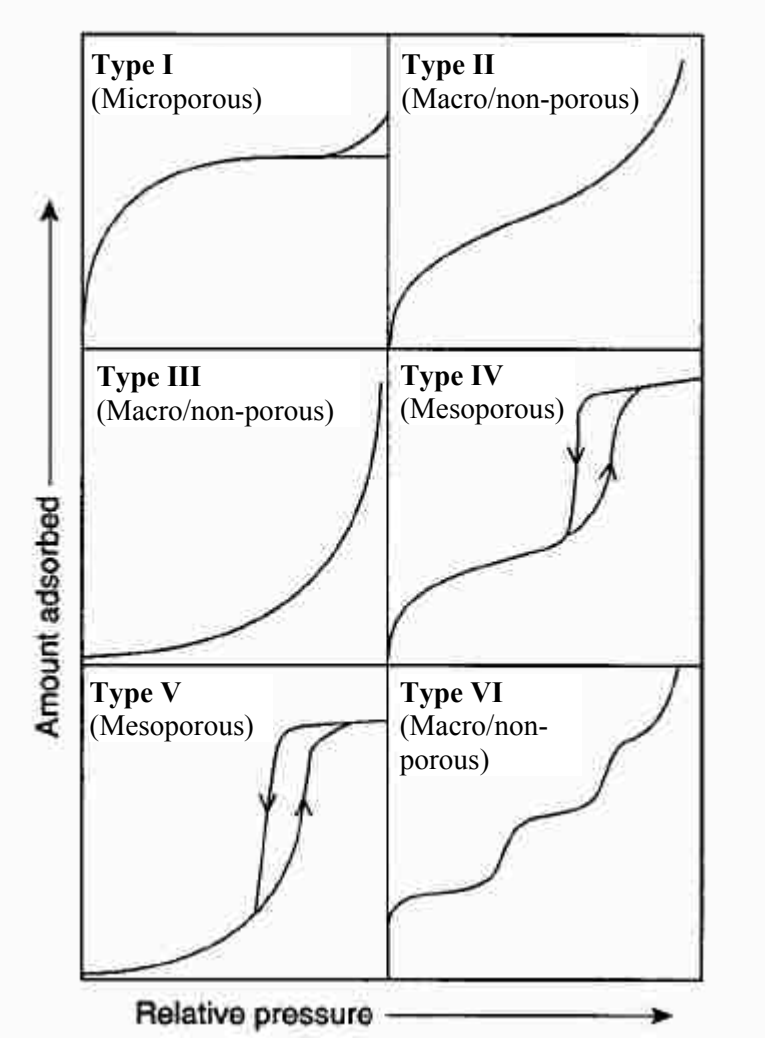

Figure 2.2. IUPAC classification of gas adsorption isotherms (adapted from Sing et al.[5])

CHAPTER 3

TERNARY LYOTROPIC LIQUID CRYSTAL PHASE DIAGRAM OF AQUEOUS MIXTURES OF MALTOSIDE AND CATIONIC SURFACTANTS AND ITS USE FOR PREDICTIVE SYNTHESIS OF ORDERED MESOPOROUS SILICA

3.1 Summary

Self-assembled nonionic alkyl glycoside surfactants are of interest for creating functional adsorption and catalytic sites at the surface of mesoporous sol-gel-derived materials, but they typically impart poor long-range order when they are used as pore templates. Improved order and control over the functional site density can be achieved by mixing the alkyl polyglycoside surfactant with a cationic surfactant. Here, we investigate the lyotropic liquid crystalline (LLC) phase behavior of aqueous solutions of the functional nonionic surfactant n-dodecyl-β-D-maltoside ($C_{12}G_2$/DM) and cetyltrimethylammonium bromide (C_{16}TAB) by low-angle powder x-ray diffraction (XRD) and polarized optical microscopy (POM). An approximate ternary phase diagram of C_{16}TAB-$C_{12}G_2$-water system is developed at 50°C, which includes 2-D hexagonal (P6mm symmetry), bicontinuous cubic (Ia3d symmetry), lamellar, and rectangular (cmm symmetry) liquid crystalline phases. By replacing the volume of water in the phase diagram with an equivalent volume of silica, ordered mesoporous materials are prepared by a nanocasting technique with variable $C_{12}G_2$/C_{16}TAB ratios. A hypothesis underlying this approach is that the hydrogen bonding interactions between the maltoside headgroup and silanols at the material surface resemble the interactions with water enough to allow the same phase to form. X-ray diffraction, transmission electron microscopy, and nitrogen sorption confirm the formation of the phases predicted from the ternary phase diagram in most cases. However, silica materials synthesized with comparatively higher $C_{12}G_2$/C_{16}TAB ratios are only very weakly-ordered in a way that does not correspond to their lyotropic liquid crystalline phase behavior.

3.2 Introduction

Since the discovery of surfactant templated mesoporous materials possessing long range order and narrow pore size distributions by Mobil researchers in 1992,[8, 9] a tremendous amount of research has been directed towards synthesizing different mesostructured silicas with various surfactant templates for applications in the areas of separation, adsorption, catalysis, drug delivery, electronic devices, etc.[2, 4, 6, 24, 39, 43, 143-146] Classes of surfactants employed include cationic,[8] anionic,[39, 147] nonionic,[20, 24, 34, 42, 148] cationic / anionic mixtures,[27, 149] cationic / nonionic mixtures,[28, 121, 150, 151] and anionic / nonionic mixtures.[115, 116] Despite this range of investigations, sugar-based surfactants (mainly alkyl glycosides) have been largely neglected. Sugar surfactants are a novel class of nonionic surfactants synthesized from renewable resources and are of increasing interest for industrial applications and academic research as an alternative to other types of surfactants.

Composed of a hydrophilic sugar head group and a hydrophobic hydrocarbon chain, alkyl glycoside surfactants are of interest because of (a) their ability to form liquid crystalline phases[152-155] due to the extensive hydrogen bonding capacity of sugar headgroup, (b) the possibility of forming chirally discriminative ordered mesoporous inorganic materials by transferring the chiral information from its headgroup into sol-gel derived materials,[156-158] and (c) their appealling "green" characteristics of being nontoxic, biodegradable, and synthesized from renewable resources.[159, 160] Despite their advantages as detergents, these sugar based nonionic surfactants can be difficult to assemble into ordered materials[161] because neutral surfactants (N^o) and weakly charged inorganic precursors (I^o) interact only by relatively short-ranged hydrogen bonding forces, often resulting in disordered mesostructures.[24, 25] Here, the commercially available alkylglycoside n-dodecyl β-D-maltoside ($C_{12}G_2$/DM) is selected as a nonionic alkyl glycoside surfactant to study the isothermal lyotropic phase behavior when mixed with the widely used cationic surfactant cetyltrimethylammonium bromide (C_{16}TAB) in water. Good ordering of materials and control over the functional site density at the material surface can be gained by mixing a nonspecific but charged cationic surfactant with the nonionic but highly functional and chiral $C_{12}G_2$ surfactant. The maltoside surfactant $C_{12}G_2$ has the advantage over a glucose-based surfactant such as dodecyl-β-D-

glucopyranoside (DG/$C_{12}G_1$) because its larger headgroup should increase the curvature of the micellar aggregates. A larger headgroup area favors high-curvature aggregates such as cylindrical micelles, and provide more hydroxyls for selective binding to the silica matrix.[66] The only example of using $C_{12}G_2$ surfactant as templates in synthesizing mesoporous material is from Hüsing et al., and resulted in thin films of hexagonal mesophase.[162, 163]

The liquid crystalline phase diagrams of pure $C_{12}G_2$ in water[152, 153, 164] and C_{16}TAB in water[165-167] have been reported in the literature, but not for aqueous mixture of these two surfactants. Here we report the isothermal lyotropic liquid crystalline (LLC) phase behavior of the aqueous mixtures of C_{16}TAB and $C_{12}G_2$ surfactants. All previous studies of binary phase behavior of C_{16}TAB-water system exhibited the presence of hexagonal (H_I), cubic (Q_I), and lamellar (L_α) phases. An earlier study of Warnhein and Jonsson[166] agrees qualitatively with a later study performed by Aurvay et al.,[165] where they found different phase boundaries along with a deformed hexagonal phase between the hexagonal and cubic phases identified by using small angle x-ray scattering (SAXS). Very recently, the liquid crystalline phase behavior of C_{16}TAB in water was revisited by Yang and White to clarify the regions where phase transitions from hexagonal to deformed hexagonal to cubic take place.[167] The first complete binary surfactant-water phase diagram for $C_{12}G_2$ was reported by Warr et al.,[164] who reported almost temperature-independent phase transitions from isotropic liquid (I) to lamellar (L_α) to solid surfactant (S) as the surfactant concentration increases. Later the phase behavior of $C_{12}G_2$ in water system was investigated by Auvray et al.[152] using SAXS. Their study suggested that phase behavior of $C_{12}G_2$ with water is more complex than was indicated in the previous study. Along with a lamellar phase that has low surface curvature, they also have found high surface curvature hexagonal (H_I, P6m space group) phase and intermediate curvature phases such as bicontinuous cubic (Q_I, Ia3d space group) and rectangular (R). A recent study of the binary phase diagram of the $C_{12}G_2$-water system conducted by Boyd et al.[153] was not able to indicate a phase boundary between the anisotropic phases of hexagonal and lamellar phases using polarized optical microscopy, and no intermediate cubic phase was observed. The variability in observations between these three studies suggest that $C_{12}G_2$ liquid may be very sensitive to the method of

preparation of the liquid crystals, perhaps due to the rate of assembly of surfactants with a bulky hydrated headgroup. The formation of a high surface curvature hexagonal phase by $C_{12}G_2$ can be anticipated based on its surfactant packing parameter. Without considering specific interactions, the packing parameter g is equal to $\upsilon/a_o l_c$,[66] where υ is the volume of the hydrophobic tail, a_o is the area occupied at the micelle-water interface by the surfactant headgroup, and l_c is the hydrophobic tail chain length. By taking the value of a_o as 45 $Å^2$ at 25 °C[153] along with the values of υ and l_c of the extended dodecyl hydrocarbon chain as 350 $Å^3$ and 16.7 Å respectively (calculated using Tanford's formulas[68]), the critical packing parameter value for $C_{12}G_2$ surfactant is slightly less than 0.5, which should favor cylindrical micelles. Although these calculations are over-simplified because of the dependence of a_o on temperature and degree of hydration, the ability of $C_{12}G_2$ to form a hexagonal phase is also supported by the finding of hexagonal LLC phase with other disaccharide surfactants.[168, 169]

Surfactant-templated materials with periodic mesostructures can be prepared from either dilute surfactant solutions[8, 9] or within concentrated surfactant solutions that are in or near a liquid crystalline state.[77] The mechanism that has been proposed for the first synthetic route is known as cooperative self-assembly.[40, 80] In that mechanism, the surfactant and inorganic precursor combine into a new precipitated phase and cooperative interfacial interactions between the surfactant and silicate oligomers are considered an important driving force for forming silicate-surfactant supramolecular aggregates. In this mechanism, no preformed liquid crystal phase is necessary, but because of partitioning between the bulk dilute phase and the precipitated aggregates, the structure of the product is difficult to predict. One would imagine that this problem would be particularly acute when mixed surfactants are used. The second method, proposed by Attard et al.-[77] and sometimes known as nano-casting, uses a relatively concentrated surfactant solution (≥30 wt%) in which a preformed liquid crystalline phases acts as the template for the final mesostructure. To be more precise, the silica precursors and surfactants in the concentrated solution form a homogeneous liquid crystal upon evaporation of alcohol produced during hydrolysis and of excess water that may be needed to drive hydrolysis to completion. This second method offers the advantage of being able to predict the final mesostrusture of the surfactant-silicate complex. Alberius et al.[91] outlined a general

method for predictive synthesis of surfactant templated mesostructure by taking into account the effects of solvent evaporation on the final mesostructural behavior. This method is based on a hypothesis that the volume of hydrophilic inorganic species, present in the reaction system after complete hydrolysis of the ceramic precursor, can replace the water in a LLC phases to generate a material with the same structure. Another advantage of nano-casting for our system is that both surfactants are incorporated into the as-made material in the ratio initially added to the synthesis solution.

Here we investigate the lyotropic liquid crystalline phase behavior of aqueous mixtures of $C_{12}G_2$ and C_{16}TAB surfactants by low-angle powder X-ray diffraction (XRD) and polarized optical microscopy (POM). We then use this ternary phase diagram to draw a quantitative comparison between the liquid crystal mesophases and the observed mesostrucrures of silica synthesized by using the nano-casting (LLC templating) technique of Attard et al.[77] This is accomplished by replacing the volume of water in the LLC with an equivalent volume of hydrolyzed inorganic precursor.[91] The approach follows our prior study of the octyl-β-D-glucopyranoside / C_{16}TAB system,[170] but we will show that the bulkier headgroup of $C_{12}G_2$ introduces more differences between the LLCs and materials than in the prior study, most likely due to the increase in the number and specificity of hydrogen bonding interactions with water.

3.3 Experimental

3.3.1 Materials

Tetramethyl orthosilicate (TMOS, 98%) and cetyltrimethylammonium bromide (C_{16}TAB, 99%) were purchased from Sigma Aldrich. n-dodecyl β-D-maltopyranoside (β-$C_{12}G_2$, ≥99%, %α<0.2) was purchased from Anatrace. Deionized ultra-filtered water (DIUF), 0.1N HCl, and absolute ethanol were purchased from Fisher Scientific. All chemicals were used as received without any further purification.

3.3.2 Phase characterization

Precisely weighted surfactants and DIUF water were mixed in small vials that were securely closed and sealed with Parafilm. Depending on the surfactant

concentrations, the mixture was then equilibrated at 50 °C for 3-6 days until an equilibrium solution formed that was homogeneous to visual inspection. Low-angle powder X-ray diffraction (XRD) was performed at 50 °C after transferring the samples into a 1mm thick cell with flat Mylar window. For polarized optical microscope analysis, samples were transferred quickly into silicone spacers between a microscope glass slide and a microscope cover glass. Samples were placed on a heated stage at 50 °C and inspected through crossed polarizers.

3.3.3 Predictive Synthesis of Mesoporous silica

LLC phases, formed from the mixture of C_{16}TAB and $C_{12}G_2$ and/or from pure C_{16}TAB or $C_{12}G_2$, were used as direct templates to synthesize mesoporous silica materials via the nano-casting method.[77] For a general synthesis, the amount of surfactant(s) was calculated from a point with the desired phase structure selected from the ternary phase diagram of the C_{16}TAB-$C_{12}G_2$-water system. Then the volume of water that corresponds to that desired point in the phase diagram was replaced by equivalent volume of inorganic species to calculate the required amount of TMOS.[91] The H_2O/Si molar ratio used for hydrolysis varied from 4 to 10, depending on the surfactant concentration. In a representative example of the synthesis process, 0.3 g of C_{16}TAB and 0.2 g of $C_{12}G_2$ were dissolved with 0.7 gm of an 0.01 N hydrochloric acid at 50 °C. 1.2 gm of TMOS was then added into the homogeneous mixture under stirring. As discussed in Section 2.7 this quantity of TMOS was calculated by assuming the volume of fully hydrolyzed $Si(OH)_4$ is equal to that of the dense inorganic compound (SiO_2) plus the water released during condensation.[89, 91] In this case, the H_2O/Si ratio is 5.0. The reaction mixture was stirred continuously for ~10-15 min as long as exothermic hydrolysis reactions were occurring, and then transferred into a Petri dish. The mass of the TMOS was selected to correspond to a LLC containing 30 wt% C_{16}TAB, 20 wt% of $C_{12}G_2$, and 50 wt% water. In the ternary phase diagram of the C_{16}TAB-$C_{12}G_2$-water system developed at 50 °C, this falls into the hexagonal liquid crystal phase region. After transferring the sample to a Petri dish, a gentle vacuum (~5-10 inHg of pressure) was used to remove the methanol produced from the hydrolysis of TMOS. Vacuum treatment was continued until a homogeneous viscous solution formed which was then heated at

50°C for 2-3 days in an uncovered dish to allow polycondenstion to continue. Upon drying, transparent but cracked pieces of silica-surfactant composite material were formed. The as-synthesized material was then heated at 550°C for 1hr in flowing nitrogen (after ramping at 1 °C/min to this temperature), then held at that temperature in flowing air for another 5 hr. This two-step pyrolysis/calcination is used in an effort to preserve the structure of the as-prepared materials.

3.3.4 Characterization

LLC phases were characterized with a Bruker D8 Discover diffractometer using 0.154056 nm CuKα radiation. A Labrolux S Leitz optical microscope with polarizers was used for POM studies. Powder XRD patterns were recorded with a Siemens 5000 diffractometer using 0.154098 nm Cu K_α radiation. TEM images were recorded with a JEOL 2000FX microscope operated at 200 kV. TEM samples were prepared by grinding a small amount of the bulk material and suspending the powder on a lacey carbon grid. Nitrogen adsorption-desorption isotherms were measured at 77 K using a Micromeritics Tristar 3000 analyzer. Before measurement, all samples were degassed at 150 °C for 4 hr. Nitrogen sorption isotherms data were used to obtain information about specific surface area and pore structure of the synthesized materials. Specific surface area of the porous silica materials were evaluated by fitting the experimental adsorption data to the linearized form of the Brunauer-Emmett-Teller (BET) equation[5, 123] in the range of relative pressures (P/P_O) from 0.04 to 0.2.[124] The commonly used value of 0.162 nm^2 as the molecular cross-sectional area of N_2 on silica material assuming hexagonal packing was used to estimate the specific surface area (S_{BET}) of the material.[5, 127] Pore size distributions were estimated from the adsorption branch of the isotherms using the Barrett-Joyner-Halenda (BJH) method[125] with the corrected form of the Kelvin equation and the Harkins-Jura statistical film thickness equation as described by Kruk, Jaroniec and Sayarai (the KJS method).[126]

3.4 Results and Discussion

3.4.1 Phase Behavior of the Ternary C_{16}TAB-$C_{12}G_2$-Water System

The isothermal LLC phase behavior at 50°C of $C_{12}G_2$ and C_{16}TAB with water along with the phase behavior of the binary $C_{12}G_2$-water and C_{16}TAB-water systems were studied by means of low-angle powder x-ray diffraction (XRD) and polarized optical microscopy (POM). Representative low-angle powder XRD patterns of the observed phases, including the ordinary columnar hexagonal phase (H_I, P6mm), bicontinuous cubic (Q_I, Ia3d), lamellar (L_I), and centered rectangular phase (R_I, cmm), are shown in Figure 3.1. The hexagonal liquid crystalline phase that appears on the water rich side of lamellar phase is generally assumed to be a normal hexagonal or Type I hexagonal phase, H_I.[171] The hexagonal phase (H_I) shown in Figure 3.1(a) (composition: 35 wt% C_{16}TAB, 35 wt% $C_{12}G_2$ and 30 wt% water), is identified by three well defined XRD reflections with reciprocal d-spacing ratios of 1:√3:√4. These are indexed to the (100), (110), and (200) Bragg reflections respectively. This pattern is typical for a two-dimensional hexagonal phase with P6mm symmetry. In some cases, the higher order (200) reflection and sometimes even the (110) reflection could not be observed. In those situations where both of the the higher order reflections were missing, the hexagonal phase was characterized based on a fan-like optical texture under POM.[172, 173] The next type of LLC phase observed during this study is isotropic (as indicated by being dark in POM). The intermediate phase that appears on the water-poor side of the H_I phase is generally considered to be a normal bicontinuous cubic phase, Q_I.[72] Figure 3.1(b) shows a representative low-angle powder XRD pattern of the Q_I LLC phase formed from an equilibrated mixture of 35 wt% C_{16}TAB, 40 wt% $C_{12}G_2$, and 25 wt% water. No more than two diffraction peaks could be resolved for most of the samples studied in the Q_I region. This indicates that they do not posses very long range order in their liquid crystalline state. The reciprocal d-spacing ratios of the two reflections in Figure 1b is √6:√8, which corresponds to the (211) and (220) Bragg of a bicontinuous cubic phase with Ia3d symmetry. The absence of lower order XRD reflections eliminates the candidacy of other type I cubic phases with symmetry other than Ia3d.[174] Moreover, both the C_{16}TAB-water[165, 166] and $C_{12}G_2$-water[152] systems exhibit the presence of a bicontinuous Ia3d cubic LLC phase on the water poor side of their respective H_I phases.

Figure 3.1(c) shows a representative XRD pattern of a lamellar phase (L_α) with two well resolved peaks from the (100) and (200) reflections. The composition of this sample is 30 wt% C_{16}TAB, 65 wt% $C_{12}G_2$, and 5 wt% water. In some L_α samples, the higher order (200) reflection was absent. POM technique was then used to identify this lamellar phase by its marble-like or streaky multicolored texture.

In addition to the typical H_I, Q_I, and L_α phases, some surfactants show an alternate intermediate phase as the surfactant concentration increases beyond the H_I region. This is a ribbon-like intermediate phase is also known as a deformed hexagonal phase, composed of arrays of long cylindrical aggregates of surfactants with an elliptical cross-section arranged in a 2D-rectangular lattice ($a/b \neq \sqrt{3}$) that could have either a primitive (pgg) or centered (cmm) symmetry.[175-179] The elliptical cross-section is a result of the elongation along either in *a* or *b* axis from its circular cross-section. In the binary $C_{12}G_2$-water at 50 °C, the H_I phase transforms into a cubic (Ia3d) phase before transforming into the lamellar phase; no other intermediate phase has been found.[152] On the other hand, in the C_{16}TAB-water system at 50 °C a deformed hexagonal intermediate phase of cmm symmetry has been reported between the H_I and L_α phases.[165] This 2D centered rectangular phase with cmm symmetry (labeled R) was also observed here. A representative XRD pattern of the R phase is shown in Figure 3.1(d), which was obtained from an equilibrium mixture of 75 wt% C_{16}TAB, 5 wt% $C_{12}G_2$, and 20 wt% water. Since the higher order reflections (or at least a decisive reflection of d_{12} or d_{21}) are missing, it is not possible to determine from this XRD pattern alone what type of lattice symmetry (pgg or cmm) it exhibits.[176, 180, 181] However, the R phase of the binary C_{16}TAB-water system displays a large number of weak reflections that allowed it to be assigned to a cmm symmetry class.[165] Therefore, consistent with the previous studies of C_{16}TAB-water and $C_{12}G_2$-water systems, it is assumed here that the symmetry of the R phase is cmm. This implies elongation along the rectangular *a* axis, which means that the two peaks are indexed to (20) and (11) which gives $a/b > \sqrt{3}$.[182] From the last phase, solid C_{16}TAB salt, has XRD reflections at 2θ values of 3.5 and 7.0° (not shown here).

Using the characteristics of the LLC phases discussed above, a complete ternary equilibrium phase diagram of C_{16}TAB-$C_{12}G_2$-water system was developed at 50 °C and is shown in Figure 3.2. The accuracies of the phase boundaries indicated by solid lines

should lie within ±1 wt%, whereas for the phase boundaries indicated by long dashed lines, they could be higher than that. This could be due to the combination of ambiguity in the identity of the phases near the boundary and of relatively fewer samples investigated near those boundaries, as those areas in the phase diagram are less important for thermally stable materials synthesis. Seven different regions have been identified; six (I, H_I, Q_I, R, L_α, and S) of them are single phase regions and the remaining one (L_α phase equilibrium with S) is biphasic. This ternary system exhibits a relatively simple phase behavior that follows the usual sequence of phase transitions: isotropic fluid phase (I) to normal hexagonal (H_I) to bicontinuous cubic (Q_I) to lamellar (L_α) as water concentration decreases.[171] The L_α region is followed by the biphasic region where L_α is in equilibrium with the solid surfactant crystals. In this study, very few samples were actually analyzed along the binary axes of C_{16}TAB-water and $C_{12}G_2$-water. Instead, the details binary phase behavior studies of C_{16}TAB-water[165, 167] and $C_{12}G_2$-water[152] were used as references. Some samples were analyzed along these binary axes but those were concentrated around the phase transition points. Good consistency was found with prior studies of binary systems as shown in Figure 3.2.

As seen from Figure 3.2, the H_I phase occupies the largest single-phase area in the phase diagram. This is consistent with the large hexagonal regions of both pure surfactants in water; the H_I region extends from ~27 wt% to ~78 wt% C_{16}TAB in water and from ~48 wt% to ~76 wt% of $C_{12}G_2$ in water along the $C_{12}G_2$-water axis. These two edges are joined by a large continuous region across the phase diagram. H_I phase is followed by the bicontinuous Ia3d region which starts on the $C_{12}G_2$-water axis from ~76 wt% to ~90 wt% of $C_{12}G_2$ in water. This is consistent with the report of Auvray et al. that the Ia3d cubic phase can form for the $C_{12}G_2$ / water system at temperatures between 38°C and 74°C.[152] This region extends almost the whole way across the ternary diagram, but a centered rectangular phase, R (cmm symmetry) appears within a very small region near the C_{16}TAB/water axis. The R phase is formed between ~15 wt% and ~21 wt% of water and can include up to ~15 wt% of $C_{12}G_2$. Auvray et al. first reported the appearance of the R phase in the binary C_{16}TAB-water system at temperatures above 38 °C[165]. Beyond these intermediate phases, a pure L_α is found only for $C_{12}G_2$ content more than ~24 wt% in the ternary mixture. In this study, at 50 °C the L_α phase formed when the $C_{12}G_2$

content is ~90-95 wt% in water along the $C_{12}G_2$-water axis. However in an earlier study, the L_α phase had only been seen at temperatures greater than 74 °C.[152] When the $C_{12}G_2$ content in the ternary mixture is less than ~24 wt%, no pure L_α phase is seen, and instead the cubic phase transforms to a biphasic phase where L_α is in equilibrium with solid surfactant crystals. This biphasic region extends all the way to the $C_{12}G_2$-water axis. The rest of the area of this ternary phase diagram is occupied by solid surfactants (S).

3.4.2 Predictive Synthesis of Mesoporous Silica

The ternary phase diagram of the C_{16}TAB-$C_{12}G_2$-water system was used as a quantitative tool for the predictive synthesis of mesoporous silica. The approach used here was adapted from Alberius et. al.,[91] where a direct quantitative comparison was made between a binary liquid crystal phase diagram and the final structure of silica-surfactant composites. Here we are going to examine that how well the final meso-structure of the silica-surfactant composite could be predicted from the ternary phase diagram of the C_{16}TAB-$C_{12}G_2$-water system developed at the synthesis temperature used for nano-casting. For this purpose at first, several points from the hexagonal (P6mm) and cubic (Ia3d) phase regions of the phase diagram were selected as starting points during materials syntheses. These points are shown in the phase diagram by small stars in Figure 3.2. During material synthesis, the volume of water needed at the point of interest in the phase diagram was replaced by the equivalent volume of condensed silica plus the volume of water generated during condensation to find out the required amount of TMOS[89, 91] (as discussed in the Experimental section). The phases of the as-synthesized mesoporous silica were identified from their powder XRD patterns. In all of the cases represented by stars in both the hexagonal and cubic phase regions, good agreement was found between the LLC phase of the C_{16}TAB-$C_{12}G_2$-water system and the final meso-structures of the as-synthesized silica-surfactant composite. Thus the LLC phases observed during the phase diagram study can be used to predict the final mesophase of C_{16}TAB-$C_{12}G_2$ templated silica materials prepared via nanocasting. Representative powder XRD patterns for the as-synthesized silica materials with 2-D hexagonal (p6mm) and bicontinuous cubic (Ia3d) structures are shown in Figure 3.3. In Figure 3(a), the highly ordered hexagonal structure of the as-synthesized silica is identified from the

presence of three well-resolved Bragg reflections that can be indexed to (100), (110) and (200) Similarly, consistency was found between the phase behavior of the points selected from the cubic phase region of the ternary phase diagram and the mesostructure of the as-synthesized silica materials. Cubic mesophase with Ia3d space group are identified from their XRD patterns with five well-resolved Bragg reflections that can be indexed to (211), (220), (321), (420), and (332), as shown in Figure 3(b). The compositions corresponding to points in the ternary phase diagram from which these two silica materials were synthesized are shown in the captions of their respective figures.

Series-1: Materials Synthesized with 60 wt% of Total Surfactant

To gain more understanding of the effects of $C_{12}G_2$ inclusion on the resulting materials, a first series of silica materials was synthesized along a line corresponding to 60 wt% of total surfactant in the ternary phase diagram with variable relative amounts of $C_{12}G_2$ and C_{16}TAB. Samples 1 to 6 belong to Series-1 and represent increasing fractions of $C_{12}G_2$ in the surfactant mixture. Sample 1 was synthesized at the first point on the line, using 60 wt% of pure C_{16}TAB surfactant as the structure directing template. Compositions of all of these samples (in wt%) can be read from Figure 3.2 and are also shown in Table 3.1.

Powder XRD patterns of the as-synthesized and calcined Series-1 materials are compared in Figure 3.4. Samples 1-3 are well-ordered 2D-hexagonal (P6mm) materials, as indicated for Sample 1 by the presence of (100), (110), (200), and (210) reflections and for Samples 2 and 3 by the presence of (100), (110), (200), (210) and (300) reflections. In Figure 3.4(a), reflections from crystalline C_{16}TAB salt are also present, located at 2θ values of ~3.5 and 7°. In the case of Sample 4, (Figure 3.4(d)), three clearly discernible hexagonal reflections are observed. However, for Sample-5, (Figure 3.4(e)) only a strong (100) reflection and a weak broad shoulder from the combined effect of (110) and (200) reflections can be seen. This indicates that the pore structure of this sample is disordered and wormhole-like due to the lack of long-range crystallographic order.[24, 42, 183, 184] The last sample of this series, Sample 6, exhibits a single XRD reflection, which is consistent with weak ordering, although the symmetry cannot be inferred from one reflection. The mesopore structure of sample 6 collapses upon calcination (Figure 3.4(f)) giving rise to no low angle XRD reflection. For rest of the samples in Series-1, in Figure 3.4(a) to

3.4(e), peak broadening and disappearance of high order diffraction peaks are observed upon calcination. This implies some losses of long-range order due to removal of surfactants and possibly sintering of the pore structure.

As the $C_{12}G_2/C_{16}TAB$ ratio is increased in Series-1, we have observed that the well- ordered 2D-hexagonal (P6mm) meso-structure observed with pure $C_{16}TAB$ changes to a disordered hexagonal or wormhole like, which is followed by a very weakly-ordered meso-structure. Well-ordered 2D-hexagonal materials were synthesized from phase points corresponding to between 60 wt% of pure $C_{16}TAB$ and a 48 wt% $C_{12}G_2$ / 12 wt% $C_{16}TAB$ mixture in water. The disordered hexagonal / wormhole-like structure extends from a $C_{12}G_2/C_{16}TAB$ mass ratio of 48/12 to 57/3. The structural order deteriorates further when even more $C_{12}G_2$ is used. Figurse 3.5(a) and (b) show representative TEM images of the as-synthesized ordered 2D-hexagonal and disordered hexagonal mesoporous silica respectively. Compositions of these two samples are shown in the captions of the respective figures. Figure 3.5(a) reveals an array of highly ordered hexagonal mesopores viewed from the side. Figure 3.5(b) shows the disordered wormhole-like framework in the as-synthesized material.[24]

The observed deviations between the lyotropic liquid crystalline phases in the $C_{12}G_2$-$C_{16}TAB$-water phase diagram and the phases of the final mesostructured silica materials could be caused by different hydrogen bonding arrangements of the hydroxyl groups of $C_{12}G_2$ with water molecules vs. silicate species. Weaker and less highly coordinated hydrogen bonding would be expected for the silicates, and this may lead to a poorly ordered structure. Another related factor is that the kinetics of assembly of the mesophases rich in $C_{12}G_2$ may be too slow relative to the rate of silica polycondensation, which results in poor long-range order. The stronger long-range cationic interactions of $C_{16}TAB$ with silicates and with neighboring micelles are beneficial to the formation of well ordered mesoporous silica compare to weaker, short-range hydrogen bonding interactions between the maltoside headgroups and silicates.

The nitrogen sorption isotherms for all calcined silica samples in Series-1 are shown in Figure 3.6(a). All the isotherms are type IV according to IUPAC classification[5]. This type of isotherm is typically observed for mesoporous solids when multilayer adsorption is followed by capillary condensation in uniformly sized mesopores[127]. For

samples 1-5, absence of any hysteresis loop indicates that the capillary condensation and evaporation is reversible, whereas sample 6 displays a hysteresis loop. This type of triangle-shaped hysteresis loop has been attributed to the presence of narrow mouthed "ink-bottle" shape pores[127] or nonuniform pores, either of which would be consistent with the collapse of sample 6 upon calcination. The isotherms of all samples except sample 6 exhibit sharp capillary condensation steps, which indicate the presence of uniform pores. This can be quantified using the pore size distributions obtained from the KJS method from their corresponding adsorption branches[127] (Figure 3.6(b)). Narrow pore size distributions are observed, indicating well-defined uniform pores in all calcined materials except for sample 6, which has a broader distribution consistent with the collapse of long-range mesopore order during calcination.

Table 3.1 summarizes some of their structural properties of the Series-1 samples. An increase in the d-spacing values of the as-synthesized hexagonal materialsis observed as the $C_{12}G_2/C_{16}TAB$ ratio increases. The increase in the d-spacing of the mesopores with increasing $C_{12}G_2/C_{16}TAB$ ratio is also preserved in the calcined samples. Along with this d-spacing increase, the peak in the KJS pore size distribution shifts towards larger pores. This can also be shown by calculating the pore width by assuming cynlindrical pore shape. For cylinders, the primary mesopore diameter $w_d = 1.213d(\rho V_P/(1+\rho V_P))^{1/2}$; where d is the (100) interplanar spacing obtained from XRD spectrum, ρ is the density of amorphous silica wall (2.2 gm/cm^3), and V_P is the primary specific mesopore volume.[126] Values of w_d are listed in Table 3.1. The primary mesopore volume (V_P) was calculated by using the high resolution α_s-plot method.[124, 133] Wall thickness was calculated from the differences between unit cell parameter (a_o) of the calcined materials and the primary mesopore diameter. The wall thicknesses increase slightly in the mixed surfactant templated silica materials relative to those templated with pure $C_{16}TAB$. Consistent with these trends, as the relative amount of $C_{12}G_2$ surfactant with respect to $C_{16}TAB$ surfactant decreases, the corresponding BET specific surface area decreases from 1136 m^2/g to 528 m^2/g. These structural parameters indicate that well-ordered 2D-hexagonal mesoporous silica with tunable pore size can be synthesized by adjusting the $C_{12}G_2/C_{16}TAB$ ratio. The concentration of maltoside groups at the micelle-

material interface is also adjusted in this series, which provides for more synthetic opportunities to be explored in the future.

Series-2: Materials Synthesized with Pure $C_{12}G_2$ Surfactant

In Series-1, we found that while a weakly-ordered material could be isolated when it was made with pure $C_{12}G_2$, it was not stable to calcination. Therefore, it seems that there are regions of the phase diagram that cannot replicated in a solid mesoporous material. In an effort to clarify the regions in the ternary phase diagram where the final mesostructures of silica-surfactant composite materials could be predicted, a second series of silica materials, Series-2, was synthesized using pure $C_{12}G_2$ surfactant as the structure directing agent. Samples 7-9 belong to this series and correspond to 50 wt%, 70 wt%, and 80 wt% $C_{12}G_2$ in water, as shown in Figure 3.2 along the $C_{12}G_2$-water axis. We have studied the mesostructural ordering of these materials by low angle powder XRD. Their XRD patterns are compared in Figure 3.7 along with the representative XRD patterns of the hexagonal and cubic lyotropic liquid crystal phases observed with pure $C_{12}G_2$ surfactant in water. 2D-hexagonal ordering in Sample 7 is revealed by the appearance of three discernible diffraction peaks indexed to (100), (110), and (200) (Figure 3.7(a)). As the $C_{12}G_2$ surfactant concentration used during material synthesis increases, the phase of the surfactant-silica composites changes from 2D-hexagonal to a weakly-ordered structure that collapses upon calcination to give a featureless XRD pattern (as described for Sample 6). A higher surfactant concentration corresponds to a lower silicate concentration, which helps to explain why the samples with more $C_{12}G_2$ are less stable. However, in the phase diagram along the $C_{12}G_2$-water axis, H_I lies between ~48 wt% and ~76 wt% and the Q_I phase lies between ~76 wt% and ~88 wt% of $C_{12}G_2$ surfactant at 50 °C. Representative small-angle XRD patterns of the hexagonal (P6mm) and cubic (Ia3d) liquid crystal mesophases, obtained from 60 wt% and 76.5 wt% of pure $C_{12}G_2$ surfactant in water respectively, are shown in Figure 3.7(b). In contrast, by replacing the volume of water by the equivalent volume of $Si(OH)_4$, we were able to synthesize hexagonal $C_{12}G_2$-silica composites using only less than 52 wt% of $C_{12}G_2$ in water; beyond that materials are lamellar. This is in agreement with the previous results of Štangar and Hüsing,[163] who prepared thermally stable silica thin films with hexagonal

ordering with a range of low $C_{12}G_2$ concentrations, which is followed by lamellar phase only at higher $C_{12}G_2$ concentration.

Therefore we conclude that the mesophase of silica prepared with pure $C_{12}G_2$ surfactant can be predicted precisely from the phase diagram only at high silicate concentrations. The materials are weakly-ordered or lamellar at low silica content (corresponding to > 52 wt% of $C_{12}G_2$ on the ternary phase diagram). As discussed earlier, this deviation could be because of different hydrogen bonding ability with hydroxyl groups of maltoside of $C_{12}G_2$ of water molecules compared to silicates. Because of its tetrahedral geometry, a single liquid water molecule can form four simultaneous hydrogen bonds which gives it unique properties. The difference in hydrogen bonding behavior is prominent when only a small amount of silicate is available for hydrogen bonding with polar headgroups, resulting in poor ordering. The transition to a lamellar phase would be consistent with silicates (perhaps just due to their size) being unable to "hydrate" the headgroups of $C_{12}G_2$, thus giving a smaller area per headgroup and a larger packing parameter. Slow kinetics of co-operative assembly of surfactant micelles and silicate species present in the reaction mixture might also have played a role in preventing the formation of well-ordered materials.

Series-3: Materials Synthesized Along the H_I-Q_I Phase Boundary

A third series of materials was synthesized along the phase boundary separating the hexagonal and cubic LLC regions in the phase diagram. Samples 10-16 are members of Series-3. In order to synthesize these materials, starting points from the phase diagram were selected from both sides of the phase boundary, as shown in Figure 3.2. To predict the final mesostructure of the materials correctly from the phase diagram or to avoid the deviations observed from the Series-1 materials, these mixed surfactant templated silicas were synthesized at relatively low $C_{12}G_2/C_{16}TAB$ ratios. The x-ray diffraction patterns of Samples 10-16, are shown in Figures 3.8(a) to 3.8(g) respectively. The surfactant compositions of these as-synthesized materials are shown in the caption of Figure 3.8. Figures 3.8(a) to 3.8(d) reveal the long range 2-D hexagonal mesostructural ordering of Samples 10-13. The final structure of Sample 11, synthesized with a composition corresponding to 52.5 wt% $C_{16}TAB$ and 22.5 wt% $C_{12}G_2$, is correctly predicted to be hexagonal from the phase diagram. Although the other three samples (Samples 10—13)

lie just within the cubic LLC phase region, they turned out to be 2D-hexagonal. However, in the cases of Samples 14-16 (whose compositions falls within the cubic LLC region and far away from the H_I phase boundary), we were able to synthesize cubic mesostructured silica with Ia3d symmetry. Figures 3.8(e) to 3.8(g) show XRD diffraction patterns of the as-synthesized Samples 14-16 (respectively) that are consistent with cubic Ia3d symmetry. This implies that a ~3-5 wt% adjustment toward the Q_I phase region from the H_I-Q_I phase boundary is required to get cubic mesostructured silica materials. Samples 14-16 were synthesized with a total surfactant content of 80 wt% but with an increasing ratio of $C_{12}G_2$/C_{16}TAB. The d_{211} spacing increases from 29.1 to 33.8 Å to 34.0 Å in this series, and the corresponding cubic unit cell parameter (calculated using an equation $a = \sqrt{6}d_{211}$) increases from 71.3 to 82.7 Å to 83.4 Å as we move from Sample 14 to 16. This is consistent with the increase in lattice parameter observed for the hexagonal phase upon incorporation of more $C_{12}G_2$ in Series-1.

3.5 Conclusions

A complete ternary phase diagram of the C_{16}TAB-$C_{12}G_2$-water system at 50 °C with approximate phase boundaries was reported. This diagram was then used to test how well the hypothesis holds for this system that mesoporous materials structures can be predicted from the phase diagram by replacing the water in a lyotropic liquid crystal with an equal volume of silicic acid. Highly ordered hexagonal and cubic silica mesoporous materials could be synthesized within the predicted regions by a mixed surfactant templating route. A series of materials was synthesized keeping the total amount of surfactant constant but varying the relative amounts of the two surfactants. The pore size of the materials could be increased somewhat by increasing the ratio of $C_{12}G_2$ to C_{16}TAB surfactants. However, because of changes in hydrogen bonding between silica and $C_{12}G_2$, increasing disorder of the mesoporous structures was observed as the relative amount of $C_{12}G_2$ surfactant increased with respect to C_{16}TAB surfactant for fixed total surfactant content. The structure of mesoporous silica changed from well-ordered 2D-hexagonal to disordered hexagonal to very weakly-ordered (the last of which collapsed during calcination) at $C_{12}G_2$ contents corresponding to 48 wt% and 57 wt% with 40 wt% water,

respectively. Synthesized materials corresponding to over 70 wt% of total surfactant in the aqueous system are not stable during calcination, however, because of very thin silica walls. Difficulties predicting the silica-surfactant mesophase were encountered near the boundaries of the hexagonal phase. Materials synthesized with pure $C_{12}G_2$ surfactant at the highest silicate concentrations were correctly predicted to be hexagonal. However, the materials were only weakly ordered at low silica content / higher $C_{12}G_2$ surfactant concentration and could have been lamellar (and thus unstable to calcination). The hexagonal-cubic boundary also needed to be shifted by approximately 3-5% towards the cubic phase in order to predict the phase of the silica-surfactant mesophase. The observed deviations from the LLC phase behavior could be because of differences in hydrogen bonding of the hydroxyl groups of the $C_{12}G_2$ surfactant with water molecules vs. silicates. This would be expected to lead to less "solvation" of the headgroups and an increase in packing parameter (which would favor low-curvature structures). A related problem may be that the small driving force for ordering due to hydrogen bonding leads to slow ordering kinetics relative to the rate of silicate polycondensation. Differences of hydrogen bonding behavior are most significant when only a small amount of silicates are available for hydrogen bonding with polar headgroups, and result in poorly ordered silica. In the case of the hexagonal-cubic boundary, poor "solvation" by silica may "push" the $C_{12}G_2$ further into micelles, thus expanding the average area per headgroup and favoring the hexagonal phase over a cubic phase.

Table 3.1: Structural Properties of Series-1 Materials (Samples 1 to 6)

Sample #	Mass ratio of $C_{12}G_2/C_{16}TAB$ (wt%)	Mesophase observed	d_{100} as-syn.[a] (Å)	d_{100} calcined (Å)	S_{BET}[b] (m^2/g)	w_d[c] (Å)	t_W[d] (Å)
1	0/60	2D-hexagonal	36.3	30.9	1136	27.6	8.0
2	20/40	2D-hexagonal	36.9	31.8	1131	27.9	8.8
3	30/30	2D-hexagonal	38.8	32.5	1027	28.1	9.4
4	40/20	2D-hexagonal	39.2	33.8	930	28.6	10.4
5	50/10	d-hexagonal	39.9	36.3	854	31.4	10.4
6	60/0	weakly ordered	40.2	-	528	-	-

a: d(100) spacing of as-synthesized products; b: BET specific surface area; c: primary mesopore diameter, and d: wall thickness

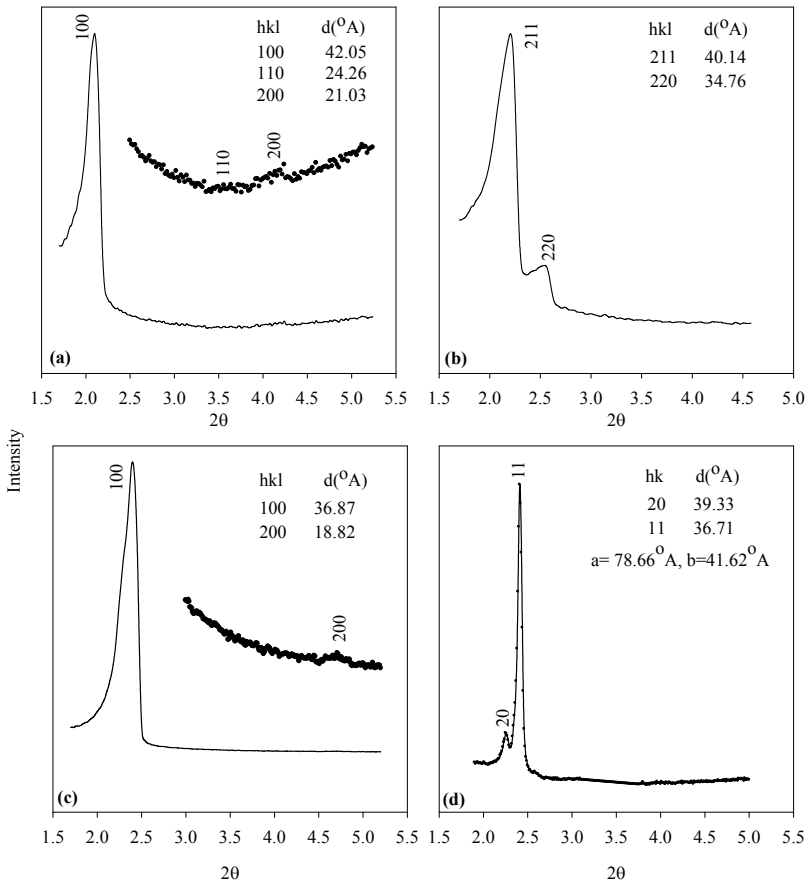

Figure 3.1. Low angle powder XRD patterns of the representative LLC phases observed with the C_{16}TAB-$C_{12}G_2$-water system investigated at 50 °C. (a) H_I phase (C_{16}TAB = 35 wt%, $C_{12}G_2$ = 35 wt%, H_2O = 30 wt%); (b) Q_I phase (C_{16}TAB = 35 wt%, $C_{12}G_2$ = 40 wt%, H_2O = 25 wt%); (c) L_α phase (C_{16}TAB = 30 wt%, $C_{12}G_2$ = 65 wt%, H_2O = 5 wt%), (d) R phase (C_{16}TAB = 75wt%, $C_{12}G_2$ = 5wt%, H_2O = 20 wt%).

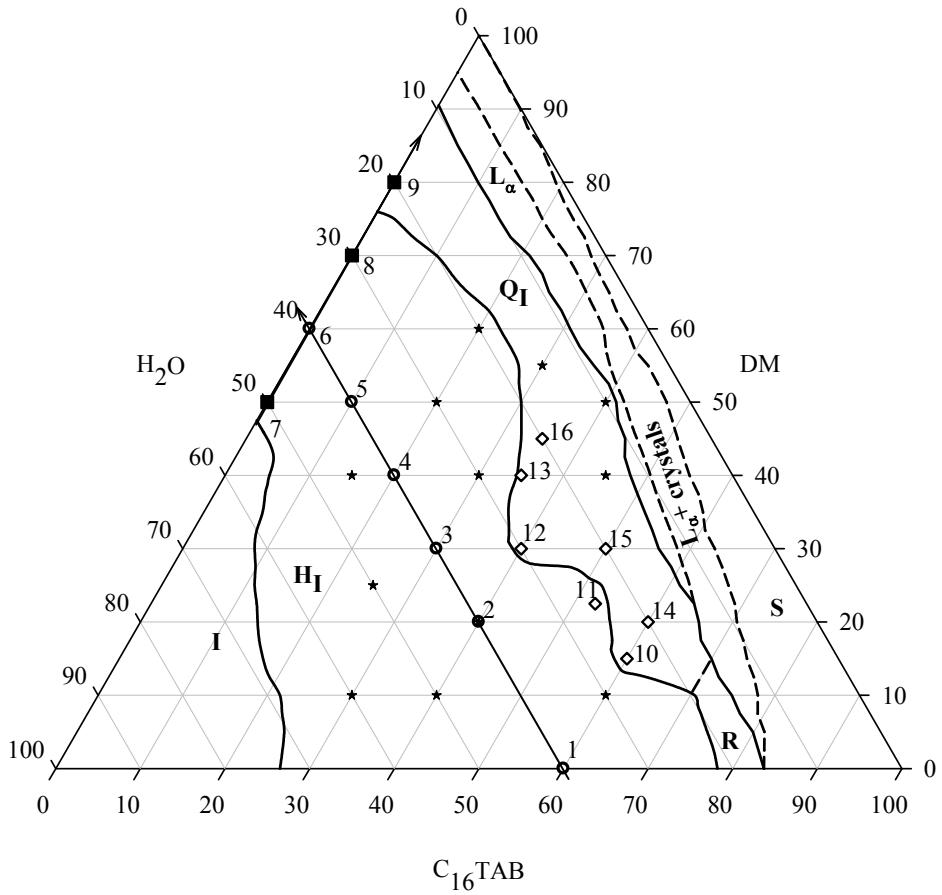

I: isotropic fluid phase; H_I: 2D-hexagonal, P6mm; Q_I: bicontinuous cubic, Ia3d; R: centered rectangular, cmm; L_α: lamellar; L_α+crystals: lamellar phase in equlibrium w/ solid surfactant & S: solid surfactant

Figure 3.2. Ternary phase diagram of $C_{16}TAB$-$C_{12}G_2$-water system at 50 °C. The accuracy of all phase boundaries except the ones plotted with dashed lines should be within ±1 wt%. The accuracy of dashed phase boundaries could be > ±1 wt%. Black stars represent a set of synthesized mesoporous silica materials consistent with the phase diagram. ○: Series-1 materials (Samples 1-6); ■: Series-2 materials (Samples 7-9); ◊: Series-3 materials (Samples 10-16).

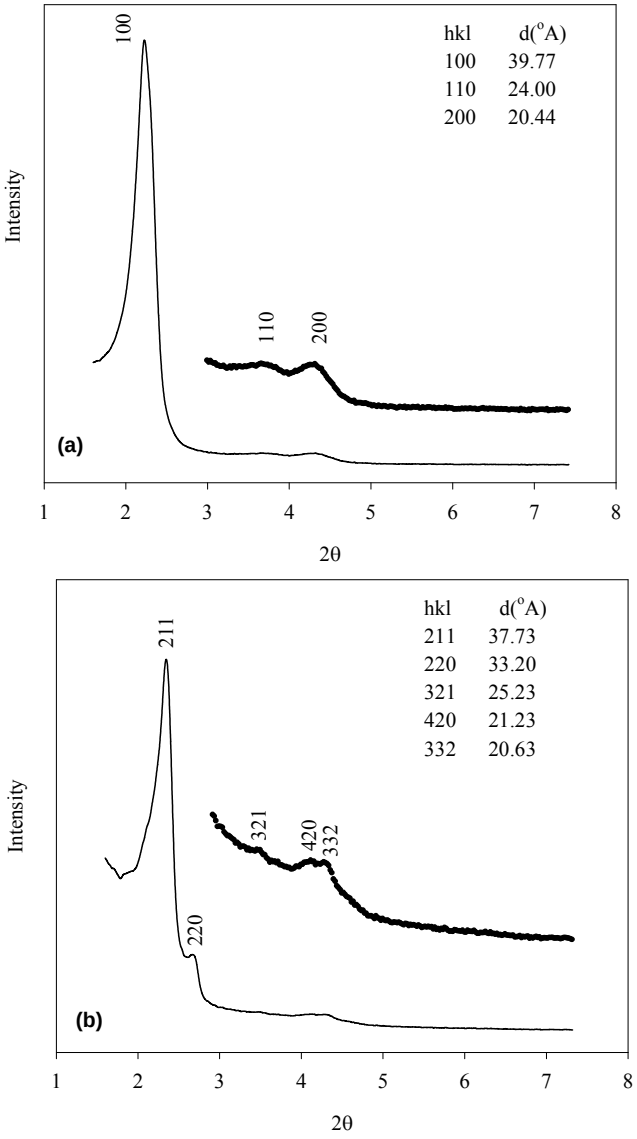

Figure 3.3. Representative powder XRD patterns of the as-synthesized silica with (a) 2D-hexagonal phase with p6mm space group (C_{16}TAB = 20 wt%, $C_{12}G_2$ = 50 wt%, H_2O = 30 wt%) and (b) cubic phase with Ia3d space group (C_{16}TAB = 40 wt%, $C_{12}G_2$ = 50 wt%, H_2O = 10 wt%).

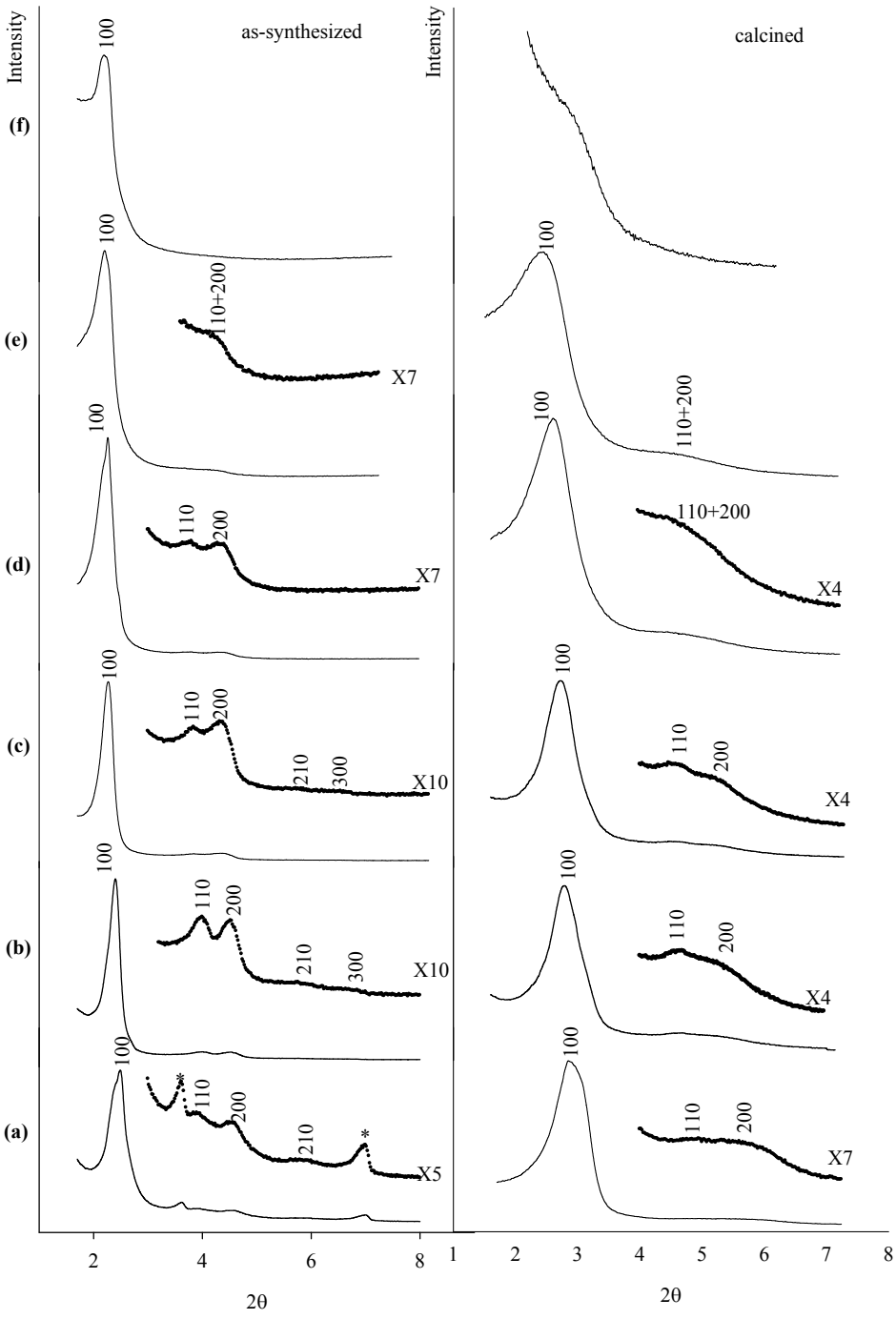

Figure 3.4. Powder X-ray diffraction patterns of the as-synthesized (left column) and calcined (right column) mesoporous silica materials of Series-1, Sample-1 to -6, prepared from mixed micelles of C_{16}TAB and $C_{12}G_2$ with various ratios (wt%) of $C_{12}G_2/C_{16}$TAB. The ratios are (a) 0/60, (b) 20/40, (c) 30/30, (d) 40/20, (e) 50/10, and (f) 60/0.

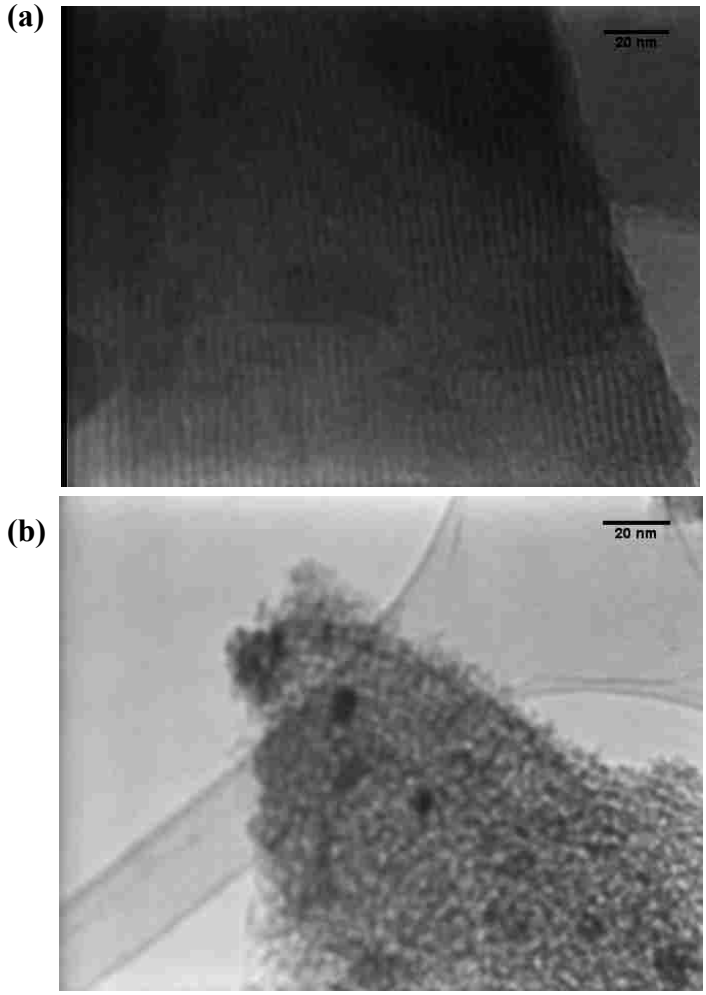

Figure 3.5. Representative TEM images of as-synthesized silica with (a) well-ordered 2D-hexagonal structure (C_{16}TAB = 20 wt%, $C_{12}G_2$ = 40 wt%, H_2O = 40 wt%) and (b) disordered hexagonal or wormhole-like structure C_{16}TAB = 10 wt%, $C_{12}G_2$ = 50 wt%, H_2O = 40 wt%).

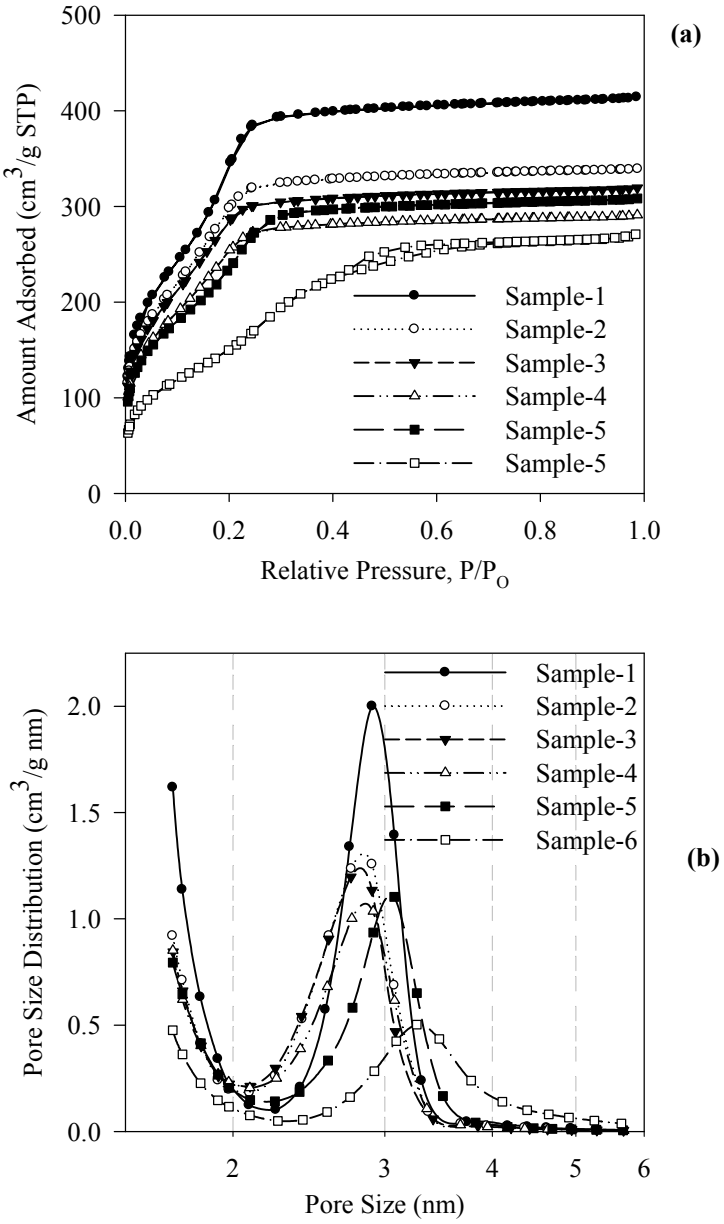

Figure 3.6. (a) Nitrogen adsorption-desorption isotherms of the calcined Samples -1 to -6. (b) KJS (modified BJH) pore size distributions for Samples -1 to -6, derived from their corresponding adsorption isotherm branches.

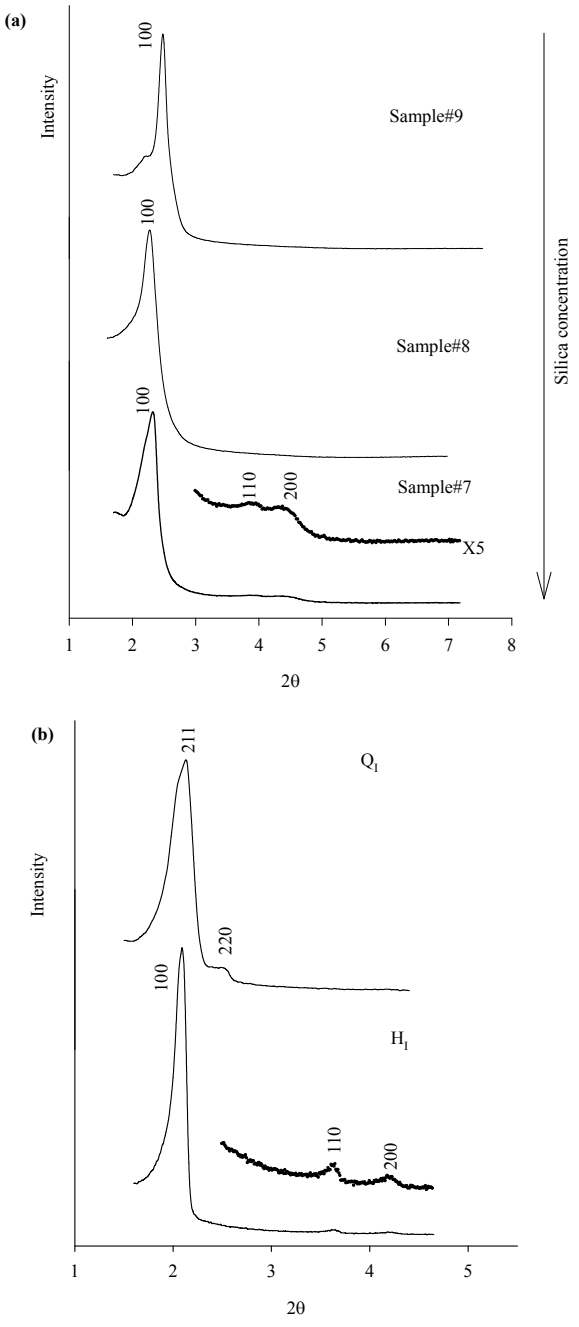

Figure 3.7. (a) Powder XRD patterns of the as-synthesized Series-2 (Sample-7 to -9) materials prepared with pure $C_{12}G_2$ surfactant; (b) representative low angle powder XRD patterns of the H_I (60 wt% $C_{12}G_2$ in water) and Q_I (76.5 wt% $C_{12}G_2$ in water) LLC phases observed with pure $C_{12}G_2$ surfactant.

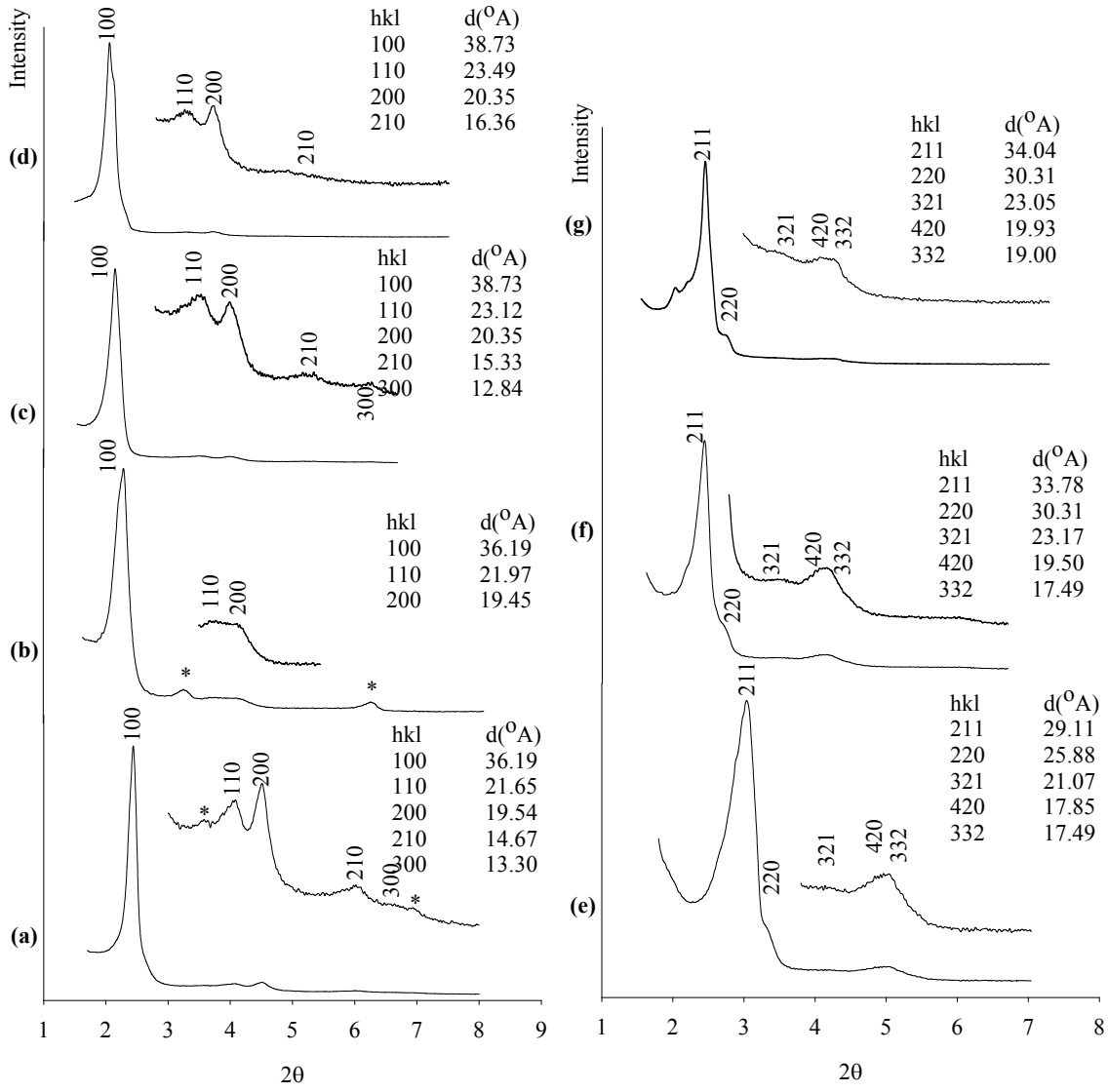

Figure 3.8. Comparison of powder XRD patterns of the as-synthesized Series-3 materials synthesized along the phase boundary separating H_I from Q_I phase: (a) Sample-10 (C_{16}TAB = 65 wt%, $C_{12}G_2$ = 12.5 wt%); (b) Sample-11 (C_{16}TAB = 52.5 wt%, $C_{12}G_2$ = 22.5 wt%); (c) Sample-12 (C_{16}TAB = 40 wt%, C12G2 = 30 wt%); (d) Sample-13 (C_{16}TAB = 35 wt%, $C_{12}G_2$ = 40 wt%); (e) Sample-14 (C_{16}TAB = 60 wt%, $C_{12}G_2$ = 20 wt%); (f) Sample-15 (C_{16}TAB = 50 wt%, $C_{12}G_2$ = 30 wt%); (g) Sample-16 (C_{16}TAB = 35 wt%, $C_{12}G_2$ = 45 wt%). The peaks represented by star are from the C_{16}TAB crystalline salt.

CHAPTER 4

INCORPORATION OF ISOLATED Ti SITES INTO SILICA THIN FILMS WITH 3-D ACCESSIBLE PORES BY SURFACTANT COMPLEXATION

4.1 Summary

One of the challenges in heterogeneous catalysis is the generation of supports with well-defined porosity containing transition metal sites of uniform coordination, complexity, and spacing. One example of the importance of being able to generate well-defined transition metal sites is for heterogeneous epoxidation catalysis; tetrahedrally coordinated titanium atoms incorporated into a silica network are believed to be the active oxidation sites for heterogeneous epoxidation catalysis. Sol-gel chemistry provides an opportunity to produce well mixed metal oxides, but the high reactivity of titanium precursors compare to silicon precursors impedes the uniform incorporation of isolated Ti(IV) sites in a silica matrix by Si-O-Ti bridges. The difference in reactivities often generates titanium in unwanted states- either isolated titanium with coordination numbers greater than four or aggregated titania nanoparticles. Here, a homogeneous distribution of titanium at the pore surface is promoted by a ligand-assisted templating method with n-dodecyl β-D-maltoside ($C_{12}G_2$) surfactant. Preferred interactions or possible complexation between the titanium atoms of a Ti precursor and maltose headgroups of maltoside surfactant should have two favorable effects. First, complexation inhibits fast hydrolysis and condensation, thus promoting homogeneous incorporation of titania. Second, complexation with the surfactant fixes titanium at the micelle surface, allowing it to be incorporated selectively only at the micelle/silica interface during templated synthesis. To promote well-ordered materials and to allow control over titania site density, a mixed surfactant system of $C_{12}G_2$ and the cationic surfactant cetyltrimethylammonium bromide (C_{16}TAB) is used for pore templating. A series of Si-Ti mixed oxide thin films is synthesized with different amount titanium loading by utilizing any pre-existing complexation between $C_{12}G_2$ and titanium precursor. The degrees of homogeneity (indicated by tetracoordinated Ti) in these films are compared with those of films synthesized with the same loading of titanium but without $C_{12}G_2$ surfactant or without pre-complexation. The titanium in films synthesized using maltoside complexation is highly dispersed, while site isolated titanium atoms with octahedral coordination and/or

uncontrolled segregation of titania in the silica support occurs without sugar-based surfactant and without pre-complexation. Highly ordered cubic (Pm3n space group) mesoporous Si-Ti mixed oxide thin films with 3-D accessible pores are synthesized by a solvent evaporation-driven self-assembly method. The final mesostructural order of the mixed oxide films decreases more as Ti is added in films with titanium-carbohydrate complexation than in those without $C_{12}G_2$ due to combined effects of Ti and nonionic surfactant, $C_{12}G_2$.

4.2 Introduction

Supported titania has drawn a great deal of attention during the last two decades as an important class of active and selective heterogeneous catalysts for different types of oxidation reactions, especially for epoxidation of hydrocarbons, alcohols, and ketones.[45, 52, 56, 57, 185, 186] Synthesis of highly active and selective supported titania heterogeneous catalysts for epoxidation reactions is of paramount importance, as epoxides are major intermediates in organic synthesis.[187] Silica is the most promising candidate as a support for this application because it is photoinert, chemically nonreactive, and provides a high active surface area.[188] Titanium atoms in a tetrahehral coordination environment connected with silica networks by Si-O-Ti bridges are believed to be the active sites for oxidation catalysis in titanosilicates.[189-191] A high dispersion of accessible, tetrahedrally coordinated titanium into a silica matrix is essential for these types of silica-titania mixed oxides materials. Titanium-containing zeolites, such as TS-1, TS-2, where titanium ions are in tetrahedral coordination environment, have drawn a great amount of attention initially as mixed metal oxide catalysts for different selective epoxidation reactions of small alkenes using hydrogen peroxide as the oxidizing agent.[51, 192, 193] However, the size of the molecules that can be oxidized can be expanded over that of zeolites (pore size ~0.6 nm) by using ordered mesoporous (pore size in the order of 2-50 nm) silica supported titania with high active surface area, such as Ti-MCM-41 (p6mm),[53, 54] Ti-MCM-48 (Ia3d),[194, 195] or Ti-SBA-1 (Pm3n).[196].

Sol-gel synthesis of mixed metal oxide materials provides the best flexibility in terms of control over the surface and pore-structural properties of the materials.[14, 44, 45] During the sol-gel process, self-assembled organic surfactant molecules co-assemble with hydrolyzed alkoxysilane precursors to form a liquid crystal-like phase that gradually condenses to give a

mesoscopically ordered composite material. Cooperative structure directing interactions among surfactants and inorganic species bring inorganic species to the micelle interfaces and the ongoing polycondensation reactions of metal oxide oligomers contribute to the formation of metal oxide walls. Two types of sol-gel processes have been used to introduce heterometals into metal oxide supports: co-condensation of different metal precursors and post synthesis grafting. For synthesizing mesoporous silica-transition metal mixed oxides, co-condensation of silicon precursor with a transition metal precursor is advantageous over the post treatment method, where the transition metal oxide is grafted onto the pre-synthesized mesoporous silica. Co-condensation provides better control over the dispersion and composition of the transition metal sites, and pore blocking can be avoided if the reactions are carefully controlled. Another advantage of co-condensation is that it allows incorporation of transition metals onto the inner surface of silica, whereas internal pore loading by the grafting method is often limited. The main problem associated with the co-condensation method is the formation of transition metal oxide-rich domains due to the higher reactivity of transition metal precursors compared to analogous silicon precursors.[197] To overcome this problem, several methodologies have been proposed such as- prehydrolysis of Si precursor with a sub-stoichiometric amount of water before adding the transition metal precursor;[58, 59] ligand assisted methods where bidentate molecules are used to modify transition metal precursors chemically to reduce their reactivity,[60-62] and the non-hydrolytic sol-gel method.[63, 64]

In this chapter, we will focus on titanium as a representative transition metal which, as noted above, has utility when supported on silica for selective epoxidation reactions. Modification of transition metal alkoxides by bidentate chelating agents has been shown to be a viable approach for stabilizing transition metal alkoxides for subsequent hydrolysis. Different types of chelating agents such as β-diketones,[198, 199] carboxylic acids,[61] glycols,[200] and peroxide have been used to modify titanium alkoxides. Ligand exchange or addition of these molecules leads to chelation of these molecules to Ti atoms and modification of the titanium precursor. Amorphous Si-Ti mixed oxide gels with high Ti dispersion have been synthesized by Pickup et al.[60] and Mendez-Vivar et al.[201] using acetylacetone and acetic acid to stabilize Ti alkoxides. When these ligands are used to make ordered mesoporous mixed oxide materials, they normally remain in the materials and negatively affect the structure of

the final materials.[202] To get ordered mesoporous Si-Ti mixed oxide materials with high tetrahedral titanium oxide dispersion, a better approach would be to use a surfactant which will act not only as a template but also as a stabilizing agent for the transition metal alkoxide. One such class of surfactants, poly (alkylene-oxide) block copolymer, has been reported. This approach is known as ligand-assisted templating. Polar hydrophilic headgroup of these types of surfactants form complexes with transition metal alkoxides and help to position Ti atoms into the silica network. Celik and Dag[203] have observed the formation of hexagonal and cubic liquid crystalline phases from a nonionic oligo (ethylene oxide) block copolymer complexed with different transition metal salts. Later, Hüsing et al.[204] took this finding to the next level by synthesizing mesoporous Si-Ti mixed oxide thin films using oligo(ethylene oxide) based lyotropic liquid crystalline phases. Modification of the metal alkoxide by the ethylene oxide headgroup of the surfactant reduced the reactivity of the metal alkoxide, and that along with prehydrolysis of the silica precursor helped to prevent uncontrolled segregation of transition metal oxide in silica.[204, 205] The Hüsing group reported hexagonal mesostructured films only for a small window opening of Ti loading of Si/Ti= 15 to 11. Beyond this limit, the films were found to be lamellar, and they collapsed upon calcination and hence would be expected to have limited catalytic application.[206]

In addition to the chelating ligands commonly used in the sol-gel literature, naturally occurring sacchrides and their derivatives are well known as potential ligands for transition metals in the field of transition metal-carbohydrate chemistry and biology.[207, 208] Rao et al.[209, 210] studied the complexation of various mono- and di-saccharides and their derivatives with different transition metals. Tani et al.[211] have studied the chromatographic retention behavior of saccharides on titania. The saccharide recognition ability of titania has been attributed to the complex formation between a titanium ion and two oxygen atoms of the OH group and carboxylate anion of 2-hydroxycarboxylic acids. Recently, the complexation of Ti alkoxides with bulky ligands derived from natural sugars has also been reported.[212]

Here, for the first time we build upon the possibility of transition metal- saccharide chelation and report a systemic way of introducing isolated titanium oxide sites into silica network of Si-Ti mixed oxide thin films by stabilizing a Ti precursor with a sugar-based non-ionic surfactant. We used a commercially available sugar-based surfactant with a disaccharide headgroup, n-dodecyl β-D-maltopyranoside ($C_{12}G_2$). The function of this

surfactant during the synthesis of Si-Ti mixed oxide thin films is hypothesized to be three-fold: (a) the hydrophilic maltoside headgroup of $C_{12}G_2$ surfactant is expected to act as a bidendate ligand to Ti atoms of Ti precursors that helps to reduce their reactivity, (b) the self-assembled nonionic $C_{12}G_2$ surfactant can act as a structure directing agent for mesopores, and (c) complexation with the surfactant fixes Ti at the micelle surface, allowing it to be incorporated selectively only at the micelle/ silica interface. Before starting the materials synthsis work, we observed the phase behavior of $C_{12}G_2$ in water at 50 °C and found that while the surfactant forms ordered materials, it is difficult to co-assemble $C_{12}G_2$ as the sole template with silica to form mesoporous materials with good long-range order (Chapter 3). In order to realize improved order and control over the functional site density of Ti into silica matrix a non-complexing cationic surfactant, cetyltrimethylammonium bromide (C_{16}TAB), that has strong ionic interactions with the silica matrix will be used as a second surfactant. In Chapter 3, we have developed the full ternary phase diagram of the aqueous mixture of C_{16}TAB and $C_{12}G_2$ and showed that it can be used to predict the synthesis of mesostructured silica with a range of surfactant compositions and structures.

Here we will use that phase diagram to guide the synthesis of Si-Ti mixed oxide thin films using the solvent evaporation induced self-assembly (EISA) technique. In this technique, an initial solution with specified amounts of surfactant(s), metal alkoxide precursor(s), and very small amount of acidic water (pH ~2, close to the isoelectric point of silica to slow polycondensations) diluted with alcohol (which acts as a mutual solvent for water and metal alkoxide) is used to prepare thin films by dip coating. Due to drying, self-assembly of surfactants takes place due to a co-operative mechanism between both the inorganic and organic components by charge density matching. Due to their morphology, thin films serve more as model systems for heterogeneous catalysis (compared to bulk materials), but they have potential applications in specialized applications, catalytic microfluidics, sensors, photoelectric semiconductor devices, optical devices, etc.

During film preparation for this chapter, the volume of water corresponding to a point in the ternary phase diagram of C_{16}TAB / $C_{12}G_2$ / water (discussed in Chapter 3) is replaced with an equivalent total volume of silica and titania.[91] Ti loadings in the films are increased by increasing the ratio of $C_{12}G_2$/ C_{16}TAB along a line of constant surfactant content in the ternary phase diagram, while keeping a 1:1 molar ratio between $C_{12}G_2$ surfactant and Ti

precursor. Pre-complexation between the Ti precursor and $C_{12}G_2$ is used in an effort to prepare highly dispersed, Ti^{4+} sites, and the coordination environment of Ti in the resulting mixed oxide films are compared with that of films synthesized with C_{16}TAB only or without pre-complexation between $C_{12}G_2$ and Ti. The coordination environment of Ti atoms in the films deposited on quartz glass substrate by dip-coating method is determined here by UV-vis transmission spectroscopy, and mesopore structure is characterized by x-ray diffraction (XRD), scanning transmission electron microscopy (STEM), and N_2 sorption analysis.

4.3 Experimental

4.3.1 Materials

Tetraethyl orthosilicate (TEOS, 98%) and cetyltrimethylammonium bromide (C_{16}TAB, 99%) were purchased from Sigma Aldrich. Titanium isopropoxide (TIP, 99%) was purchased from Gelest. n-dodecyl β-D-maltopyranoside ($C_{12}G_2$, ≥99%, %α < 0.2) was purchased from Anatrace. Deionized ultra-filtered water (DIUF), 0.1N HCl, absolute ethanol, NoChromix cleaning reagent, and concentrated sulfuric acid were purchased from Fisher Scientific. All chemicals were used as received without any further purification.

4.3.2 Film Synthesis

Surfactant templated Si-Ti mixed oxide mesoporous thin films with variable ratios of Si/Ti were synthesized using TEOS and TIP as Si and Ti precursors respectively, by employing the dip coating technique. Three different types of Si-Ti mixed oxide thin films were synthesized by using three different approaches. In Type-1 films, pores are templated by the mixed surfactant system of C_{16}TAB and $C_{12}G_2$ along with pre-complexation between the maltoside headgroups and TIP. A series of Type-1 films with Si/Ti ranging from 86 to 8 was synthesized. In Type-2 films, pores are templated by C_{16}TAB only. For comparison, Type-2 films with Si/Ti also ranging from 86 to 16. I In the case of Type-3 film, pores are templated by the mixed surfactant system but without any pre-existing surfactant complexation. For comparison, a single Type-3 film with a Ti loading of Si/Ti= 42 was synthesized. Whenever $C_{12}G_2$ surfactant was used, a 1:1 molar ratio between $C_{12}G_2$ and TIP was employed. All films were synthesized with a total surfactant content corresponding to 46

wt% surfactant in water according to the ternary phase diagram of C_{16}TAB / $C_{12}G_2$ / water (reported elsewhere). This particular amount of surfactant keeps a total surfactant to metal molar ratio less than 0.15, which is necessary to get thermally stable thin films.[92]

In a typical Type-1 sol synthesis, 0.08 g of $C_{12}G_2$ surfactant was dried at 50°C under vacuum overnight, and then dissolved in 1.9 g of dry EtOH in a bottle initially flushed with dry nitrogen. 46 mL of TIP was added into this solution in a nitrogen atmosphere and then the mixture was stirred for 3 hrs in a nitrogen-purged glove bag to promote complexation between the maltoside headgroups and Ti. The amount of TIP was always enough to give a 1:1 molar ratio of $C_{12}G_2$ to TIP. In a separate beaker, TEOS was prehydrolyzed at room temperature for an hour by adding1.39 g of TEOS to 0.77 g of EtOH, followed by addition of a mixture of 0.21 mL of DIUF water and 0.27 mL of 0.1 N HCl. This mixture of TEOS, water, and ethanol gives a molar ratio of 1: 4: 2.5 and this specified amount of 0.1 N HCl brings the solution pH to 2. The quantity of TEOS was calculated from the ternary phase diagram of C_{16}TAB / $C_{12}G_2$ / water system by replacing the volume of water in the phase diagram with equivalent volume of fully hydrolyzed silica and titania precursor, as described earlier. Prehydrolyzed TEOS solution was then added dropwise by a syringe to the alcoholic solution of TIP under vigorous stirring in N_2 atmosphere. Following this, 0.12 mL of DIUF water mixed with 0.81 g of EtOH was added to the reaction mixture dropwise under stirring. Finally, a mixture of 0.288 g of C_{16}TAB and 2.7 g of EtOH were added. The amounts of β-$C_{12}G_2$ and C_{16}TAB added were chosen for this example to give a composition corresponding to 5 wt% $C_{12}G_2$ and 41 wt% C_{16}TAB in the ternary phase diagram. This composition falls within the hexagonal phase region of the C_{16}TAB/ $C_{12}G_2$/ water system. The final molar ratio of TEOS: TEOT: EtOH: H_2O: $C_{12}G_2$: C_{16}TAB for this sample was 1: 0.024: 20: 5: 0.004: 0.024: 0.119. The final sol solution was then stirred for one additional hr at room temperature before dip-coating onto silicon wafer and quartz substrates. Before coating, all substrates were cleaned by using a NoChromix solution. Substrates were dipped into a NoChromix solution at least for 3 hrs, those were then rinsed with DIUF water, then acetone and finally dried before coating. Quartz and Si wafer substrates were dip-coated with sol solutions at a withdrawal speed of 10 cm/min and 12.5 cm/min, respectively. After withdrawal, films were immediately transferred into an oven, and aged at 50 °C for 48 hrs. Ti loadings in the Si-Ti mixed oxide films are expressed here by Si/Ti (molar), which for this example is 42.

Using this synthetic route, a series of Type-1 Si-Ti mixed oxide thin films with different Ti loadings were synthesized from this mixed surfactant templates along with the utilization of pre-complexation of $C_{12}G_2$ and TIP. Ti loading in films was increased by increasing the ratio of $C_{12}G_2/C_{16}TAB$ in the phase diagram along a line corresponding to a constant surfactant content of 46 wt%. The amount of $C_{12}G_2$ was increased from 5 wt% to 46 wt% in the phase diagram, which gives Ti loading of Si/Ti= 86-8 (note that for the highest Ti loading, the only surfactant used was $C_{12}G_2$, but silica still needed to be added to give the correct volume of inorganic species). For comparison purposes, a series of Type-2 mixed oxide films, templated by $C_{16}TAB$ alone, were synthesized with Ti loadings of Si/Ti= 86 to 16. The total amount of the mixed surfactant was replaced in this case by pure $C_{16}TAB$ only, but otherwise the process of preparing the sols was the same as described above for Type-1 films. During Type-3 film synthesis, similar to Type-1 and Type-2 films synthesis, prehydrolyzed TEOS was added dropwise to an alcoholic TIP solution, but $C_{12}G_2$ surfactant was added later along with $C_{16}TAB$.

For some analyses, powders of Type-1 and Type-2 thin films were collected by scraping off as-synthesized films from the substrates using razor blades. Calcination of both thin films and powders was performed at 450°C for 3 hr in air. Materials were first heated at 120°C for 6 hr in a N_2 atmosphere and then heated to 450°C with a heating ramp of 1°C/min (still in N_2 atmosphere), then held at 450°C for 3 hr in air.

4.3.3 Characterization

Transmission UV-vis spectra of the thin films on quartz substrates mounted at 45 degrees with respect to the incident beam were collected by using a HP8453 UV-visible (UV-vis) spectrophotometer. Powder x-ray diffraction patterns of the thin films and powder samples were recorded using a Bruker D8 Discover diffractometer with 0.154056 nm Cu K_α radiation and a Siemens 5000 diffractometer with 0.154098 nm Cu K_α radiation, respectively. For transmission electron microscopy (TEM) and scanning transmission electron microscopy (STEM), powder samples were loaded onto lacey carbon grids before putting them into a JEOL 2010F instrument operated at 200 kV. Nitrogen adsorption-desorption isotherms of calcined powders were collected at -196 °C with a Micromeritics Tristar 3000 analyzer. Before measurement, all of the samples under study were degassed at 150°C for 4 hrs under

flowing nitrogen. Specific surface areas of the materials were calculated using the standard Brunauer-Emmett-Teller (BET) equation.[123] Pore size distributions were obtained from the Barrett-Joyner-Halenda (BJH) method with the corrected form of Kelvin equation and Harkins-Jura statistical film thickness equation. These Kruk-Jaroniec-Sayari (KJS)[126] modified BJH[125] pore size distributions were derived from theadsorption branches of the nitrogen sorption isotherms.

4.4 Results and Discussion

UV-vis spectroscopy is one of the most commonly used technical tools to study the coordination of titanium atoms supported on a silica matrix in silica-titania mixed oxide materials. This is a bulk characterization technique, and in our case we are able to use direct transmission analysis of the thin films on quartz substrates – one of the advantages of analyzing thin films. The positions of absorption bands are sensitive to the coordination environment of Ti. UV-vis transmission spectra for a series of calcined Type-1 films, templated by C_{16}TAB and Ti-complexed-$C_{12}G_2$ surfactants, are shown in Figure 4.1(a) for different Ti loadings. The spectra for a series of calcined Type-2 films (templated by C_{16}TAB only) with different loading of Ti, along with a spectrum of a Type-3 film (templated by C_{16}TAB and non-complexed $C_{12}G_2$ surfactants) with Si/Ti= 42 are shown in Figure 4.1(b). The absence of any absorption band around 325 nm in both Figure 4.1(a) and 4.1(b) indicates that extra-framework segregated bulk titania clusters are not present in these Si-Ti mixed oxide thin films. The absorption band centered at around 325 nm has been assigned to the ligand-to-metal charge transfer from O^{2-} to Ti^{6+}, associated with bulk aggregated Ti(VI) in octahedral co-ordination environment linked by Ti-O-Ti bridges.[213] Therefore this finding suggests that Ti rich domain did not form in our films under any synthetic conditions studied here.

The distinguishing features between the spectra of Type-1 films and those of Type-2 and Type-3 films, as shown in Figure 4.1, are the number of absorption peaks, absorption intensity for the same Ti loading, and the position of the first peak. All Type-1 films, synthesized with Ti loading from Si/Ti= 86 to 8, gave only one sharp peak, centered at around 206 nm. Along with the first strong peak, a low intense broad absorption shoulder

with a maximum around 260 nm and the onset of band-edge absorption around 290 nm is found with all Type-2 films and Type-3 film, as shown in Figure 4.1(b). The absorption band centered at around 210 nm wavelength light has been assigned to the ligand-to-metal charge transfer from O^{2-} to Ti^{4+}, associated with isolated framework Ti sites that are tetracoordinated.[214, 215] This band implies isomorphic substitution of Si^{4+} by Ti^{4+} ions in the silicate framework. This UV radiation-induced electron transfer generates active $[Ti^{3+} -O_L^-]^*$ sites present in silica network, which are believed to be the catalytically active sites for different oxidation reactions.[189, 215, 216] This absorption band is commonly found with zeolite-supported Ti-containing materials, such as TS-1 and TS-2, where the Ti content is low. Absence of any other peak or broad shoulder besides this first strong sharp peak suggests that titanium is predominantly incorporated into the silicate network with tetrahedral coordination. It can be seen from Figure 4.1 that the peak intensity for the Type-1 films are always higher than in Type-2 and Type-3 films for the same loading of Ti. This indicates that more Ti is incorporated into the silica network by Si-O-Ti bonds in Type-1 films. Lower intensity for the Type-2 and Type-3 films is because a portion of Ti is in penta- or hexa-coordinated which is evident from the appearance of a shoulder (described below). The UV spectrum of Type-3 film synthesized with a Ti loading of Si/Ti= 42 has showed same behavior of Type-2 film with same loading, as shown in Figure 4.1(b). This means that if $C_{12}G_2$ surfactant is not complexed initially with Ti^{4+} ions of Ti precursor, $C_{12}G_2$ surfactant then acts only as pore structure directing agent, not as a director for depositing Ti into the silica network. The third distinguishing feature between Figure 4.1(a) and 4.1(b) is the position of the first peak. The first absorption band of all Type-1 films are found to be centered at around 206 nm, whereas it is varies from 209 nm to 220 nm for the Type-2 films and Type-3 film. This slight red shift may be due to the distortion in tetrahedral coordination.[54, 217] The cause of this distorted environment has been attributed to the presence of amorphous walls, where Si-O-Ti bond angles vary over a wide range.[54] However, in Type-1 films, the hydrophilic carbohydrate headgroups of $C_{12}G_2$ apparently reduces the range of Si-O-Ti bond angles by positioning Ti into a consistent relationship with respect to the silica matrix.

To identify the exact nature of titanium in silica that causes the appearance of absorption band around 250-280 nm, three different theories have been proposed.[218] It is

obvious from all theories that the coordination environment of Ti is quite different from tetrahedral if the titanium is not pre-complexed with $C_{12}G_2$. According to some researchers, the absorption band around 250-280 nm is due to the formation of octahedral coordination sphere by TiO_4 units with two water or alcohol molecules.[219] Some believe that this band is associated with the presence of isolated titanium sites, as TiO_x with coordination number higher than four, such as penta- or hexa-coordinated.[220] This isolated, mononuclear TiO_x species could be single- or double-bonded with its host silica frame via isolated or vicinal OH groups.[221] Another proposed theory regarding the assignment of this absorption band is that it is due to the presence of extra-framework partially polymerized hexa-coordinated Ti on the silica network.[222-224] Thus, the absorption shoulders centered at around 260 nm in Type-2 and Type-3 films corresponds to partially aggregated titanium and/or site isolated Ti with coordination number higher than four.

To summarize, the UV-vis spectra suggest that acidic medium (pH= 2) prehydrolysis of Si precursors and alcoholic dilution might have prevented the formation of extra-framework bulk titania in Type-2 and Type-3 films. However, these experimental conditions are not sufficient to prevent the formation of isolated TiO_x and/or partially polymerized Ti species with variable coordination environment. Along with these experimental conditions, utilization of pre-existing complexation of β-$C_{12}G_2$ surfactant with Ti precursor is required to place Ti^{4+} ions into the silicate network with well-defined coordination environment (Type-1 films).

To support the assignment to dispersed Ti in Type-1 films, we have studied the crystallization behavior of titania using wide angle XRD (WAXRD). Films with all Ti loadings were heated at different temperatures up to at most 800°C for 3 hr with a heating rate of 1 °C/min. No peaks in the WAXRD patterns due to crystalline titania were observed, suggesting a high degree of dispersion and thermal stability of the Si-O-Ti bridges, which keeps the crystallite size below a size detectable by XRD.

4.4.1 Pore Structure Characterization by XRD and TEM

Figure 4.2 shows the XRD patterns of both the as-synthesized and calcined Si-Ti mixed oxide thin films, coated on silicon wafer substrates, as a function of titanium loading. Intensity scales are logarithmetric for easy visualization of weak higher order reflections.

XRD patterns of the as-synthesized and calcined Type-1 films at different Ti loadings are shown in Figure 4.2(a) and 4.2(b) respectively. Similarly for comparison, the XRD patterns of the as-synthesized and calcined Type-2 films at different Ti loadings are reported in Figure 4.2(c) and 4.2(d) respectively. All patterns in Figure 4.2 are offset vertically to avoid overlapping, but the scaling of each XRD pattern remains the same, to allow easy comparison among patterns. Periodic mesostructure of the as-synthesized Type-1 and Type-2 films is confirmed by the appearance of discernible diffraction peaks in their XRD patterns over a 2θ range of 1.5-7°, as shown in Figures 4.2(a) and 4.2(c). The appearance of only two reflections for Type-1 films makes the identification of the actual mesophase difficult. However, we have successfully assigned the mesophase of the as-synthesized Type-1 films as a 3-D cubic phase with a space group of Pm3n (see below for more details). Based on that, these two peaks can be indexed as (210) and (420) reflections. The absence of other reflections indicates that the (210) crystallographic planes are aligned parallel to the polished Si wafer substrate.[225] Highly ordered 3D primitive cubic structure with Pm3n space group of the as-synthesized Type-2 films is identified from the presence of five well-resolved peaks that can be indexed to (210), (211), (310), (222), and (420) Bragg reflections, as shown in Figure 4.2(c). Also in this case, high intensity reflections from the (210) planes compare to other reflections indicate that the (210) crystallographic planes are predominantly parallel to the substrate (although not as well-aligned as in Type-1 films).

The degree of ordering of the as-synthesized Type-1 and Type-2 films decreases as Ti loading increases. It can be seen from both Figure 4.2(a) and 4.2(c) that the intensities of (210) Bragg reflections decreases along with an increase in the full width at half maximum (FWHM) of the (210) reflections as the loading of Ti increases. The relationship between the FWHM of (210) reflection of as-synthesized films and the loading of Ti is shown in the insets of the corresponding figures. The findings suggest that the incorporation of Ti disrupts the self-assembly process of both the nonionic $C_{12}G_2$ and cationic $C_{16}TAB$ surfactants into periodic arrays. The decrease of mesostructural ordering of silica-titania mixed oxide mesoporous materials with the increase of Ti loading has also been observed earlier by several researchers.[226-229] The rate at which the FWHM of (210) reflections of as-synthesized Type-1 films increases with Ti loading is much higher than that of as-synthesized Type-2 films. This implies that orderliness of materials decreases more rapidly in Type-1 films, most

likely due to the increase of $C_{12}G_2/C_{16}TAB$ ratio in the mixed surfactant system. Earlier we have found that increasing the amount of $C_{12}G_2$ with respect to $C_{16}TAB$ for a constant percentage of total surfactant system leads to less long-range order of the mesoporous structures prepared with only silica (see Chapter 3). During isomorphous substitution of Ti(IV) atoms into the silicate matrix, such loss of mesophase order has also been observed by Alba et al.[228] They proposed that because Ti(IV) tetrahedra (0.68Å) are larger in size than regular Si(IV) tetrahedra (0.41Å) the silica matrix is distorted, which disrupts mesophase ordering. The d-spacing values of (210) planes of as-synthesized Type-1 and Type-2 films synthesized at different Ti loadings varied from 30.7Å to 36.3Å and from 29.5Å to 33.5Å, respectively, which is consistent with this idea. Calcination causes a large contraction of unit cell dimensions, in a range of approximately 25-47 % combined, in Type-1 and Type-2 thin films. This is evident from the large movement of d_{210} reflections to larger 2θ values. Due to calcination, this kind of large shrinkage of pores is common with pure silica[230, 231] and silica-titania mixed oxide[205, 226] thin films prepared under acidic condition by the EISA process. Thin films coated at low temperature (such as 50 °C used in this study) and acidic medium generate low density silica walls.[232] That allows them to shrink signifcantly during heat treatment due to the ongoing polycondensation of silanol groups. During calcination, surfactant removal and wall densification happen simultaneously.[230] The ratio of surfactant(s) to metal precursor(s) also determines the structural stability of mesopores,[232] with a lower ratio providing better stability. Another factor that influences the structural stability of a mesostructure is the type of surfactants used as templates.[233] Weak interactions of both $C_{16}TAB$ and $C_{12}G_2$ with weakly charged silicates present in an acidic medium are expected to allow large pore contraction during calcination. Also in thin films, pore contraction is asymmetric. Strong adhesion between the substrate and film allows films to shrink primarily in the thickness direction.[234] These large asymmetric shrinkages of pores caused distortion to mesostructures that can be seen from Figure 4.2(b) and 4.2(d), as the intensities of (210) reflections decrease a lot along with the disappearance of higher order reflections.

As we have seen for Type-1 films especially, the orientation of (210) planes parallel to the substrate imposes some limitations in the determination of true mesophase of the Si-Ti mixed oxide thin films. For this reason we have prepared the corresponding power samples

by scraping thin films off of the substrates, as described in the experimental section, to study the mesostructure by powder XRD and TEM. Figure 4.3(a) and 3(b) show the low angle XRD patterns of the corresponding power samples of Type-1 and Type-2 films, respectively, synthesized with Si/Ti= 86. Films loaded with the lowest amount of Ti are selected here as they possess the best long range order, which makes true phase identification easier. The XRD pattern of the as-synthesized powder sample of Type-1 films, as shown in Figure 4.3(a), shows eight well-resolved Bragg reflections with reciprocal d-spacing ratios of √4: √5: √6: √12: √14: √17: √20: √24 that can be indexed to the (200), (210), (211), (222), (321), (410), (420), and (422) reflections, respectively, of a three-dimensional cubic phase with Pm3n symmetry (the same space group as SBA-1). The presence of seven well-resolved Bragg reflections, indexed to (200), (210), (211), (321), (410), (420), and (422) of Pm3n cubic symmetry, in the XRD pattern of the calcined sample indicates that the high order of the mesostructure is preserved upon calcination. Similarly, Figure 4.3(b) shows the presence of twelve well-resolved Bragg reflections in the XRD diffraction pattern of the as-synthesized Type-2 powder sample indexed to a highly ordered cubic mesophase of Pm3n symmetry. The high degree of cubic Pm3n mesostructural ordering is well preserved upon surfactant removal, as indicated by the presence of a large number of peaks in the low-angle XRD diffraction pattern of the calcined Type-2 sample.

The relationship between $1/d_{hkl}$ and $(h^2 + k^2 + l^2)^{1/2}$ of all well-resolved (hkl) reflections for both the as-synthesized and calcined powder samples of Type-1 and Type-2 films, synthesized with a Si/Ti = 86, are shown on insets of Figures 4.3(a) and 4.3(b). In all the cases, very good straight line fit passing through the origin of the plots are consistent with primitive 3D-cubic mesostructure with Pm3n space group.[41] The unit cell parameter, a_0 was calculated from the slopes of those plots. Upon calcination, the unit cell parameter a_0 of the Type-1 film changes from 89 Å to 76 Å, and for the Type-2 film, it changes from 87 Å to 81 Å. These shrinkages by calcination are due to the removal of organic surfactants and further densifications of metal oxide walls due to polycondensation or sintering.

STEM images, as shown in Figure 4.4, further confirm the highly-ordered 3-D cubic Pm3n mesophase (the same as SBA-1) of Type-1 and Type-2 Si-Ti mixed oxide thin films (Si/Ti = 86). All images in Figure 4.4 are recorded from their corresponding calcined samples. STEM images in Figure 4.4(a) – 4.4(c) are taken from Type-1 film (Si/Ti = 86)

along the [100], [110], and [210] zone axes, respectively. The STEM images in Figures 4.4(d) and 4.4(e) are taken from Type-2 film (Si/Ti = 86) along the [110], and [111] zone axes, respectively.

4.4.2 N_2 Sorption Characterization

Because of the high dispersion of titanium in Type-1 films, they have potential applications in heterogeneous oxidation catalysis. For that reason, it is very important to know the specific surface area and pore structure parameters of these materials. Nitrogen adsorption-desorption isotherms were obtained to determine these characteristics. Figure 4.5 shows the nitrogen sorption isotherms along with the corresponding pore size distributions (inset) of the powders scraped off of a Type-1 film synthesized with a Si/Ti = 86. According to IUPAC classifications[5] it is a Type-IV isotherm, typical of mesoporous materials where multilayer adsorption is followed by capillary condensation. Absence of any hysteresis loop in the isotherm indicates that nitrogen capillary condensation and evaporation are reversible due to the presence of uniform mesopores. The BET specific surface area of the sample was found from the data in the relative range from 0.05 to 0.2[124] to be 805 m^2/g. The commonly used value of 0.162 nm^2 as the molecular cross-sectional area of N_2 was used to estimate the specific surface area of the material.[5] An average pore size of 2.8 nm with a narrow pore size distribution is observed for the Type-1 film. A width at half of the maximum peak height in the pore size distribution is ~5 Å, indicating that Type-1 Si-Ti mixed oxide thin film (Si/Ti = 86) have well-defined uniform pores. Zero micropore volume was found in this material by the high-resolution α_s-plot method.[124]

4.5 Comparison between the Liquid Crystalline Phase and the Observed Mesostructure

As described in the experimental section, a constant surfactant content line equivalent to 54 wt% water in the ternary phase diagram, which falls within the hexagonal liquid crystalline phase region, was used to guide the synthesis of all Si-Ti mixed oxide thin films. We used the predictive synthesis procedure outlined by Alberius et al.[91] to determine the initial sol compositions for our film preparation procedures. However, we found that the final mesostructure of both Type-1 and Type-2 films with Si/Ti = 86 are Pm3n cubic. While

this may at first seem to be a disappointing outcome, we need to be careful when comparing the non-equilibrated mesostructures in metal oxide / surfactant nanocomposite films with thermodynamically equilibrated lyotropic liquid crystalline phases of surfactants in water. An additional important factor in the films is to that they are open, dynamically evolving systems. In particular, their drying behavior, which depends of the relative humidity, needs to be considered before making the comparison. It has been demonstrated that relative humidity pays an important role in forming the mesophase in thin films during solvent evaporation-driven self-assembly.[88, 90] Humidity directly affects the kinetics of surfactant self-assembly by influencing solvent evaporation, and thereby affects the equilibrium volume of polar material in the films, and therefore micelle interfacial curvature. Quantitative difference in lyotropic phase behavior also could be due to different hydrogen and screened electrostatic bonding behavior of water compared to the silica and titania intermediates present in the solution during material synthesis. In our synthetic protocol, films were coated at room temperature and then aged at 50˚C. This could have influenced the outcome, but from the binary phase diagrams of DM-water[152] and CTAB-water[165] systems, no change from their hexagonal phases due to temperature change from room temperature to 50˚C has been observed. A major limitation of the predictive synthesis method established by Alberius et al. is that they assume the presence of only completely hydrolyzed metal precursors such as $Si(OH)_4$ and $Ti(OH)_4$, but in reality they could be partially cross-linked in solution prior to dip-coating, which would change the calculated equivalent amounts of metal precursors by changing the molar volume of water released during complete cross-linking. The difference in the phases between the liquid crystalline hexagonal (p6mm) and final cubic (Pm3n) mesostructure of the mixed oxide films can be best understood in terms of the previously reported mesophases found with C_{16}TAB templated silica thin films prepared via the EISA method. Among all of the factors that can influence the formation of mesostructure in thin films, such as initial sol composition, pH of the sol, coating parameters, extent of precursors condensations, etc., the initial sol composition (specifically initial surfactant concentration) has the greatest influence.[235] Usually, the molar ratio between the amount of surfactant and the amount of precursor present in the initial solution is represented by R. Type-1 and Type-2 Si-Ti mixed oxide thin films loaded with Si/Ti = 86 are synthesized with R values of 0.14 and 0.15, respectively. In the literature, Pm3n cubic silica mesostructured thin films have

been reported for R (C_{16}TAB/Si) values from 0.12 to 0.16,[87, 236] although this range clearly falls within the hexagonal phase region of the binary C_{16}TAB-water phase diagram. Our findings are consistent with the C_{16}TAB-silica film findings, even though we are dealing with Si-Ti mixed oxide thin films. Alternatively, the formation of the Pm3n cubic mesophase films may be related to confinement in this films, but equilibrated lyotropic Pm3n phases between the isotropic micellar phase and regular hexagonal phase in binary surfactant-water phase diagram are not uncommon. For instance, Clerc et al.[237] and Auvray et al.[152] have reported such cubic phases in binary surfactant-water systems.

4.6 Conclusions

The complexation or preferential interactions between the titanium ions of titanium propoxide and the maltoside headgroup of the sugar-based surfactant ($C_{12}G_2$) was utilized in an effort to inhibit fast hydrolysis and condensation of titanium alkoxide (TIP), thus promoting the dispersion of Ti^{4+} in the Si-Ti mixed oxides thin films synthesized with Ti loadings in the range of Si/Ti = 86 to 8. Uniform, isolated tetrahedral titanium sites were found in Type-1 films prepared with pre-complexation between $C_{12}G_2$ and the titanium precursor. Site isolated Ti atoms with a mix of tetrahedral and octahedral coordination on silica support were observed without $C_{12}G_2$ or Ti-complexed-$C_{12}G_2$. However, while the synthesis conditions were chosen to mimic the phase of the lyotropic mixed surfactant / water system, a highly-ordered 3D-cubic phase (Pm3n space group) mesostructure was instead found in the metal oxide films. The long-range order of the mesostructures in these mixed oxide thin films were found to decrease as the Ti loadings increases. The order of Type-1 films decreases more rapidly as Ti loading increases than that for Type-2 films (prepared with no $C_{12}G_2$) due to the combined effect of Ti alkoxide reactivity and the negative effects of $C_{12}G_2$ on lyotropic ordering.

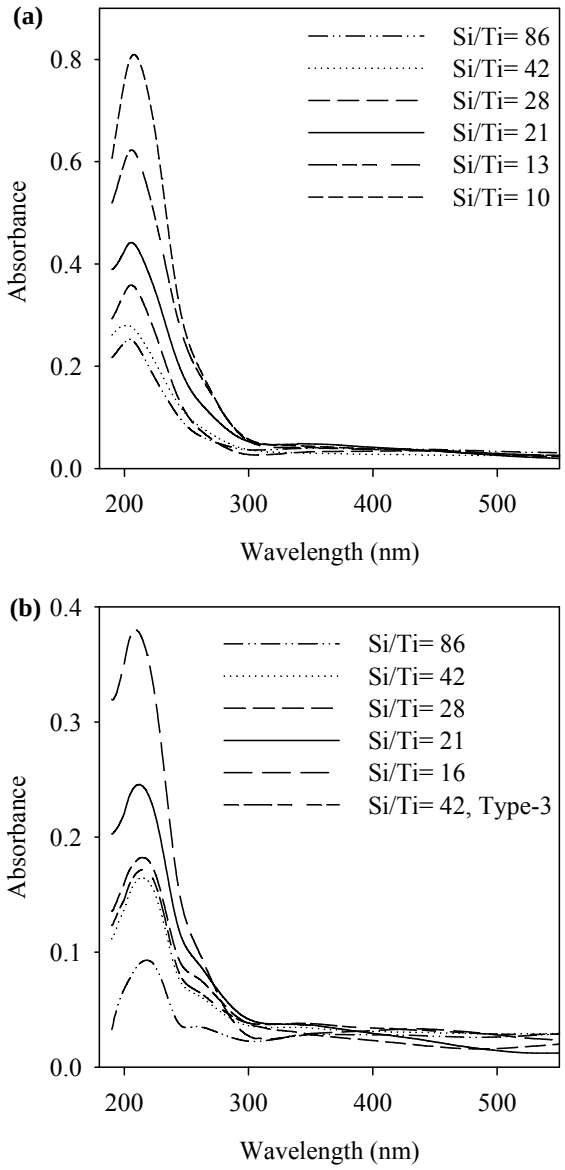

Figure 4.1. UV-visible transmission spectra of calcined Si-Ti mixed oxide thin films coated on quartz glass substrate. (a) Spectra of Type-1 films at different Ti loadings and (b) Type-2 films at different Ti loadings and Type-3 film with a Ti loading of Si/Ti= 42.

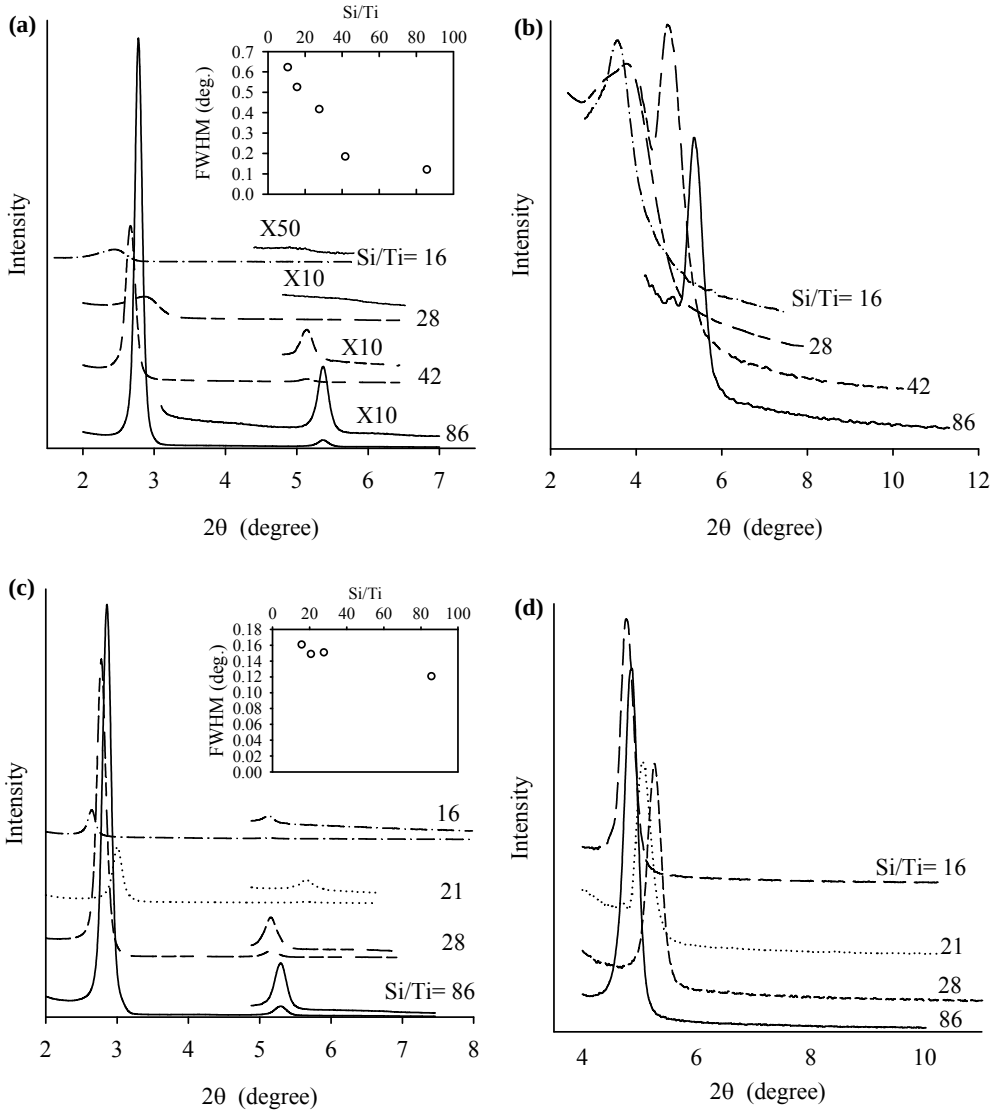

Figure 4.2. XRD patterns of as-synthesized and calcined Si-Ti mixed oxide thin films at various Ti loadings coated on Si wafer substrate. (a) As-synthesized Type-1 films. Inset: variation of FWHM width of (100) reflection with Ti loading; (b) calcined Type-1 films; (c) as-synthesized Type-2 films. Inset: FWHM width of (100) reflection as a function of Ti loading, and (d) calcined Type-2 films.

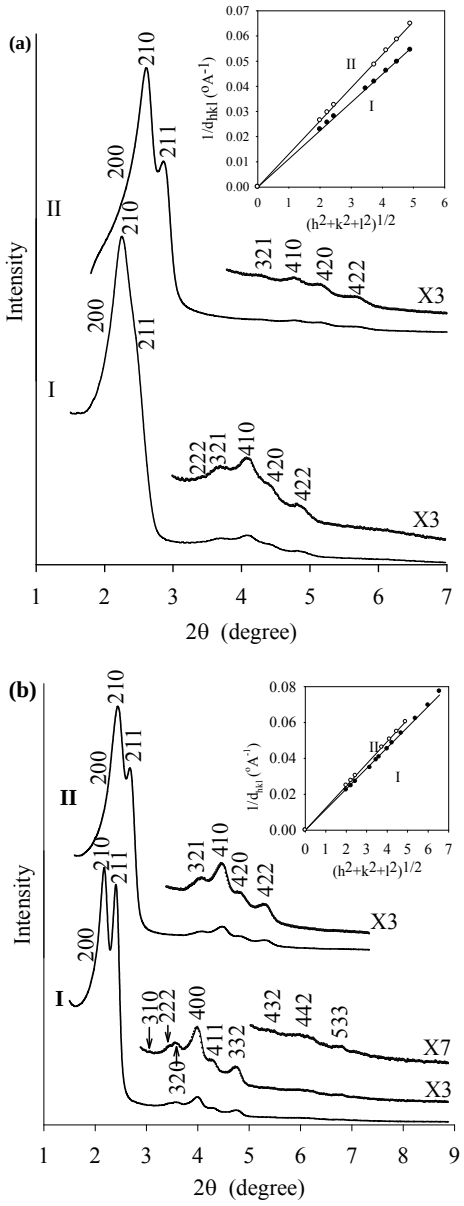

Figure 4.3. Low-angle X-ray diffraction patterns obtained from the corresponding powder samples of Si-Ti mixed oxides thin films prepared with Si/Ti = 86. (a) Type-1 films: I- as-synthesized and II- calcined. (b) Type-2 films: I- as-synthesized and II- calcined. Both confirm the formation of Pm3n cubic phases. In both figures (a) and (b), inset shows the relationship between $1/d_{hkl}$ and $(h^2 + k^2 + l^2)^{1/2}$.

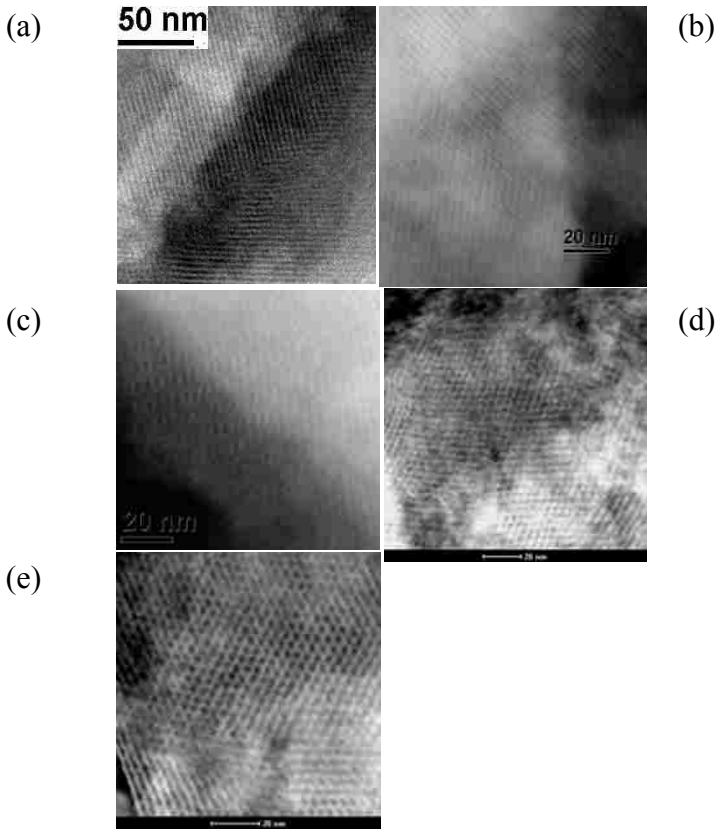

Figure 4.4. STEM images for the Pm3n cubic mesostructured Si-Ti mixed oxides thin films prepared with Si/Ti = 86. Images a – c of the calcined Type-1 film are recorded along the [100], [110], and [210] directions, respectively. Images e and f of the calcined Type-2 film are recoded along the [110] and [111] directions, respectively.

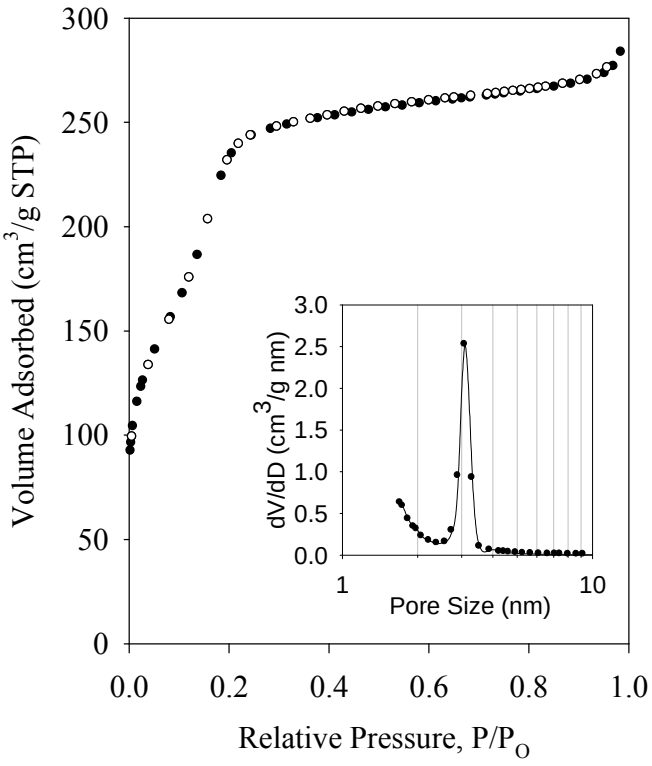

Figure 4.5. N2 adsorption-desorption isotherms obtained from the calcined power sample of Type-1 films (Si/Ti = 86). (•): adsorption and (o): desorption. Inset: The corresponding KJS pore size distribution curve obtained from the adsorption branch.

CHAPTER 5

SYNTHESIS OF Si-Ti MIXED OXIDE MESOPOROUS POWDERS BY SUGAR SURFACTANT COMPLEXATION

5.1 Summary

A series of Si-Ti mixed oxide powders are synthesized at different titanium loadings with predictable hexagonal mesostructure using the lyotropic liquid crystal nanocasting approach. They are synthesized with the aid of complexation or preferential interactions between one of the co-surfactant templates, β-D-maltoside ($C_{12}G_2$) and the titanium alkoxide precursor. The objective, as in the case of the thin films prepared previously in our group (Chapter 4), is to load a large fraction of isolated tetrahedrally coordinated Ti(IV) ions into the pore walls of the silica support. The ternary phase diagram of the C_{16}TAB-$C_{12}G_2$-water system measured previously (Chapter 3) is used as a quantitative guide to predict the final mesostructures of the mixed metal oxide materials. Pores are templated here by the mixed surfactant system of C_{16}TAB and $C_{12}G_2$ with compositions corresponding to a constant surfactant content of 46 wt% in the mixed surfactant phase diagram. The loading of Ti is increased by increasing the ratio of $C_{12}G_2/C_{16}$TAB in the templates while keeping a constant molar ratio of 1:1 between $C_{12}G_2$ and titanium isopropoxide. The degree of ordering of the hexagonal mesostructure decreases as Ti loading increases. When Ti loading reaches at Si/Ti = 10, materials became completely disordered although uniform mesoporosity and a uniform distribution of titanium sites is maintained.

5.2 Introduction

Nanoporous silica supports loaded with isolated transition metals have drawn great deal of attention over the last decades as active and selective catalysts for different types of oxidation reactions. Among all transition metal-containing catalysts, titanium containing silica molecular sieves have been the most widely investigated both experimentally and theoretically, in part because of the well-defined nature of the titanium substitution sites in microporous crystalline titanosilicates such as TS-1, TS-2,

and TS-β.[238-241] These types of materials show very high activity and selectivity[14, 52, 53] for different industrially important oxidation reactions in the presence of dilute hydrogen peroxide, a relatively inexpensive and environmentally friendly oxidant.[241, 242] Older technologies use much harsher oxidants and reaction conditions, and generate byproduct wastes that have to be separated from the products and effluent streams. While titanosilicate catalysts show desirable catalytic properties, TS-1 and TS-2 molecular sieves are formed by titanium cation substitution in MFI and MEL zeolites, respectively, and hence their applications are limited to organic molecules with kinetic diameters less than 5.5 Å. To extend the advantages of peroxide chemistry to larger molecules, titanium has been incorporated successfully into zeolite beta (TS-β).[243, 244] However, this zeolite still is only able to admit molecules with kinetic diameter smaller than 7 Å.[243]

The discovery of surfactant templated mesoporous silica molecular sieves by Mobil researchers in 1992[8, 9] showed a new way to overcome the limitation of pore size in traditional crystalline zeolites. Surfactant templated silica mesoporous materials can be synthesized with pore sizes in the range from 15 Å to over 100 Å, and they are potential candidates as supports for mesoporous titanosilicate materials. Among them, titanium doped MCM-41, MCM-48, and SBA-15 have been widely synthesized and their catalytic performance for different epoxidation reactions has been measured.[13, 195, 245, 246] Recent results indicate that the catalytic activities of Ti-containing mesoporous silica materials are strongly affected by the presence of water in the reaction system due to the large concentration of hydrophilic silanol groups at the silica surface compared to that in zeolites. Catalytic activities for selective epoxidation of small hydrocarbons with aqueous hydrogen peroxide have been found to be much lower than those obtained with Ti-containing zeolites, such as TS-1.[52, 53] However, higher activities compared with TS-1 have been obtained when the oxidant was changed from H_2O_2 to tertbutyl hydroperoxide (TBHP). Ti-containing mesoporous materials also showed higher selectivities and activities than TS-1 for oxidation of large organic molecules with even a mild oxidant such as H_2O_2, presumably due to easy access of catalytic sites.[53] Other studies have shown that the difference in the catalytic activity between mesoporous and microporous supported titania increases as the size of the reactant increases.[52, 54] These successful demonstrations of epoxidation activity justify sustained interest in the preparation of

well-defined titanium-containing silica mesoporous materials for oxidation of bulky organic molecules for fine chemicals production.

In these microporous and mesoporous silica-supported titania mixed oxide materials, titanium can be found in two different positions- extra-framework and framework. Titanium ions in an extraframework positions are usually either penta- or hexa-coordinated. They can also be either isolated or partly polymerized into small oligomers and clusters. Isolated and mononuclear TiO_x species with coordination number higher than four are connected to the silica host via one or two oxo bonds. Partly polymerized octahedrally coordinated titanium oxide species are also linked together by oxo bonds and connected to the silica host by Si-O-Ti bridges. Aggregation of these titania nanoclusters can lead to extraframework titanium-rich domains. However, these extraframework ions are not desirable, as the catalytic properties of Si-Ti mixed oxide materials have been attributed to titanium ions in a framework state, connected to the silicate matrix by Si-O-Ti bridges. These tetrahedrally coordinated, isolated titanium ions, incorporated into the framework by isomorphic substitution of Si(IV) by Ti(IV), are believed to be the active oxidation sites for heterogeneous Si-Ti mixed oxide catalysts.[55-57] These Ti(IV) ions are most effective when they are homogeneously distributed into the silica network and isolated by long O-Si-O-Si-O structural fragments in all directions.

Because it is based on the "bottom-up" formation of materials by polycondensation of metal alkoxides precursors, the sol-gel process provides the opportunity to produce well-mixed metal oxides. However, the high reactivity of titanium alkoxides in comparison with analogous silicon precursors impedes the molecular level incorporation of Ti(IV) into a silica matrix. The stabilization of titanium alkoxide is required to generate catalytically active sites in Si-Ti mixed oxides materials. Stabilized Ti alkoxides should inhibit fast hydrolysis and condensation, thus promoting isomorphic substitution of Si(IV) by Ti(IV). Here we have used the "ligand-assisted self-assembly" method to synthesize mesoporous Si-Ti mixed oxide materials for catalysis applications, as described in Chapter-4. The hydrophilic maltose headgroup of nonionic surfactant dodecyl β-D-maltoside ($C_{12}G_2$) is proposed to act as a bi-dentate chelating agent for the titanium alkoxide precursors.

The applications of these mixed metal oxides materials in heterogeneous oxidation catalysis require the production of bulk powder samples. Surfactant templated metal oxide powders can be prepared by two different alkoxide based sol-gel routes. In the first approach, the initial surfactant solution is heavily diluted with co-solvent or water. Here charge density matching between the organic surfactants and inorganic oxides dictates the cooperative assembly of components into a new liquid crystal-like phase that precipitates and cures to form the final product.[247] In this mechanism, no preformed liquid crystal phase is necessary, but because of partitioning between the bulk dilute phase and the precipitated aggregates, the structure of the product is difficult to predict. In the second synthetic approach, a concentrated surfactant solution (≥ 30 wt%) is employed, and a preformed lyotropic liquid crystalline phases acts as a "template" for the oxide/surfactant composite. This method was first proposed by Attard et al.[77] and is also known as the nanocasting or true liquid crystal templating method. To be more precise, the polymerizing metal oxide precursors and surfactants in the concentrated solution form a homogeneous liquid crystal upon evaporation of the hydrolysis-generated alcohol and of excess water that may be needed to drive hydrolysis to completion. This second approach offers the advantage of potentially being able to predict the final mesostrusture of the surfactant-silicate complex. The nano-casting method is a bulk form of evaporation induced self-assembly (EISA), because initially the generation of alcohol during alkoxide hydrolysis destroys the lyotropic order. Subsequent evaporation of alcohol and excess water induces the self-assembly of surfactant again into a lyotropic ordered phase that cures further to form the final material. This method is effective in producing long-range ordered nanoporous materials from nonionic surfactants, where the high surfactant concentration drives the self-assembly process in the presence of weak organic-inorganic interactions.

Here, Si-Ti mixed oxides bulk powder materials with variable compositions of Si/Ti are synthesized via a modified nano-casting method, adapted from the procedure suggested by Attard et al.[77] To dissolve the sugar based $C_{12}G_2$ surfactant, alcohol must be added at the beginning of the process, which is different than the original approach. Similar to the original approach however, solvent evaporation induces self-assembly of surfactants. Here pores are templated by the mixed surfactants system of

cetyltrimethylammonium bromide (C_{16}TAB) and $C_{12}G_2$. Materials are synthesized with the assistance of pre- complexation between the headgroup of the $C_{12}G_2$ surfactant and Ti-alkoxide. These casted powder materials are somewhat analogous to the Type-1 Si-Ti mixed oxides thin films described in Chapter 4. Si-Ti mixed oxides materials with predictable hexagonal mesostructures are synthesized using the general predictive synthesis method outlined by Alberius et al.[91] According to this method, the sol compositions are calculated by replacing the volume of water in a known lyotropic liquid crystalline phase with the volume of non-volatile hydrophilic inorganic species present in the system after complete hydrolysis of precursors. Here we used the ternary phase diagram of the C_{16}TAB / $C_{12}G_2$ / water system as described in Chapter 3 to predict the final material structure. Ti loading is changed by changing the molar ratio of $C_{12}G_2$/C_{16}TAB with a constant molar ratio of 1:1 between $C_{12}G_2$ and Ti-alkoxide. The structural properties of the materials are characterized by using low-angle x-ray diffraction (XRD) and N_2 physisorption.

5.3 Experimental

5.3.1 Materials

Tetraethyl orthosilicate (TEOS, 98%) and cetyltrimethylammonium bromide (C_{16}TAB, 99%) were purchased from Sigma Aldrich. Titanium isopropoxide (TIP, 99%) was purchased from Gelest. n-dodecyl β-D-maltopyranoside ($C_{12}G_2$, ≥99%, %α<0.2) was purchased from Anatrace. Deionized ultra-filtered water (DIUF), 0.1N HCl, absolute ethanol, NoChromix cleaning reagent, and concentrated sulfuric acid were purchased from Fisher Scientific. All chemicals were used as received without any further purification.

5.3.2 Synthesis

Si-Ti mixed oxide nanostructured bulk powders were synthesized by a modified nano-casting or liquid crystal templating method. A predictive synthesis approach was used to prepare the mixed oxide materials based on the ternary phase diagram of the C_{16}TAB / $C_{12}G_2$ / water system, as shown in Figure 5.1. For materials synthesis, the volume of water corresponding to a point in the ternary phase diagram was replaced with

an equivalent volume of silica and titania.[91] Titanium loadings in the materials were increased by increasing the ratio of $C_{12}G_2$/C_{16}TAB along a constant surfactant line in the ternary phase diagram while maintaining a 1:1 molar ratio between $C_{12}G_2$ and TIP. All silica-titania mixed oxide materials were synthesized with a total surfactant content corresponding to 46 wt% water in the ternary phase diagram. The amount of $C_{12}G_2$ was increased along that constant surfactant line corresponding to points from 5 wt% to 35 wt% with an increment of 10 wt%. The corresponding Ti loadings expressed in term of Si/Ti are 46, 28, 16, and 10, respectively.

In a representative synthesis procedure, 0.05 g of $C_{12}G_2$ surfactant was first dried overnight at 50 °C under vacuum, and then dissolved in 2.3 g of dry EtOH in a bottle initially flushed with dry nitrogen. 28.7 μL of TIP was added into this solution in a nitrogen atmosphere and then the mixture was stirred for 3 hrs in a nitrogen-purged glove bag to promote complexation between the maltoside headgroups and TIP. The amount of TIP was always enough to give a 1:1 molar ratio of $C_{12}G_2$ to TIP. In a separate beaker, TEOS was prehydrolyzed at room temperature for an hour by adding 1.76 g of TEOS to 0.78 g of EtOH, followed by addition of a mixture of 0.27 mL of DIUF water and 0.34 mL of 0.1 N HCl. This mixture of TEOS, water, and ethanol gives a molar ratio of 1: 4: 2 and the specified amount of 0.1 N HCl brings the solution pH to 2. The quantity of TEOS was calculated from the ternary phase diagram of C_{16}TAB / $C_{12}G_2$ / water system by replacing the volume of water in the phase diagram with equivalent volume of fully hydrolyzed silica and titania precursor, as described earlier. The prehydrolyzed TEOS solution was then added dropwise by a syringe to the alcoholic solution of TIP under vigorous stirring in N_2 atmosphere. Finally, 0.41 gm of C_{16}TAB was added and stirred to dissolve it. For this example, the amounts of $C_{12}G_2$ and C_{16}TAB added were chosen to give a composition corresponding to 5 wt% of $C_{12}G_2$ and 41 wt% of C_{16}TAB in the ternary phase diagram. The final molar ratios of TEOS: TIP: EtOH: H_2O: $C_{12}G_2$: C_{16}TAB for this example were 1: 0.0116: 8: 4: 0.004: 0.0116: 0.1335. After mixing all ingredients, the sol solution was transferred into a Petri dish and a gentle vacuum (~5-10 in Hg of vacuum) was used to remove the alcohol from the sol solution. Vacuum degassing was continued until a viscous solution formed which was then heated at 50°C for 2-3 days at ambient conditions in an uncovered dish to allow polycondenstion to

reach completion. Upon completion of this step, transparent but cracked pieces of composite material were formed. As-synthesized material was then calcined at 450°C for 3 hr in flowing air atmosphere with a heating ramp of 1 °C/min under flowing nitrogen. Titanium loading in the Si-Ti mixed oxide powder materials is expressed by the molar ratio of Si/Ti, which is 86 for this sample. Using the same synthetic protocol, different batches of Si-Ti mixed oxide powders with different Ti loadings were synthesized from this mixed surfactant templates. Selected points on the ternary phase diagram to guide our synthesis are shown in Figure 5.1.

5.3.3 Characterization

Powder XRD patterns were recorded on a Siemens 5000 diffractometer with 0.154098 nm CuK_{α} radiation. Nitrogen adsorption-desorption isotherms were measured at 77K using a Micromeritics Tristar 3000 analyzer. Before measurement, all the samples under study were degassed at 120°C for 6 hrs under flowing nitrogen. Nitrogen sorption isotherms data was used to obtain information about specific surface area and pore structure of the synthesized materials.

5.4 Results and Discussion

Si-Ti mixed oxides powder materials synthesized using a modified nano-casting method were characterized by low-angle powder XRD and nitrogen physisorption techniques. Low-angle powder X-ray diffraction patterns of the both as-synthesized and calcined samples prepared with variable compositions of Si/Ti are presented in Figure 5.2. Hexagonal structures in the as-synthesized and calcined samples prepared with Si/Ti = 86 and 28, shown in Figures 5.2(a) and (b) can easily be identified by the three well defined diffraction peaks with reciprocal d-spacing ratios of 1: √3: √4, indexed to the (100), (110), and (200) Bragg reflections, respectively. These patterns are typical for a two-dimensional hexagonal phase with P6mm symmetry. When the Ti loading was increased to Si/Ti = 16, we see a strong (100) reflection and a weak broad shoulder, which may be from the combined effects of (110) and (200) reflections. This indicates that the pore structure of this sample is disordered hexagonal or wormhole-like. The

XRD patterns of the calcined samples, as shown in Figure 5.2, indicate that the long-range order of the materials is preserved upon calcination. Low levels of contraction of pores in all samples are observed due to calcination. For instance, the first sample synthesized with Si/Ti = 86 has a unit cell parameter, a_0, of 37.3 Å. After calcination, a_0 decreases to 33.1 Å, corresponding to about 11 % unit cell shrinkage. When the Ti loading is further increased to Si/Ti = 10, a featureless XRD pattern is obtained (not shown), indicating a disordered material. We also observed a similar trend with Si-Ti mixed oxide thin films in that the degree of long-range pore ordering decreases as Ti loading increases, as discussed in Chapter 4. This is due to the combined effects of increase in $C_{12}G_2/C_{16}$TAB ratio and the increase in Ti loading. Earlier we have found (Chapter 3) that increasing the amount of $C_{12}G_2$ with respect to C_{16}TAB for a constant percentage of total surfactant leads to less long-range order of the mesoporous structures prepared with only silica. Also because of the larger ionic radius of Ti(IV) compare to that of Si(IV), isomorphic substitution of Si(IV) by Ti(IV) is detrimental to long-range pore ordering.[228]

Before the application of these Si-Ti mixed oxide materials in heterogeneous oxidation catalysis, it is very important to know the pore texture characteristics such as surface area and pore size of these materials. Nitrogen adsorption-desorption isotherms data were used here to evaluate these properties. Nitrogen sorption isotherms measured at 77 K from these mixed oxides materials with variable compositions of Si/Ti are displayed in Figure 5.3 (a). All of them exhibit Type-IV isotherms, typical of mesoporous oxides. We can see from the isotherms that in all cases, the nitrogen condensation steps are not well-pronounced. But they are more clearly visible when isotherms data are plotted in a logarithmic plot, as shown in Figure 5.3 (b). This kind of short condensation step has been observed earlier with MCM-41 silica materials when pores are small, closer to the lowest range of mesoporous materials, which is 2 nm.[126, 134] Nitrogen sorption isotherms with less-pronounced condensation step have also been observed by Hüsing et al. in transition metal-doped silica mesostructured materials with pores diameters in the range of 2 – 2.5 nm.[204] The absence of a hysteresis loop in all samples indicates that capillary condensation is reversible, which is consistent with uniform small mesopores. The pore properties of all materials were calculated by the α_s-plot method, where the amount

adsorbed on the porous material under study is plotted against the reduced standard adsorption α_s.[124] α_s is defined as the ratio of the volume adsorbed on a macroporous silica reference material at a given relative pressure to the volume adsorbed by the reference material at the relative pressure of 0.4. The α_s-plot method of the first sample synthesized with a Ti loading equivalent to Si/Ti = 86 is presented in Figure 5.4. In this study, literature data for Li-Chrospher Si-1000 silica gel with BET surface area of 25 m^2/g were used to prepare α_s plots.[133] From this plot we calculate the total surface area (S_t, combined surface area of mesopores and macropores), primary mesopore volume (V_p), micropore volume (V_{mi}), and primary mesopore surface area (S_p, difference between the total surface area and external surface area). The micropore volume is determined by extrapolating the curve at low pressure back to the vertical axis, and we can see for this sample that the micropore volume is approximately zero. All of these parameters for all samples are listed in Table 5.1. Assuming cylindrical pore shape, the primary mesopore diameter w_d was also calculated using an equation in the form of $w_d = 1.213 d_{100}(\rho V_P/(1+\rho V_P))^{1/2}$; where d_{100} is the XRD (100) interplanar spacing as listed in the second column of Table 5.1, ρ is the density of amorphous silica walls (2.2 gm/cm^3) and V_p is the primary mesopore volume. Calculated values of w_d are listed in Table 5.1. From the XRD study, we have seen that when Ti loading was increased to a value equivalent to Si/Ti= 10, we obtained a disordered material. For this sample we were unable to calculate w_d. We observe high active mesopore surface areas in the range of 898-733 m^2/g, for our mixed oxide samples having Si/Ti ratios of 86 - 10. Micropores are absent in the materials synthesized with Si/Ti = 86 and 28. Small amount of micropore volume equal to 0.01 cm^3/g is present in the sample with Si/Ti = 16 and this volume increases to 0.03 cm^3/g when Si/Ti was further increased to 10. As we have seen from Figure 5.2 that calcined Si/Ti = 16 sample is a disordered hexagonal material and collapsed structures give rise to some micropore volume. For the Si/Ti = 10 sample disordered structures collapsed during calcination and that contributes to the formation of substantial amount of micropores.

Figure 5.5 shows the pore size distributions obtained from the Barrett-Joyner-Halenda (BJH) method[125] with the corrected form of the Kelvin equation and the Harkins-Jura statistical film thickness equation. This approach of determining pore size

distributions (PSD) is known as Kruk-Jaroniec-Sayari (KJS)[126] method. And this modified BJH pore size distributions are derived from their corresponding adsorption branches. We employed KJS pore size distribution technique here as the BJH method without correction underestimates the size of pores.[130] Figure 5.5 shows narrow pore size distributions for these mixed oxides samples with variable Si/Ti ratios (Si/Ti = 86, 28, and 16), indicating well defined uniform pores. The disordered material, when Si/Ti= 10, during nitrogen adsorption study gives a very broad pore size distributions. The primary mesopore diameters, obtained from the maximum on these KJS pore size distributions, are also reported in Table 5.1. We can see very good agreements between pore diameters estimated by using two different techniques- one based on the simple geometrical consideration and the other from the maximum on the PSD.

5.5 Conclusions

A series of Si-Ti mixed oxide nanostructured powder samples with predictively-synthesized hexagonal mesostructures were synthesized with different titanium loadings by employing a 1:1 molar ratio of $C_{12}G_2$ to titanium iso-propoxide (TIP). A modified nano-casting method was used to synthesize these materials and the ternary phase diagram of the C_{16}TAB / $C_{12}G_2$ / water system (developed in Chapter 3) was used as a quantitative guide in predicting the final mesostructures of the materials. As found earlier in Chapter 4, the degree of ordering of the final mesostructures of these mixed oxide materials decreases as Ti loading increases and when Si/Ti = 10, the material becomes disordered. Pore sizes, calculated using two different techniques, indicate that the materials are mesoporous with pore sizes slightly greater than 2.0 nm. This is substantially greater than the pore size available in titanium-substituted zeolites, and future catalytic and spectroscopic studies will be employed to confirm that TIP complexation with maltoside surfactants leads to isolated Ti sites, as in films prepared by dip coating.

Table 5.1. Structural Properties of the calcined materials[a]

Sample with Si/Ti molar ratio	d_{100} Spacing (nm)	S_t (m^2/g)	S_p (m^2/g)	V_p (cm^3/g)	w_d (nm)	w_{KJS} (nm)
86	3.31	921	898	0.410	2.4	2.3
28	2.93	853	837	0.341	2.1	2.2
16	3.36	768	751	0.302	2.2	2.3
10	-	733	728	0.288	-	-

[a] d_{100} spacing obtained from the XRD patterns; S_t: total surface area; S_p: primary mesopore surface area; V_p: primary mesopore volume; w_d: pore diameter; w_{KJS}: mean pore size obtained from the KJS method.

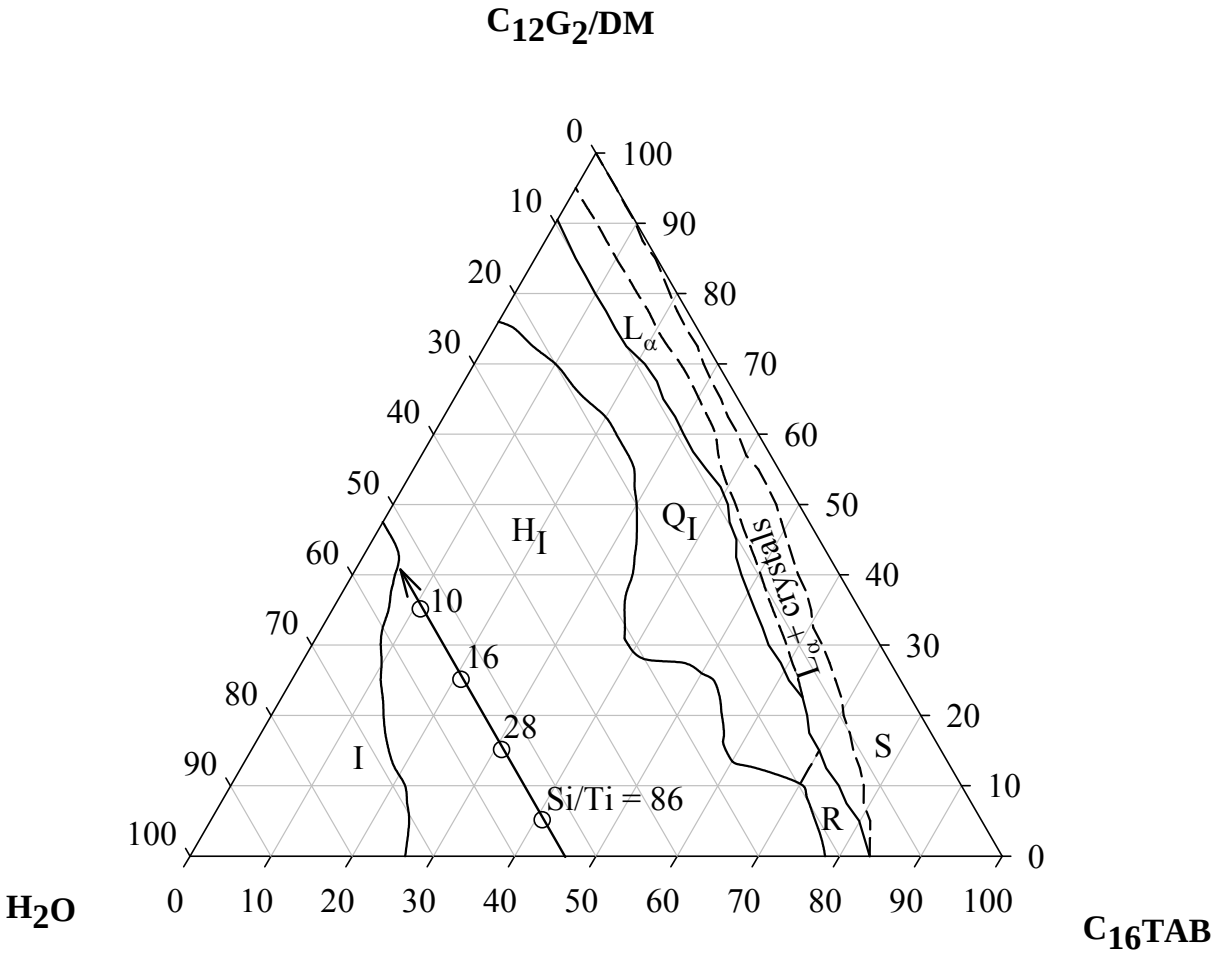

Figure 5.1. Ternary phase diagram of the β-$C_{12}G_2$-C16TAB-water system at 50 ˚C, used to guide the synthesis of Si-Ti mixed oxides materials. Selected surfactants compositions for predictive synthesis are shown on the arrow, indicating a constant surfactant content line equivalent of 54 wt% of water.

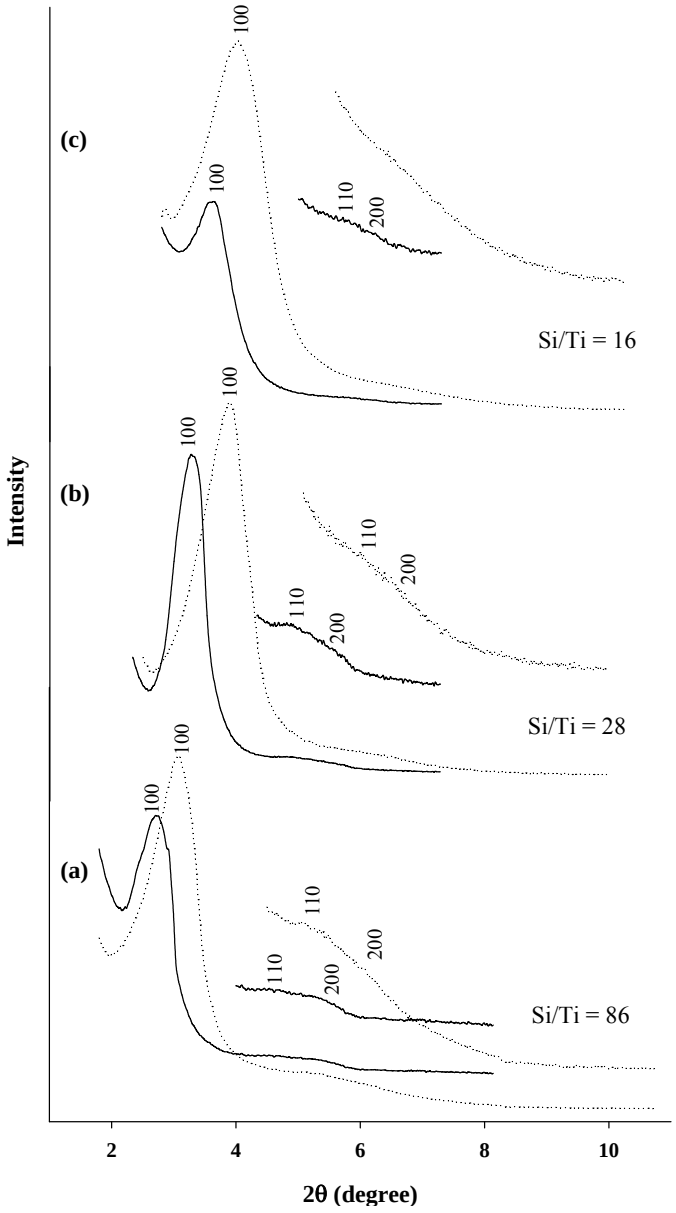

Figure 5.2. Low angle powder XRD patterns recorded on both the as-synthesized and calcined Si-Ti mixed oxides materials with variable Ti loadings: (a) Si/Ti = 86, (b) Si/Ti = 28, and (c) Si/Ti = 16. Solid lines represent as-synthesized samples and dotted lines are for the calcined samples.

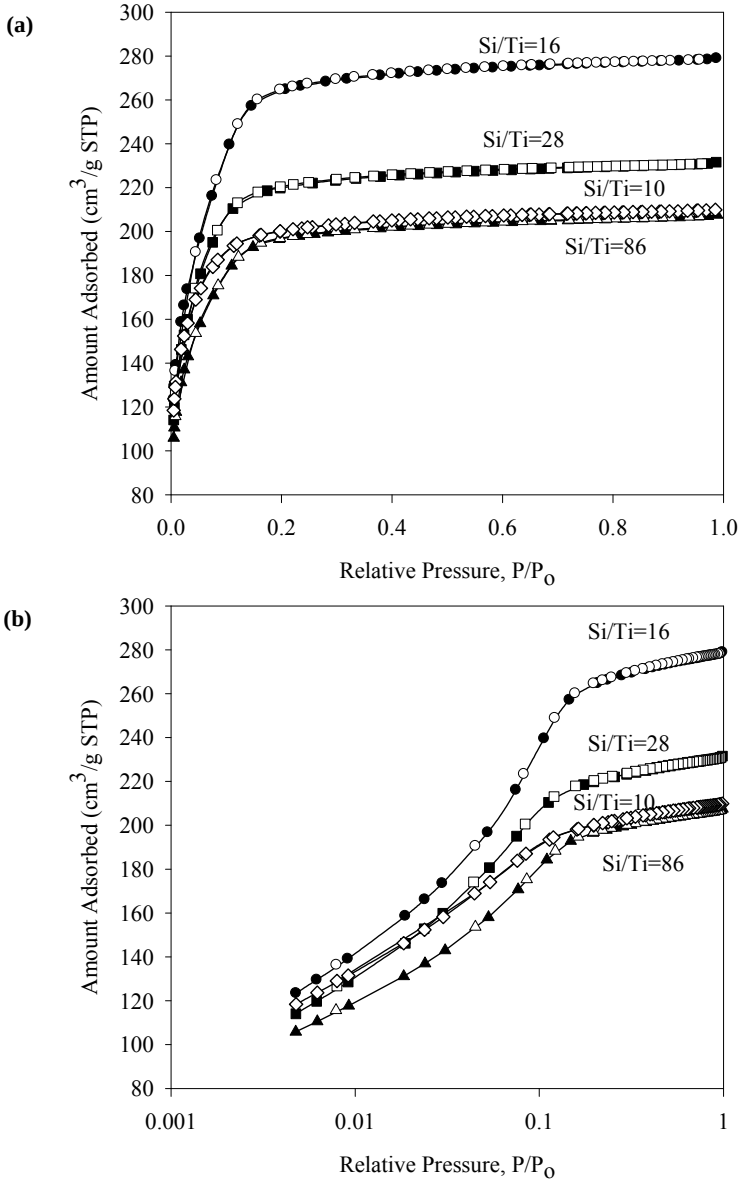

Figure 5.3. Nitrogen sorption isotherms of the calcined samples at 77 K. (a) Nitrogen adsorption-desorption isotherms obtained from the different Si-Ti mixed oxides materials with variable compositions of Si/Ti, (b) adsorption-desorption isotherms shown in logarithmic scale.

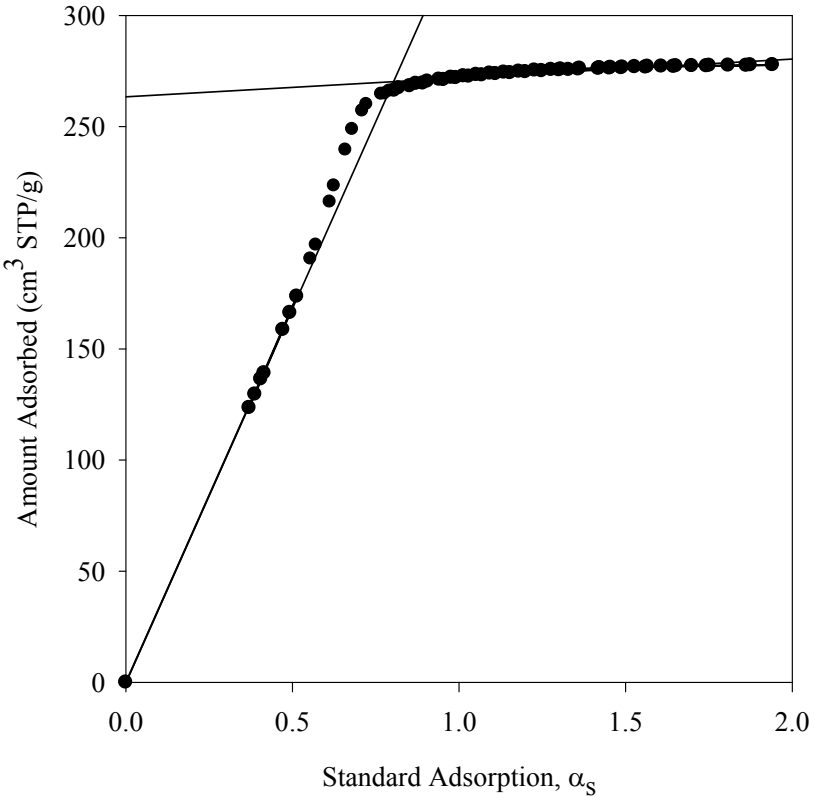

Figure 5.4. Representative standard high-resolution α_s-plot for the sample prepared with Si/Ti = 86.

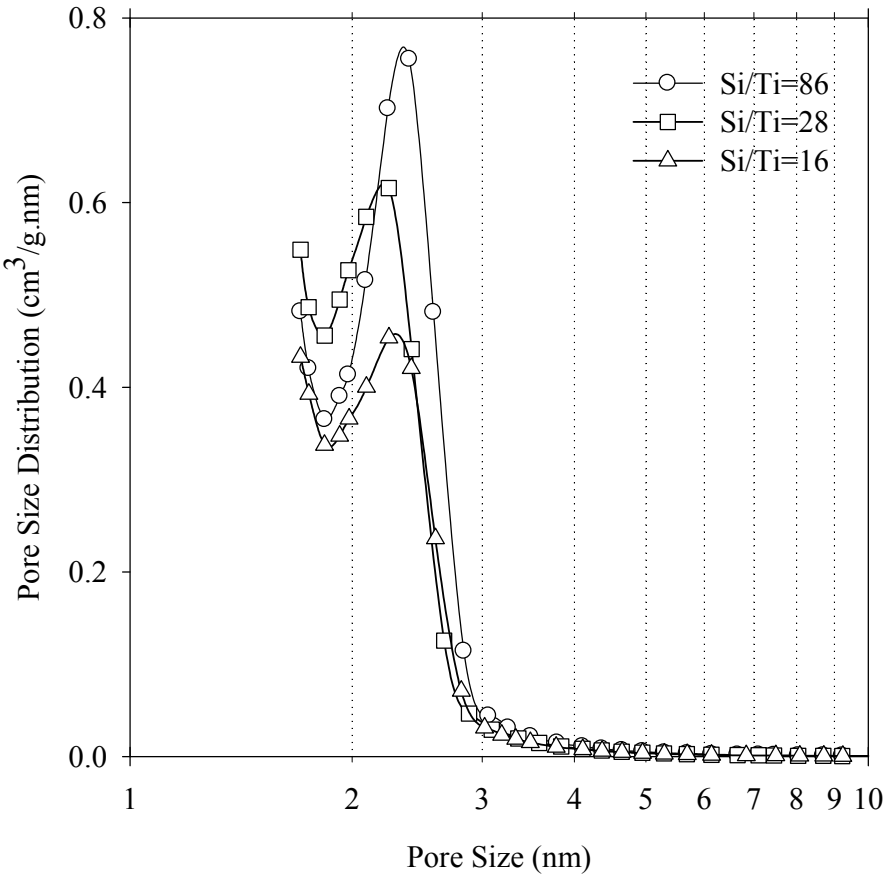

Figure 5.5. KJS pore-size distributions of the samples with variable Si/Ti ratios, obtained from their corresponding adsorption branches.

CHAPTER 6
GLUCOSE MOLECULAR IMPRINTING OF SILICA

6.1 Summary

A non-covalent molecular imprinting approach is utilized in an attempt to synthesize both bulk silica and thin films with selective saccharide binding sites by polymerization of silicon alkoxide precursors in the presence of site templates. To examine the effects of imprinting process parameters on the performance of the materials as adsorbents, different types of imprinted silica materials were synthesized. D-(+)-glucose imprinted materials were prepared (presumably) utilizing the hydrogen bonding between the hydroxyl groups of glucose molecule and the binding groups of silica precursors in the absence of any organofunction silane. The resulting silica structures are stable mesoporous powders that do not collapse during aging and drying. Pore characteristics of these types of synthesized silica materials were determined from the nitrogen sorption isotherm data. In an effort to make the gels from fully hydrolyzed, partially condensed gel precursors, a two-step acid-base silica sol-gel process with long initial acid-step (~24 hrs) was used to prepare these materials. An increase in the amount of base catalyst added at the beginning of the second step decreases the gelation time and generate porous silica with more mesoporous character. Upon removal of the glucose template molecules by solvent extraction, silica materials with imprinted cavities were used to develop adsorption isotherms by studying their rebinding capacity from aqueous solutions of pure glucose of different concentrations. As control experiments, the adsorption of glucose in non-imprinted silica prepared under the same conditions but in the absence of glucose was compared. Enhanced adsorption of glucose from an aqueous (polar) solution in the imprinted material was not observed because of non-specific adsorption which is evident from the adsorption level of glucose in the both imprinted and non-imprinted silica materials and thin films. This is probably because hydrophilic vicinal and geminal silanols are the only potential binding groups on the silica surface.

In the next step, the effects of incorporating different organic functional groups into the silica matrix on the rebinding capacity are investigated. Amine functionalized

porous silicas, both glucose imprinted and non-imprinted, are synthesized by one pot co-condensation of tetraethoxysilane (TEOS) and the aminosaline 3-aminopropyltriethoxysilane (APTES) under acidic conditions. It is found that the comparatively stronger hydrogen bonding between the amine functional group and the hydroxyl groups of glucose increases the glucose binding affinity over that of non-functionalized silica. However, the non-specific nature of this binding still limits the selectivity of the materials toward D-glucose. The amino functionalized non-imprinted material had very little porosity (specific surface area was ~7 m^2/g) and the surface embedded amino groups adsorbed a great deal of glucose from solutions, which gave a very high amount of glucose adsorbed per unit area of solid.

6.2. Introduction

Molecular imprinted organic polymers or inorganic polymers such as silica gels and thin films with highly specific recognition sites have great potential for applications in separations, catalysis, chemical sensing, and enzyme mimicry.[15, 17-19, 248-253] Molecular imprinting is a process of synthesizing materials with recognition sites that are organized spatially in the material through the polymerization of monomers around a suitable imprint / template molecule. Covalent or non-covalent interactions of the imprint molecule with the functional groups of binding monomers are hypothesized to lead to selective adsorption sites. In order for this approach to be successful, interactions between the template and the binding functional groups of monomers should be strong enough to keep the predetermined orientation of the groups during polymerization and the subsequent processing steps.[18] Removal of template molecules from the synthesized material are expected to leave behind active functional binding groups capable of rebinding template molecules in the cavities. Recognition properties of these imprinted cavities are mainly due the defined shape of the imprinted sites and the predetermined orientation of the functional groups on the material surface.[18] Prearrangement of binding groups is determined by the chemical nature of the template molecule.

In a general non-covalent imprinting approach, polymerization of monomers is carried out in liquid state in the presence of the imprint molecules. On the other hand, in

the covalent technique, the imprint molecule is first covalently bound with monomer molecule(s) and then added to the reaction mixture.[18] Heterogeneity in the imprinted cavities is the major problem for the imprinted materials synthesized utilizing non-covalent interactions,[248, 249] and this can be overcome by the covalent imprinting technique.[15, 17] The covalent interaction between the functional groups of template molecules and those of complementary monomers was first utilized by Wulff[18] and Whitcombe et al.[17] in polymeric material and by Katz & Davis[248] in silica. However, the choice of imprint molecules with covalent imprinting is very limited. Also, non-covalent interactions have been widely and successfully used to promote self-assembly during polymerization, in which case template-solid binding reversibility allows easy removal of imprinting molecules from the matrix. In contrast, removal of the imprint molecules from a covalently imprinted matrix requires either selective chemical or thermal cleavage, which makes this process less flexible.[253]

Most organic polymers suffer from swelling or shrinkage when placed in an aqueous mobile phase.[254, 255] However, an aqueous environment is desirable in biomedical and environmental applications. The extent of swelling of polymer network depends on the degree of cross-linking.[256] The use of more than 80% cross-linking agent is required to obtain a physically stable non-swelling polymer network for aqueous applications. A high degree of crosslinking is also required to generate a stable network that will be able to retain the shapes of pores upon template removal.[19] However, a very high degree of cross-linking in a polymer usually makes the complete removal of templates difficult due to restricted diffusion which limits the extraction of templates from the polymers. Continuous extraction can remove up to 97-99% of the templates but a small portion of the template left unextracted even after several stages can introduce inaccuracies in quantification methods if unextracted templates bleed from polymer to solution.[257] Thus, highly crosslinked organic polymers are not necessarily ideal materials for use in aqueous environments, such as those required for saccharide separations (explored here). Molecularly imprinted silica, produced by sol-gel process, is a better alternative to produce materials with recognition property for the application in aqueous solutions. Stability and swelling in solutions are not problems with silica because mesoporous silica is typically a highly crosslinked, but still mesoporous, material.

Sometimes incorporation of organic moieties into the silica network improves the molecular selectivity of the imprinted material.[16] The final material composed of an inorganic (SiO_2) network cross-linked or substituted by organosilanes with organic functional groups is known as a "hybrid inorganic-organic material".[258-260] The low temperature of the sol-gel process enables the controlled incorporation of organic groups into the final material. In general, there are two approaches to incorporate organic functional group(s) into sol-gel silica. In the first method, known as (post-synthesis) grafting, an organosilane with desired functional group(s) is covalently coupled with the silica network after it has already been formed and dried.[261, 262] In the second method, known as one-pot synthesis or co-condensation, functional groups are introduced by co-polymerization of organosilane(s) with silica precursors in a single sol.[263-267] The latter approach is advantageous over the former because it allows better control of the composition and distribution of organic groups throughout the matrix, especially when molecular imprinting is to occur.[268] Moreover, the grafting method reduces the pore size and pore volume[266] and the pores have been shown to be less stable than in the same material synthesized by a co-condensation approach.[269] In figure 6.1, a schematic representation of the formation of a recognition cavity into the silica matrix with organosilane(s) with desired functional group(s) by non-covalent molecular imprinting is shown.

Using either grafting or co-condensation method, it is also possible to prepare organic-inorganic hybrid thin films on suitable substrates. Non-covalent molecular imprinted bulk silica materials sometimes suffer from diffusion and accessibility limitations[270] that can reduce the effectiveness of the material. Organic-inorganic hybrid thin films are generally free from these types of disadvantages and therefore have offered a superior alternative in many chemical and biological sensing applications[271, 272] and can be applied for separations and catalysis as well.

The first imprinted silica gel was prepared by F. H. Dickey[15] in 1949. He precipitated the silica gel from an acidic sol in the presence of a specific dye, which acted as an imprint molecule. The non-covalent interaction between the imprint molecules and the silanol groups were intended to promote imprinting of the material. After template removal, Dickey showed that imprinted silica had higher adsorption affinity for that

particular dye than that of a blank silica gel. Since then, advances in understanding how to prepare and dry controlled-porosity sol-gel silica have sustained interest in perfecting the molecular imprinting of silica. Some examples of non-covalent molecular imprinting in silica (both bulk and thin film) using co-condensation are listed in Table 6.1.

The goal of the work discussed in this chapter is to synthesize non-covalent molecularly imprinted sol-gel materials (e.g. porous bulk silica and porous silica thin films) which can adsorb the imprint molecule from an aqueous solution at a higher level compare to their non-imprinted counterparts. The second goal is to demonstrate the degree of recognition for the imprint molecule relative to other interfering and competing molecules in solutions. The effects of matrix pore structure and organic modifiers on the efficacy of imprinting are explored as well, which is a subject rarely discussed in the sol-gel molecular imprinting literature.

6.2.1 Non-covalent Imprinting in Silica

In this work D-(+)-glucose imprint molecule is selected in order to examine the dependency of the non-covalent interactions between the template molecules and the binding groups on the recognition properties of the materials. This molecule has specific functional moieties in its structure those are able to self-assemble in the presence of silane precursors in the solution via non-covalent interactions.[273] D-(+)-glucose is commercially available and good analytical techniques are available to quantify it accurately in solution.

Imprinting with Glucose

To study the non-covalent molecular imprinting of saccharides in silica gels, D-glucose molecule was selected as a first imprint molecule in our group, and it forms the basis for the studies presented here. The low temperature of the sol-gel process makes the incorporation of glucose molecule into the silica network possible. Saccharide-specific binding is of interest in many areas including glycobiology and biofuels processing, but glucose-selective materials are of specific interest for glucose monitoring in diabetes treatment. Diabetes is caused because of the inability of the body to produce enough insulin resulting in poor control of blood glucose levels. Current treatment of diabetes

calls for the delivery of insulin in response to elevated blood glucose levels. Thus accurate monitoring of the blood glucose level for the diabetic patients is important in the management of this disease. Accurate monitoring of blood glucose levels requires biocompatible, glucose-sensitive materials for the development of glucose sensors and self-regulated insulin delivery systems. There has already been extensive research directed towards developing the best possible materials for continuous monitoring of blood glucose levels.[255,274-278] However, very little research has been performed with silica materials. Immobilization of glucose oxidase (GO_X) enzyme in silica for sensing glucose in solution has been examined by some researchers,[279, 280] but to date no effort has been focused on developing glucose imprinted silica polymers or thin films for non-enzymatic glucose detection.

There are four possible types of interactions between the imprint molecule(s) and the binding groups of monomers during the non-covalent imprinting. They are hydrogen bonding, hydrophobic interactions, van der Waals interactions, and ionic co-ordination.[255] The dominant interaction expected for nonionic imprint molecules is hydrogen bonding. Nonionic imprint molecules can participate in hydrogen bonding not only with the organic functional groups introduced via organosilanes, but also with hydrophilic vicinal and geminal silanols (along with strongly adsorbed water molecules).[270] It has been found that it is possible to combat this nonspecific adsorption by introducing hydrophobicity onto the silica surface through methyl and/or phenyl group(s), and thereby to increase the level of adsorption and selectivity of imprint molecules and nonionic surfactants in an aqueous solution.[255, 281] It has been suggested that almost all hydroxyl groups of the glucose molecule can form at least one hydrogen bond with the silica surface directly through terminal hydroxyl groups or bound water molecules.[255] Organic functionality introduces new interactions; for example, phenyl groups promote Π-Π interactions with the pyranose ring of glucose.[270] The amine of aminopropyltriethoxysilane (APTES) provides interaction with the acidic hydroxyl groups of glucose. With a combination of organic functional groups and silanols, a network of non-covalent interactions present during gelation should help to form recognition cavities of specific shapes, and the subsequent polymerization of tetralkoxysilanes fixes the shapes of the cavities. The only challenge that this approach (and it is one to be addressed by anchoring the imprinting

molecule in future studies) is that site heterogeneity can arise during non-covalent imprinting due to variation in the orientation of functional groups during imprinting.[249] Nevertheless, the hypothesis of this chapter is that glucose imprinting molecules can participate in non-covalent interactions with both silane-anchored functional groups and surface hydroxyl groups as an isolated molecule or as an aggregate, to form selective sites for rebinding of that specific saccharide.

6.2.2 Imprinting Process

As discussed in Chapter 2, the low temperature used for sol-gel processing enables the incorporation of organic imprint molecules into the silica network. The sol-gel process is a convenient route to pure, homogeneous silica materials and the structural properties of the fabricated materials, such as mean pore size, pore size distribution, and pore interconnectivity, can be tuned using the process parameters described in Section 2.6. In this study, the alkoxide sol-gel method is used to make SiO_2. In principle, the first step in this method is the generation of silicic acid via the hydrolysis reactions of silicon alkoxides. Here the most commonly used tetraalkoxysilane, tetraethyl orthosilicate (TEOS) was used as silicon precursor to build silica framework. Sol-gel reactions are usually carried out in a batch reactor in the presence of water, which acts both as a reactant and (in some cases) as either a solvent or an anti-solvent. Hydrolysis is initially facilitated in the presence of alcohol that acts as a mutual solvent for water, precursor and siloxane oligomers. The alcohol usually matches the alkoxides ligands to avoid ligand exchange, e.g.. TEOS is usually solubilized with ethanol. Hydrolysis reaction is followed by the condensation reaction. The main purpose of the condensation reaction is to produce siloxane bonds $(\equiv Si-O-Si\equiv)$ from silanol groups. Condensation reactions produce dimmers, trimers, etc. and continue to build larger and larger silicon containing polymers or particles through the polymerization process. Then the formed particles link together to form chains, the networks that extend into the liquid medium and the solution thickens into a gel.[96] The structural properties of the porous silica materials depend on the relative rates of hydrolysis and condensation reactions and precipitation of siloxane oligomers, which are influenced by the catalyst employed in sol-gel reactions.[97] Details

of the mechanism of sol-gel process and the effects of several sol-gel process parameters on the structural properties of the final sol-gel material are discussed in Chapter 2.

Here, a two-step (acid-base) sol-gel process is used to prepare silica or organo-functionalized silica. In the latter case, extra restrictions are imposed because it is sometimes necessary to avoid rapid precipitation with organofunctional silanes. However, in both cases the polymerization mechanism is similar. In the two-step method, the sol-gel process is divided into an acidic step and a basic step. A two-step process is often selected to eliminate the possibility of phase separation and precipitation (common in base-catalyzed reaction) and to decrease the gelation time significantly relative to an acid-catalyzed reaction.[98] In this work HCl is used as a catalyst in the acidic-step and NaOH in the base catalyzed step. Acid catalyzes the hydrolysis much faster than condensation. Hydrolysis of multifunctional silanes, such as TEOS, under acidic condition is usually fast enough to reach to a pseudoequilibrium condition with an equilibrium coefficient of about 15-20.[99] It has been found that the extent of hydrolysis in the acidic-step strongly influences the gelation time in the basic-step.[97] The gelation time, which is defined as the time interval between the addition of base to the acidic mixture and the time when the fluid looses its fluidity completely, is inversely proportional to the HCl concentration.[100] An increase in hydrolysis rate constant has been found with the extent of hydrolysis of a monomer,[101, 102] which in turn has a linear relationship with the concentration of H^+ in acidic mixtures of TEOS, ethanol and water.[103] A longer acid-catalyzed step compare to that used in prior studies was selected here to allow not only the hydrolysis of TEOS to reach pseduoeqilibrium, but also the partial condensation of monomers to form small siloxane oligomers. With a short acid-step, mainly hydrolyzed monomers are present at the start of the base-step. These monomers rapidly precipitate after base addition to form large particles, which may produce meso / macro porous rather than micro / meso porous silica. For the acid step an HCl concentration of 0.01M, which corresponds to a pH value of 2.0, was used because gelation has been found to be extremely slow at this concentration.[104] When the pH value is close to the point-of-zero-charge (PZC) of silica, condensation is the rate limiting step. At moderate pH (~3.5-8) condensation is fast relative to hydrolysis and also at very high HCl concentration (pH<1), it has been found that sols gel quite rapidly due to increased condensation rates

but they also tend to be cloudy and heterogeneous due to precipitation of monomeric precursors.[104] The two-step procedure seeks to avoid this possibility by controlling the relative reaction rates of hydrolysis and condensation in each step.

In the second step, which is base-catalyzed, the condensation reaction is expected to be faster than in the acid catalyzed step because it has been found that bases catalyze condensation preferentially over hydrolysis above the isoelectric point of silica (pH ~ 2).[96] In the acid step under mild acidic condition, hydrolysis steps are fast but because they are at equilibrium, they have little influence on the development of the silica network.[105] In contrast during the base step, polymerization of both isolated and partially condensed molecules into macromolecules determines the nature and properties of the pores created in the final material.[105] At an intermediate pH value (~ 3.5-8), condensation is fast relative to hydrolysis.[96] Therefore gelation occurs rapidly in this pH range and gives rise to a mesoporous or micro/mesoporous silica gel. Gels prepared at pH less then 3.5 are typically microporous.[96] As the pH increases, silica precipitates with increasing particle size, and the gel time decreases. Thus the microstructure of the dried silica gels can be controlled by adjusting the pH during the second, base-catalyzed step of the two-step acid/base sol-gel process.

When amine-functional organosilane is added to the sol to modify the nature of the imprinted site, a one step acidic sol-gel process instead of a two-step process will be used. Amine group is basic in character and any increase in pH value beyond the point-of-zero-charge of silica (pH~ 2.0) in the presence of amine functional groups may lead to rapid condensation and precipitation. Even when the pH is adjusted, the amine-containing systems still gel reasonably quickly, so a two-step procedure is not required. Also, some silica gels have been prepared by a one-step acidic process when the goal is to prepare microporous material with a pore size based on the size and shape of the imprint molecule.

(a) Water to TEOS Molar Ratio: The water to tetraethyoxysilane (TEOS) molar ratio is a very important factor that significantly affects the structural properties of the final sol-gel product. A mole ratio of 2 is sufficient for complete hydrolysis and condensation.[97] However, because the hydrolysis equilibrium coefficient is only moderately large, an insufficient initial amount of water in the system may lead to incomplete hydrolysis

(especially in the presence of added ethanol).[106] Therefore in all experiments described in this chapter, a water to TEOS molar ratio greater than 2 is used. In the acid catalyzed system, the hydrolysis reaction has been found to be first order with respect to both TEOS and water concentrations.[107] Therefore an additional advantage to conducting the hydrolysis reaction with a water/TEOS molar ratio higher than the stoichiometric requirement is that the gelation time should decrease the in the base-step (due to faster, more complete hydrolysis). Note however that there is a limit to how much water is desirable. As the water/TEOS ratio is increased while maintaining a constant solvent/TEOS ratio, the TEOS is diluted, which reduces the rates of hydrolysis and condensation, leading to an increase in the gel time. Thus, there is an optimal amount of water for each concentration of TEOS to get a minimum gel time. Also for imprinting, it is desirable to avoid excess water, to minimize competitive hydrogen bonding with the silica network.

(b) Ethanol to TEOS Molar Ratio: The effect of the initial alcohol to TEOS molar on gelation kinetics is important. Ethanol acts as a mutual solvent to allow a mixture of water, TEOS and polymerization products to form a homogeneous mixture. However, dilution of TEOS with excessive ethanol increases the gel time by decreasing the rate of both hydrolysis and condensation. A second and important effect of excessive alcohol also is that it promotes the alcoholysis of siloxane bonds and silanols. Also because alcohols are protic solvents with a labile protons, they can influence the extent of the reverse reaction such as siloxane bond alcoholysis and hydrolysis.[96] Therefore, a balance in the alcohol-water-TEOS needs to be found to homogenize the solution and promote forward sol-gel reactions without promoting reverse reactions.

Gelation and Aging

In sol-gel processing, a gel will form from the sol after hydrolysis and condensation proceed for a certain period of time. Gelation happens as clusters of condensed silica species or colloidal particles grow through condensation into a network. Eventually a cluster of particles links together into a sample-spanning three-dimensional network, called the gel. At the gelation point, the viscosity of the sol increases sharply and the gel (a solid object) takes the shape of the vessel. The network formed has a large

enough elastic modulus that it can support a small stress, for example by tilting the vessel, without flowing. The sudden increase in viscosity with a loss of fluidity indicates the gel point, so the gelation time can be approximated (at least as a lower estimate) as the time at which the fluid looses its fluidity. While the gel point signals a dramatic change in connectivity of the network in the sample, hydrolysis and condensation are not complete, and they continue after the gelation point so that during aging, short chain polymers adhere to the gel.[96] This strengthens the gel, but also can create internal stress which causes a gel to shrink and react through a process called syneresis. In this way, the properties of the gel continue to evolve for a significant time after gelation.

As noted above, the synthesis pH plays an important role on the pore structure and the morphology of the gels by controlling the relative rate of hydrolysis, condensation and their reverse reactions, and this continues to be true after gelation. Gels prepared under mild acidic condition (pH<3.5) are microporous, whereas gels prepared at higher pH (~3.5-8) are mesoporous.[108] Silica has a greater dissolution rate in basic solutions due to deprotonation of silanols.[96] Depolymerization of siloxane bonds by alcoholysis (reverse of alcohol-producing condensation) and hydrolysis (reverse of water-producing condensation) occur in basic conditions, which facilitates the continual restructuring of the growing polymers to cause the formation of highly condensed colloidal particles. This leads to the redistribution of silica from low-molecular-weight polymers to high-molecular-weight polymers and particles. Therefore, gels formed at high pH tend not only to form as heterogeneous colloidal aggregates, but also to have walls that thicken during aging. The resulting materials are fairly stable towards drying and tend to produce mesoporous xerogels. At low pH condition, the rate of siloxane bond breaking is low, and the kinetics of condensation can be modeled as irreversible. Homogeneous gels form by slow condensation of small silicates and bond breakage and restructuring do not occur rapidly, which results in weakly branched gels.[104] Shrinkage during the drying of these weak gels usually gives microporous xerogels. The drying behavior of gels is discussed in Chapter 2.

6.3 Experimental

6.3.1Chemicals

Tetraethyl orthosilicate (TEOS) (98%) and tetramethyl orthosilicate (TMOS) (98%) were purchased from Fluka, and 3-aminopropyl- triethoxysilane (APTES) was purchased from Gelest. Deionized ultra-filtered water (DIUF), 6 N HCl, 0.1 N HCl, absolute ethanol, concentrated ammonium hydroxide (33.5-38%), and 0.1 N NaOH were purchased from Fisher Scientific. D-(+)-Glucose (99%) was purchased from Sigma Aldrich. All chemicals were used as received without any further purification.

6.3.2 Synthesis methods

(a) Synthesis of Non-functionalized Glucose Imprinted and Non-imprinted Silicas

Both the non-imprinted and glucose imprinted porous silica materials were prepared by the two step acid-base silica sol-gel method and dried under ambient conditions to produce xerogels. The same procedure was used to allow quantification of the effect of glucose imprinting on subsequent glucose adsorption. As an example of a typical synthesis procedure for non-imprinted silica, 15mL of TEOS was mixed with 14.7 mL of stock solution, which was prepared by mixing DIUF, ethanol and 0.1 N HCl in accordance with the following ratios: 12.2 vol% DIUF, 66.9 vol% ethanol, and 20.9 vol% 0.1 N HCl. This mixture of TEOS, water and ethanol gives a molar ratio of 1:4.0:2.5 and this specified amount of acid brings the solution pH to 2. HCl added during this step acts as a catalyst for hydrolysis of TEOS. This ratio of water to TEOS added in this step (including the water added with the dilute HCl solution) is called the acidic fraction and the basic fraction is the corresponding mole ratio of water to TEOS added at the beginning of the second base catalyzed step. Hydrolysis of silane precursors at a pH value of 2.0 (which is close to the isoelectric point of silica) is favorable because it allows hydrolysis to occur with only slow condensation in a one-phase system.[93] The only difference in the sample solution mixture to synthesize glucose imprinted silica was the addition of 1.57 g of D-glucose, which gives a D-glucose to TEOS molar ratio of 0.13. Glucose was added to the stock solution before adding TEOS, so that it had time to dissolve. The reaction mixture was allowed to react under acidic conditions at room temperature for 24 hrs under continuous stirring in a closed vessel. A longer acid

hydrolysis step was used than in prior studies to allow not only the complete hydrolysis of TEOS but also partial condensation to form polymeric or cage-like gel precursors. At the end of the 24-hr acidic hydrolysis step, different amounts of 0.1 N NaOH were added to obtain samples with different gelation times (as well as different pore structures). The second step is known as the base-step and the NaOH added at this point neutralized the acid initially present and raised the pH to induce rapid condensation of the precursors formed in the first step without the rapid precipitation observed in a one-step base-catalyzed sol-gel process.

The gels formed at the end of the base step were covered with parafilm with a few holes (~8-10) and were allowed to age at room temperature for 24 hrs to promote complete crosslinking. Following aging, the samples were dried for 48 hrs under mild vacuum (5 to 10 in Hg vacuum) at approximately 50°C.

Following drying, the glucose imprint molecules were extracted from the samples using DIUF water. First the samples were ground into fine powder. At each extraction step, 10 mL of DIUF water was added for every 0.5 g of dried powder and the suspension was gently stirred at room temperature for 24 hrs. Four to five extraction steps were performed to extract more than 99% of the imprint molecules. Centrifugation was performed at the end of the each extraction step, except the last one, to separate solids from liquid. After decanting the supernatant, the samples were placed in fresh DIUF water for the next extraction step. At the end of the last extraction step, solids were separated using vacuum filtration and washed with DIUF water, and then dried under vacuum in an oven at approximately 50° C for 24 hrs. The extent of template removal was observed by FTIR. The quantity of glucose extracted into the supernatant was measured at each step by either ATR-FTIR (for the first extraction step only) or a colorimetric assay (see below). To remove the residual ethanol from the non-imprinted samples, finely ground powders were immersed into a large amount of DIUF water under agitation for a couple of hours. At the end of this step, vacuum filtration was used to separate the solids. Then the non-imprinted materials were dried at 50°C for 24 hrs. After drying, both imprinted and non-imprinted samples were analyzed by nitrogen sorption, after degassing at 150 °C for 4 hrs, to characterize their pore structures.

(b) Synthesis of glucose imprinted and non-imprinted amine functionalized silicas

In addition to studying the glucose adsorption properties of silicas formed via hydrolysis of TEOS alone, it was desired to determine how the incorporation of amine functional groups of silica would affect the pore structure as well as glucose adsorption properties. Amine functionalized porous silicas were synthesized by one pot co-condensation of TEOS and aminopropyltriethoxysilane (APTES) under acidic conditions. In a typical synthesis process for glucose imprinted amine functionalized silica, 10 mL of TEOS, 1.05 mL of APTES and 6.55 mL of EtOH were mixed together in a glass beaker. The mixture was stirred vigorously and acidic water containing glucose was added quickly to protonate the $–NH_2$ group of APTES. Acidic water was prepared by dissolving 1.5 g of D-glucose into a mixture of 3.39 mL of DIUF water and 1.87 mL of 6.0 N HCl. The final molar composition of the reaction mixture was 1 TEOS: 0.10 APTES: 0.15 HCl: 2.5 EtOH: 6.0 H_2O: 0.13 D-glucose. The basic character of the amine group of APTES catalyzes the hydrolysis of TEOS and APTES.[24] Rapid hydrolysis, which causes fast gelation or precipitation, was prevented by protonating $–NH_2$ groups with a strong acid. Initially, the reaction mixture was not clear, but within ~1-2 min it became clear. The resulting reaction mixture was continuously stirred in a covered glass beaker for 24 hr at ambient temperature. After this sol aging period, the pH of the sol was raised to close to 2 (~1.9) by adding 0.1N NaOH dropwise. The sol was then transferred into a Petri dish covered with paraffin film with ~8-10 pinholes and allowed to gel under ambient conditions. Upon gelation and aging for 24 hrs at room temperature, the sample was dried for 4 days at approximately 38°C in a vacuum oven (a vacuum pressure of ~5-10 inHg was maintained). Following oven drying, the sample was ground into a powder and glucose was extracted using water extraction as described in section 2.2(a). Water extraction was continued until the glucose concentration in the extracting solvent measured by phenol-sulfuric acid assay method was negligible.

Non-imprinted amine functionalized silica materials were also synthesized under identical experimental conditions without adding any glucose template. Trapped residual ethanol was extracted from samples by stirring with DIUF water for a couple of hours.

Vacuum filtration was used to separate solids from the solvent. Before drying, all amine functionalized materials were deprotonated to generate reactive amino function

groups on silica surface by ammonia post synthesis treatment. This was done by dipping samples in a dilute (~0.001N) ammonia aqueous solution for 30 min.

(c) Synthesis of Glucose Imprinted and Non-imprinted Thin Films

In addition to studying the effectiveness of glucose molecular imprinting in bulk silica, it was also desired to see how glucose imprinting of thin silica films would affect their recognition ability for the imprint molecule in aqueous solution. Films were prepared by dip coating dilute acidic sols onto borosilicate glass substrates (22 mm x 75 mm). Before coating, all glass substrates were cleaned with a NoChromix solution. NoChromix was purchased from Fisher Scientific and the cleaning solution was prepared by completely dissolving a packet (17 g) powder in 500 mL of concentrated H_2SO_4 (96-98 wt%). All slides were dipped into this cleaning solution for 30 min, followed by 30 min in water to remove any contamination from the surface. Finally, the slides were given a final rinse with acetone and dried with a heat gun. The coating solution used for dip-coating was prepared following the procedure of Lu et al.[86] First a sol containing a 1: 3.8: 1 molar ratio of TEOS: EtOH: H_2O was hydrolyzed under acidic conditions at 70°C for 90 min. The pH value of the sol was set at 4.0 by adding HCl. After this initial hydrolysis period, the additional water and HCl were added, decreasing the pH value to 2.0 and adjusting the total TEOS: H_2O ratio to 1:5. For the imprinted thin films, D-glucose with a molar ratio of 1 TEOS: 0.13 D-glucose was dissolved into the acidic water that was added to the pre-hydrolyzed sol at this stage. After stirring this mixture at 25 °C for 30 min, the sols were aged at 50°C for 15 min. The final step before coating was to dilute the aged sol under constant stirring to give the final molar ratios of 1 TEOS: 22.5 EtOH: 5 H_2O: 0.13 D-glucose. Both the imprinted and non-imprinted films were prepared by dip coating with their respective sols onto glass substrates withdrawn at 7.6 cm/min. The films were then dried first at ambient temperature for 24 hrs and then at 50°C for another 24 hrs in an oven. Water extraction was used to remove the template molecules. Two to three extraction steps were required to extract the glucose molecules completely. At each extraction step, slides where simply dipped into a beaker of DIUF. To observe the extent of glucose removal, thin films were prepared on silicon wafers using the same procedure and FTIR was used to see how many extraction steps were required to remove

template molecules completely within the limits of detection of the instrument. Only when template removal was complete were thin films used for adsorption studies.

6.3.3 Glucose Adsorption Experiments

The glucose adsorption experiments were conducted in a batch reactor, where a measured amount of either glucose molecular-imprinted porous silica or non-imprinted porous silica was added to a certain amount of aqueous D-glucose solution. Imprinted silica from which more than 99% of the template was extracted was used in the glucose adsorption experiments. The main purpose of this experiment was to establish the adsorption isotherm of glucose from aqueous solution onto the porous silica samples. D-glucose aqueous solutions of different concentration were mixed with imprinted or non-imprinted silica powders and allowed to stand for five hours under continuous gentle stirring. Filtered aliquots were taken periodically to determine the amount of glucose adsorbed by the sample. The adsorption capacities were calculated as follows:

$$glu\cos e\,adsorbed\,(g/m^2) = \frac{(C_o - C_f)V_s}{m_{SiO_2}S_t}(180.16) \qquad (6.1)$$

where, C_o and C_f are the initial and final glucose concentrations (M) in the sample solution used, V_s is the volume (mL) of test solution, m_{SiO_2} is the amount of silica sample used (mg), and S_t is the total specific surface area of the silica sample. All suspensions were centrifuged before sampling to separate solid silica from aqueous solutions of glucose. To collect filtered aliquots, syringe filters with 0.02μm pores (Whatman Anotop Disposable Syringe Filter purchased from Fisher Scientific) were used. Removal of silica is important for accurate quantification of the glucose concentration. Initially, a kinetic adsorption experiment was performed to know approximately how long the imprinted silica takes to reach adsorption equilibrium. Adsorption experiments were conducted in two different glucose concentration ranges. The dilute concentration range was from 25 μg/mL to 200 μg/mL, where glucose concentrations were assayed by the phenol-sulfuric acid colorimetric assay at 485 nm using a HP-8453 UV-vis spectrophotometer.[282] For the higher concentration range, which was from 0.1M to 0.45M, glucose concentrations were determined by ATR-FTIR.

6.3.4 Methods

(a) Fourier Transform Infrared (FTIR) Spectroscopy

Fourier transform infrared (FTIR) spectroscopy in the mid-infrared (MIR) range coupled with an attenuated total reflectance (ATR) accessory was used to quantify glucose in aqueous solutions. Glucose concentration in highly absorbing liquids, such as aqueous solutions, can be measured accurately by ATR because the IR beam penetrates the sample only a short distance (1-50 μm), which means the effective path length is short. The path length of transmission IR is usually too long for this application, and strong water absorption bands would obscure the characteristic peaks from glucose. The infrared spectra were collected with a ThermoNicolet Nexus 470 FT-IR spectrometer equipped with a deuterated triglycine sulphate (DTGS) detector (spectral range 4000-650 cm^{-1}) and potassium bromide (KBr) beam-splitter. In order to get a satisfactory signal-to-noise ratio, 128 scans at 4 cm^{-1} resolution were used. The instrument was purged with nitrogen gas to suppress spectral contributions from atmospheric carbon dioxide and water vapor. The IR beam from the spectrometer was directed into the horizontally aligned zinc selenide (ZnSe) internal reflection element at a 45° angle of incidence. Under these experimental conditions, the sample on the crystal was exposed to 12 reflections with a penetration depth of 2.0 μm.

For ATR-FTIR experiments, a background spectrum was first collected with the ZnSe crystal in contact with air. Then MIR absorption spectra of aqueous glucose solutions were collected after pouring samples onto the crystal. Since mid-infrared ATR spectroscopy is not an inherently quantitative method, a calibration curve, (Figure 6.2) was generated for glucose using a wide range of concentrations. In the 950-1200 cm^{-1} region, the MIR spectrum of glucose in aqueous solution can be characterized by five absorbance bands, located at ~992, 1035, 1080, 1107, 1150 cm^{-1}, as shown in Figure 6.3(a). These bands are assigned to C-O stretching vibrational modes.[283] Two pronounced peaks at ~ 1035 and 1080 cm^{-1} arise from C_1-O_5 stretching. C_1-O_1 stretching contributes the band at ~1150 cm^{-1} and the remaining two bands are from the other C-O stretching modes. Typical FTIR-ATR spectra of aqueous glucose solutions showing the fingerprint region used for calibration purpose are shown in Figure 6.3(a). The water spectrum was subtracted from that of glucose to remove the spectral contribution of the solvent.

Difference spectra of glucose are shown in Figure 6.3(b). Integrated intensities under the above mentioned fingerprint peaks (~950-1184 cm^{-1}) were used for quantification purpose. ATR analysis was used for aqueous glucose solutions with concentrations above 0.025 M. Below this concentration, the peaks observed are too weak to quantify accurately.

(b) Colorimetric Glucose Determination Method

A colorimetric technique was used to quantify glucose in dilute aqueous solutions. As noted above, the ATR-FTIR method is best for aqueous glucose solutions with concentrations higher than 0.025 M. Below this concentration, the colorimetric method was used. The method was originally developed to determine submicrogram amounts of sugars. The method works best for glucose concentrations between 50 μg/mL and 200 μg/mL, so higher concentrations were diluted prior to analysis. The analytical method was developed by Dubois et al.[282] In this method, sulfuric acid reacts with glucose and a fixed amount of phenol to produce products with a stable orange-yellow color. A HP 8453 UV-vis Spectrophotometer was used to determine the absorbance of the mixture at 485 nm, which is the peak absorption for products of the glucose reaction, as illustrated in the characteristic curves of the products of the Dubois assay measured with various concentrations of glucose shown in Figure 6.4(a). Figure 6.4(b) provides a calibration curve generated with a series of standard glucose aqueous solutions by this method.

(c) Nitrogen Physisorption

One of the characteristic properties of a sol-gel material is its pore structure. Nitrogen adsorption-desorption isotherms of samples were measured to obtain information about specific surface area and pore structure parameters. Isotherms were measured at 77K with a Micromeritics Tristar 3000 automated nitrogen adsorption instrument using the static volumetric determination technique. Before measurement, all the samples under study were degassed at 150°C for 4 hrs. Specific surface areas of the finely divided porous materials were evaluated using the standard Brunauer-Emmett-Teller (BET) method. The BET monolayer capacity was estimated using the relative pressure data in the range from 0.05 to 0.2. The commonly used value of 0.162 nm^2 as

the molecular cross-sectional area of N_2 on silica material assuming hexagonal packing was used to estimate the specific surface area of the material.[5] The pore size distribution (PSD) was calculated using the Barrett-Joyner-Halenda (BJH) method.[125] The adsorption branch rather than desorption branch was used to calculate the PSD.[127] In order to improve the reliability of the BJH method used in this study a correction for the statistical film thickness on pore walls was incorporated with the Kelvin equation to evaluate the PSD in the pore size range 0.5-300 nm.[131] The Harkins-Jura statistical film thickness equation was used here.

Structural properties including micropore volume (V_{mi}), total surface area (S_t), primary mesopore volume (V_P), and external surface area of the samples (S_{ex}) were determined here using the high resolution α_s-plot method.[124, 134] In the α_s-method, the amount adsorbed on the porous material under study is plotted against the reduced standard adsorption α_s. α_s is defined as $\alpha_s = V_{ref}(p/p_O)/V_{ref}(0.4)$, where $V_{ref}(p/p_O)$ is the amount adsorbed on the reference material as a function of the relative pressure p/p_O, and $V_{ref}(0.4)$ is the amount adsorbed at the relative pressure of 0.4. In this study, literature data for Li-Chrospher Si-1000 silica gel with BET surface area of 25 m^2/g were used to prepare α_s plots.[133] Total pore volumes were calculated using single point nitrogen adsorption data close to the saturation point.

6.4. Results and Discussion

6.4.1 Materials Characterization

All of the materials synthesized here are characterized using BET surface area analysis, and in some cases FTIR spectroscopy.

(a) Glucose imprinted and non-imprinted non-functionalized silicas

Porous dried silica gels with varying degrees of microporous and mesoporous character were synthesized using the two-step acid-base silica sol-gel process. As mentioned in the experimental methods, the gelation time was controlled by using different amounts of 0.1N NaOH in the base-step, and is expected to be correlated with changes in the pore structure of the final dried gels. To explore the range of pore sizes

available by this approach, the structural properties of non-imprinted dried silica gels prepared from sols made with 3.0, 3.5, 4.0, 5.0, and 7.0 mL of 0.1 N NaOH were studied. The relationship between gelation times and the amount of 0.1N NaOH added to induce gelation is shown in Figure 5. For all of these samples the molar ratio of TEOS: water (acidic fraction): ethanol was maintained at 1.0: 4.0: 2.5 with a fixed concentration of HCl (0.01 M) corresponding to a pH value of 2. The base catalyst was added at the end of the 24 hr hydrolysis step. A relatively long acid-catalyzed step was used compared to prior studies to allow not only the complete hydrolysis of TEOS, but also the partial condensation to form small oligomers and cage-like gel precursors. Gelation times were long for samples made with small amount of 0.1N NaOH and decreased faster than exponentially as the amount of base catalyst was increased. In all the cases, transparent gels with no bubbles were formed except the gel formed with 7.0 mL of base catalyst, where some bubbles generated either by the sample itself or trapped due to stirring were observed. In keeping with the greater-than-exponential drop in gel time, a sharp difference in gelation time was observed between 3.0 mL and 3.5 mL of added 0.1 N NaOH, while the rest of the gel time decreases only slightly beyond tht point..

The porosity of the samples prepared with 3.0, 4.0, 5.0, 7.0 mL of 0.1N NaOH were analyzed by nitrogen adsorption isotherms. The nitrogen adsorption-desorption isotherms and corresponding modified BJH pores size distributions of these four samples are shown in Figure 6.6. The isotherm for the sample prepared with 3 mL of 0.1N NaOH is clearly of Type I with no indication of a hysteresis loop. This indicates that the sample is microporous or non-porous. Increasing the amount of 0.1N NaOH from 3 mL to 5 mL causes a qualitative change in the N_2 sorption isotherm from Type I to Type IV with H2 type hysteresis loop, as shown in Figure 6.6(a). This type of triangle shape hysteresis loop with a steep desorption branch has been attributed to the presence of narrow-mouthed (ink-bottle shaped) pores.[127] The area traced out by the H2 hysteresis loop becomes greater and the closing point moves toward a higher relative pressure as the amount of added 0.1 N NaOH increases. This indicates an increase in primary mesopore volume as the amount of 0.1 N NaOH increases from 4 mL to 7 mL, as shown in Table 6.2. The structural characteristics derived from the isotherms are shown in Table 6.2. As the pore volume increases in this series, the corresponding BET specific surface area

decreases from 746 m^2/g to 531 m^2/g. Consistent with the increase in relative pressure at which capillary evaporation takes place, quantitative α_s plot analysis indicates an enlargement of pore size as more base is used to induce gelation.[124] Broadening of hysteresis loop with more base could be due to increasingly nonuniform pore structure, and possibly poor connectivity between pores. A broad pore size distribution is observed for all the samples, as shown in Figure 6.6(b).

Based on the studies of the effect of NaOH on gel time, a moderate amount of NaOH that gives substantial mesoporosity and some microporosity was selected to synthesize D-glucose imprinted silica- 5 mL of 0.1 N NaOH. The added amount of glucose gives a molar ratio of D-glucose: TEOS of 0.13. This amount should give a theoretical template content of 28 wt% in the final dried product based on the amounts used as the starting materials, if it is assumed that all ethoxy groups are hydrolyzed and that all volatile compounds (ethanol, water) evaporate during drying. However, the actual template content was found to be 25.5 wt%, which was calculated based on the initial amount of glucose used and the mass of non-imprinted silica obtained with the same starting sol. The difference is most likely due to entrapment or binding of solvent within the silica gel. Four to five extraction steps with distilled water were found to be necessary to remove more than 99% of the glucose template. The extent of template removal by water was quantified by ATR-FTIR measurements and phenol-sulfuric acid assays of the aqueous extraction medium. Glucose removal was also monitored from the IR spectra of dried solid samples pressed into KBr pellets, as shown in Figure 6.7. The removal of glucose template could be confirmed by a comparison of the IR spectra between the as-synthesized and extracted silica. The appearance of two bands at ~2925 and ~2854 cm^{-1}, compare to non-imprinted pure silica materials, due to the asymmetric and symmetric vibrations of $–CH_2$ group respectively can be attributed to the presence of glucose in silica, as shown in the IR spectrum of the as-synthesized silica.[284] Decrease in the intensity of theses two bands after the 2nd extraction, as shown in Figure 6.7(b), indicates the partial removal of glucose. The complete disappearance of C-H absorption peaks indicates the complete removal of glucose template, although there may be residual ethoxy groups still present even after complete extraction. Other bands between 400 and 1200 cm^{-1} are mainly due to either Si-O-Si or Si-OH vibrational modes in the silica

network. For instance, the bands near 1225 and 1085 cm^{-1} are associated with Si-O-Si asymmetric bond stretching; the band around 801 cm^{-1} is due to symmetric Si-O-Si bond stretching; and the band at ~473 cm^{-1} is associated with Si-O-Si bond bending.[285] A relatively weak band in the range of 940-960 cm^{-1} is due to stretching of noncondensed Si-OH bonds. The broad band around 3400 cm^{-1} is due to the vibrations of OH in molecular water and H-bonded silanols.[284]

The nitrogen adsorption-desorption isotherm for this D-glucose imprinted sample after removal of the glucose template and the corresponding BJH pore size distribution are shown in Figures 6.8(a) and Figure 6.8(b), respectively. The sample has a Type IV isotherm with H2 hysteresis loop. The calculated BET surface area is 603 m^2/g and, based on calculations from the α_s-plot (not shown here), the sample has a micropore volume of 0.01 cm^3/g, a mesopore volume of 0.51 cm^3/g, and total surface area of 533 m^2/g. The gel drying condition used for the non-imprinted silica samples was 50 °C for 48 hrs under mild vacuum. This moderate temperature of 50 °C was used because of imprinted glucose molecules to avoid dehydration or browning reactions of glucose. When the non-imprinted silica gels used in glucose adsorption experiments were dried at the same experimental conditions used for the imprinted silicas, a BET specific surface area of 867 m^2/g was measured and based on α_s-plot analysis, the total specific surface area was found to be 830 m^2/g. The micropore and mesopore volumes of this non-imprinted silica material were calculated to be 0.003 cm^3/g and 0.61 cm^3/g, respectively. The nitrogen sorption isotherm and the corresponding BJH pore size distribution derived from its adsorption branch are shown in Figure 6.8(a) and 6.8(b) along with their counter part from glucose imprinted sample. The non-imprinted sample also has a Type-IV isotherm. Average pore sizes of the glucose imprinted and non-imprinted samples calculated from the BJH pore size distributions are found to be 2.9 and 1.6 nm, respectively.

(b) Glucose imprinted and non-imprinted amine functionalized silicas

In addition to studying the glucose adsorption properties of silica samples formed with only TEOS, a goal of this chapter was also to clearly determine how amine functionalization affects the pore structure and glucose adsorption properties of silica.

Both glucose imprinted and non-imprinted amine-functionalized porous silicas were synthesized by one pot co-condensation of TEOS and aminopropyltriethoxysilane (APTES) under acidic conditions. Figure 6.9 shows the FTIR spectrum of a non-imprinted sample prepared with 10 mol% of APTES with respect to TEOS in comparison with the spectrum of non-functionalized, non-imprinted silica. There are three distinguishable bands in the spectrum of the amine-functionalized sample. The first band near 687 cm^{-1} is due to N-H bending vibration; the second band is around 1510 cm^{-1} which is due to the symmetric $–NH_2$ bending vibration, and the third distinguishable broad band near ~2700-3400 cm^{-1} is attributed to the NH_2 stretching vibration.[286] The presence of these three bands in the IR spectrum of the amine-functionalized silica is consistent with the incorporation of amino groups in the sample.

Nitrogen sorption isotherms and BJH pore size distributions of the amine-functionalized D-glucose imprinted sample after template removal and of the dried amine-functionalized non-imprinted sample are shown in Figures 6.10 and 6.11, respectively. For the imprinted functionalized silica, a type IV isotherm with H2 hysteresis loop is observed (Figure 6.10). It implies the presence of uniform narrow-mouthed mesopores which is confirmed from the BJH pore size distribution in the inset of Figure 6.10. The calculated BET specific surface area of the sample was found to be 602 m^2/g. The nitrogen sorption isotherm of the non-imprinted functionalized material is of type I with textural porosity, which usually arise from microporous or nonporous solids.[127] The latter is more likely to be the case, as suggested by the very small specific surface area (7 m^2/g) and total pore volume (0.004 cm^3/g). Because of the small absolute area of the sample, the hysteresis loop does not appear to close in Figure 6.11, but this is an instrumental artifact.

6.4.2 Glucose Adsorption

The number of silanol groups present on silica surface strongly influences the chemical properties of silica. As silica is heated at different temperatures, the number of OH groups per unit area changes. The number of OH groups on silica surface is the highest if it is not treated at temperature higher than 100 °C and they are found as isolated geminal, and vicinal silanol groups.[287] If silica is heated at 100- 200 °C to desorb

moisture, partial dehydroxylation of OH groups occurs that reduces the number of OH groups. At this condition silica surface has mainly strongly hydrogen-bonded and isolated silanols. As the heat treatment continues to increase, dehydroxylation is expected to continue. In the temperature range of 200-400 °C, the vicinal OH groups react and form isolated silanols. At temperature higher than 600 °C the silica surface is mainly covered with isolated silanols, which interact with one another to form stable siloxane bridges at a temperature of 600-800 °C. The number of OH groups and their organization on the silica surface are important for glucose adsorption on silica. That is why no sample used for glucose adsorption study was heated to more than 100 °C during the synthesis process.

Here, two different glucose concentration ranges were used to conduct glucose adsorption experiments for the both imprinted and non-imprinted silica samples. For the dilute concentration range (0.3 mM to 1.4 mM) the phenol-sulfuric acid assay method was used to quantify glucose in aqueous solution. For the higher concentration range (0.1 M to 0. 4 M) the ATR-FTIR method was used to determine the glucose concentration. Figure 6.12 shows the D-glucose adsorption isotherms developed with the non-functionalized glucose imprinted and non-imprinted silica samples for both concentration ranges. The BET specific surface area of each sample was used to normalize the results so that differences would not be observed due to the amount of imprinted and non-imprinted silica used in the adsorption experiments. We have seen that a non-imprinted silica sample has a higher BET specific surface area than its analogous glucose imprinted sample, 867 m^2/g compare to 603 m^2/g (described in Section 6.4.1(a)). The results in Figure 6.12(a) show that glucose imprinting is not very effective at improving the affinity for glucose adsorption. The imprinted and non-imprinted samples show approximately equal levels of adsorption per unit of surface area. Figure 6.12(b) indicates a small difference in the amounts of glucose adsorbed onto the imprinted and non-imprinted silica samples at higher glucose concentrations. These results are contrary to the expected trend (the glucose imprinted sample adsorbs more glucose) and the opposite of the earlier trend reported by Elswick [*P. Elswick, M.S. Thesis, University of Kentucky 2005*] for sol-gel silica prepared by a two-step route. Contributing factors to the differences observed are the non-specific binding and the weak interaction between saccharides and silica. Silica surface in the presence of excess water at room temperature is usually covered with

multilayers of physically adsorbed water, bounded by hydrogen bonding.[288] Most likely hydrogen bonding between the hydroxyl groups of glucose molecules and the hydroxyl groups of silica alone is not strong enough in an aqueous solution to remove the adsorbed water molecules in order to strongly bind the imprint molecule. Also in Section 6.4, we have seen that multiple extraction steps (~ 4-5) were required to remove the imprinted glucose molecules completely. This long time washing might have changed the required pre-determined orientation of the functional groups on silica surface, determined by the interactions between glucose and hydroxyl groups of silicates during imprinting process, for selective adsorption. As a result, the observed trends are highly dependent on the sample preparation procedures, and the thorough washing and removal of imprint molecules performed here may have changed the silica structure sufficiently to reverse the observed adsorption trend, in the presence of non-specific binding comparable to the imprinting-induced binding.

Figure 6.13 shows the glucose adsorption isotherms developed with the amine-functionalized non-imprinted and imprinted silica samples in the dilute concentration range. The non-imprinted silica containing amino groups adsorbs much more glucose per unit area than either non-functionalized silica sample. However, the level of glucose adsorption per unit area for the glucose-imprinted functionalized material is only slightly higher than in the imprinted non-functionalized material. Improved binding is expected because the interaction between an amine group and a hydroxyl group is stronger than that between two hydroxyl groups. However, the high level of glucose adsorption in the non-imprinted material indicates poor effectiveness of non-covalent imprinting of amine-modified silica with glucose. This may mostly reflect the availability of amine functional groups relative to the pore area; recall that the amino functionalized non-imprinted material had very little surface area (~7 m^2/g) and even a small amount of glucose adsorption indicates that amino groups at the external particle surface are effective at adsorbing glucose from solution. The trend was observed from the glucose imprinted and non-imprinted amine functionalized materials at the high glucose concentration range, as shown in Figure 6.14. The levels of glucose adsorption per unit mass of the amine functionalized imprinted and non-imprinted materials are not significantly different, but

when the adsorption levels are normalized with their respective specific areas, they become significantly different.

The results of the rebinding experiments of glucose molecule to the extracted glucose imprinted and non-imprinted thin films in the lower concentration range are presented in Figure 6.15. The adsorption levels are reported in this case on an absolute mass scale because of the limitation to the determination of the specific surface area of the thin films. As in the bulk samples, the levels of glucose bindings on the non-imprinted films and glucose imprinted films are not statistically different.

6.5 Conclusions

In this chapter, procedures were developed to prepare series of D-glucose imprinted and non-imprinted silica gels by a 2-step acid/base sol-gel procedure with fine control over the pore size distributions of the resulting materials. More limited control was available with amine-functionalized materials, but a method was developed for also preparing D-glucose imprinted and non-imprinted aminosilica by a one-step procedure. Analytical techniques were developed to accurately measure glucose removal from and D-glucose adsorption onto the porous silica-based materials.

Based on the outcomes of the glucose binding experiments with D-glucose imprinted and non-imprinted non-functionalized samples, it seems that hydrogen bonding between the hydroxyl groups of glucose molecules and the hydroxyl groups of silica alone is not strong enough in an aqueous solution to strongly bind the imprint glucose molecule. In this situation this is probably because hydrophilic vicinal and geminal silanols are the only potential binding groups on the silica surface. During glucose rebinding experiments with the D-glucose imprinted and non-imprinted amine ($-NH_2$) functionalized materials, it is found that the comparatively stronger hydrogen bonding between the amine functional group and the hydroxyl groups of glucose increases the glucose binding affinity over that of non-functionalized silica. However, the non-specific nature of this binding still limits the selectivity of the materials toward D-glucose. This non-specific adsorption of glucose at the outer surface of silica particles plays a significant role in the results that are observed, and that the accessibility of glucose

molecule to the imprinted pores may be limited. Consistent with this, it was found that specific areas of functionalized imprinted and non-imprinted silica gels differ significantly: 602 m^2/g for the amine functionalized imprinted gel and 7 m^2/g for the amine functionalized non-imprinted gel. However it is possible to get a porous non-imprinted silica gel, when no organic group is introduced. This suggests that the flexibility imparted to the silica network by the organosilane makes the resulting material almost nonporous in the absence of any imprint molecule.

Table 6.1. Examples of successful non-covalent molecular imprinting of silica.

Imprint Molecule(s)	Inorganic Precursors (Types of organic functional groups)	Major Findings	Ref.
Dopamine (DA)	TMOS, PTMOS, MTMOS (phenyl, methyl)	• Imprinted thin films showed greater affinity for DA over that of structurally related molecules. • Non-imprinted thin films showed little to no affinity for DA.	[16]
Propranolol, 2,2,2-trifluro-1-(9-anthryl)-ethanol & dopa	TEOS, PTMOS, MTMOS, APTES (phenyl, methyl, amine)	• Synthesized thin films with chiral discriminative recognition abilities. • Levels of adsorptions on imprinted films were 8-11 times higher than that on non-imprinted films.	[270]
Uranyl ion	TMOS	• Imprinted silica material showed greater affinity and selectivity toward the imprint molecule over the non-imprinted material.	[289]
Both metal ions and CTAC micelles	BTSE, (TMS)en (ethylenediamine)	• The formation of coordination complexes between the bifunctional organosilane and divalent metal inos and their sunsequent coupling into the silica network helped to form pores with enhanced recognition properties for the metal ion templates. • Imprinted sorbents showed higher levels of adsorptions of the imprinted metal ions compare to non-imprinted analogues.	[290]
DDT	BTEB	• Covalent imprinting has been found to be better than non-covalent imprinting with the same imprint molecule considering the selectivity for the same molecule.	[291]

Abbreviations: TMOS: tetramethylorthosilicate; TEOS: tetraethylorthosilicate; PTMOS: phenyltrimethoxysilane; MTMOS: methyltrimethoxysilane; APTES: 3-aminopropyltriethoxysilane; BTSE: 1,2-bis(triethoxysiyl)ethane; BTEB: bis-(trimethoxysilylethyl)benzene; (TMS)en: N-[3-(trimethoxysiyl)propyl]ethylenediamine; CTAC: cetyltrimethylammonium chloride; DDT: 1,1-bis(4-chlorophenyl)-2,2,2-trichloroethane.

Table 6.2. Structural properties of some non-imprinted silicas.

Amount of 0.1N NaOH added (mL)	t_g (min)	S_{BET} (m^2/g)	V_t (cm^3/g)	V_{mi} (cm^3/g)	S_t (m^2/g)	V_p (cm^3/g)	S_{ex} (m^2/g)
3.0	83.0	548	0.27	0.23	55	0.03	8.6
4.0	4.5	746	0.44	0.008	670	0.37	19.2
5.0	3.0	680	0.54	0.005	597	0.51	14.7
7.0	1.4	531	0.72	0.0	486	0.70	10.9

Symbol used: t_g:gelation time; S_{BET}: BET surface area; V_t: total pore volume; V_{mi}: micropore volume; S_t: total surface area; V_p: primary mesopore volume; S_{ex}: external surface area.

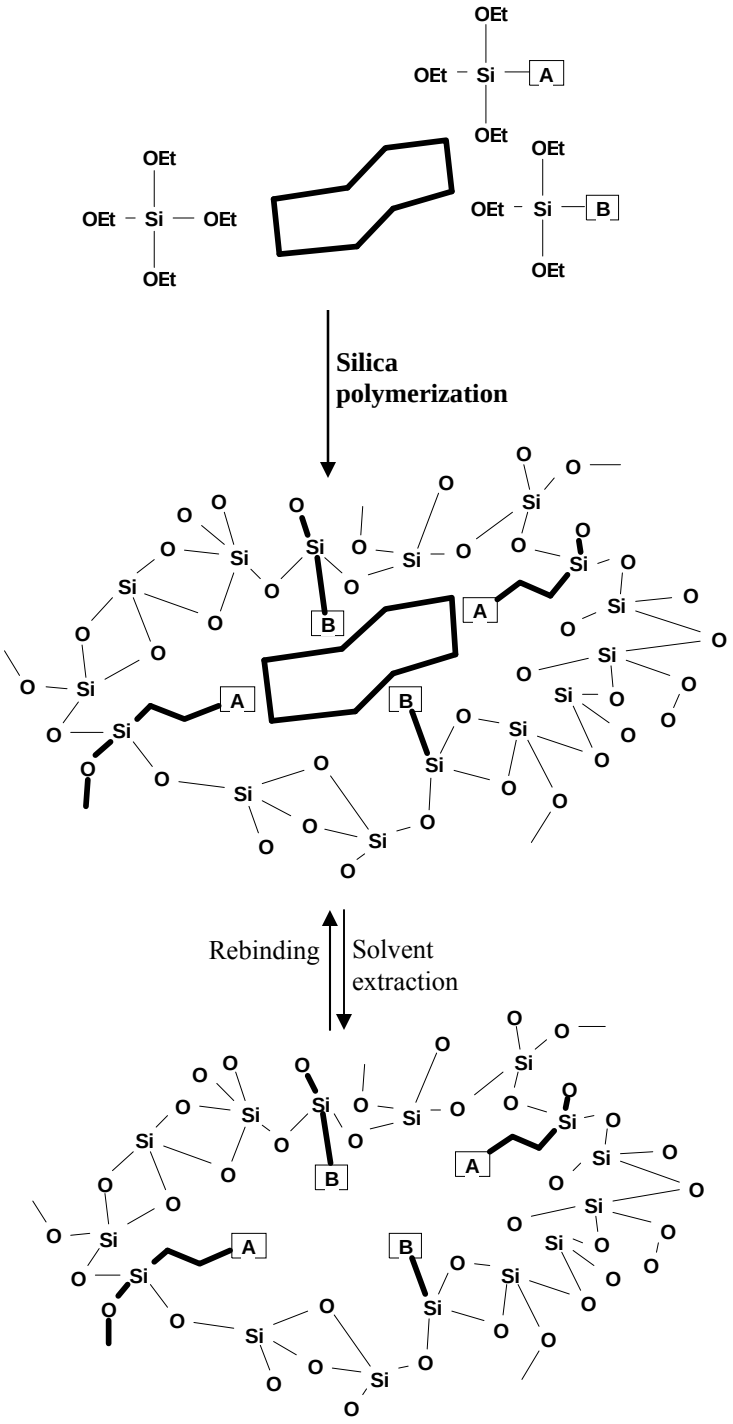

Figure 6.1. Schematic representation of the formation of recognition cavity into the silica matrix by non-covalent molecular imprinting. A and B could be different organic functional groups with silanes, such as -$CH_2CH_2CH_2NH_2$ or -$CH_2CH_2CH_2NHCONH_2$.

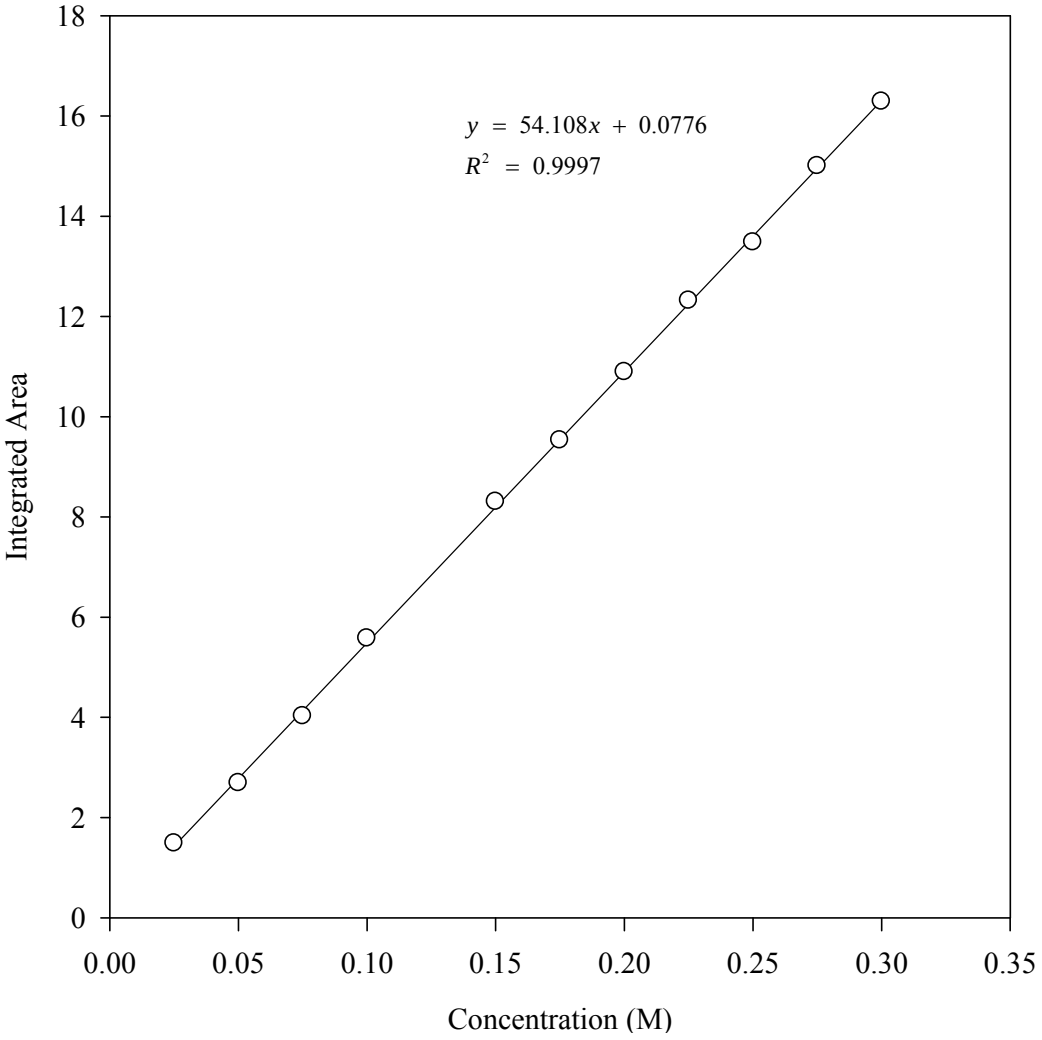

Figure 6.2. FTIR-ATR Calibration curve of aqueous glucose solution

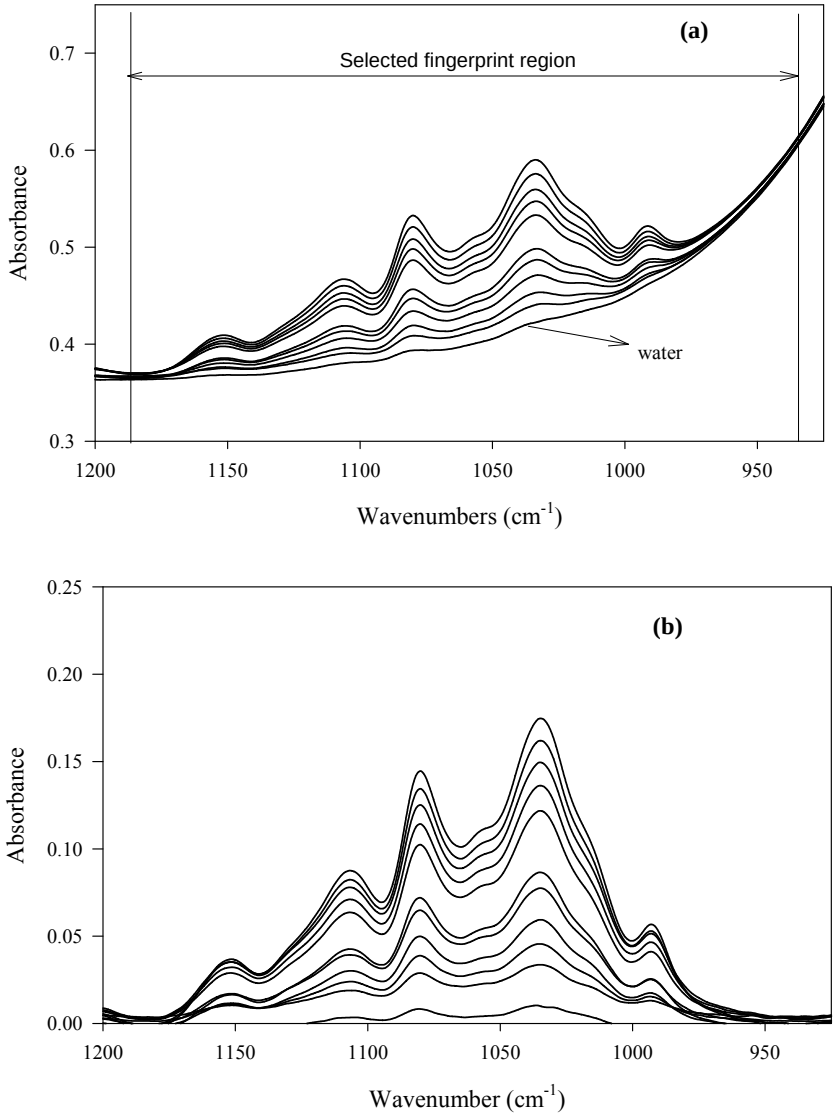

Figure 6.3. FTIR-ATR absorption spectra of aqueous glucose solutions used to construct calibration curve. (a) Spectra of nine different aqueous glucose samples ranging from 0.025M to 0.35M with water spectrum, and (b) difference spectra of the same samples when spectrum of water subtracted from that of different glucose solutions.

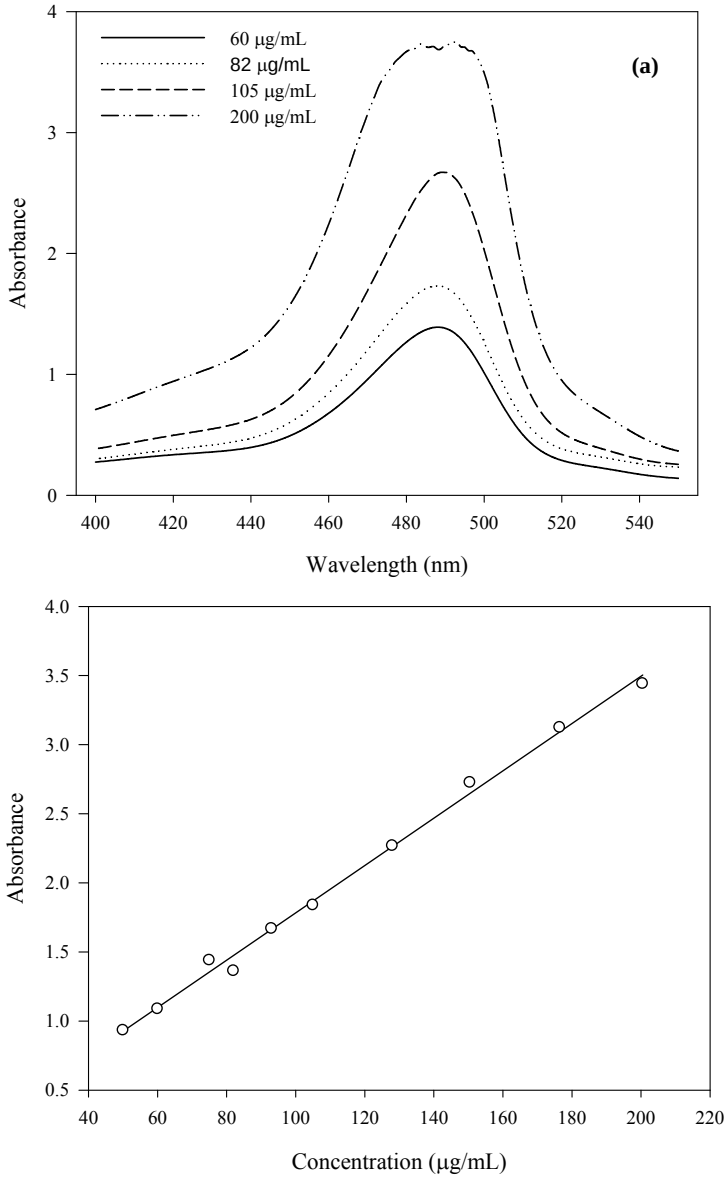

Figure 6.4. Results of the colorimetric glucose assay. (a) Characteristic absorption curves of D-glucose, and (b) calibration curve for D-glucose.

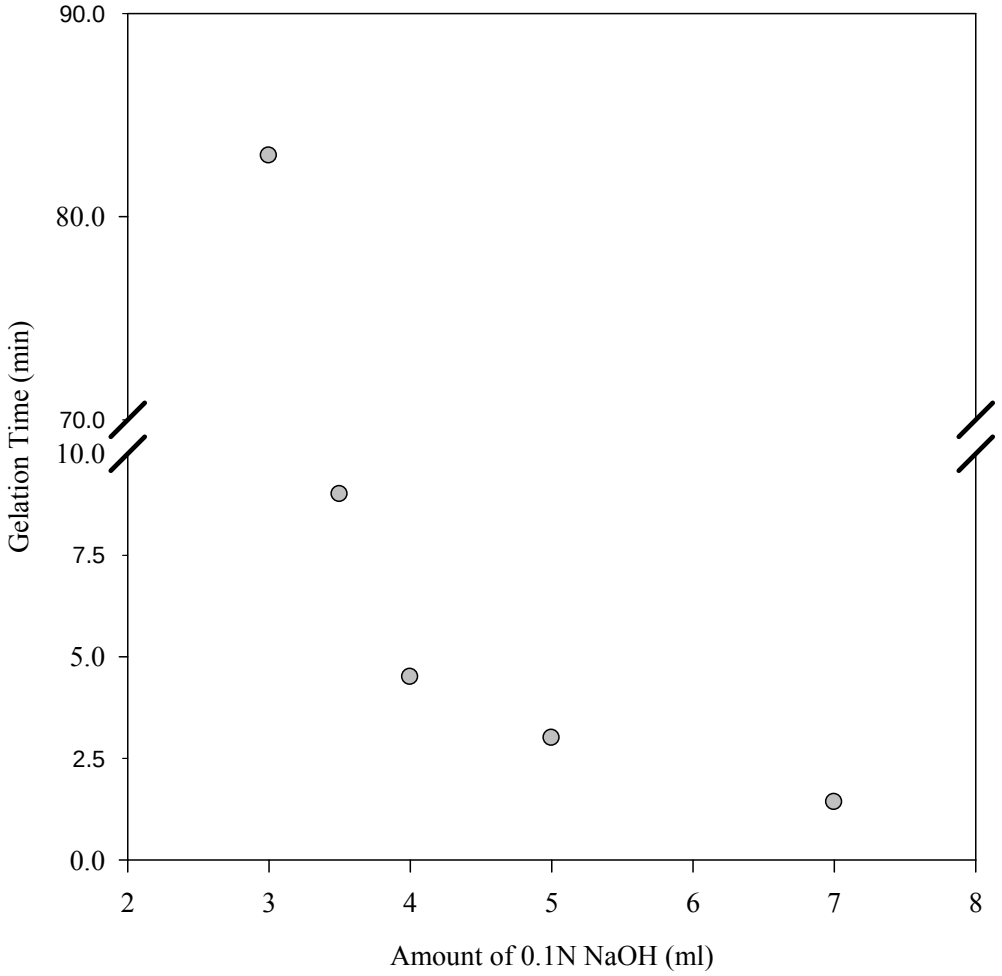

Figure 6.5. The relation between the gelation time in the base-step and the amount of 0.1N NaOH added as a base catalyst. Molar ratio of TEOS: water (acidic fraction): ethanol is 1.0:4.0:2.5 with [HCl]= 0.01 M.

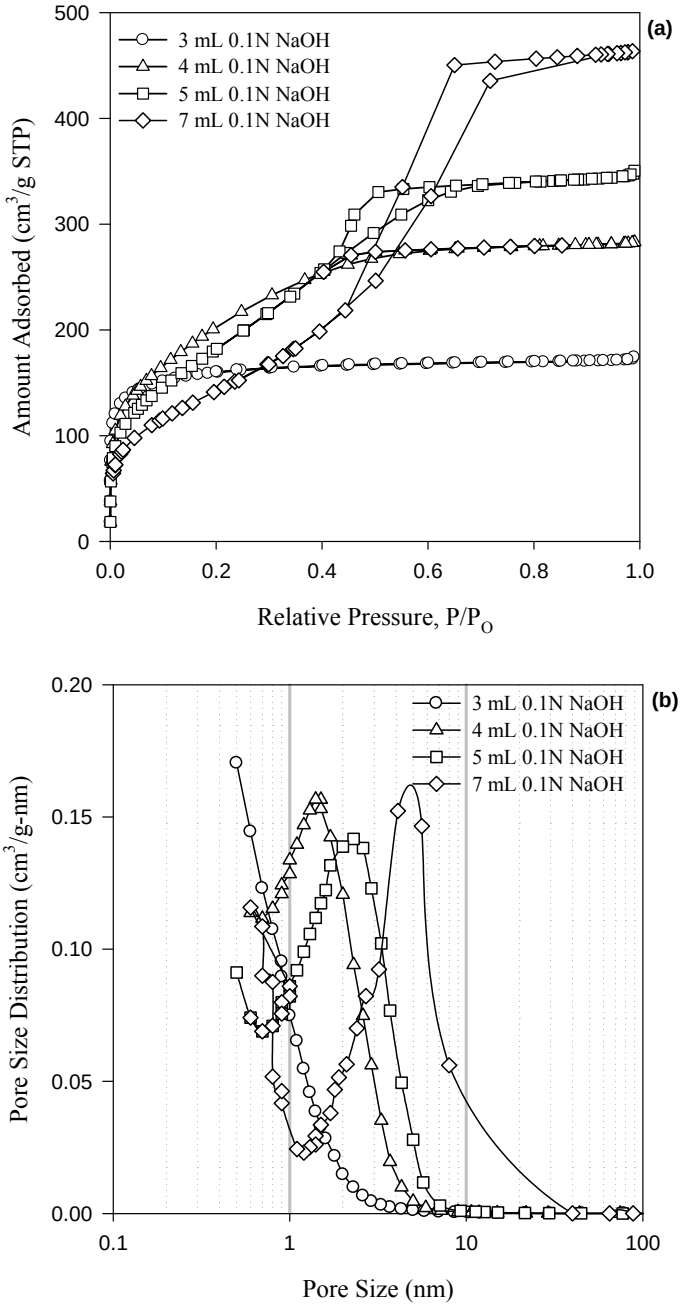

Figure 6.6. (a) Nitrogen adsorption-desorption isotherms of the non-imprinted silica prepared with different amount of 0.1 N NaOH base catalyst and (b) their corresponding BJH pore size distribution derived from adsorption branches.

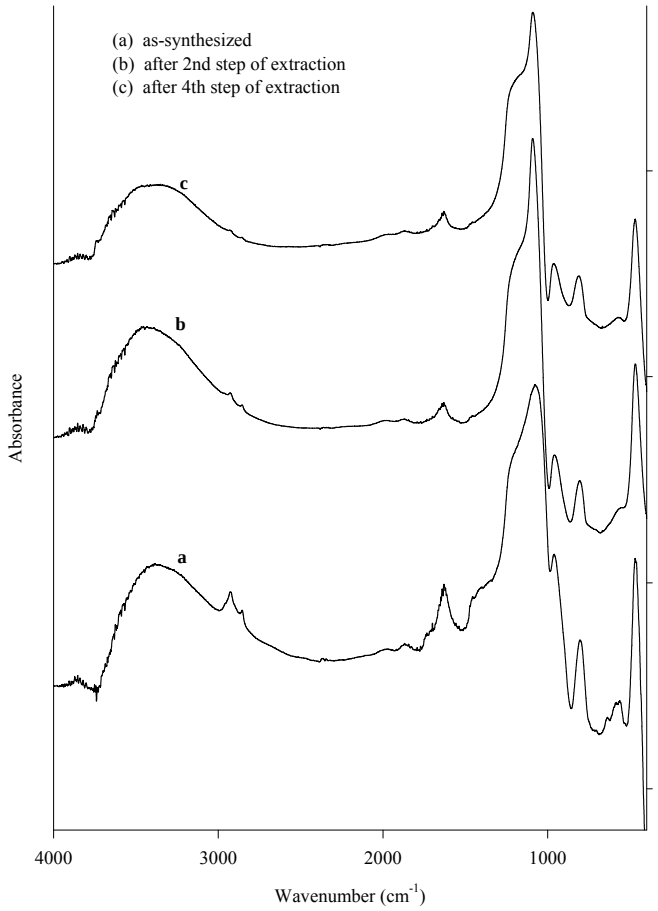

Figure 6.7. FT-IR absorption spectra of glucose imprinted non-functionalized silica. (a) as-synthesized; (b) after 2nd step of water extraction; (c) after 4th step of water extraction.

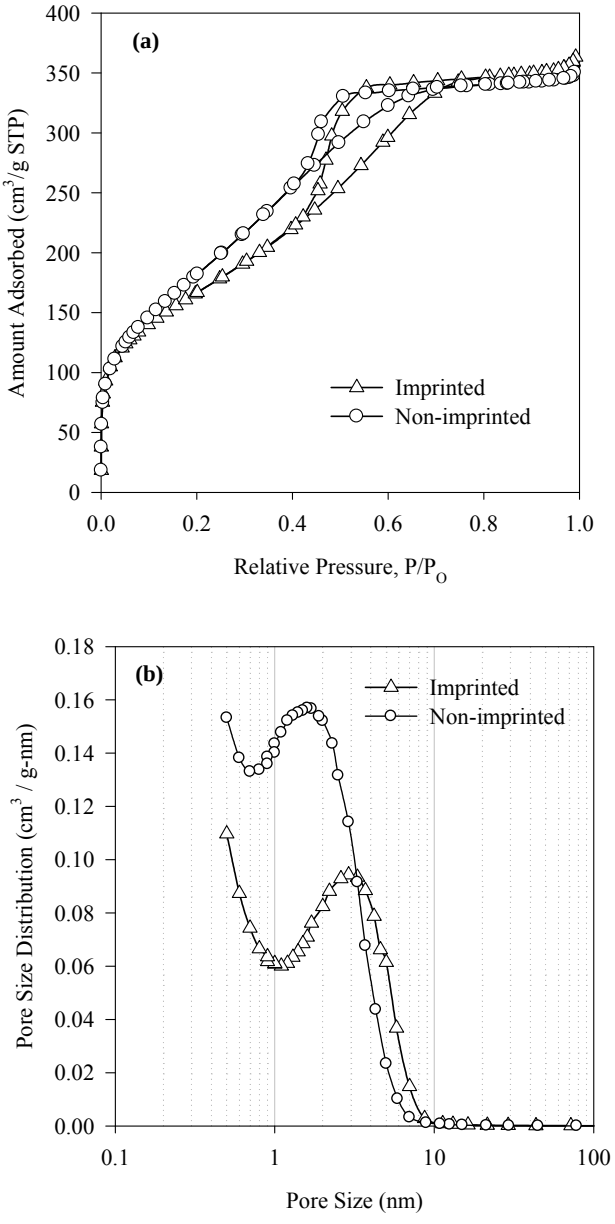

Figure 6.8. (a) Nitrogen adsorption-desorption isotherms for the imprinted silica upon removal the template glucose and the non-imprinted sample, and (b) the corresponding BJH pore size distributions derived from their adsorption branches.

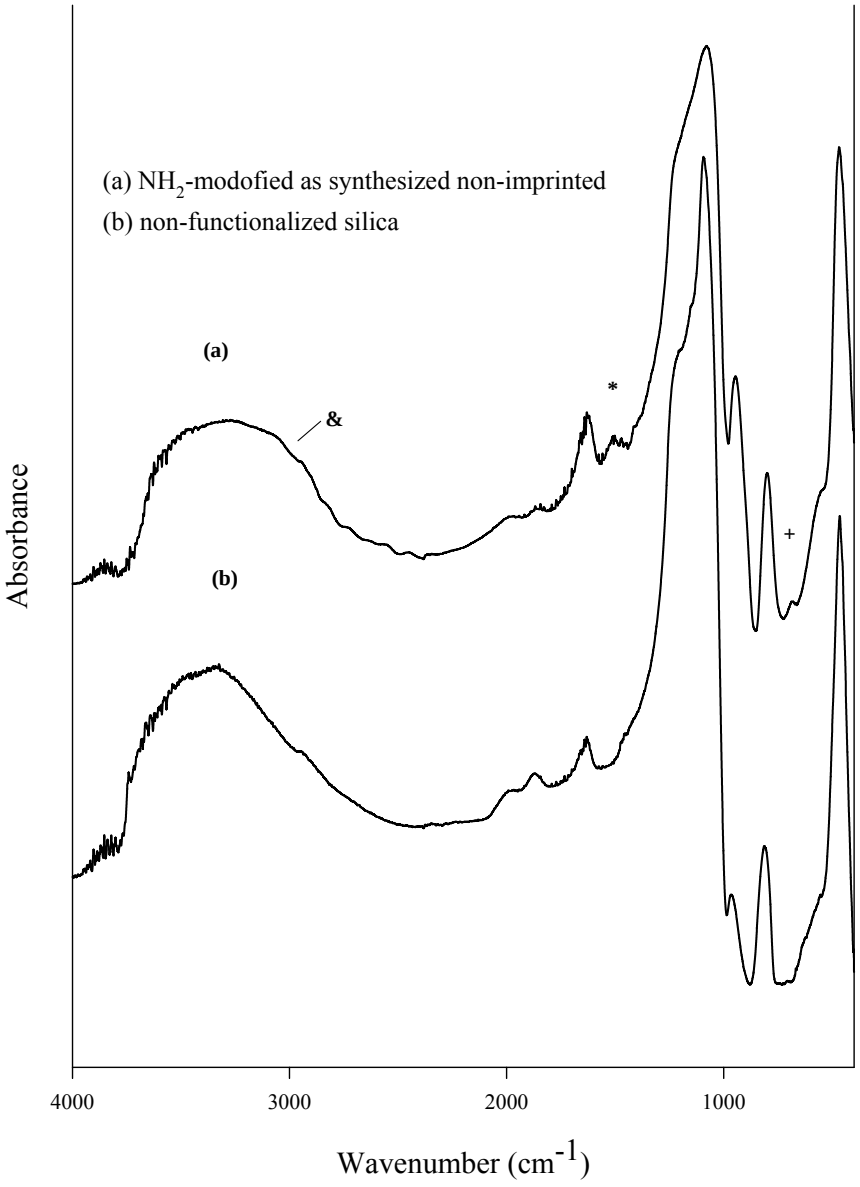

Figure 6.9. FTIR spectra of (a) amine-functionalized as-synthesized non-imprinted silica, and (b) non-functionalized non-imprinted silica. The first band near 687 cm^{-1} is due to N-H bending vibration (+); the second band is around 1510 cm^{-1} which is due to the symmetric $–NH_2$ bending vibration (*), and the third distinguishable broad band near ~2700-3400 cm^{-1} is attributed to the $-NH_2$ stretching vibration (&).

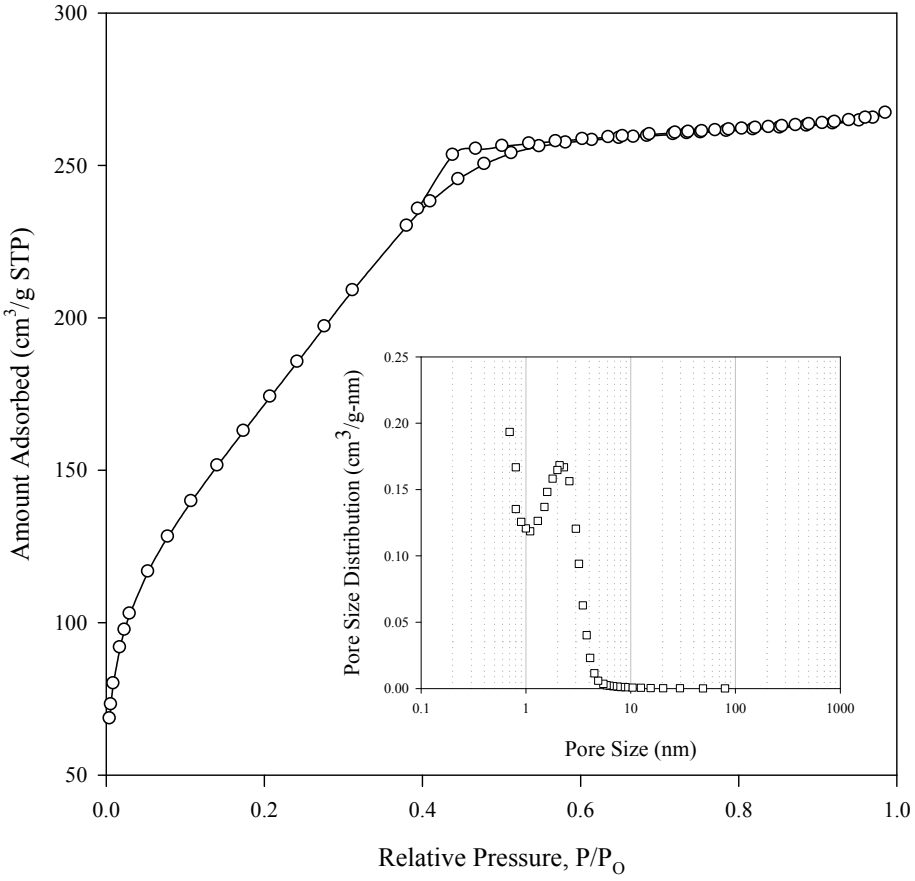

Figure 6.10. Nitrogen adsorption-desorption isotherms of the glucose imprinted amine functionalized silica upon removal of templates. Insert: Corresponding BJH pore size distribution derived from the adsorption branch.

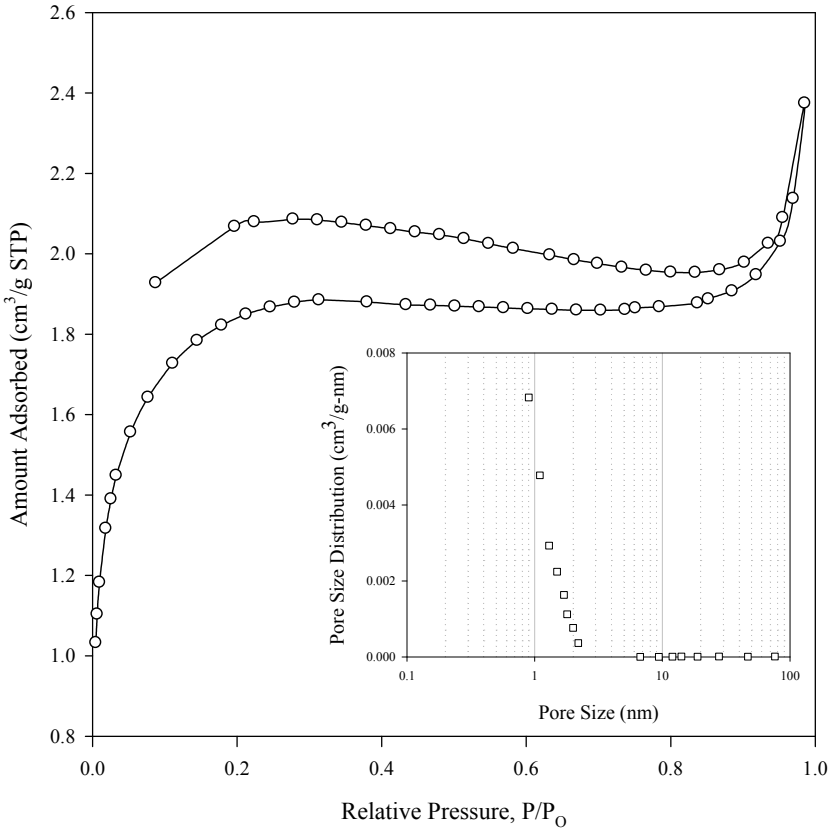

Figure 6.11. Nitrogen adsorption-desorption isotherms of the non-imprinted amine functionalized silica. Insert: Corresponding BJH pore size distribution derived from the adsorption branch.

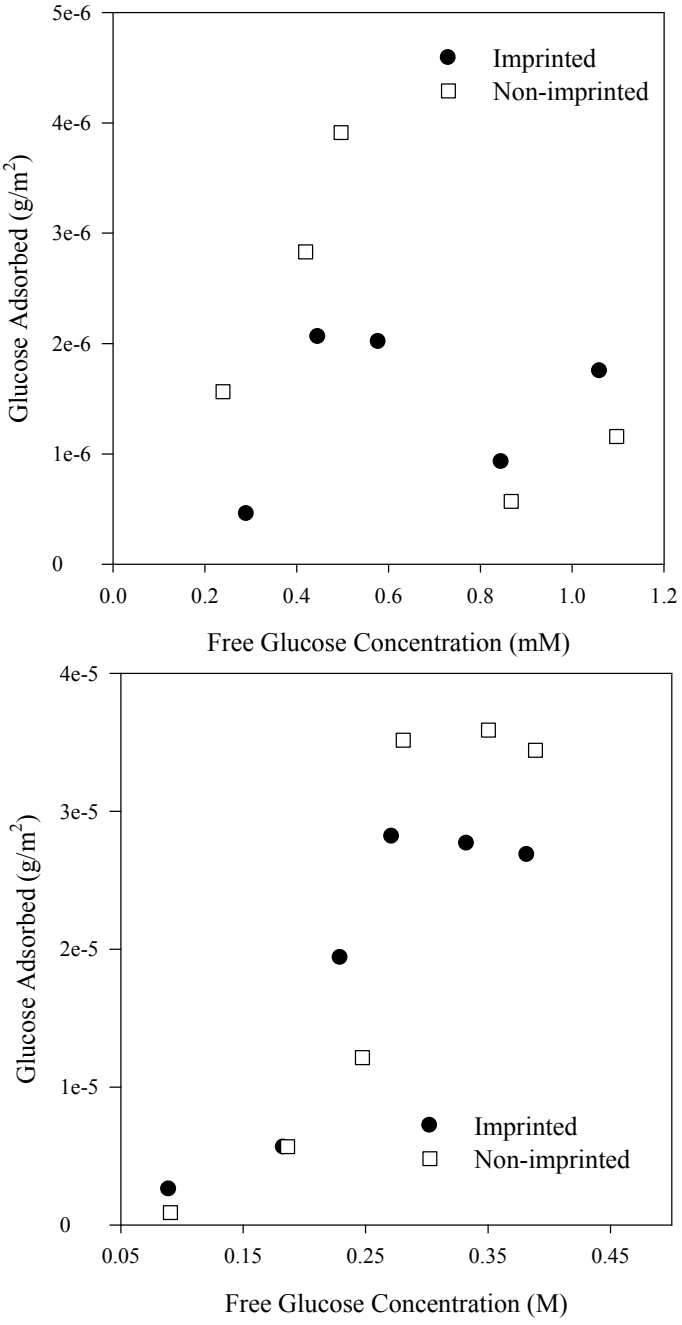

Figure 6.12. D-glucose adsorption isotherms developed from the glucose imprinted and the non-imprinted silicas. (a) In the dilute concentration range, and (b) in the higher concentration range.

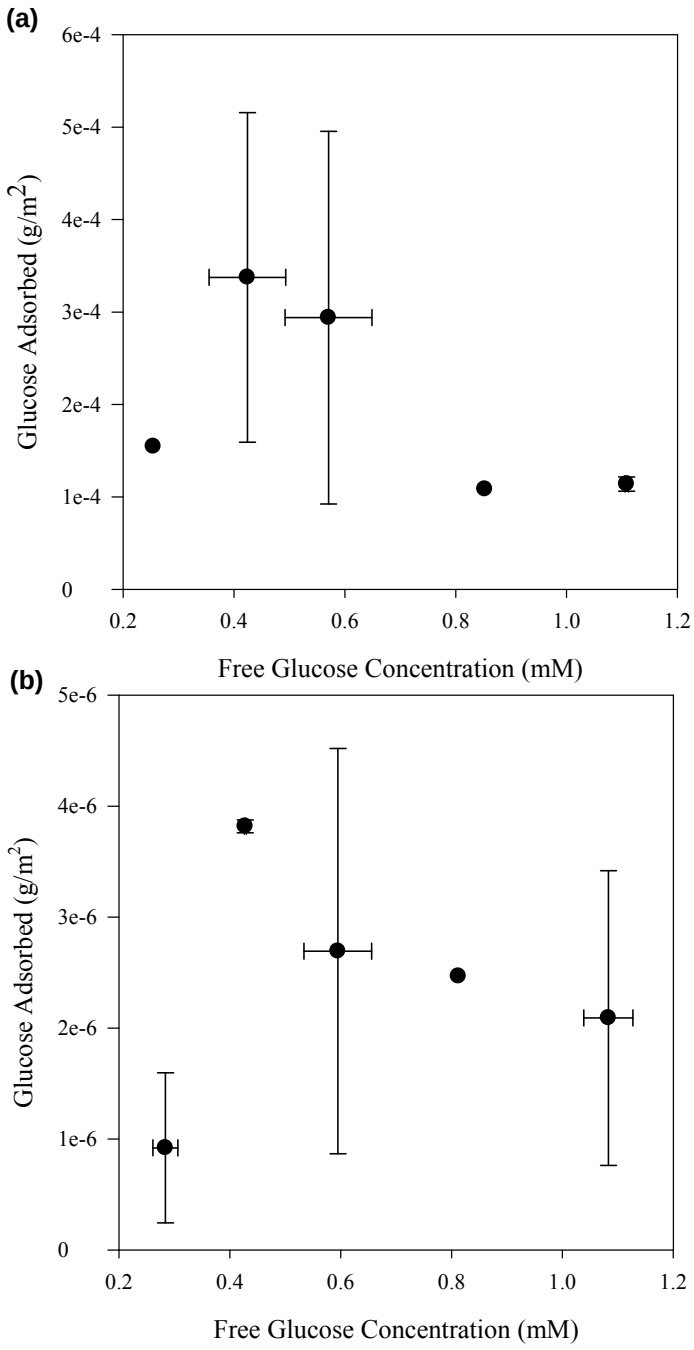

Figure 6.13. D-Glucose adsorption isotherms estimated in the lower glucose concentration range. (a) The amine-functionalized non-imprinted silica, and (b) the amine-functionalized D-glucose imprinted silica.

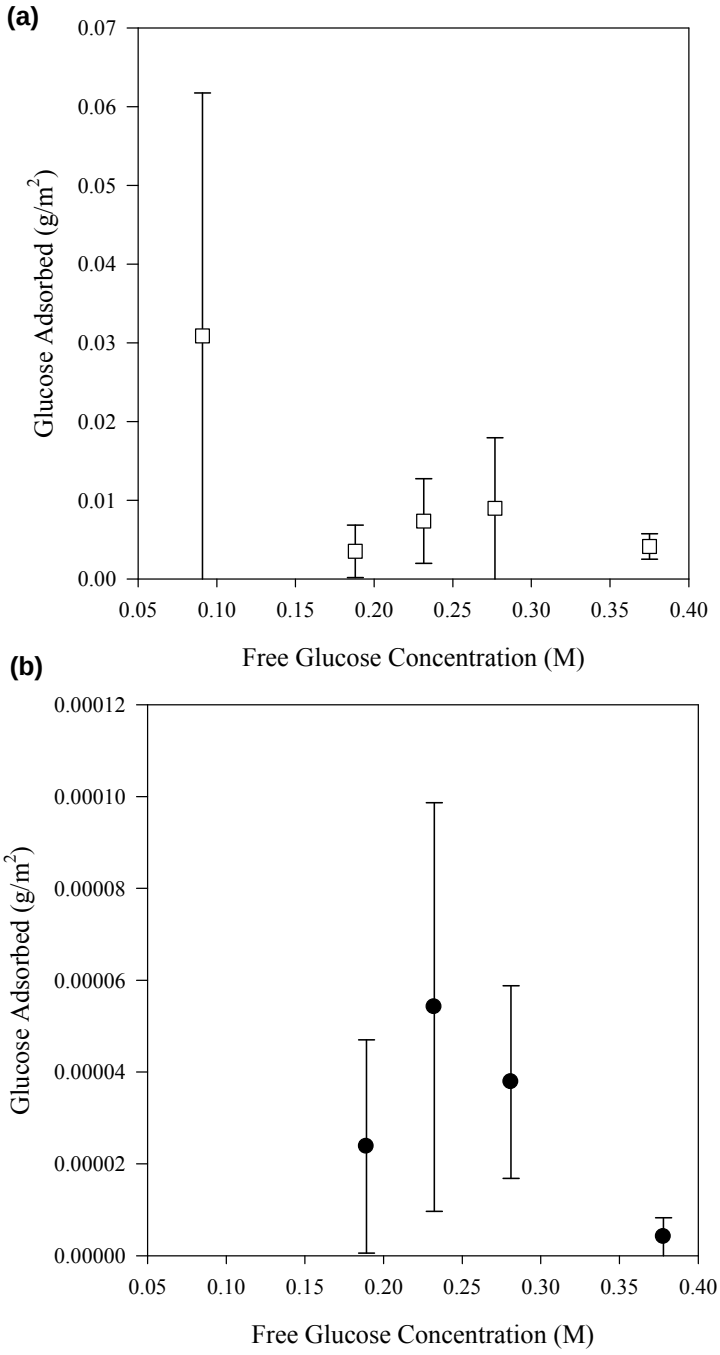

Figure 6.14. D-glucose adsorption isotherms for the amine-functionalized silica estimated in the higher concentration range: (a) non-imprinted, and (b) imprinted silica.

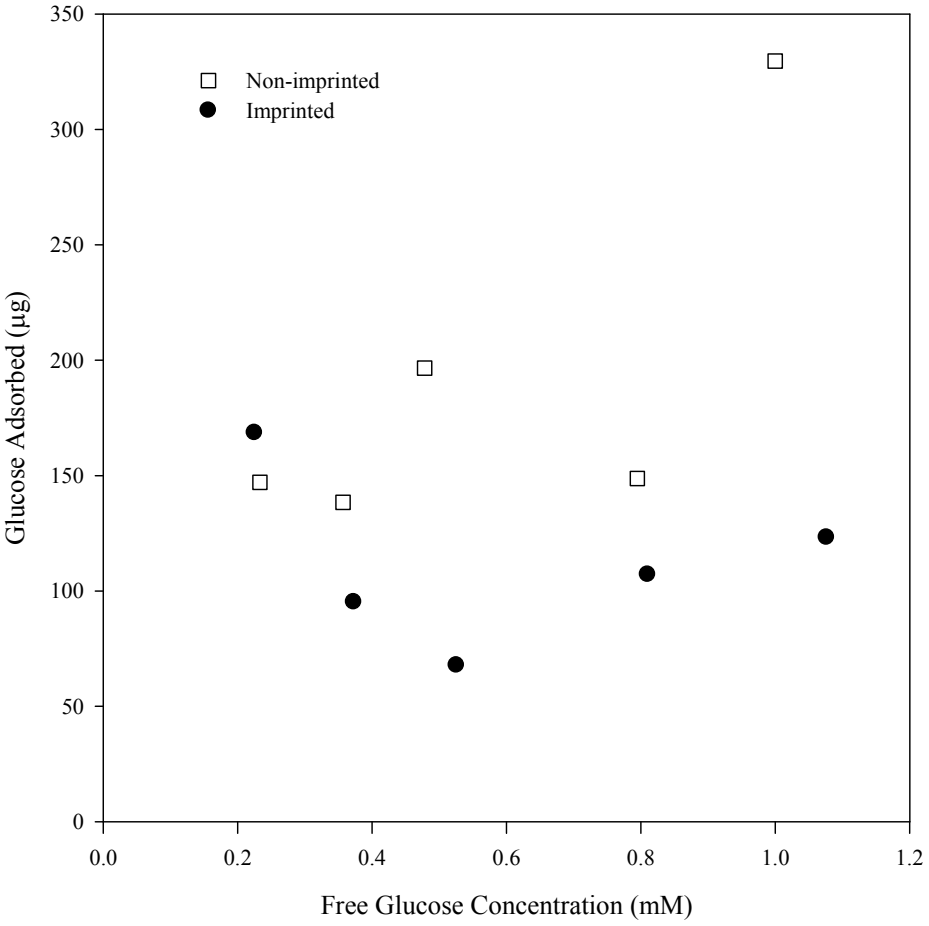

Figure 6.15. Glucose adsorption isotherms derived from the glucose imprinted and non-imprinted silica thin films.

CHAPTER 7
CONCLUSIONS AND FUTURE WORK

7.1 Conclusions

As discussed in Chapter 3, nonionic alkyl (poly)glycoside surfactants synthesized from naturally occurring renewable resources are considered to be environmentally friendly surfactants because they display less toxicity and good dermatological compatibility relative to ionic surfactants, and they are biodegradable. Despite the applications of this group of surfactant in cleaning products, laundry and dishwashing formulations, and cosmetics preparations, they have been largely neglected as templates for mesoporous materials. Here we have employed one member of this class surfactants, namely n-dodecyl β-D-maltoside ($C_{12}G_2$), as a template in the synthesis of mesoporous silica materials. These type sugar-based surfactants are of interest for creating chiral functional adsorption / catalytic sites at the surface of silica materials. However, because they are nonionic surfactants, they participate in only short-ranged hydrogen bonding interactions with silicates during material synthesis, results in poor ordering. To improve order and control over the functional site density at the silica surface, the nonspecific but charged cationic surfactant cetyltrimethylammonium bromide (C_{16}TAB) was mixed with $C_{12}G_2$.

As a guide to materials synthesis, the first step was to develop a complete ternary phase diagram of the C_{16}TAB-$C_{12}G_2$-water system at 50 °C with approximate phase boundaries using low-angle powder X-ray diffraction (PXRD) in combination with polarized optical microscopy (POM). The phase diagram was found to include 2-D hexagonal (p6mm symmetry), bicontinuous cubic (Ia3d symmetry), centered rectangular (cmm symmetry), and lamellar lyotropic liquid crystalline phases. This phase diagram was then used as a quantitative guide for predictive synthesis of ordered mesoporous silica materials by using true liquid crystal templating, also known as the nano-casting method. Materials structures were predicted from the phase diagram by replacing the water in a lyotropic liquid crystal with an equal volume of silicic acid ($Si(OH)_4$), under the hypothesis that the bonding interactions between surfactants' heagroups and silanols

at the material surface might resemble the interactions with water enough to allow the formation of the same phase. In this dissertation, this hypothesis was tested for the $C_{12}G_2$ / C_{16}TAB system. In chapter 3, it was found that highly ordered 2-D hexagonal (p6mm symmetry) and bicontinuous cubic (Ia3d symmetry) silica mesoporous materials could be synthesized within the predicted regions by this mixed surfactant templating route. A series of materials was synthesized keeping the total amount of surfactant constant but varying the relative amounts of the two surfactants. The pore size of the materials could be increased somewhat by increasing the ratio of $C_{12}G_2$ to C_{16}TAB surfactants. However, because of changes in hydrogen bonding between silica and $C_{12}G_2$, increasing disorder of the mesoporous structures was observed as the relative amount of $C_{12}G_2$ surfactant increased with respect to C_{16}TAB for fixed total surfactant content. The structure of mesoporous silica changed from well-ordered 2D-hexagonal to disordered hexagonal and then to very weakly-ordered (the last of which collapsed during calcination) at $C_{12}G_2$ contents corresponding to 48 wt% and 57 wt% respectively, all at compositions corresponding to 60 wt% total surfactant. Another limitation found in the nanocasting approach is that siliceous materials corresponding to over 70 wt% of total surfactant in the aqueous liquid crystal are not stable during calcination, because of their thin silica walls.

Difficulties predicting the silica-surfactant mesophase were encountered near the boundaries of the hexagonal phase in the $C_{12}G_2$ / C_{16}TAB / H_2O phase diagram. Materials synthesized with pure $C_{12}G_2$ surfactant at the highest silicate concentrations were correctly predicted to be hexagonal. However, the materials were only weakly ordered at low silica content and could have been lamellar (and thus unstable to calcination). The hexagonal-cubic boundary also needed to be shifted by approximately 3-5% towards the cubic phase from the aqueous system in order to predict the phase of the siliceous system. The observed deviations from aqueous LLC phase behavior could be because of differences in hydrogen bonding of the hydroxyl groups of the $C_{12}G_2$ surfactant with water molecules vs. silicates. This would be expected to lead to less "solvation" of the headgroups and an increase in packing parameter (which would favor low-curvature structures). A related problem may be that the small driving force for ordering due to hydrogen bonding leads to slow ordering kinetics relative to the rate of

silicate polycondensation. Differences of hydrogen bonding behavior are most significant when only a small amount of silicates are available for hydrogen bonding with polar headgroups, and result in poorly ordered silica. In the case of the hexagonal-cubic boundary, poor "solvation" by silica may "push" the $C_{12}G_2$ further into micelles, thus expanding the average area per headgroup and favoring the hexagonal phase over a cubic phase.

As demonstrated in Chapter 4, the functionality of the maltoside surfactants can be used to direct the incorporation of transition metals at the mespore surface. Isolated Ti(IV) ions connected to the silica matrix by Si-O-Ti bridges are believed to be the active sites required for oxidation reactions. Sol-gel chemistry provides an excellent opportunity to prepare well-mixed metal oxides materials. However, the higher reactivity of titanium alkoxides compared with analogous silicon alkoxides impedes the uniform incorporation of isolated tetrahedrally coordinated titanium. Sacchrides are known to be good ligands for transition metals, and chemical modification of transition metal alkoxides by bidentate ligand is a viable approach to reduce their reactivity. Here we have utilized the complexation or preferential interactions between the titanium ions and the maltoside headgroup of the sugar-based surfactant $C_{12}G_2$ to inhibit the fast hydrolysis and condensation of titanium isopropoxide (TIP). A second non-complexing and non-specific cationic surfactant (C_{16}TAB) was employed with the $C_{12}G_2$ surfactant to control the functional site density at the material surface. Three different types of Si-Ti mixed oxides thin films were synthesized using a solvent evaporation induced self-assembly (EISA) route in combination with the general predictive synthesis method. The ternary phase diagram of the C_{16}TAB-$C_{12}G_2$-water system (discussed in Chapter 3) was used as a quantitative basis to guide our synthesis of thin films. Initial sol compositions of all synthesized films fall on the constant surfactant content line equivalent to 54 wt% of water in the ternary phase diagram. The amount of Ti loading in Type-1 films was increased by increasing the molar ratio of $C_{12}G_2$/C_{16}TAB along that constant surfactant content line and by keeping a constant molar ratio of 1: 1 between $C_{12}G_2$ and TIP. All Type-1 films were synthesized by attempting to encourage complexation between $C_{12}G_2$ and TIP by mixing them together prior to additional processing steps. This approach helped to promote the dispersion of Ti^{4+} in Type-1 Si-Ti mixed oxide thin films with Ti

loadings in the range of Si/Ti = 86 to 8. Uniform, isolated tetrahedral titanium sites were found in Type-1 films. Type-2 films were templated by C_{16}TAB only, and Type-3 films were templated by C_{16}TAB and $C_{12}G_2$ added after alkoxide hydrolysis started (without pre-complexation with $C_{12}G_2$). Site isolated Ti atoms with a mix of tetrahedral and (undesirable) octahedral coordination on silica supports were observed without $C_{12}G_2$ or Ti-complexed-$C_{12}G_2$. However, while the synthesis conditions were chosen to mimic the hexagonal lyotropic phase of the aqueous surfactant system, a primitive cubic mesostructure (Pm3n space group) with 3-D accessible pores was instead found in the metal oxide films. The long-range order of the mesostructures in these mixed oxides thin films was found to decrease as the Ti loading increased. The order of Type-1 films decreased more rapidly as Ti loading increased than that for Type-2 films (prepared with no $C_{12}G_2$) due to the combined effect of Ti alkoxide reactivity and the negative effects of $C_{12}G_2$ on lyotropic ordering (discussed in Chapter 3). Nitrogen sorption measurements demonstrated the evidence that mesopores (average pore size of 2.8 nm) with a very narrow pore size-distribution are presence in the thin film synthesized with Si/Ti = 86. Thus we showed that ordered cubic mesoporous Si-Ti mixed oxides thin films with isolated Ti(IV) sites can be synthesized over a wide range of titanium contents by employing the mixed surfactant system of C_{16}TAB and $C_{12}G_2$ along with pre-complexation between $C_{12}G_2$ and the Ti precursor.

By taking the advantages of maltoside surfactant pre-complexation, in Chapter 5 we discussed the synthesis of Si-Ti mixed oxide mesoporous powders for potential application in heterogeneous oxidation catalysis. A series of Si-Ti mixed oxide powder samples with predictively synthesized hexagonal mesostructures were synthesized with different titanium loadings by employing a 1:1 molar ratio of $C_{12}G_2$ to titanium iso-propoxide (TIP). A modified nano-casting method was used to synthesize these materials and the ternary phase diagram of the C_{16}TAB- $C_{12}G_2$- water system (developed in Chapter 3) served as a quantitative guide in predicting the final mesostructures of the materials. As found earlier in Chapter 4, the degree of ordering of the final mesostructures of these mixed oxide materials decreased as Ti loadings increased and when Si/Ti = 10, the materials became disordered. Pore sizes, calculated using two different techniques, indicated that the materials were mesoporous with pore sizes

slightly greater than 2.0 nm. This is substantially greater than the pore size available in titanium-substituted zeolites, and future catalytic and spectroscopic studies will be employed to confirm that TIP complexation with maltoside surfactants leads to isolated Ti sites, as in the films prepared by dip coating.

In Chapter 6 a non-covalent molecular approach was pursued to synthesize D-(+)-glucose molecular imprinted binding sites in both silica gels and thin films through the template guided polymerization of silicon precursors. A two-step acid-base silica sol-gel process with long initial acid-step (~24 hrs) was used to prepare silica gels and a single acidic step was used to prepare glucose imprinted thin films. An increase in the amount of base catalyst added at the beginning of the second step decreases the gelation time. Sols containing more base catalyst produced porous silica with more mesoporous character. Upon removal of the glucose template molecules by solvent extraction, silica materials with imprinted cavities were used to develop adsorption isotherms by studying their rebinding capacity from aqueous solutions of pure glucose of different concentrations. As control experiments, the adsorption of glucose in non-imprinted silica prepared under the same conditions but in the absence of glucose was compared. In this work, two different glucose concentration ranges were used to conduct glucose adsorption experiments for the both imprinted and non-imprinted silica samples. For the dilute concentration range, which was from 0.3 mM to 1.4 mM, the phenol-sulfuric acid assay method was used to quantify glucose in aqueous solution. For the higher concentration range, which was from 0.1 M to 0.4 M, the ATR-FTIR method was used to determine the glucose concentration. Enhanced adsorption of glucose from an aqueous (polar) solution in the imprinted material was not observed, most likely because of non-specific adsorption which is evident from the adsorption level of glucose in both imprinted and non-imprinted silica materials and thin films. These results suggest that the non-functionalized imprinted cavities in the silica material do not have the ability to recognize glucose from an aqueous solution. Most likely, hydrogen bonding between the hydroxyl groups of glucose molecule and the hydroxyl groups of silica alone is not strong enough in an aqueous solution to rebind the imprint molecule effectively.

In the next part of the glucose imprinting work, the effects of incorporating amine organic functional groups into the silica matrix on the rebinding capacity were

investigated. Amine functionalized silicas, both glucose imprinted and non-imprinted, were synthesized by one pot co-condensation of tetraethoxysilane (TEOS) and 3-aminopropyltriethoxysilane (APTES) under acidic conditions. It was found that the comparatively stronger hydrogen bonding between the amine functional group and the hydroxyl groups of glucose increases the glucose binding affinity over that of non-functionalized silica. As indicated by the isotherms, the non-imprinted silica containing amino groups adsorbed much more glucose per unit area than the non-functionalized non-imprinted and imprinted functionalized materials. However, the level of glucose adsorption per unit area for the glucose imprinted functionalized material is slightly higher than that with the imprinted non-functionalized material. Comparing imprinted and non-imprinted amino functionalized materials, non-imprinted materials exhibited much more glucose adsorption, which indicates the ineffectiveness of the non-covalent imprinting of silica with glucose in this case. However, non-specific binding still limits the selectivity of the materials toward D-glucose. The amino functionalized non-imprinted material had very little porosity (specific surface area was ~7 m^2/g) and the surface embedded amino groups adsorbed a great deal of glucose from solutions, which gave a very high glucose adsorbed per area of solid.

7.2 Future Work

The research described in Chapter 3 is focused on the development of highly ordered mesoporous silica materials using as the template a new class of sugar-based surfactant, specifically n-dodecyl β-D-maltoside ($C_{12}G_2$) carrying chiral information in their polar disaccharide headgroup. This class of nonionic surfactants is of long-term interest for the possibility of imprinting their chiral information into metal oxide surfaces while using them as structure directing agents. As discussed above, a nonspecific cationic surfactant was added to improve the mesostructural ordering and to control the functional site density at the silica surface. Probing the synthesis of imprinted mesostructured silica materials with controlled functionality and selective recognition capacity for the imprint molecules remains to be investigated in the near future. As discussed in Chapter 3 good ordering of the mesoporous materials and the control over the functional site density at

the silica surface can be achieved by mixing this functional chiral sugar surfactant with a non-functional but charged cationic surfactant. Silica with chiral recognition ability can be synthesized either in powder or thin film form using this mixed surfactant system for templating. The key steps in the synthesis of pure silica material with carbohydrate recognition property will be to create imprinted cavities by keeping the predetermined orientation of the hydroxyl groups, determined by the interactions between the polar headgroups and intermediate silicates, during silicates polymerization and the subsequent sol-gel processing steps. For this, material synthesis reaction conditions need to be optimized in order to maximize the interactions between the polar headgroups and silicates. Also a quick and effective method of templates removal such as by ozone oxidation would help to keep functional groups in their predetermined orientation.

In Chapter 4, a novel methodology for the preparation of mesoporous silica supporting isolated tetrahedrally coordinated titanium by using the mixed surfactant system of C_{16}TAB and $C_{12}G_2$. The hydrophilic maltose headgroup of nonionic $C_{12}G_2$ surfactant is proposed to act as a bi-dentate chelating agent for the titanium alkoxide precursor. In Chapter 5, this methodology was extended to the synthesis of Si-Ti mixed oxide powders with predictable mesostructure. Tetrahedrally coordinated titanium atoms incorporated at the mesopore silica surface are believed to be the active oxidation sites in titanosilicate catalysts such as the zeolite TS-1, and thus they are promising candidates for heterogeneous silica-supported titania oxidation catalysis of larger hydrocarbons. The immediate goal of this work is to employ this mixed oxide materials in testing their catalytic performance in oxidation reactions, for example in epoxidation of cyclohexene. This would be the next logical and immediate extension of this synthesis work. Further characterization of these mixed oxide materials by X-ray absorption near-edge structure (XANES) and X-ray photoelectron spectroscopy (XPS) would also be extremely valuable in order to explore the local structural environment around titanium atoms. Good understanding of the coordination environment of titanium atoms is very important for understanding adsorption and catalysis within these materials. Mesoporous silica molecular sieves doped with small amounts of different transition metals such as zirconium (Zr), tantalum (Ta), vanadium (V), niobium (Nb), etc. have significant potential for a variety of catalytic and electronic applications.[47, 292] Most transition metal

alkoxides have much higher reactivity compare to their analogous silicon alkoxides, because the usual coordination number of transition metal alkoxides is higher than their oxidation states in alkoxides. Therefore the most important step in the synthesis of transition metals doped silica by sol-gel synthesis process is the proper stabilization of highly reactive transition metal alkoxides. The ability to stabilize titanium alkoxides with molecules that also serve as pore templates and guide the transition metals to the pore surface has opened a new pathway to stabilize other transition metal alkoxides that will provide a new means of obtaining isolated transition metal supported silica mesoporous materials.

REFERENCES

1. Stein, A., Advances in microporous and mesoporous solids-highlights of recent progress. *Adv. Mater. (Weinheim, Ger.)* **2003,** 15, (10), 763-775.
2. Corma, A., From Microporous to Mesoporous Molecular Sieve Materials and Their Use in Catalysis. *Chemical Reviews (Washington, D. C.)* **1997,** 97, (6), 2373-2419.
3. Barton, T. J.; Bull, L. M.; Klemperer, W. G.; Loy, D. A.; McEnaney, B.; Misono, M.; Monson, P. A.; Pez, G.; Scherer, G. W.; Vartuli, J. C.; Yaghi, O. M., Tailored Porous Materials. *Chem. Mater.* **1999,** 11, (10), 2633-2656.
4. Ying, J. Y.; Mehnert, C. P.; Wong, M. S., Synthesis and applications of supramolecular-templated mesoporous materials. *Angewandte Chemie, International Edition* **1999,** 38, (1/2), 56-77.
5. Sing, K. S. W.; Everett, D. H.; Haul, R. A. W.; Moscou, L.; Pierotti, R. A.; Rouquerol, J.; Siemieniewska, T., Reporting physisorption data for gas/solid systems with special reference to the determination of surface area and porosity (Recommendations 1984). *Pure and Applied Chemistry* **1985,** 57, (4), 603-19.
6. Soler-Illia Galo, J. d. A. A.; Sanchez, C.; Lebeau, B.; Patarin, J., Chemical strategies to design textured materials: from microporous and mesoporous oxides to nanonetworks and hierarchical structures. *Chem Rev FIELD Full Journal Title:Chemical reviews* **2002,** 102, (11), 4093-138.
7. Mitchell, I. V., *Pillared Layered Structures: Current Trends and Applications*. 1990; p 252 pp.
8. Kresge, C. T.; Leonowicz, M. E.; Roth, W. J.; Vartuli, J. C.; Beck, J. S., Ordered mesoporous molecular sieves synthesized by a liquid-crystal template mechanism. *Nature (London, United Kingdom)* **1992,** 359, (6397), 710-12.
9. Beck, J. S.; Vartuli, J. C.; Roth, W. J.; Leonowicz, M. E.; Kresge, C. T.; Schmitt, K. D.; Chu, C. T. W.; Olson, D. H.; Sheppard, E. W.; et al., A new family of mesoporous molecular sieves prepared with liquid crystal templates. *Journal of the American Chemical Society* **1992,** 114, (27), 10834-43.
10. Zhang, W.; Pinnavaia, T. J., Transition metal substituted derivatives of cubic MCM-48 mesoporous molecular sieves. *Catalysis Letters* **1996,** 38, (3,4), 261-265.
11. Zhang, W.; Wang, J.; Tanev, P. T.; Pinnavaia, T. J., Catalytic hydroxylation of benzene over transition-metal substituted hexagonal mesoporous silicas. *Chemical Communications (Cambridge)* **1996**, (8), 979-980.
12. Luan, Z.; Cheng, C.-F.; Zhou, W.; Klinowski, J., Mesopore Molecular Sieve MCM-41 Containing Framework Aluminum. *J. Phys. Chem.* **1995,** 99, (3), 1018-24.
13. Corma, A.; Navarro, M. T.; Perez Pariente, J., Synthesis of an ultralarge pore titanium silicate isomorphous to MCM-41 and its application as a catalyst for selective oxidation of hydrocarbons. *J. Chem. Soc., Chem. Commun.* **1994**, (2), 147-8.
14. Tanev, P. T.; Chibwe, M.; Pinnavaia, T. J., Titanium-containing mesoporous molecular sieves for catalytic oxidation of aromatic compounds. *Nature (London, United Kingdom)* **1994,** 368, (6469), 321-3.
15. Dickey, F. H., Preparation of specific adsorbents. *Proceedings of the National Academy of Sciences of the United States of America* **1949,** 35, 227-9.

16. Makote, R.; Collinson, M. M., Template Recognition in Inorganic-Organic Hybrid Films Prepared by the Sol-Gel Process. *Chem. Mater.* **1998,** 10, (9), 2440-2445.
17. Whitcombe, M. J.; Rodriguez, M. E.; Villar, P.; Vulfson, E. N., A New Method for the Introduction of Recognition Site Functionality into Polymers Prepared by Molecular Imprinting: Synthesis and Characterization of Polymeric Receptors for Cholesterol. *J. Am. Chem. Soc.* **1995,** 117, (27), 7105-11.
18. Wulff, G., Molecular imprinting in crosslinked materials with the aid of molecular templates - a way towards artificial antibodies. *Angew. Chem., Int. Ed. Engl.* **1995,** 34, (17), 1812-32.
19. Wulff, G., Enzyme-like Catalysis by Molecularly Imprinted Polymers. *Chem. Rev. (Washington, D. C.)* **2002,** 102, (1), 1-27.
20. Kim, J. M.; Sakamoto, Y.; Hwang, Y. K.; Kwon, Y.-U.; Terasaki, O.; Park, S.-E.; Stucky, G. D., Structural Design of Mesoporous Silica by Micelle-Packing Control Using Blends of Amphiphilic Block Copolymers. *Journal of Physical Chemistry B* **2002,** 106, (10), 2552-2558.
21. Kim, J. M.; Stucky, G. D., Synthesis of highly ordered mesoporous silica materials using sodium silicate and amphiphilic block copolymers. *Chemical Communications (Cambridge)* **2000**, (13), 1159-1160.
22. Chao, M.-C.; Wang, D.-S.; Lin, H.-P.; Mou, C.-Y., Control of single crystal morphology of SBA-1 mesoporous silica. *J. Mater. Chem.* **2003,** 13, (12), 2853-2854.
23. Che, S.; Garcia-Bennett, A. E.; Yokoi, T.; Sakamoto, K.; Kunieda, H.; Terasaki, O.; Tatsumi, T., A novel anionic surfactant templating route for synthesizing mesoporous silica with unique structure. *Nat. Mater.* **2003,** 2, (12), 801-805.
24. Bagshaw, S. A.; Prouzet, E.; Pinnavaia, T. J., Templating of mesoporous molecular sieves by nonionic polyethylene oxide surfactants. *Science (Washington, D. C.)* **1995,** 269, (5228), 1242-4.
25. Kim, S.-S.; Pauly, T. R.; Pinnavaia, T. J., Non-ionic surfactant assembly of wormhole silica molecular sieves from water soluble silicates. *Chemical Communications (Cambridge)* **2000**, (10), 835-836.
26. Han, S.; Hou, W.; Dang, W.; Xu, J.; Hu, J.; Li, D., Synthesis of rod-like mesoporous silica with hexagonal appearance using sodium silicate as precursor. *Colloid Polym. Sci.* **2004,** 282, (7), 761-765.
27. Chen, F.; Huang, L.; Li, Q., Synthesis of MCM-48 Using Mixed Cationic-Anionic Surfactants as Templates. *Chemistry of Materials* **1997,** 9, (12), 2685-2686.
28. Ryoo, R.; Joo, S. H.; Kim, J. M., Energetically Favored Formation of MCM-48 from Cationic-Neutral Surfactant Mixtures. *Journal of Physical Chemistry B* **1999,** 103, (35), 7435-7440.
29. Song, M.-G.; Kim, J.-Y.; Cho, S.-H.; Kim, J.-D., Mixed Cationic-Nonionic Surfactant Templating Approach for the Synthesis of Mesoporous Silica. *Langmuir* **2002,** 18, (16), 6110-6115.
30. Huo, Q.; Margolese, D. I.; Stucky, G. D., Surfactant Control of Phases in the Synthesis of Mesoporous Silica-Based Materials. *Chemistry of Materials* **1996,** 8, (5), 1147-60.
31. Tanev, P. T.; Pinnavaia, T. J., Biomimetic assembly of porous lamellar silica molecular sieves with a vesicular particle architecture. *Supramolecular Science* **1998,** 5, (3-4), 399-404.

32. Tanev, P. T.; Liang, Y.; Pinnavaia, T. J., Assembly of Mesoporous Lamellar Silicas with Hierarchical Particle Architectures. *J. Am. Chem. Soc.* **1997,** 119, (37), 8616-8624.
33. Zhao, D.; Huo, Q.; Feng, J.; Chmelka, B. F.; Stucky, G. D., Nonionic triblock and star diblock copolymer and oligomeric surfactant syntheses of highly ordered, hydrothermally stable, mesoporous silica structures. *Journal of the American Chemical Society* **1998,** 120, (24), 6024-6036.
34. Zhao, D. Y.; Yang, P. D.; Melosh, N.; Feng, Y. L.; Chmelka, B. F.; Stucky, G., Continuous mesoporous silica films with highly ordered large pore structures. *Advanced Materials (Weinheim, Germany)* **1998,** 10, (16), 1380-1385.
35. Oye, G.; Sjoblom, J.; Stocker, M., Synthesis, characterization and potential applications of new materials in the mesoporous range. *Advances in colloid and interface science* **2001,** 89-90, 439-66.
36. Ciesla, U.; Froeba, M.; Stucky, G.; Schueth, F., Highly Ordered Porous Zirconias from Surfactant-Controlled Syntheses: Zirconium Oxide-Sulfate and Zirconium Oxo Phosphate. *Chemistry of Materials* **1999,** 11, (2), 227-234.
37. Selvam, P.; Bhatia, S. K.; Sonwane, C. G., Recent Advances in Processing and Characterization of Periodic Mesoporous MCM-41 Silicate Molecular Sieves. *Industrial & Engineering Chemistry Research* **2001,** 40, (15), 3237-3261.
38. Huo, Q.; Leon, R.; Petroff, P. M.; Stucky, G. D., Mesostructure design with gemini surfactants: supercage formation in a three-dimensional hexagonal array. *Science (Washington, D. C.)* **1995,** 268, (5215), 1324-7.
39. Huo, Q.; Margolese, D. I.; Ciesla, U.; Feng, P.; Gier, T. E.; Sieger, P.; Leon, R.; Petroff, P. M.; Schueth, F.; Stucky, G. D., Generalized synthesis of periodic surfactant/inorganic composite materials. *Nature (London, United Kingdom)* **1994,** 368, (6469), 317-21.
40. Monnier, A.; Schuth, F.; Huo, Q.; Kumar, D.; Margolese, D.; Maxwell, R. S.; Stucky, G. D.; Krishnamurty, M.; Petroff, P.; et al., Cooperative formation of inorganic-organic interfaces in the synthesis of silicate mesostructures. *Science (Washington, DC, United States)* **1993,** 261, (5126), 1299-303.
41. El-Safty, S. A.; Hanaoka, T., Microemulsion Liquid Crystal Templates for Highly Ordered Three-Dimensional Mesoporous Silica Monoliths with Controllable Mesopore Structures. *Chemistry of Materials* **2004,** 16, (3), 384-400.
42. Tanev, P. T.; Pinnavaia, T. J., A neutral templating route to mesoporous molecular sieves. *Science (Washington, D. C.)* **1995,** 267, (5199), 865-7.
43. Sayari, A., Periodic mesoporous materials: Synthesis, characterization and potential applications. *Studies in Surface Science and Catalysis* **1996,** 102, (Recent Advances and New Horizons in Zeolite Science and Technology), 1-46.
44. Solberg, S. M.; Kumar, D.; Landry, C. C., Synthesis, Structure, and Reactivity of a New Ti-Containing Microporous/Mesoporous Material. *Journal of Physical Chemistry B* **2005,** 109, (51), 24331-24337.
45. Klein, S.; Thorimbert, S.; Maier, W. F., Amorphous microporous titania-silica mixed oxides: preparation, characterization, and catalytic redox properties. *Journal of Catalysis* **1996,** 163, (2), 476-488.

46. Schultz, P. C.; Smyth, H. T., Ultralow-expansion glasses and their structure in the silicon dioxide-titanium dioxide system. *Amorphous Mater., Pap. Int. Conf. Phys. Non-Cryst. Solids, 3rd* **1972**, 453-61.
47. He, X.; Antonelli, D., Recent advances in synthesis and applications of transition metal containing mesoporous molecular sieves. *Angew. Chem., Int. Ed.* **2002,** 41, (2), 214-229.
48. Perego, G.; Taramasso, M.; Notari, B. Porous crystalline synthetic material consisting of silicon and titanium oxides. 80-203283
886812, 19801222., 1981.
49. Reddy, J. S.; Kumar, R.; Ratnasamy, P., Titanium silicalite-2: synthesis, characterization and catalytic properties. *Appl. Catal.* **1990,** 58, (2), L1-L4.
50. Clerici, M. G., Catalytic oxidations with hydrogen peroxide: new and selective catalysts. *Studies in Surface Science and Catalysis* **1993,** 78, (Heterogeneous Catalysis and Fine Chemicals III), 21-33.
51. Gao, H.; Lu, G.; Suo, J.; Li, S., Epoxidation of allyl chloride with hydrogen peroxide catalyzed by titanium silicalite 1. *Applied Catalysis, A: General* **1996,** 138, (1), 27-38.
52. Liu, Z.; Crumbaugh, G. M.; Davis, R. J., Effect of structure and composition on epoxidation of hexene catalyzed by microporous and mesoporous Ti-Si mixed oxides. *Journal of Catalysis* **1996,** 159, (1), 83-9.
53. Blasco, T.; Corma, A.; Navarro, M. T.; Perez Pariente, J., Synthesis, characterization, and catalytic activity of Ti-MCM-41 structures. *Journal of Catalysis* **1995,** 156, (1), 65-74.
54. Zhang, W.; Froeba, M.; Wang, J.; Tanev, P. T.; Wong, J.; Pinnavaia, T. J., Mesoporous Titanosilicate Molecular Sieves Prepared at Ambient Temperature by Electrostatic and Neutral Assembly Pathways: A Comparison of Physical Properties and Catalytic Activity for Peroxide Oxidations. *Journal of the American Chemical Society* **1996,** 118, (38), 9164-9171.
55. Sankar, G.; Rey, F.; Thomas, J. M.; Greaves, G. N.; Corma, A.; Dobson, B. R.; Dent, A. J., Probing active sites in solid catalysts for the liquid-phase epoxidation of alkenes. *J. Chem. Soc., Chem. Commun.* **1994**, (19), 2279-80.
56. Hutter, R.; Mallat, T.; Baiker, A., Titania-silica mixed oxides. III. Epoxidation of a-isophorone with hydroperoxides. *Journal of Catalysis* **1995,** 157, (2), 665-75.
57. Hutter, R.; Mallat, T.; Baiker, A., Titania-silica mixed oxides. II. Catalytic behavior in olefin epoxidation. *Journal of Catalysis* **1995,** 153, (1), 177-89.
58. Yoldas, B. E., Formation of titania-silica glasses by low temperature chemical polymerization. *Journal of Non-Crystalline Solids* **1980,** 38-39, (1), 81-6.
59. Holland, M. A.; Pickup, D. M.; Mountjoy, G.; Tsang, E. S. C.; Wallidge, G. W.; Newport, R. J.; Smith, M. E., Synthesis, characterization and performance of (TiO2)0.18.(SiO2)0.82 xerogel catalysts. *Journal of Materials Chemistry* **2000,** 10, (11), 2495-2501.
60. Pickup, D. M.; Mountjoy, G.; Wallidge, G. W.; Anderson, R.; Cole, J. M.; Newport, R. J.; Smith, M. E., A structural study of (TiO2)x(SiO2)1-x (x=0.18, 0.30 and 0.41) xerogels prepared using acetylacetone. *Journal of Materials Chemistry* **1999,** 9, (6), 1299-1305.

61. Doeuff, S.; Henry, M.; Sanchez, C.; Livage, J., Hydrolysis of titanium alkoxides: modification of the molecular precursor by acetic acid. *Journal of Non-Crystalline Solids* **1987,** 89, (1-2), 206-16.
62. Guglielmi, M.; Carturan, G., Precursors for sol-gel preparations. *Journal of Non-Crystalline Solids* **1988,** 100, (1-3), 16-30.
63. Lafond, V.; Mutin, P. H.; Vioux, A., Control of the Texture of Titania-Silica Mixed Oxides Prepared by Nonhydrolytic Sol-Gel. *Chemistry of Materials* **2004,** 16, (25), 5380-5386.
64. Andrianainarivelo, M.; Corriu, R.; Leclercq, D.; Mutin, P. H.; Vioux, A., Mixed oxides SiO2-ZrO2 and SiO2-TiO2 by a non-hydrolytic sol-gel route. *Journal of Materials Chemistry* **1996,** 6, (10), 1665-1671.
65. Rosen, M. J., *Surfactants and Interfacial Phenomena, 3rd Edition*. 2004; p 464 pp.
66. Israelachvili, J. N., *Intermolecular and Surface Forces*. 2nd ed.; Academic Press Inc.: San Diego, 1998; p 366.
67. Nagarajan, R., Molecular Packing Parameter and Surfactant Self-Assembly: The Neglected Role of the Surfactant Tail. *Langmuir* **2002,** 18, (1), 31-38.
68. Tanford, C., *The Hydrophobic Effect: Formation of Micelles and Biological Membranes. 2nd Ed*. 1980; p 233 pp.
69. Puvvada, S.; Blankschtein, D., Molecular-thermodynamic approach to predict micellization, phase behavior and phase separation of micellar solutions. I. Application to nonionic surfactants. *Journal of Chemical Physics* **1990,** 92, (6), 3710-24.
70. Nagarajan, R.; Ruckenstein, E., Theory of surfactant self-assembly: a predictive molecular thermodynamic approach. *Langmuir* **1991,** 7, (12), 2934-69.
71. Kumar, V. V., Complementary molecular shapes and additivity of the packing parameter of lipids. *Proceedings of the National Academy of Sciences of the United States of America* **1991,** 88, (2), 444-8.
72. Fontell, K., Cubic phases in surfactant and surfactant-like lipid systems. *Colloid and Polymer Science* **1990,** 268, (3), 264-85.
73. Alexandridis, P.; Olsson, U.; Lindman, B., A Record Nine Different Phases (Four Cubic, Two Hexagonal, and One Lamellar Lyotropic Liquid Crystalline and Two Micellar Solutions) in a Ternary Isothermal System of an Amphiphilic Block Copolymer and Selective Solvents (Water and Oil). *Langmuir* **1998,** 14, (10), 2627-2638.
74. Mariani, P.; Luzzati, V.; Delacroix, H., Cubic phases of lipid-containing systems. Structure analysis and biological implications. *Journal of Molecular Biology* **1988,** 204, (1), 165-89.
75. Luzzati, V.; Vargas, R.; Gulik, A.; Mariani, P.; Seddon, J. M.; Rivas, E., Lipid polymorphism: a correction. The structure of the cubic phase of extinction symbol Fd-- consists of two types of disjointed reverse micelles embedded in a three-dimensional hydrocarbon matrix. *Biochemistry* **1992,** 31, (1), 279-85.
76. Vargas, R.; Mariani, P.; Gulik, A.; Luzzati, V., Cubic phases of lipid-containing systems. The structure of phase Q223 (space group Pm3n). An x-ray scattering study. *Journal of Molecular Biology* **1992,** 225, (1), 137-45.
77. Attard, G. S.; Glyde, J. C.; Goltner, C. G., Liquid-crystalline phases as templates for the synthesis of mesoporous silica. *Nature (London)* **1995,** 378, (6555), 366-8.

78. Chen, C. Y.; Burkett, S. L.; Li, H. X.; Davis, M. E., Studies on mesoporous materials. II. Synthesis mechanism of MCM-41. *Microporous Mater.* **1993,** 2, (1), 27-34.
79. Vartuli, J. C.; Kresge, C. T.; Leonowicz, M. E.; Chu, A. S.; McCullen, S. B.; Johnson, I. D.; Sheppard, E. W., Synthesis of mesoporous materials: liquid-crystal templating versus intercalation of layered silicates. *Chemistry of Materials* **1994,** 6, (11), 2070-7.
80. Huo, Q.; Margolese, D. I.; Ciesla, U.; Demuth, D. G.; Feng, P.; Gier, T. E.; Sieger, P.; Firouzi, A.; Chmelka, B. F.; et al., Organization of Organic Molecules with Inorganic Molecular Species into Nanocomposite Biphase Arrays. *Chemistry of Materials* **1994,** 6, (8), 1176-91.
81. Behrens, P., Voids in variable chemical surroundings: mesoporous metal oxides. *Angew. Chem., Int. Ed. Engl.* **1996,** 35, (5), 515-18.
82. Ciesla, U.; Demuth, D.; Leon, R.; Petroff, P.; Stucky, G.; Unger, K.; Schueth, F., Surfactant controlled preparation of mesostructured transition-metal oxide compounds. *Journal of the Chemical Society, Chemical Communications* **1994**, (11), 1387-8.
83. Ogawa, M., Formation of Novel Oriented Transparent Films of Layered Silica-Surfactant Nanocomposites. *J. Am. Chem. Soc.* **1994,** 116, (17), 7941-2.
84. Ogawa, M., Preparation of transparent thin films of silica-surfactant mesostructured materials. *Supramolecular Science* **1998,** 5, (3-4), 247-251.
85. Ogawa, M.; Wada, T.; Kuroda, K., Intercalation of Pyrene into Alkylammonium-Exchanged Swelling Layered Silicates: The Effects of the Arrangements of the Interlayer Alkylammonium Ions on the States of Adsorbates. *Langmuir* **1995,** 11, (11), 4598-600.
86. Lu, Y.; Ganguli, R.; Drewien, C. A.; Anderson, M. T.; Brinker, C. J.; Gong, W.; Guo, Y.; Soyez, H.; Dunn, B.; Huang, M. H.; Zink, J. I., Continuous formation of supported cubic and hexagonal mesoporous films by sol-gel dip-coating. *Nature (London)* **1997,** 389, (6649), 364-368.
87. Grosso, D.; Babonneau, F.; Albouy, P.-A.; Amenitsch, H.; Balkenende, A. R.; Brunet-Bruneau, A.; Rivory, J., An in Situ Study of Mesostructured CTAB-Silica Film Formation during Dip Coating Using Time-Resolved SAXS and Interferometry Measurements. *Chem. Mater.* **2002,** 14, (2), 931-939.
88. Crepaldi, E. L.; de Soler-Illia, G. J.; Grosso, D.; Cagnol, F.; Ribot, F.; Sanchez, C., Controlled Formation of Highly Organized Mesoporous Titania Thin Films: From Mesostructured Hybrids to Mesoporous Nanoanatase TiO2. *J. Am. Chem. Soc.* **2003,** 125, (32), 9770-9786.
89. Hayward, R. C.; Alberius, P. C. A.; Kramer, E. J.; Chmelka, B. F., Thin Films of Bicontinuous Cubic Mesostructured Silica Templated by a Nonionic Surfactant. *Langmuir* **2004,** 20, (14), 5998-6004.
90. Cagnol, F.; Grosso, D.; Soler-Illia, G. J. d. A. A.; Crepaldi, E. L.; Babonneau, F.; Amenitsch, H.; Sanchez, C., Humidity-controlled mesostructuration in CTAB-templated silica thin film processing. The existence of a modulable steady state. *J. Mater. Chem.* **2003,** 13, (1), 61-66.
91. Alberius, P. C. A.; Frindell, K. L.; Hayward, R. C.; Kramer, E. J.; Stucky, G. D.; Chmelka, B. F., General Predictive Syntheses of Cubic, Hexagonal, and Lamellar Silica and Titania Mesostructured Thin Films. *Chemistry of Materials* **2002,** 14, (8), 3284-3294.

92. Besson, S.; Gacoin, T.; Ricolleau, C.; Jacquiod, C.; Boilot, J.-P., Phase diagram for mesoporous CTAB-silica films prepared under dynamic conditions. *J. Mater. Chem.* **2003,** 13, (2), 404-409.
93. Sakka, S.; Kamiya, K., Glasses from metal alcoholates. *J. Non-Cryst. Solids* **1980,** 42, (1-3), 403-21.
94. Rabinovich, E. M., Preparation of glass by sintering. *J. Mater. Sci.* **1985,** 20, (12), 4259-97.
95. Segal, D. L., Sol-gel processing: routes to oxide ceramics using colloidal dispersions of hydrous oxides and alkoxide intermediates. *J. Non-Cryst. Solids* **1984,** 63, (1-2), 183-91.
96. Brinker, C.; Scherer, G., *Sol-Gel Science: The Physics and Chemistry of Sol-Gel Processing*. 1990; p No pp given.
97. Boonstra, A. H.; Meeuwsen, T. P. M.; Baken, J. M. E.; Aben, G. V. A., A two-step silica sol-gel process investigated with static and dynamic light-scattering measurements. *J. Non-Cryst. Solids* **1989,** 109, (2-3), 153-63.
98. Brinker, C. J., Hydrolysis and condensation of silicates: effects on structure. *J. Non-Cryst. Solids* **1988,** 100, (1-3), 31-50.
99. Rankin, S. E.; Sefcik, J.; McCormick, A. V., Similarities in the Hydrolysis Pseudoequilibrium Behavior of Methyl-Substituted Ethoxysilanes. *Industrial & Engineering Chemistry Research* **1999,** 38, (9), 3191-3198.
100. Boonstra, A. H.; Bernards, T. N. M., The dependence of the gelation time on the hydrolysis time in a two-step silica sol-gel process. *J. Non-Cryst. Solids* **1988,** 105, (3), 207-13.
101. Sanchez, J.; McCormick, A., Kinetic and thermodynamic study of the hydrolysis of silicon alkoxides in acidic alcohol solutions. *J. Phys. Chem.* **1992,** 96, (22), 8973-9.
102. Damrau, U.; Marsmann, H. C., The hydrolysis of oligomer intermediates in the sol-gel process. *J. Non-Cryst. Solids* **1994,** 168, (1-2), 42-8.
103. Boonstra, A. H.; Baken, J. M. E., Relation between the acidity and reactivity of a TEOS, ethanol, and water mixture. *J. Non-Cryst. Solids* **1990,** 122, (2), 171-82.
104. Curran, M. D.; Stiegman, A. E., Morphology and pore structure of silica xerogels made at low pH. *J. Non-Cryst. Solids* **1999,** 249, (1), 62-68.
105. Rankin, S. E.; McCormick, A. V., Hydrolysis pseudoequilibrium: challenges and opportunities to sol-gel silicate kinetics. *Chem. Eng. Sci.* **2000,** 55, (11), 1955-1967.
106. Colby, M. W.; Osaka, A.; Mackenzie, J. D., Temperature dependence of the gelation of silicon alkoxides. *J. Non-Cryst. Solids* **1988,** 99, (1), 129-39.
107. Chen, K. C.; Tsuchiya, T.; Mackenzie, J. D., Sol-gel processing of silica. I. The role of the starting compounds. *J. Non-Cryst. Solids* **1986,** 81, (1-2), 227-37.
108. Brinker, C. J.; Keefer, K. D.; Schaefer, D. W.; Ashley, C. S., Sol-gel transition in simple silicates. *J. Non-Cryst. Solids* **1982,** 48, (1), 47-64.
109. Scherer, G. W., Drying gels. VI. Viscoelastic plate. *J. Non-Cryst. Solids* **1988,** 99, (2-3), 324-58.
110. Fidalgo, A.; Rosa, M. E.; Ilharco, L. M., Chemical Control of Highly Porous Silica Xerogels: Physical Properties and Morphology. *Chem. Mater.* **2003,** 15, (11), 2186-2192.
111. Prakash, S. S.; Brinker, C. J.; Hurd, A. J., Silica aerogel films at ambient pressure. *J. Non-Cryst. Solids* **1995,** 190, (3), 264-75.

112. Rosen, M. J.; Zhou, Q., Surfactant-surfactant interactions in mixed monolayer and mixed micelle formation. *Langmuir* **2001,** 17, (12), 3532-3537.
113. Rosen, M. J.; Sulthana, S. B., The Interaction of Alkylglycosides with Other Surfactants. *Journal of Colloid and Interface Science* **2001,** 239, (2), 528-534.
114. Pang, J.; Eric Hampsey, J.; Hu, Q.; Wu, Z.; John, V. T.; Lu, Y., Mesoporous silica with Ia3d cubic structure and good thermal stability. *Chem. Commun. (Cambridge, U. K.)* **2004**, (6), 682-683.
115. Chen, D.; Li, Z.; Wan, Y.; Tu, X.; Shi, Y.; Chen, Z.; Shen, W.; Yu, C.; Tu, B.; Zhao, D., Anionic surfactant induced mesophase transformation to synthesize highly ordered large-pore mesoporous silica structures. *Journal of Materials Chemistry* **2006,** 16, (16), 1511-1519.
116. Chen, D.; Li, Z.; Yu, C.; Shi, Y.; Zhang, Z.; Tu, B.; Zhao, D., Nonionic Block Copolymer and Anionic Mixed Surfactants Directed Synthesis of Highly Ordered Mesoporous Silica with Bicontinuous Cubic Structure. *Chemistry of Materials* **2005,** 17, (12), 3228-3234.
117. Ryoo, R.; Ko, C. H.; Park, I.-S., Synthesis of highly ordered MCM-41 by micelle-packing control with mixed surfactants. *Chem. Commun. (Cambridge)* **1999**, (15), 1413-1414.
118. Tian, B.; Liu, X.; Zhang, Z.; Tu, B.; Zhao, D., Syntheses of High-Quality Mesoporous Materials Directed by Blends of Nonionic Amphiphiles under Nonaqueous Conditions. *Journal of Solid State Chemistry* **2002,** 167, (2), 324-329.
119. Lind, A.; Spliethoff, B.; Linden, M., Unusual, Vesicle-like Patterned, Mesoscopically Ordered Silica. *Chem. Mater.* **2003,** 15, (3), 813-818.
120. Jana, S. K.; Mochizuki, A.; Namba, S., Progress in Pore-Size Control of Mesoporous MCM-41 Molecular Sieve Using Surfactant Having Different Alkyl Chain Lengths and Various Organic Auxiliary Chemicals. *Catalysis Surveys from Asia* **2004,** 8, (1), 1-13.
121. Dai, L. R.; Wang, T. W.; Bu, L. T.; Chen, G., Mixed surfactant templating route for mesoporous silica. *Colloids and Surfaces, A: Physicochemical and Engineering Aspects* **2001,** 181, (1-3), 151-157.
122. Liang, Y.; Hanzlik, M.; Anwander, R., Periodic mesoporous organosilicas: mesophase control via binary surfactant mixtures. *Journal of Materials Chemistry* **2006,** 16, (13), 1238-1253.
123. Brunauer, S.; Emmett, P. H.; Teller, E., Adsorption of gases in multimolecular layers. *Journal of the American Chemical Society* **1938,** 60, 309-19.
124. Sayari, A.; Liu, P.; Kruk, M.; Jaroniec, M., Characterization of Large-Pore MCM-41 Molecular Sieves Obtained via Hydrothermal Restructuring. *Chemistry of Materials* **1997,** 9, (11), 2499-2506.
125. Barrett, E. P.; Joyner, L. G.; Halenda, P. P., The determination of pore volume and area distributions in porous substances. I. Computations from nitrogen isotherms. *Journal of the American Chemical Society* **1951,** 73, 373-80.
126. Kruk, M.; Jaroniec, M.; Sayari, A., Adsorption Study of Surface and Structural Properties of MCM-41 Materials of Different Pore Sizes. *Journal of Physical Chemistry B* **1997,** 101, (4), 583-589.
127. Kruk, M.; Jaroniec, M., Gas adsorption characterization of ordered organic-inorganic nanocomposite materials. *Chemistry of Materials* **2001,** 13, (10), 3169-3183.

128. Gregg, S. J.; Sing, K. S. W., *Adsorption, Surface Area and Porosity. 2nd Ed*. 1982; p 303 pp.
129. Lastoskie, C.; Gubbins, K. E.; Quirke, N., Pore size distribution analysis of microporous carbons: a density functional theory approach. *J. Phys. Chem.* **1993,** 97, (18), 4786-96.
130. Ravikovitch, P. I.; Domhnaill, S. C. O.; Neimark, A. V.; Schueth, F.; Unger, K. K., Capillary Hysteresis in Nanopores: Theoretical and Experimental Studies of Nitrogen Adsorption on MCM-41. *Langmuir* **1995,** 11, (12), 4765-72.
131. Kruk, M.; Jaroniec, M.; Sayari, A., Application of Large Pore MCM-41 Molecular Sieves To Improve Pore Size Analysis Using Nitrogen Adsorption Measurements. *Langmuir* **1997,** 13, (23), 6267-6273.
132. Naono, H.; Hakuman, M.; Shiono, T., Analysis of nitrogen adsorption isotherms for a series of porous silicas with uniform and cylindrical pores: a new method of calculating pore size distribution of pore radius 1-2 nm. *Journal of Colloid and Interface Science* **1997,** 186, (2), 360-368.
133. Jaroniec, M.; Kruk, M.; Olivier, J. P., Standard Nitrogen Adsorption Data for Characterization of Nanoporous Silicas. *Langmuir* **1999,** 15, (16), 5410-5413.
134. Qiao, S. Z.; Bhatia, S. K.; Zhao, X. S., Prediction of multilayer adsorption and capillary condensation phenomena in cylindrical mesopores. *Microporous Mesoporous Mater.* **2003,** 65, (2-3), 287-298.
135. Pavia, D. L.; Lampman, G. M.; Kriz, G. S., *Introduction to Spectroscopy*. 3rd ed.; Thomson Learning: Australia, 2001.
136. Stuart, B. H., *Infrared Spectroscopy-Fundamentals and Applications*. John Wiley & Sons: Chichester, UK, 2004.
137. Fultz, B.; Howe, J. M., *Transmission electron microscopy and diffractometry of materials*. 2nd ed.; Springer: Berlin, 2002.
138. Donlon, W. T.; Chen, A. E.; Hangas, J. W.; Paputa Peck, M. C., Automotive Applications of Scanning and Transmission Electron Microscopy. In *Industrial Applications of Electron Microscopy* Li, Z. R., Ed. Marcel Dekker, Inc.: New York, 2003.
139. Bozzola, J. J.; Russell, L. D., *Electron Microscopy Principles and Techniques for Biologists*. 2nd ed.; Jones and Bartlett Publishers: Canada, 1999.
140. Sickafus, K. E.; Mitchell, E. T., Electron Microscopy of Ceramic Materials. In *Industrial Applications of Electron Microscopy* Li, Z. R., Ed. Marcel Dekker, Inc.: New York, 2003.
141. Hamley, I. W., *Introduction To Soft Matter: Polymers, Colloids, amphiphiles and Liquid Crystals*. John Wiley & Sons, Ltd.: Chichester, 2000.
142. Holmberg, K.; Lindman, B.; Joensoon, B.; Kronberg, B., *Surfactants and Polymers in Aqueous Solution, 2nd Edition*. 2002; p 544 pp.
143. Maschmeyer, T., Derivatized mesoporous solids. *Current Opinion in Solid State & Materials Science* **1998,** 3, (1), 71-78.
144. Kisler, J. M.; Dahler, A.; Stevens, G. W.; O'Connor, A. J., Separation of biological molecules using mesoporous molecular sieves. *Microporous and Mesoporous Materials* **2001,** 44-45, 769-774.
145. Gruen, M.; Kurganov, A. A.; Schacht, S.; Schueth, F.; Unger, K. K., Comparison of an ordered mesoporous aluminosilicate, silica, alumina, titania and zirconia in normal-

phase high-performance liquid chromatography. *Journal of Chromatography, A* **1996,** 740, (1), 1-9.
146. Beck, J. S.; Vartuli, J. C., Recent advances in the synthesis, characterization and applications of mesoporous molecular sieves. *Current Opinion in Solid State & Materials Science* **1996,** 1, (1), 76-87.
147. Inagaki, S.; Fukushima, Y.; Kuroda, K., Synthesis of highly ordered mesoporous materials from a layered polysilicate. *Journal of the Chemical Society, Chemical Communications* **1993**, (8), 680-2.
148. Templin, M.; Franck, A.; Du Chesne, A.; Leist, H.; Zhang, Y.; Ulrich, R.; Schadler, V.; Wiesner, U., Organically modified aluminosilicate mesostructures from block copolymer phases. *Science (Washington, D. C.)* **1997,** 278, (5344), 1795-1798.
149. Lind, A.; Andersson, J.; Karlsson, S.; Aagren, P.; Bussian, P.; Amenitsch, H.; Linden, M., Controlled Solubilization of Toluene by Silicate-Catanionic Surfactant Mesophases as Studied by in Situ and ex Situ XRD. *Langmuir* **2002,** 18, (4), 1380-1385.
150. Ryoo, R.; Kim, J. M., Structural order in MCM-41 controlled by shifting silicate polymerization equilibrium. *Journal of the Chemical Society, Chemical Communications* **1995**, (7), 711-12.
151. Zhao, W.; Li, Q., Synthesis of Nanosize MCM-48 with High Thermal Stability. *Chemistry of Materials* **2003,** 15, (22), 4160-4162.
152. Auvray, X.; Petipas, C.; Anthore, R.; Rico-Lattes, I.; Lattes, A., X-ray Diffraction Study of the Ordered Lyotropic Phases Formed by Sugar-Based Surfactants. *Langmuir* **1995,** 11, (2), 433-9.
153. Boyd, B. J.; Drummond, C. J.; Krodkiewska, I.; Grieser, F., How Chain Length, Headgroup Polymerization, and Anomeric Configuration Govern the Thermotropic and Lyotropic Liquid Crystalline Phase Behavior and the Air-Water Interfacial Adsorption of Glucose-Based Surfactants. *Langmuir* **2000,** 16, (19), 7359-7367.
154. Nilsson, F.; Soederman, O.; Johansson, I., Physical-Chemical Properties of the n-Octyl b-D-Glucoside/Water System. A Phase Diagram, Self-Diffusion NMR and SAXS Study. *Langmuir* **1996,** 12, (4), 902-8.
155. Boyd, B. J.; Drummond, C. J.; Krodkiewska, I.; Weerawardena, A.; Furlong, D. N.; Grieser, F., Alkyl Chain Positional Isomers of Dodecyl b-D-Glucoside: Thermotropic and Lyotropic Phase Behavior and Detergency. *Langmuir* **2001,** 17, (20), 6100-6107.
156. Jung, J. H.; Amaike, M.; Nakashima, K.; Shinkai, S., Preparation of novel silica structures using a library of carbohydrate gel assemblies as templates for sol-gel transcription. *Journal of the Chemical Society, Perkin Transactions 2* **2001**, (10), 1938-1943.
157. Farnik, D.; Binder, W. H.; Huesing, N., Novel carbohydrate-based surfactants for the preparation of imprinted silica. *Polymer Preprints (American Chemical Society, Division of Polymer Chemistry)* **2005,** 46, (2), 1140-1141.
158. Morihara, K.; Takiguchi, M.; Shimada, T., Footprint catalysis. XI. Molecular footprint cavities imprinted with chiral amines and their chiral molecular recognition. *Bulletin of the Chemical Society of Japan* **1994,** 67, (4), 1078-84.
159. Garcia, M. T.; Ribosa, I.; Campos, E.; Leal, J. S., Ecological properties of alkylglucosides. *Chemosphere* **1997,** 35, (3), 545-556.
160. Schmid, K. T., H, In *Detergency of Specialty Surfactants.*, Friedli, F. E., Ed. Dekker: New York, 2001; Vol. 98, p 1.

161. Huesing, N.; Launay, B.; Kickelbick, G., Synthesis and functionalization of mesostructured silica-based films. *Silicon Chemistry* **2003**, 451-459.
162. Lavrencic-Stangar, U.; Puchberger, M.; Husing, N., Meso-ordered silica films formed by sugar-based surfactants. *Materials Research Society Symposium Proceedings* **2002,** 726, (Organic/Inorganic Hybrid Materials--2002), 111-116.
163. Stangar, U. L.; Huesing, N., Alkyl-glycoside surfactants in the synthesis of mesoporous silica films. *Silicon Chemistry* **2003,** 2, (3-4), 157-165.
164. Warr, G. G.; Drummond, C. J.; Grieser, F.; Ninham, B. W.; Evans, D. F., Aqueous solution properties of nonionic n-dodecyl b-D-maltoside micelles. *Journal of Physical Chemistry* **1986,** 90, (19), 4581-6.
165. Auvray, X.; Petipas, C.; Anthore, R.; Rico, I.; Lattes, A., X-ray diffraction study of mesophases of cetyltrimethylammonium bromide in water, formamide, and glycerol. *Journal of Physical Chemistry* **1989,** 93, (21), 7458-64.
166. Waernheim, T.; Joensson, A., Phase diagrams of alkyltrimethylammonium surfactants in some polar solvents. *Journal of Colloid and Interface Science* **1988,** 125, (2), 627-33.
167. Yang, B.; White, J. W., Isotope effects on the phase behaviour of cetyltrimethylammonium bromide in H2O and D2O studied by time resolved X-ray diffraction. *Colloids and Surfaces, A: Physicochemical and Engineering Aspects* **2006,** 277, (1-3), 171-176.
168. Soederberg, I.; Drummond, C. J.; Furlong, D. N.; Godkin, S.; Matthews, B., Non-ionic sugar-based surfactants: self assembly and air/water interfacial activity. *Colloids and Surfaces, A: Physicochemical and Engineering Aspects* **1995,** 102, 91-7.
169. Drummond, C. J.; Wells, D., Nonionic lactose and lactitol based surfactants: comparison of some physicochemical properties. *Colloids and Surfaces, A: Physicochemical and Engineering Aspects* **1998,** 141, (1), 131-142.
170. Xing, R.; Rankin, S. E., Use of the ternary phase diagram of a mixed cationic/glucopyranoside surfactant system to predict mesostructured silica synthesis. *Journal of Colloid and Interface Science* **2007,** 316, (2), 930-938.
171. Pindzola, B. A.; Jin, J.; Gin, D. L., Cross-Linked Normal Hexagonal and Bicontinuous Cubic Assemblies via Polymerizable Gemini Amphiphiles. *Journal of the American Chemical Society* **2003,** 125, (10), 2940-2949.
172. Rosevear, F. B., The microscopy of the liquid crystalline neat and middle phases of soaps and synthetic detergents. *Journal of the American Oil Chemists' Society* **1954,** 31, 628-39.
173. Rosevear, F. B., Liquid crystals: the mesomorphic phases of surfactant compositions. *Journal of the Society of Cosmetic Chemists* **1968,** 19, 581-94.
174. Hajduk, D. A.; Harper, P. E.; Gruner, S. M.; Honeker, C. C.; Kim, G.; Thomas, E. L.; Fetters, L. J., The Gyroid: A New Equilibrium Morphology in Weakly Segregated Diblock Copolymers. *Macromolecules* **1994,** 27, (15), 4063-75.
175. Husson, F.; Mustacchi, H.; Luzzati, V., The structure of association colloids. II. Description of the liquid-crystalline phases of several amphiphile-water systems: anionic, cationic, nonionic amphiphiles. *Acta Cryst.* **1960,** 13, 668-77.
176. Gustafsson, S.; Quist, P.-O., Nuclear magnetic resonance and x-ray study of a rectangular phase. *Journal of Colloid and Interface Science* **1996,** 180, (2), 564-573.

177. Charvolin, J., Evolution of cylindrical structures in the system sodium decyl sulfate/decanol/water. *Liquid Crystals* **1993,** 13, (6), 829-42.
178. Hagslaett, H.; Soederman, O.; Joensson, B., The structure of intermediate ribbon phases in surfactant systems. *Liquid Crystals* **1992,** 12, (4), 667-88.
179. Hagslaett, H.; Soederman, O.; Joensson, B., Ribbon phases in surfactant systems. Comparisons between exptl. results and predictions of a theoretical model. *Liquid Crystals* **1994,** 17, (2), 157-77.
180. Acharya, D. P.; Kunieda, H.; Shiba, Y.; Aratani, K., Phase and Rheological Behavior of Novel Gemini-Type Surfactant Systems. *Journal of Physical Chemistry B* **2004,** 108, (5), 1790-1797.
181. Auvray, X.; Perche, T.; Anthore, R.; Petipas, C.; Rico, I.; Lattes, A., Structure of lyotropic phases formed by sodium dodecyl sulfate in polar solvents. *Langmuir* **1991,** 7, (10), 2385-93.
182. Zhao, D.; Huo, Q.; Feng, J.; Kim, J.; Han, Y.; Stucky, G. D., Novel Mesoporous Silicates with Two-Dimensional Mesostructure Direction Using Rigid Bolaform Surfactants. *Chemistry of Materials* **1999,** 11, (10), 2668-2672.
183. Zhang, W.; Pauly, T. R.; Pinnavaia, T. J., Tailoring the Framework and Textural Mesopores of HMS Molecular Sieves through an Electrically Neutral (S DegI Deg) Assembly Pathway. *Chemistry of Materials* **1997,** 9, (11), 2491-2498.
184. Ryoo, R.; Kim, J. M.; Ko, C. H.; Shin, C. H., Disordered Molecular Sieve with Branched Mesoporous Channel Network. *Journal of Physical Chemistry* **1996,** 100, (45), 17718-17721.
185. Sreethawong, T.; Yamada, Y.; Kobayashi, T.; Yoshikawa, S., Catalysis of nanocrystalline mesoporous TiO2 on cyclohexene epoxidation with H2O2: Effects of mesoporosity and metal oxide additives. *Journal of Molecular Catalysis A: Chemical* **2005,** 241, (1-2), 23-32.
186. Hutter, R.; Mallat, T.; Baiker, A., Selective epoxidation of a-isophorone with mesoporous titania-silica aerogels and tert-butyl hydroperoxide. *Journal of the Chemical Society, Chemical Communications* **1995**, (24), 2487-8.
187. Dusi, M.; Mallat, T.; Baiker, A., Epoxidation of functionalized olefins over solid catalysts. *Catalysis Reviews - Science and Engineering* **2000,** 42, (1 & 2), 213-278.
188. Pozzo, R. L.; Baltanas, M. A.; Cassano, A. E., Supported titanium oxide as photocatalyst in water decontamination: state of the art. *Catalysis Today* **1997,** 39, (3), 219-231.
189. Yamashita, H.; Kawasaki, S.; Ichihashi, Y.; Harada, M.; Takeuchi, M.; Anpo, M.; Stewart, G.; Fox, M. A.; Louis, C.; Che, M., Characterization of Titanium-Silicon Binary Oxide Catalysts Prepared by the Sol-Gel Method and Their Photocatalytic Reactivity for the Liquid-Phase Oxidation of 1-Octanol. *Journal of Physical Chemistry B* **1998,** 102, (30), 5870-5875.
190. Thomas, J. M.; Sankar, G.; Klunduk, M. C.; Attfield, M. P.; Maschmeyer, T.; Johnson, B. F. G.; Bell, R. G., The Identity in Atomic Structure and Performance of Active Sites in Heterogeneous and Homogeneous, Titanium-Silica Epoxidation Catalysts. *Journal of Physical Chemistry B* **1999,** 103, (42), 8809-8813.
191. Beck, C.; Mallat, T.; Buergi, T.; Baiker, A., Nature of Active Sites in Sol-Gel TiO2-SiO2 Epoxidation Catalysts. *Journal of Catalysis* **2001,** 204, (2), 428-439.

192. Clerici, M. G., Oxidation of saturated hydrocarbons with hydrogen peroxide, catalyzed by titanium silicalite. *Applied Catalysis* **1991,** 68, (1-2), 249-61.
193. Clerici, M. G.; Ingallina, P., Epoxidation of lower olefins with hydrogen peroxide and titanium silicalite. *Journal of Catalysis* **1993,** 140, (1), 71-83.
194. Pena, M. L.; Dellarocca, V.; Rey, F.; Corma, A.; Coluccia, S.; Marchese, L., Elucidating the local environment of Ti(IV) active sites in Ti-MCM-48: a comparison between silylated and calcined catalysts. *Microporous and Mesoporous Materials* **2001,** 44-45, 345-356.
195. Koyano, K. A.; Tatsumi, T., Synthesis of titanium-containing mesoporous molecular sieves with a cubic structure. *Chemical Communications (Cambridge)* **1996**, (2), 145-46.
196. Ji, D.; Zhao, R.; Lu, G.; Qian, G.; Yan, L.; Suo, J., Direct synthesis, characterization and catalytic performance of novel Ti-SBA-1 cubic mesoporous molecular sieves. *Applied Catalysis, A: General* **2005,** 281, (1-2), 39-45.
197. Livage, J.; Sanchez, C., Sol-gel chemistry. *Journal of Non-Crystalline Solids* **1992,** 145, (1-3), 11-19.
198. Schroeder, T.; Ugrinova, V.; Noll, B. C.; Brown, S. N., A chelating b-diketonate/phenoxide ligand and its coordination behavior toward titanium and scandium. *Dalton Transactions* **2006**, (8), 1030-1040.
199. Dutoit, D. C. M.; Schneider, M.; Baiker, A., Titania-silica mixed oxides. I. Influence of sol-gel and drying conditions on structural properties. *Journal of Catalysis* **1995,** 153, (1), 165-76.
200. Froba, M.; Muth, O.; Reller, A., Mesostructured TiO2: ligand-stabilized synthesis and characterization. *Solid State Ionics* **1997,** 101-103, (Pt. 1), 249-253.
201. Mendez-Vivar, J.; Mendoza-Serna, R.; Gomez-Lara, J.; Gavino, R., Spectroscopic study of SiO2-TiO2 sols prepared using stabilizing agents. *Journal of Sol-Gel Science and Technology* **1997,** 8, (1/2/3), 235-241.
202. Sun, D.; Huang, Y.; Han, B.; Yang, G., Ti-Si Mixed Oxides Prepared by Polymer in Situ Sol-Gel Chemistry with the Aid of CO2. *Langmuir* **2006,** 22, (10), 4793-4798.
203. Celik, O.; Dag, O., A new lyotropic liquid crystalline system: oligo(ethylene oxide) surfactants with [M(H2O)n]Xm transition metal complexes. *Angewandte Chemie, International Edition* **2001,** 40, (20), 3800-3803.
204. Huesing, N.; Launay, B.; Kickelbick, G.; Gross, S.; Armelao, L.; Bottaro, G.; Feth, M. P.; Bertagnolli, H.; Kothleitner, G., Transition metal oxide-doped mesostructured silica films. *Applied Catalysis, A: General* **2003,** 254, (2), 297-310.
205. Huesing, N.; Launay, B.; Doshi, D.; Kickelbick, G., Mesostructured Silica-Titania Mixed Oxide Thin Films. *Chemistry of Materials* **2002,** 14, (6), 2429-2432.
206. Huesing, N.; Launay, B.; Kickelbick, G.; Hofer, F., Silica-Titania Mesostructured Films. *Journal of Sol-Gel Science and Technology* **2003,** 26, (1/2/3), 615-619.
207. Saltman, P., The role of chelation in iron metabolism. *J Chem Educ FIELD Full Journal Title:Journal of chemical education* **1965,** 42, (12), 682-7.
208. Mukhopadhyay, A.; Karkamkar, A.; Kolehmainen, E.; Rao, C. P., Transition metal-saccharide chemistry: synthesis, characterization and solution stability studies of cis-dioxomolybdenum saccharide complexes. *Carbohydrate Research* **1998,** 311, (3), 147-154.

209. Geetha, K.; Raghavan, M. S. S.; Kulshreshtha, S. K.; Sasikala, R.; Rao, C. P., Transition-metal saccharide chemistry: synthesis, spectroscopy, electrochemistry and magnetic susceptibility studies of iron(III) complexes of mono- and disaccharides. *Carbohydrate Research* **1995,** 271, (2), 163-75.
210. Rao, C. P.; Geetha, K.; Raghavan, M. S. S.; Sreedhara, A.; Tokunaga, K.; Yamaguchi, T.; Jadhav, V.; Ganesh, K. N.; Krishnamoorthy, T.; Ramaiah, K. V. A.; Bhattacharyya, R. K., Transition metal saccharide chemistry and biology: syntheses, characterization, solution stability and putative bio-relevant studies of iron-saccharide complexes. *Inorganica Chimica Acta* **2000,** 297, (1-2), 373-382.
211. Tani, K.; Kitada, M.; Tachibana, M.; Koizumi, H.; Kiba, T., Retention behavior of monosaccharides and disaccharides on titania. *Chromatographia* **2003,** 57, (5/6), 409-412.
212. Perez, Y.; del Hierro, I.; Fajardo, M.; Otero, A., Synthesis and structure of titanium alkoxide complexes with bulky ligands derived from natural products. Asymmetric epoxidation of cinnamyl alcohol. *Journal of Organometallic Chemistry* **2003,** 679, (2), 220-228.
213. Vayssilov, G. N., Structural and physicochemical features of titanium silicalites. *Catalysis Reviews - Science and Engineering* **1997,** 39, (3), 209-251.
214. Gao, X.; Wachs, I. E., Titania-silica as catalysts: molecular structural characteristics and physico-chemical properties. *Catalysis Today* **1999,** 51, (2), 233-254.
215. Notari, B., Microporous crystalline titanium silicates. *Advances in Catalysis* **1996,** 41, 253-334.
216. Murata, C.; Yoshida, H.; Kumagai, J.; Hattori, T., Active Sites and Active Oxygen Species for Photocatalytic Epoxidation of Propene by Molecular Oxygen over TiO2-SiO2 Binary Oxides. *Journal of Physical Chemistry B* **2003,** 107, (18), 4364-4373.
217. Wang, X.; Lian, W.; Fu, X.; Basset, J.-M.; Lefebvre, F., Structure, preparation and photocatalytic activity of titanium oxides on MCM-41 surface. *Journal of Catalysis* **2006,** 238, (1), 13-20.
218. Zhang, F.-Z.; Guo, X.-W.; Wang, X.-S.; Li, G.; Zhou, J.-C.; Yu, J.-Q.; Li, C., The active sites in different TS-1 zeolites for propylene epoxidation studied by ultraviolet resonance Raman and ultraviolet visible absorption spectroscopies. *Catalysis Letters* **2001,** 72, (3-4), 235-239.
219. Geobaldo, F.; Bordiga, S.; Zecchina, A.; Giamello, E.; Leofanti, G.; Petrini, G., DRS UV-visible and EPR spectroscopy of hydroperoxo and superoxo complexes in titanium silicalite. *Catalysis Letters* **1992,** 16, (1-2), 109-15.
220. Klaas, J.; Schulz-Ekloff, G.; Jaeger, N. I., UV-Visible Diffuse Reflectance Spectroscopy of Zeolite-Hosted Mononuclear Titanium Oxide Species. *Journal of Physical Chemistry B* **1997,** 101, (8), 1305-1311.
221. Morrow, B. A.; McFarlan, A. J., Chemical reactions at silica surfaces. *Journal of Non-Crystalline Solids* **1990,** 120, (1-3), 61-71.
222. Tuel, A., Synthesis, characterization, and catalytic properties of the new TiZSM-12 zeolite. *Zeolites* **1995,** 15, (3), 236-42.
223. Blasco, T.; Camblor, M. A.; Corma, A.; Perez-Pariente, J., The state of Ti in titanoaluminosilicates isomorphous with zeolite b. *Journal of the American Chemical Society* **1993,** 115, (25), 11806-13.

224. Petrini, G.; Cesana, A.; De Alberti, G.; Genoni, F.; Leofanti, G.; Padovan, M.; Paparatto, G.; Roffia, P., Deactivation phenomena on titanium silicalite. *Studies in Surface Science and Catalysis* **1991,** 68, (Catal. Deact. 1991), 761-6.
225. Inoue, T.; Gunjishima, I.; Kumai, Y.; Inagaki, S.; Okamoto, A., Structural characteristic of outermost surface of cubic mesoporous silica film. *Chemistry Letters* **2007,** 36, (7), 862-863.
226. Wu, C.-W.; Kuwabara, M., Direct Synthesis and Characterization of High Titanium-Loading Hexagonal Mesostructured Silica Thin Films. *Journal of Inorganic and Organometallic Polymers* **2003,** 13, (3), 131-141.
227. Newalkar, B. L.; Olanrewaju, J.; Komarneni, S., Direct Synthesis of Titanium-Substituted Mesoporous SBA-15 Molecular Sieve under Microwave-Hydrothermal Conditions. *Chemistry of Materials* **2001,** 13, (2), 552-557.
228. Alba, M. D.; Luan, Z.; Klinowski, J., Titanosilicate Mesoporous Molecular Sieve MCM-41: Synthesis and Characterization. *Journal of Physical Chemistry* **1996,** 100, (6), 2178-82.
229. Rajakovic, V. N.; Mintova, S.; Senker, J.; Bein, T., Synthesis and characterization of V- and Ti-substituted mesoporous materials. *Materials Science & Engineering, C: Biomimetic and Supramolecular Systems* **2003,** C23, (6-8), 817-821.
230. Grosso, D.; Balkenende, A. R.; Albouy, P. A.; Ayral, A.; Amenitsch, H.; Babonneau, F., Two-Dimensional Hexagonal Mesoporous Silica Thin Films Prepared from Block Copolymers: Detailed Characterization and Formation Mechanism. *Chemistry of Materials* **2001,** 13, (5), 1848-1856.
231. Doshi, D. A.; Gibaud, A.; Liu, N.; Sturmayr, D.; Malanoski, A. P.; Dunphy, D. R.; Chen, H.; Narayanan, S.; MacPhee, A.; Wang, J.; Reed, S. T.; Hurd, A. J.; van Swol, F.; Brinker, C. J., In-Situ X-ray Scattering Study of Continuous Silica-Surfactant Self-Assembly during Steady-State Dip Coating. *Journal of Physical Chemistry B* **2003,** 107, (31), 7683-7688.
232. Nishiyama, N.; Tanaka, S.; Egashira, Y.; Oku, Y.; Ueyama, K., Enhancement of Structural Stability of Mesoporous Silica Thin Films Prepared by Spin-Coating. *Chemistry of Materials* **2002,** 14, (10), 4229-4234.
233. Lin, H. P.; Mou, C. Y.; Liu, S. B.; Tang, C. Y.; Lin, C. Y., Post-synthesis treatment of acid-made mesoporous silica materials by ammonia hydrothermal process. *Microporous and Mesoporous Materials* **2001,** 44-45, 129-137.
234. Boissiere, C.; Grosso, D.; Lepoutre, S.; Nicole, L.; Bruneau, A. B.; Sanchez, C., Porosity and Mechanical Properties of Mesoporous Thin Films Assessed by Environmental Ellipsometric Porosimetry. *Langmuir* **2005,** 21, (26), 12362-12371.
235. Honma, I.; Zhou, H. S.; Kundu, D.; Endo, A., Structural control of surfactant-templated hexagonal, cubic, and lamellar mesoporous silicate thin films prepared by spin-casting. *Advanced Materials (Weinheim, Germany)* **2000,** 12, (20), 1529-1533.
236. Matheron, M.; Bourgeois, A.; Brunet-Bruneau, A.; Albouy, P.-A.; Biteau, J.; Gacoin, T.; Boilot, J.-P., Highly ordered CTAB-templated organosilicate films. *J. Mater. Chem.* **2005,** 15, (44), 4741-4745.
237. Clerc, M., A new symmetry for the packing of amphiphilic direct micelles. *Journal de Physique II* **1996,** 6, (7), 961-968.
238. Taramasso, M. P., G.; Notari, B 4,410,501, 1983.
239. Notari, B., Titanium silicalites. *Catal. Today* **1993,** 18, (2), 163-72.

240. Huybrechts, D. R. C.; De Bruycker, L.; Jacobs, P. A., Oxyfunctionalization of alkanes with hydrogen peroxide on titanium silicalite. *Nature (London)* **1990,** 345, (6272), 240-2.
241. van der Waal, J. C.; Rigutto, M. S.; van Bekkum, H., Zeolite titanium beta as a selective catalyst in the epoxidation of bulky alkenes. *Appl. Catal., A* **1998,** 167, (2), 331-342.
242. Arends, I. W. C. E.; Sheldon, R. A.; Wallau, M.; Schuchardt, U., Oxidative transformations of organic compounds mediated by redox molecular sieves. *Angew. Chem., Int. Ed. Engl.* **1997,** 36, (11), 1145-1163.
243. Camblor, M. A.; Corma, A.; Martinez, A.; Perez-Pariente, J., Synthesis of a titanium silicoaluminate isomorphous to zeolite beta and its application as a catalyst for the selective oxidation of large organic molecules. *J. Chem. Soc., Chem. Commun.* **1992**, (8), 589-90.
244. Corma, A.; Esteve, P.; Martinez, A.; Valencia, S., Oxidation of olefins with hydrogen peroxide and tert-butyl hydroperoxide on Ti-beta catalyst. *J. Catal.* **1995,** 152, (1), 18-24.
245. Chandra, D.; Bhaumik, A., Highly Active 2D Hexagonal Mesoporous Titanium Silicate Synthesized Using a Cationic-Anionic Mixed-Surfactant Assembly. *Industrial & Engineering Chemistry Research* **2006,** 45, (14), 4879-4883.
246. Wu, P.; Tatsumi, T.; Komatsu, T.; Yashima, T., Postsynthesis, Characterization, and Catalytic Properties in Alkene Epoxidation of Hydrothermally Stable Mesoporous Ti-SBA-15. *Chem. Mater.* **2002,** 14, (4), 1657-1664.
247. Firouzi, A.; Kumar, D.; Bull, L. M.; Besier, T.; Sieger, P.; Huo, Q.; Walker, s. A.; Zasadzinski, J. A.; Glinka, C.; et al., Cooperative organization of inorganic-surfactant and biomimetic assemblies. *Science (Washington, D. C.)* **1995,** 267, (5201), 1138-43.
248. Katz, A.; Davis, M. E., Molecular imprinting of bulk, microporous silica. *Nature (London)* **2000,** 403, (6767), 286-289.
249. Katz, A.; Davis, M. E., Investigations into the Mechanisms of Molecular Recognition with Imprinted Polymers. *Macromolecules* **1999,** 32, (12), 4113-4121.
250. Matsui, J.; Miyoshi, Y.; Doblhoff-Dier, O.; Takeuchi, T., A molecularly imprinted synthetic polymer receptor selective for atrazine. *Anal. Chem.* **1995,** 67, (23), 4404-8.
251. Vlatakis, G.; Andersson, L. I.; Mueller, R.; Mosbach, K., Drug assay using antibody mimics made by molecular imprinting. *Nature (London)* **1993,** 361, (6413), 645-7.
252. Shea, K. J., Molecular imprinting of synthetic network polymers: the de novo synthesis of macromolecular binding and catalytic sites. *Trends in Polymer Science (Cambridge, United Kingdom)* **1994,** 2, (5), 166-73.
253. Davis, M. E.; Katz, A.; Ahmad, W. R., Rational Catalyst Design via Imprinted Nanostructured Materials. *Chem. Mater.* **1996,** 8, (8), 1820-1839.
254. Sambe, H.; Hoshina, K.; Haginaka, J., Retentivity and enantioselectivity of Uniformly-sized molecularly imprinted polymers for (S)-nilvadipine in aqueous and non-aqueous mobile phases. *Analytical Sciences* **2005,** 21, (4), 391-395.
255. Seong, H.; Lee, H.-B.; Park, K., Glucose binding to molecularly imprinted polymers. *Journal of Biomaterials Science, Polymer Edition* **2002,** 13, (6), 637-649.

256. Piletsky, S. A.; Piletskaya, E. V.; Panasyuk, T. L.; El'skaya, A. V.; Levi, R.; Karube, I.; Wulff, G., Imprinted Membranes for Sensor Technology: Opposite Behavior of Covalently and Noncovalently Imprinted Membranes. *Macromolecules* **1998,** 31, (7), 2137-2140.
257. Ellwanger, A.; Karlsson, L.; Owens, P. K.; Berggren, C.; Crecenzi, C.; Ensing, K.; Bayoudh, S.; Cormack, P.; Sherrington, D.; Sellergren, B., Evaluation of methods aimed at complete removal of template from molecularly imprinted polymers. *Analyst (Cambridge, United Kingdom)* **2001,** 126, (6), 784-792.
258. Jal, P. K.; Patel, S.; Mishra, B. K., Chemical modification of silica surface by immobilization of functional groups for extractive concentration of metal ions. *Talanta* **2004,** 62, (5), 1005-1028.
259. Schubert, U.; Huesing, N.; Lorenz, A., Hybrid Inorganic-Organic Materials by Sol-Gel Processing of Organofunctional Metal Alkoxides. *Chem. Mater.* **1995,** 7, (11), 2010-27.
260. Wen, J.; Wilkes, G. L., Organic/Inorganic Hybrid Network Materials by the Sol-Gel Approach. *Chem. Mater.* **1996,** 8, (8), 1667-1681.
261. Walcarius, A.; Luthi, N.; Blin, J. L.; Su, B. L.; Lamberts, L., Electrochemical evaluation of polysiloxane-immobilized amine ligands for the accumulation of copper(II) species. *Electrochimica Acta* **1999,** 44, (25), 4601-4610.
262. McKittrick, M. W.; Jones, C. W., Toward Single-Site Functional Materials-Preparation of Amine-Functionalized Surfaces Exhibiting Site-Isolated Behavior. *Chem. Mater.* **2003,** 15, (5), 1132-1139.
263. Chong, A. S. M.; Zhao, X. S.; Kustedjo, A. T.; Qiao, S. Z., Functionalization of large-pore mesoporous silicas with organosilanes by direct synthesis. *Microporous Mesoporous Mater.* **2004,** 72, (1-3), 33-42.
264. Hall, S. R.; Fowler, C. E.; Mann, S.; Lebeau, B., Template-directed synthesis of bi-functionalized organo-MCM-41 and phenyl-MCM-48 silica mesophases. *Chem. Commun. (Cambridge)* **1999**, (2), 201-202.
265. Liu, N.; Assink, R. A.; Smarsly, B.; Brinker, C. J., Synthesis and characterization of highly ordered functional mesoporous silica thin films with positively chargeable -NH2 groups. *Chem. Commun. (Cambridge, U. K.)* **2003**, (10), 1146-1147.
266. Chong, A. S. M.; Zhao, X. S., Functionalization of SBA-15 with APTES and Characterization of Functionalized Materials. *J. Phys. Chem. B* **2003,** 107, (46), 12650-12657.
267. Fowler, C. E.; Burkett, S. L.; Mann, S., Synthesis and characterization of ordered organosilica-surfactant mesophases with functionalized MCM-41-type architecture. *Chem. Commun. (Cambridge)* **1997**, (18), 1769-1770.
268. Lim, M. H.; Stein, A., Comparative Studies of Grafting and Direct Syntheses of Inorganic-Organic Hybrid Mesoporous Materials. *Chem. Mater.* **1999,** 11, (11), 3285-3295.
269. Macquarrie, D. J., Direct preparation of organically modified MCM-type materials. Preparation and characterization of aminopropyl-MCM and 2-cyanoethyl-MCM. *Chem. Commun. (Cambridge)* **1996**, (16), 1961-1962.
270. Fireman-Shoresh, S.; Avnir, D.; Marx, S., General Method for Chiral Imprinting of Sol-Gel Thin Films Exhibiting Enantioselectivity. *Chem. Mater.* **2003,** 15, (19), 3607-3613.

271. Yoshikawa, M.; Izumi, J.-I.; Kitao, T., Alternative molecular imprinting, a facile way to introduce chiral recognition sites. *Reactive & Functional Polymers* **1999,** 42, (1), 93-102.
272. Deore, B.; Chen, Z.; Nagaoka, T., Potential-induced enantioselective uptake of amino acid into molecularly imprinted overoxidized polypyrrole. *Anal. Chem.* **2000,** 72, (17), 3989-3994.
273. Wei, Y.; Xu, J.; Dong, H.; Dong, J. H.; Qiu, K.; Jansen-Varnum, S. A., Preparation and Physisorption Characterization of D-Glucose-Templated Mesoporous Silica Sol-Gel Materials. *Chem. Mater.* **1999,** 11, (8), 2023-2029.
274. Wizeman, W. J.; Kofinas, P., Molecularly imprinted polymer hydrogels displaying isomerically resolved glucose binding. *Biomaterials* **2001,** 22, (12), 1485-1491.
275. Ishihara, K.; Kobayashi, M.; Ishimaru, N.; Shinohara, I., Glucose-induced permeation control of insulin through a complex membrane consisting of immobilized glucose oxidase and a polyamine. *Polymer Journal (Tokyo, Japan)* **1984,** 16, (8), 625-31.
276. Obaidat, A. A.; Park, K., Characterization of protein release through glucose-sensitive hydrogel membranes. *Biomaterials* **1997,** 18, (11), 801-806.
277. Kim, J. J.; Park, K., Modulated insulin delivery from glucose-sensitive hydrogel dosage forms. *Journal of Controlled Release* **2001,** 77, (1-2), 39-47.
278. Kim, S. W.; Pai, C. M.; Makino, K.; Seminoff, L. A.; Holmberg, D. L.; Gleeson, J. M.; Wilson, D. E.; Mack, E. J., Self-regulated glycosylated insulin delivery. *Journal of Controlled Release* **1990,** 11, (1-3), 193-201.
279. Narang, U.; Prasad, P. N.; Bright, F. V.; Ramanathan, K.; Kumar, N. D.; Malhotra, B. D.; Kamalasanan, M. N.; Chandra, S., Glucose Biosensor Based on a Sol-Gel-Derived Platform. *Anal. Chem.* **1994,** 66, (19), 3139-44.
280. MacCraith, B. D.; McDonagh, C. M.; O'Keeffe, G.; McEvoy, A. K.; Butler, T.; Sheridan, F. R., Sol-gel coatings for optical chemical sensors and biosensors. *Sens. Actuators, B* **1995,** B29, (1-3), 51-7.
281. Grant, L. M.; Ederth, T.; Tiberg, F., Influence of Surface Hydrophobicity on the Layer Properties of Adsorbed Nonionic Surfactants. *Langmuir* **2000,** 16, (5), 2285-2291.
282. Dubois, M.; Gilles, K. A.; Hamilton, J. K.; Rebers, P. A.; Smith, F., Colorimetric method for determination of sugars and related substances. *Anal. Chem.* **1956,** 28, 350-6.
283. Suzuki, T.; Sota, T., Improving ab initio infrared spectra of glucose-water complexes by considering explicit intermolecular hydrogen bonds. *Journal of Chemical Physics* **2003,** 119, (19), 10133-10137.
284. Berquier, J.-M.; Arribart, H., Attenuated total reflection Fourier transform infrared spectroscopy study of poly(methyl methacrylate) adsorption on a silica thin film: polymer/surface interactions. *Langmuir* **1998,** 14, (13), 3716-3719.
285. Hua, Z.-L.; Shi, J.-L.; Wang, L.; Zhang, W.-H., Preparation of mesoporous silica films on a glass slide: surfactant template removal by solvent extraction. *J. Non-Cryst. Solids* **2001,** 292, (1-3), 177-183.
286. Wang, X.; Lin, K. S. K.; Chan, J. C. C.; Cheng, S., Direct Synthesis and Catalytic Applications of Ordered Large Pore Aminopropyl-Functionalized SBA-15 Mesoporous Materials. *J. Phys. Chem. B* **2005,** 109, (5), 1763-1769.
287. Dijkstra, T. W.; Duchateau, R.; van Santen, R. A.; Meetsma, A.; Yap, G. P. A., Silsesquioxane Models for Geminal Silica Surface Silanol Sites. A Spectroscopic

Investigation of Different Types of Silanols. *J. Am. Chem. Soc.* **2002,** 124, (33), 9856-9864.
288. Zhuravlev, L. T., The surface chemistry of amorphous silica. Zhuravlev model. *Colloids Surf., A* **2000,** 173, (1-3), 1-38.
289. Dai, S.; Shin, Y.; Barnes, C. E.; Toth, L. M., Enhancement of Uranyl Adsorption Capacity and Selectivity on Silica Sol-Gel Glasses via Molecular Imprinting. *Chem. Mater.* **1997,** 9, (11), 2521-2525.
290. Burleigh, M. C.; Markowitz, M. A.; Spector, M. S.; Gaber, B. P., Direct Synthesis of Periodic Mesoporous Organosilicas: Functional Incorporation by Co-condensation with Organosilanes. *J. Phys. Chem. B* **2001,** 105, (41), 9935-9942.
291. Graham, A. L.; Carlson, C. A.; Edmiston, P. L., Development and characterization of molecularly imprinted sol-gel materials for the selective detection of DDT. *Anal. Chem.* **2002,** 74, (2), 458-467.
292. Antonelli, D. M.; Nakahira, A.; Ying, J. Y., Ligand-Assisted Liquid Crystal Templating in Mesoporous Niobium Oxide Molecular Sieves. *Inorganic Chemistry* **1996,** 35, (11), 3126-36.

VITA

Date of Birth:
October 1, 1974

Place of Birth:
Comilla, Bangladesh

EDUCATION

M.S. Chemical Engineering, North Carolina A&T State University (July, 2003)

B.S. Chemical Engineering, Bangladesh University of Engineering and Technology, Bangladesh (September, 1998)

PROFESSIONAL POSITIONS

Senior Engineer, Cummins Inc., Columbus, IN (July, 2008 to Present)

Lecturer, Department of Chemical Engineering, Bangladesh University of Engineering and Technology, Bangladesh (December, 1999 to December, 2000)

PUBLICATIONS

Rahman, M. S. & Rankin, S. "Lyotropic Liquid Crystalline Phases in Aqueous Mixtures of Maltoside and Cationic Surfactants: Predictive Synthesis of Ordered Mesoporous Silica" Submitted, Journal of Colloid and Interface Science, 2009

Rahman, M. S. & Rankin, S. "Si-Ti Mixed Oxide Thin Films with 3D-Accesible Pores: Incorporation of Ti by Surfactant Complexation" (manuscript under preparation)

PRESENTATIONS

Rahman, M. S. & Rankin, S. E. "Silica-Titania Mixed Oxide Mesoporous Thin Films: Incorporation of Ti By Surfactant Complexation" 2007 AIChE National Meeting, Salt Lake City, UT

Rahman, M. S. & Rankin, S. E. "Ternary Phase Diagram of Cationic and Maltoside Surfactants in Water, and Its Use for Predictive Synthesis of Ordered Mesoporous Silica" 2006 AIChE National Meeting, San Francisco, CA

Rahman, M. S. & Rankin, S. E. "Lyotropic phase behavior of aqueous cationic/maltoside surfactant mixtures and predictive synthesis of ordered mesoporous silica using these surfactants" 2006 ACS Spring National Meeting, Atlanta, GA

Rahman, M. S. & Ilias, S. “Separation of Hydrogen and Carbon Dioxide Using a Novel Membrane Reactor in Advanced Fossil Energy Conversion Processes.” Poster session presented at US DOE University of Coal Research Contractors Review Meeting, 2002, Pittsburgh, PA

Mohammed Shahidur Rahman